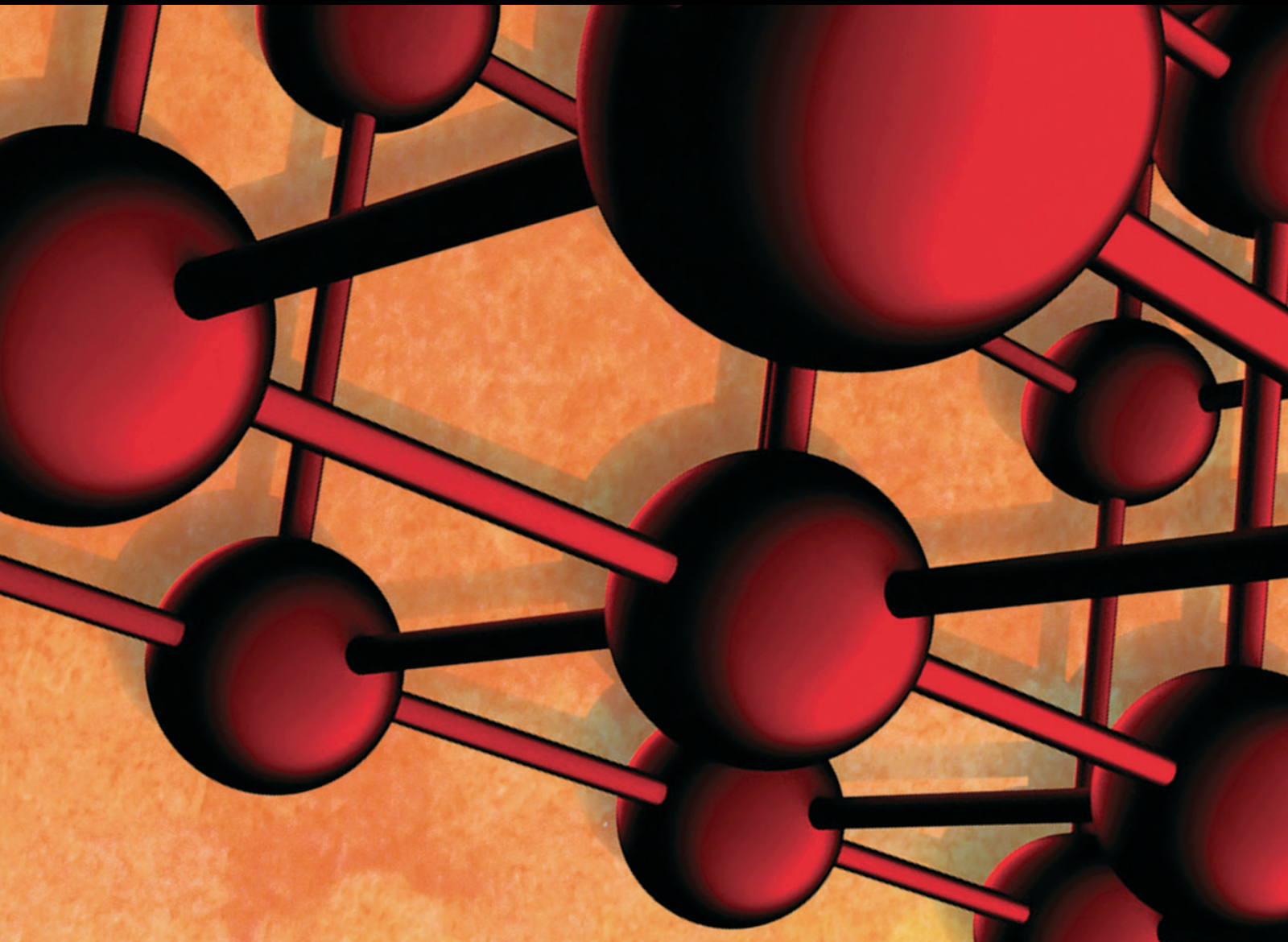


Advances in Materials Science and Engineering

Innovative Materials, New Design Methods, and Advanced Characterization Techniques for Sustainable Asphalt Pavements

Lead Guest Editor: Ghazi G. Al-Khateeb

Guest Editors: Syed W. Haider, Mujib Rahman, and Munir Nazzal





**Innovative Materials, New Design Methods,
and Advanced Characterization Techniques for
Sustainable Asphalt Pavements**

Advances in Materials Science and Engineering

**Innovative Materials, New Design Methods,
and Advanced Characterization Techniques for
Sustainable Asphalt Pavements**

Lead Guest Editor: Ghazi G. Al-Khateeb

Guest Editors: Syed W. Haider, Mujib Rahman, and Munir Nazzal



Copyright © 2019 Hindawi. All rights reserved.

This is a special issue published in “Advances in Materials Science and Engineering.” All articles are open access articles distributed under the Creative Commons Attribution License, which permits unrestricted use, distribution, and reproduction in any medium, provided the original work is properly cited.

Editorial Board

- Antonio Abate, Germany
H.P.S Abdul Khalil, Malaysia
Michael Aizenshtein, Israel
Hamed Akhavan, Portugal
Jarir Aktaa, Germany
Amelia Almeida, Portugal
Rajan Ambat, Denmark
K. G. Anthymidis, Greece
Santiago Aparicio, Spain
Raul Arenal, Spain
Alicia E. Ares, Argentina
Farhad Aslani, Australia
Apostolos Avgeropoulos, Greece
Renal Backov, France
Markus Bambach, Germany
Amit Bandyopadhyay, USA
Massimiliano Barletta, Italy
Stefano Bellucci, Italy
Avi Bendavid, Australia
Brahim Benmokrane, Canada
Jamal Berakdar, Germany
Jean-Michel Bergheau, France
G. Bernard-Granger, France
Giovanni Berselli, Italy
Patrice Berthod, France
Michele Bianchi, Italy
Hugo C. Biscaia, Portugal
Antonio Boccaccio, Italy
Susmita Bose, USA
H.- G. Brokmeier, Germany
Steve Bull, UK
Gianlorenzo Bussetti, Italy
Jose M. Cabrera, Spain
Antonio Caggiano, Germany
Veronica Calado, Brazil
Marco Cannas, Italy
Paolo Andrea Carraro, Italy
Victor M. Castaño, Mexico
Michelina Catauro, Italy
Robert Černý, Czech Republic
Jose Cesar de Sa, Portugal
Daolun Chen, Canada
Wensu Chen, Australia
Francisco Chinesta, France
- Er-Yuan Chuang, Taiwan
Gianluca Cicala, Italy
Francesco Colangelo, Italy
Marco Consales, Italy
María Criado, Spain
Gabriel Cuello, France
Lucas da Silva, Portugal
Narendra B. Dahotre, USA
João P. Davim, Portugal
Angela De Bonis, Italy
Abílio De Jesus, Portugal
Luca De Stefano, Italy
Francesco Delogu, Italy
Luigi Di Benedetto, Italy
Aldo Di Carlo, Italy
Maria Laura Di Lorenzo, Italy
Marisa Di Sabatino, Norway
Luigi Di Sarno, Italy
Ana María Díez-Pascual, Spain
Guru P. Dinda, USA
Nadka Tzankova Dintcheva, Italy
Hongbiao Dong, China
Mingdong Dong, Denmark
Frederic Dumur, France
Stanislaw Dymek, Poland
Kaveh Edalati, Japan
Philip Eisenlohr, USA
Claude Estournès, France
Luis Evangelista, Norway
Michele Fedel, Italy
Isabel J. Ferrer, Spain
Paolo Ferro, Italy
Dora Foti, Italy
Massimo Fresta, Italy
Pasquale Gallo, Japan
Germà Garcia-Belmonte, Spain
Santiago Garcia-Granda, Spain
Carlos Garcia-Mateo, Spain
Georgios I. Giannopoulos, Greece
Ivan Giorgio, Italy
Antonio Gloria, Italy
Vincenzo Guarino, Italy
Daniel Guay, Canada
Gianluca Gubbiotti, Italy
- Jenö Gubicza, Hungary
Xuchun Gui, China
Benoit Guiffard, France
Ivan Gutierrez-Urrutia, Japan
Hiroki Habazaki, Japan
Simo-Pekka Hannula, Finland
Akbar Heidarzadeh, Iran
David Holec, Austria
Satoshi Horikoshi, Japan
David Houivet, France
Rui Huang, USA
Yi Huang, UK
Michele Iafisco, Italy
Erdir Ibrahim, UK
Saliha Ilcan, Turkey
Md Mainul Islam, Australia
Iliya Ivanov, USA
Hom Kandel, USA
kenji Kaneko, Japan
Fuat Kara, Turkey
Katsuyuki Kida, Japan
Akihiko Kimura, Japan
Soshu Kirihara, Japan
Paweł Kłosowski, Poland
Jan Koci, Czech Republic
Fantao Kong, China
Ling B. Kong, Singapore
Lingxue Kong, Australia
Pramod Koshy, Australia
Hongchao Kou, China
Alexander Kromka, Czech Republic
Andrea Lamberti, Italy
Luciano Lamberti, Italy
Fulvio Lavecchia, Italy
Marino Lavorgna, Italy
Laurent Lebrun, France
Joon-Hyung Lee, Republic of Korea
Pavel Lejcek, Czech Republic
Cristina Leonelli, Italy
Ying Li, USA
Yuanshi Li, Canada
Yuning Li, Canada
Guang-xing Liang, China
Barbara Liguori, Italy

Jun Liu, China
Meilin Liu, Georgia
Shaomin Liu, Australia
Yunqi Liu, China
Zhiping Luo, USA
Fernando Lusquiños, Spain
Peter Majewski, Australia
Georgios Maliaris, Greece
Muhamamd A. Malik, UK
Dimitrios E. Manolakos, Greece
Necmettin Maraşlı, Turkey
Enzo Martinelli, Italy
Alessandro Martucci, Italy
Yoshitake Masuda, Japan
Bobby Kannan Mathan, Australia
Roshan Mayadunne, Australia
Mamoun Medraj, Canada
Shazim A. Memon, Kazakhstan
Philippe Miele, France
A. E. Miroshnichenko, Australia
Hossein Moayedi, Iran
Sakar Mohan, India
Jose M. Monzo, Spain
Michele Muccini, Italy
Alfonso Muñoz, Spain
Roger Narayan, USA
Rufino M. Navarro, Spain
Miguel Navarro-Cia, UK
Ali Nazari, Australia
Behzad Nematollahi, Australia
Luigi Nicolais, Italy
Peter Niemz, Switzerland
Hiroshi Noguchi, Japan
Chérif Nouar, France
Olanrewaju Ojo, Canada
Dariusz Oleszak, Poland
Laurent Orgéas, France
Togay Ozbakkaloglu, UK
Nezih Pala, USA
Marián Palcut, Slovakia
Davide Palumbo, Italy
Gianfranco Palumbo, Italy
A. Maria Paradowska, Australia
Zbyšek Pavlík, Czech Republic
Matthew Peel, UK
Alessandro Pegoretti, Italy
Gianluca Percoco, Italy
Claudio Pettinari, Italy
Giorgio Pia, Italy
Silvia M. Pietralunga, Italy
Daniela Pilone, Italy
Teresa M. Piqué, Argentina
Candido Fabrizio Pirri, Italy
Marinos Pitsikalis, Greece
Alain Portavoce, France
Simon C. Potter, Canada
Ulrich Prah, Germany
Viviana F. Rahhal, Argentina
Carlos R. Rambo, Brazil
Shahed Rasekh, Portugal
Manijeh Razeghi, USA
Paulo Reis, Portugal
Yuri Ribakov, Israel
Aniello Riccio, Italy
Anna Richelli, Italy
Antonio Riveiro, Spain
Marco Rossi, Italy
Sylvie Rossignol, France
Pascal Roussel, France
Fernando Rubio-Marcos, Spain
Francesco Ruffino, Italy
Mark H. Rummeli, China
Pietro Russo, Italy
Antti Salminen, Finland
F.H. Samuel, Canada
MariaGabriella Santonicola, Italy
Hélder A. Santos, Finland
Carlo Santulli, Italy
Fabrizio Sarasini, Italy
Michael J. Schütze, Germany
Raffaele Sepe, Italy
Kenichi Shimizu, USA
Fridon Shubitidze, USA
Mercedes Solla, Spain
Donato Sorgente, Italy
Charles C. Sorrell, Australia
Andres Sotelo, Spain
Costas M. Soukoulis, USA
Damien Soulat, France
Adolfo Speghini, Italy
Antonino Squillace, Italy
Koichi Sugimoto, Japan
Baozhong Sun, China
Sam-Shajing Sun, USA
Youhong Tang, Australia
Kohji Tashiro, Japan
Miguel Angel Torres, Spain
Laszlo Toth, France
Achim Trampert, Germany
Tomasz Trzepieciński, Poland
Matjaz Valant, Slovenia
Luca Valentini, Italy
Ashkan Vaziri, USA
Lijing Wang, Australia
Rui Wang, China
Zhongchang Wang, Portugal
Lu Wei, China
Jörg M. K. Wiezorek, USA
Jiang Wu, UK
Guoqiang Xie, China
Dongmin Yang, UK
Zhonghua Yao, China
Hemmige S. Yathirajan, India
Yee-wen Yen, Taiwan
Wenbin Yi, China
Ling Yin, Australia
Tetsu Yonezawa, Japan
Hiroshi Yoshihara, Japan
Belal F. Yousif, Australia
Lenka Zajíčková, Czech Republic
Michele Zappalorto, Italy
Gang Zhang, Singapore
Jinghuai Zhang, China
Li Zhang, China
Meng Zhang, USA
Mikhail Zheludkevich, Germany
Wei Zhou, China
You Zhou, Japan
Hongtao Zhu, Australia
J. A. Fonseca de Oliveira Correia, Portugal
F. J. Fernández Fernández, Spain

Contents

Innovative Materials, New Design Methods, and Advanced Characterization Techniques for Sustainable Asphalt Pavements

Ghazi G. Al-Khateeb , Syed W. Haider, Mujib Rahman, and Munir Nazzal
Editorial (3 pages), Article ID 8241071, Volume 2019 (2019)

Rutting and Fatigue Properties of Cellulose Fiber-Added Stone Mastic Asphalt Concrete Mixtures

Muhammad Irfan , Yasir Ali, Sarfraz Ahmed, Shahid Iqbal, and Hainian Wang 
Research Article (8 pages), Article ID 5604197, Volume 2019 (2019)

Size Effects of Finite Element Model for Three-Dimensional Microstructural Modeling of Asphalt Mixture

Kuanghuai Wu, Qingzi Deng, Naiming Deng, Xu Cai , and Wenke Huang 
Research Article (9 pages), Article ID 1754567, Volume 2019 (2019)

Effect of Recycling Agents on Rheological and Micromechanical Properties of SBS-Modified Asphalt Binders

Meng Guo , Yiqiu Tan, Daisong Luo, Yafei Li, Asim Farooq , Liantong Mo, and Yubo Jiao
Research Article (12 pages), Article ID 5482368, Volume 2018 (2019)

Study on Cooling Effect and Pavement Performance of Thermal-Resistant Asphalt Mixture

Jiarong Wang, Zhengqi Zhang , Datong Guo, Cheng Xu, and Ke Zhang
Research Article (11 pages), Article ID 6107656, Volume 2018 (2019)

Comparative Study on the Axial Compression and Bearing Capacity of Reactive Powder Concrete-Filled Circular Steel Tube

Mingyang Chen  and Xiaomeng Hou
Research Article (11 pages), Article ID 8038649, Volume 2018 (2019)

Superposed Incremental Deformations of an Elastic Solid Reinforced with Fibers Resistant to Extension and Flexure

Chun IL Kim 
Research Article (11 pages), Article ID 6501985, Volume 2018 (2019)

Study on Mechanics-Based Cracking Resistance of Semiflexible Pavement Materials

Duanyi Wang, Xiayi Liang , Danning Li , Hehao Liang , and Huayang Yu 
Research Article (10 pages), Article ID 8252347, Volume 2018 (2019)

Strength Characteristics and the Reaction Mechanism of Stone Powder Cement Tailings Backfill

Jianhua Hu , Qifan Ren , Quan Jiang, Rugao Gao , Long Zhang, and Zhouquan Luo
Research Article (14 pages), Article ID 8651239, Volume 2018 (2019)

Comparison of Asphalt Mixtures Designed Using the Marshall and Improved GTM Methods

Jianbing Lv , Xu Zhancheng, Yin Yingmei, Zhang Jiantong, Sun Xiaolong, and Wu Chuanhai
Research Article (7 pages), Article ID 7328791, Volume 2018 (2019)

Influence of Macrotexture and Microtexture on the Skid Resistance of Aggregates

Bowen Guan , Jiayu Wu, Chao Xie, Jianhong Fang, Haile Zheng, and Huaxin Chen 
Research Article (9 pages), Article ID 1437069, Volume 2018 (2019)

High- and Low-Temperature Properties and Thermal Stability of Silica Fume/SBS Composite-Modified Asphalt Mortar

Cao Kai, Xu Wenyuan , Chen Dan, and Feng Huimin
Research Article (8 pages), Article ID 1317436, Volume 2018 (2019)

An Assessment of Reuse of Light Ash from Bayer Process Fluidized Bed Boilers in Geopolymer Synthesis at Ambient Temperature

Washington S. Brito , André L. Mileo Ferraioli Silva , Rozineide A. A. Boca Santa, Kristoff Svensson, José Antônio da Silva Souza, Herbert Pöllmann, and Humberto Gracher Riella
Research Article (6 pages), Article ID 1287243, Volume 2018 (2019)

Editorial

Innovative Materials, New Design Methods, and Advanced Characterization Techniques for Sustainable Asphalt Pavements

Ghazi G. Al-Khateeb ¹, **Syed W. Haider**,² **Mujib Rahman**,³ and **Munir Nazzal**⁴

¹Department of Civil and Environmental Engineering, University of Sharjah, Sharjah, UAE

²Department of Civil and Environmental Engineering, Michigan State University, East Lansing, Michigan, USA

³Department of Civil and Environmental Engineering, Brunel University London, Uxbridge, London, UK

⁴Department of Civil Engineering, Ohio University, Athens, Ohio, USA

Correspondence should be addressed to Ghazi G. Al-Khateeb; galkhateeb@sharjah.ac.ae

Received 27 March 2019; Accepted 27 March 2019; Published 16 April 2019

Copyright © 2019 Ghazi G. Al-Khateeb et al. This is an open access article distributed under the Creative Commons Attribution License, which permits unrestricted use, distribution, and reproduction in any medium, provided the original work is properly cited.

New and innovative materials are continually being researched and developed by asphalt technologists, particularly in the last decade to find the most economical, efficient, and environmentally friendly product to use on roads. Parallel to that, advanced characterization techniques and methodologies are also being developed to characterize materials for best results. Innovative materials include recycled and waste materials (green materials), low-cost and high-performance materials, and materials that reduce energy consumption. Recycled asphalt pavement (RAP) material is considered among the most common materials used in asphalt pavements. The RAP material is a useful alternative to virgin materials because it reduces the need to use virgin aggregate which has limited resources in some areas of the United States and the World [1]. The FHWA continues to encourage the use of waste tire rubber for asphalt paving for its cost-effectiveness, easy handling, and better fatigue performance [2]. Plastic waste is relatively a new material recently introduced in the asphalt technology [4]. Another innovative material is the bioasphalt that is considered a breakthrough in renewable pavements. The bioasphalt is produced from non-petroleum-based renewable resources such as corn, rice, potato starches, and other plants, which are converted into a type of bitumen binder for the asphalt [3]. In this special issue, published papers are dealing with innovative materials, design methods, and characterization techniques that well agree with the main scope and goals of the special issue. The papers are mainly classified into three main categories: (1) new materials and their behavior and

performance, (2) the mechanics and performance of composite paving materials, and (3) new design and characterization methods and modeling.

A study by W. S. Brito et al. assessed the reuse of fly ash of Bayer process boilers in geopolymer synthesis. X-ray fluorescence (XRF) and scanning electron microscopy (SEM) techniques were used to characterize the raw materials and geopolymers. The study concluded that synthesized geopolymers have great potential for production of geopolymeric materials with greater mechanical compressive strength. C. Kai et al. utilized silica powder in styrene-butadiene-styrene- (SBS-) modified asphalt. The silica powder was collected from the exhaust gases produced by smelting industrial silicon often used as a cement concrete admixture in China. Rheological tests such as viscosity, dynamic shear rheometer (DSR), and bending beam rheometer (BBR) tests were used to study the behavior of the composite-modified asphalt. The results of the study showed that the high-temperature and low-temperature performances were improved by the increase in silica powder content and ratio of filler-asphalt, and by the increase in the silica powder content with an optimum value of 7%, respectively. However, the increase in the ratio of filler-asphalt reduced the low-temperature cracking resistance of the asphalt. A study by M. Irfan et al. investigated the effect of the cellulose fiber addition (0.3% by total weight of aggregates) on the performance of three stone mastic asphalt (SMA) concrete mixtures with three different nominal maximum aggregate sizes (NMASs): 12.5, 19, and 25 mm.

The results revealed that SMA mixture with an NMAS of 12.5 mm and a binder content of 5.3% showed relatively better resistance to fatigue cracking. On the other hand, SMA mixture with an NMAS of 25 mm (coarser gradation) exhibited excellent resistance to rutting based on the flow test results. D. Wang et al. also used the cement material in a semiflexible mixture to investigate cracking resistance. Optimal material design and ABAQUS numerical simulation were conducted. Matrix asphalt structures with four different air voids and different cement mortar dosages were used. The findings of their study revealed that the internal stress in this semiflexible mixture is mainly determined by the contraction rather than the expansion of cement mortar, and the larger air void and less volumetric variation of cement mortar reduced the internal stress of the matrix structure. J. Wang et al. in another study, to reduce the temperature of asphalt pavement and improve the anti-rutting performance of the asphalt mixture, produced a thermal-resistant asphalt mixture (TRAM), in which a certain proportion of mineral aggregate was replaced by ceramic (CE) or floating beads (FB) with low thermal conductivity. The results showed that the addition of thermal-resistant materials can reduce the thermal conductivity and the temperature of the asphalt mixture. Consequently, the CE and FB can improve the anti-rutting performance of the asphalt mixture by reducing the temperature inside the pavement.

Although two materials were used in two different papers for concrete structures, their improved performance results rendered them as two innovative materials. The stone powder cement (SPC) in a study by J. Hu et al. was used as a novel cement substitute material in concrete for its good gelling performance and low cost. The addition of stone powder improved the microstructure of the backfill and produced a denser three-dimensional (3D) network structure. The cement powder mixed appropriately with the stone powder could meet the strength requirement and reduce the cost of backfilling materials. M. Chen and X. Hou used the reactive powder in a concrete-filled circular steel tube to assess the axial compression and bearing capacity of the tube. The confining coefficient was found to be the main factor affecting the ultimate bearing capacity. The design proposal for an RPC-filled steel tube was recommended based on the experimental analysis results and China's "Design and construction" code for concrete-filled steel tube structure.

While the above studies focused on new materials, a study by M. Guo et al. investigated the effect of aging and rejuvenator recycling on the rheological and micro-mechanical properties of SBS-modified asphalt binders. The results of infrared spectroscopy tests demonstrated that the crosslinking structure of asphalt was destroyed and SBS modification effect gradually diminished after aging. Scanning electron microscope (SEM) tests showed that the island structure of SBS-modified asphalt disappeared after aging. Energy spectrum analysis showed that the C (carbon) content of aged SBS-modified asphalt decreased, while the O (oxygen) content and S (sulfur) content increased. Results of the fluorescence microscope, SEM, and rheological tests

showed that the epoxy functional group compounds of aliphatic glycidyl ether resin had high reactivity, and the triblock molecular structure of SBS and the mechanical performance of SBS-modified asphalt were recovered.

Two papers of this issue studied material modeling. In the first paper, K. Wu et al. studied the effect of voxel size on a three-dimensional microstructural modeling of the asphalt mixture using finite element analysis. The computed tomography (CT) image-based finite element approach was used as an effective method to simulate the micromechanical response of the asphalt mixture. Four micromechanical digital models were generated with voxel sizes of 0.5 mm, 0.67 mm, 1.0 mm, and 2.0 mm, respectively. Simulation results showed that the voxel sizes had a significant effect on creep stiffness modulus, and the most appropriate voxel size was found to be 1.0 mm. In the second paper, C. I. Kim presented a comprehensive linear model for an elastic solid reinforced with fibers resistant to extension and flexure. In particular, the complete systems of differential equations were obtained for the cases of Neo-Hookean and Mooney–Rivlin types of materials from which analytical solutions could be obtained.

Finally, two papers studied design methods and field performance. J. Lv et al. compared the traditional Marshall design method to the gyratory testing machine (GTM) method based on the oil-stone ratio, high-temperature stability, water stability, and rutting resistance of the mixes used in their study. The GTM method was recommended in this paper to be introduced and used on a large scale suitable for high temperatures and heavy traffic in Guangdong Province of China. In the second paper, the effect of macrotexture and microtexture on the skid resistance of aggregates was studied by B. Guan et al. Fractal dimension, root mean square height, and Polished Stone Value (PSV) were tested. The results showed that the PSV development was approximately divided into stages including the accelerated attenuation stage, decelerated attenuation stage, and stabilization stage. When the number of polishing cycles exceeded a critical point, microtexture replaced macrotexture to play a major role in the skid resistance of aggregates. In the accelerated attenuation stage, macrotexture was found to play a major role in the skid resistance of aggregates, whereas microtexture gradually played a major role in the skid resistance of aggregates in the other two stages.

Conflicts of Interest

The editors declare that they have no conflicts of interest regarding the publication of this special issue.

Ghazi G. Al-Khateeb
Syed W. Haider
Mujib Rahman
Munir Nazzal

References

- [1] A. Copeland, *Reclaimed Asphalt Pavement in Asphalt Mixtures: State of the Practice*, Publication No. FHWA-HRT-11-021,

- Federal Highway Administration (FHWA) Publications, Washington, DC, USA, 2011.
- [2] N. Gibson, X. Qi, A. Shenoy et al., *Performance Testing for Superpave and Structural Validation*, Publication No. FHWA-HRT-11-045, Federal Highway Administration (FHWA) Publications, Washington, DC, USA, 2012.
 - [3] M. He, D.-W. Cao, H.-Y. Zhang, Z.-R. Song, and X.-W. Wu, "Research on conventional performance of modified bio-asphalt," *Journal of Highway and Transportation Research and Development (English Edition)*, vol. 9, no. 2, pp. 1–6, 2015.
 - [4] A. A. Badejo, A. A. Adekunle, O. O. Adekoya et al., "Plastic waste as strength modifiers in asphalt for a sustainable environment," *African Journal of Science, Technology, Innovation and Development*, vol. 9, no. 2, pp. 173–177, 2017.

Research Article

Rutting and Fatigue Properties of Cellulose Fiber-Added Stone Mastic Asphalt Concrete Mixtures

Muhammad Irfan ¹, Yasir Ali,² Sarfraz Ahmed,¹ Shahid Iqbal,¹ and Hainian Wang ³

¹Military College of Engineering, National University of Sciences & Technology (NUST), Islamabad 44000, Pakistan

²National Institute of Transportation, National University of Sciences & Technology (NUST), Islamabad 44000, Pakistan

³South Erhuan Middle Section, Chang'an University, School of Highway, Xi'an 710064, China

Correspondence should be addressed to Muhammad Irfan; mirfan@mce.nust.edu.pk

Received 9 August 2018; Accepted 7 March 2019; Published 25 March 2019

Guest Editor: Munir Nazzal

Copyright © 2019 Muhammad Irfan et al. This is an open access article distributed under the Creative Commons Attribution License, which permits unrestricted use, distribution, and reproduction in any medium, provided the original work is properly cited.

This paper investigates dynamic response, rutting resistance, and fatigue behavior of three stone mastic asphalt (SMA) concrete mixtures selected on basis of nominal maximum aggregate size (NMAS): 25 mm, 19 mm, and 12.5 mm using cellulose fiber added as 0.3% of the total weight of aggregate. Superpave gyratory specimens were fabricated and subjected to the dynamic modulus ($|E^*|$) and flow tests (flow number and flow time) using an asphalt mixture performance tester. The $|E^*|$ test results were employed to develop stress-dependent master curves for each mixture, indicating that the mixture with the NMAS of 25 mm is relatively stiffer than other tested mixtures; this mixture also exhibits excellent strength against rutting failure. In addition, fatigue parameter, which is derived from dynamic response and phase angle, is determined, and results reveal that 12.5 mm NMAS mix has relatively better resistance to fatigue than other selected mixtures. Furthermore, nonlinear regression model specifications were utilized to predict accumulated strains as a function of loading cycles. Also, a flow number model is developed that predicts the rutting behavior of mixtures, and results suggest that model predicted and observed outputs of 25 mm SMA mix are found to be very close. The results of this study help in understanding the performance and behavior of cellulose fiber-added stone mastic asphalt concrete mixtures under varying simulated temperature and stress levels, which can be used in areas where the premature failure of flexible pavements is often observed. The testing protocol employed in this study will also help in evaluating pavement performance using Mechanistic-Empirical Pavement Design Guide.

1. Introduction

Rutting and fatigue in flexible pavements are two of the common distresses manifested on national highways across the globe. Various factors are associated with these distresses including overloading, high temperatures, and empirical design approach used for structural design. To this end, SMA is considered an effective solution in heavily trafficked areas because of larger single size aggregate that can be used with the increased bitumen, thus controlling rutting susceptibility. The resistance to fatigue and reflection cracking is enhanced due to higher binder content in SMA mixtures. In various parts of the world, use of SMA is very common for heavily trafficked areas. The reason for such usage could be

the design of SMA mixtures, in which wheel load is endured by the coarse aggregate skeleton that contributes towards resistance to rutting and rich binder that seals the voids and consequently makes it tougher. Thus, the contact among stones in coarse aggregate dominates, whereas the fine and intermediate aggregate sizes assist to grip the coarser particles when the mix is spaced out.

SMA texture characteristically provides good riding quality, better skid resistance along with comparatively little noise. The coarse aggregate provides durability that contributes towards tremendous resistance to permanent deformation, and higher bitumen content seals the voids and makes it exceedingly resilient. The drainage inhibitor is needed to avoid bitumen bleeding throughout the service life

of the pavement structure. To enhance the mechanical properties of SMA, modified bitumen along with suitable additives can be used; and in some situations, it can reduce or even exclude the requirement for other drainage inhibitors.

A considerable improvement has been observed in recent past in relation to the design of the pavement structure where the fundamental mechanistic properties were given substantial importance. Various new pavement mixtures have been developed along with performance-based grading and mixture design/analysis system, more commonly known as Superior Performing Asphalt Pavements (Superpave) by Strategic Highway Research Program (SHRP). Such developments have considerably reduced the industries' reliance on conventional empirical mix design methods, as proposed by Marshall and Hveem across the globe. More discussion is to follow in ensuing sections.

2. Literature Review

Bonaquist et al. [1] recommended three types of performance tests in National Cooperative Highway Research Program (NCHRP) Report 513: dynamic modulus ($|E^*|$), flow number (FN), and flow time (FT) tests for the superpave mix design procedure to predict the performance of designed asphalt mixtures. The $|E^*|$ test was already being used to predict in situ performance of asphalt mixtures, and the use of flow tests (i.e., FN and FT) was very limited. Later, it was more pronounced that the $|E^*|$ test alone is not an accurate predictor of a mix behavior at higher temperatures; more emphasis is now being given to other two performance tests, i.e., FN and FT tests [2]. To shed more light, a detailed literature review is presented below.

Judycki [3] determined the influence of low-temperature physical hardening on stiffness and tensile strength of conventional asphalt concrete and SMA. $|E^*|$ and indirect tensile strength tests were carried out on mixtures after isothermal storage at a temperature of -20°C , at different time intervals up to 16 days. This study concludes that the strength was noticeably increased after storage. Muniandy et al. [4] evaluated the fatigue behavior of modified and unmodified asphalt binder SMA mixtures using a newly developed crack meander technique. The results obtained from the crack analysis test were compared using strain plots obtained from the indirect tensile fatigue test and concluded that fatigue behavior can be determined using the crack appearance method. Iskender [5] determined the rutting resistance of basalt and basalt-limestone aggregate combination for SMA using Laboratoire Central des Ponts et Chaussées (LCPC) wheel tracking test. This research study concludes that rutting resistance was decreased with addition of limestone in SMA as fine/filler material. A study illustrates the effects of adding waste polyethylene terephthalate (PET) on stiffness and fatigue properties of SMA mixtures. This research concludes that the stiffness of mixtures increased when a lower amount of PET is added, and PET-reinforced mixtures exhibit higher fatigue lives compared to controlled mixtures (without PET) [6]. Ahmadiania et al. [7] used waste plastic bottles as an additive

for SMA mixtures, and 6% by weight of bitumen was found an optimum quantity of PET. This study concludes that introduction of PET into SMA mixtures significantly improves engineering and mechanical properties. Behnood and Ameri [8] utilized steel slag aggregate in SMA, and results indicate that use of steel slag as a surrogate to coarse aggregate enhanced the Marshall stability, resilient modulus, tensile strength, resistance to moisture damage, and resistance to the permanent deformation.

Sengul et al. [9] conducted Marshall Quotient (MQ) approach, repeated creep test (RCT), indirect tensile strength test (ITST), and Laboratoire Central des Ponts et Chaussées (LCPC) Wheel tracking tests on the SBS polymer modified SMA. The results reveal that addition of SBS increased resistance to the plastic deformation and lowered rutting values compared to conventional mixtures. In another study, lime was added to SMA in order to reduce stripping potential and moisture susceptibility. Response surface methodology was used to determine the effect of lime content and grading on stripping potential of SMA using tensile strength ratio (TSR) index and found that lime content of 1% and finest aggregate yielded a TSR optimum value of $91.8\% \pm 0.8\%$ [10]. Cao et al. [11] evaluated $|E^*|$ of SMA (basalt, B-SMA, limestone, L-SMA, and BL-SMA), and results suggest that B-SMA showed better rutting resistance than other tested mixtures. Pasetto and Baldo [12] conducted a comparative analysis of SMAs with electric arc furnace steel slag. The research has been enunciated in a preliminary study of the chemical, leaching, physical, and mechanical properties of the steel slag and concludes that steel slag has satisfied all requirements of road sector technical standards and shows higher mechanical characteristics than other mixtures. Numerous studies indicated the use of the various additives in SMA apart from cellulose fiber [4–6, 9, 11, 13–15]. Different research demonstrated the evaluation of $|E^*|$ and development of master curves [14, 16–28].

The design of the SMA mixture consists of material selection, determining optimum aggregate gradation, selection of additive and its quantity, and optimum binder content. Furthermore, SMA mixtures are supposed to ensure stability and rutting resistance obtained from aggregate contact and interlock; durability of SMA mixtures is obtained by appropriate mixture design including air voids, voids in mineral aggregate, thickness of asphalt film, and filler quantity.

The asphalt concrete material behaves like a viscoelastic material, and its stiffness varies with the temperature. Higher stiffness/modulus in low temperatures (winters) results in fatigue cracking, and lower stiffness/modulus in high temperatures (summers) results in rutting. The strength of the asphalt material is reduced tremendously with higher temperatures as in Pakistan. Hence, it is mandatory to characterize mixtures with an additive using full test protocol of simple performance ($|E^*|$, FN, and FT) for diverse loading and environmental conditions of Pakistan. This study assesses the performance of SMA mixtures having cellulose fiber using three performance tests, i.e., $|E^*|$, FN, and FT. The results obtained from these tests were further

employed to construction master curves and estimation of fatigue cracking by deriving a fatigue parameter.

3. Objective and Scope

The objective of this research is to investigate the performance of various cellulose fiber-added SMA mixtures by varying NMAS. The performance indicators used in this study are $|E^*|$, FN, and FT. The results obtained from $|E^*|$ are used to determine stiffness moduli and to estimate resistance to fatigue cracking based on $|E^*|$ and phase angle values. This study also describes the rutting potential of mixtures using statistical models that use two different nonlinear formulations to express the number of cycles to failure as a function of axial strain. Three different gradations of nominal maximum aggregate size (NMAS) of 25 mm, 19 mm, and 12.5 mm are selected from the gradation bands developed by National Center of Asphalt Technology (NCAT). A 0.3% cellulose fiber by the total weight of the SMA mixtures aggregate was added, and asphalt binder of penetration grade 60/70 was used. Note that different percentages of cellulose fiber were tested during the initial testing phase, and it was found that 0.3% is an optimum quantity that satisfies the Marshall mix design criteria.

4. Methodology

The ensuing sections explain the methodology adopted in this research study and illustrated in Figure 1.

4.1. Selection of Materials. This research study includes testing of three SMA mixtures differentiated by NMAS that are internationally practiced. Three different gradations based on NMAS of 25 mm, 19 mm, and 12.5 mm are selected from the gradation bands developed by National Center of Asphalt Pavements (NCAT) in the National Cooperative Highway Research Program (NCHRP) report [29], and gradations charts for SMA mixtures are presented in Figure 2. The cellulose fibers of 2-3 mm long pressed pellets have been used as an additive to SMA mixtures to enhance film coating on the aggregate, mix stability, and better interlocking of aggregate skeleton. The optimum bitumen content and mix volumetric analysis are presented in Table 1.

Design of SMA mixtures primarily depends on volumetric properties such as air voids, voids in mineral aggregate, voids in coarse aggregate, and binder content. Brown and Haddock [30] presented optimal proportion selection of coarse and fine aggregates. The volume of coarse aggregate is taken as proportion and bulk density of coarse aggregate. Voids in coarse aggregate for 14 mm nominal size aggregate usually range between 41 and 46% for aggregates compacted with binder with no fine aggregate.

Another important consideration in designing SMA is the filler/additive. This study uses cellulose fiber pellets, VIATOP[®] manufactured by J. Rettenmaier and Söhne, Germany (Figure 3). VIATOP[®] is pelletized blend of ARBOCEL[®] ZZ 8/1 (90% by weight) and bitumen 50/70 (10% by weight). Cellulose fibers, as a stabilizing agent, have

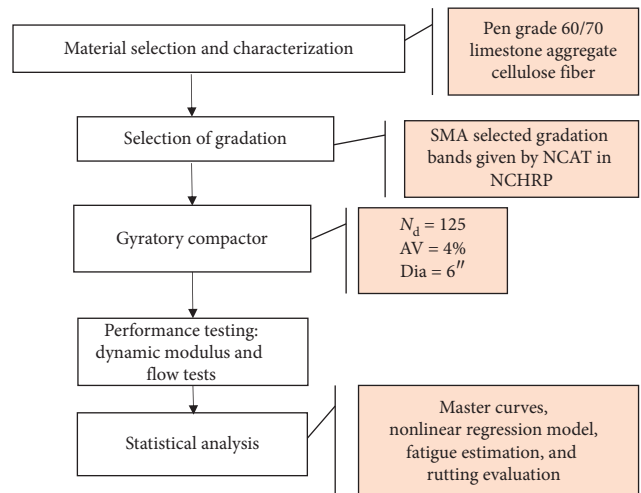


FIGURE 1: Experimental design of study.

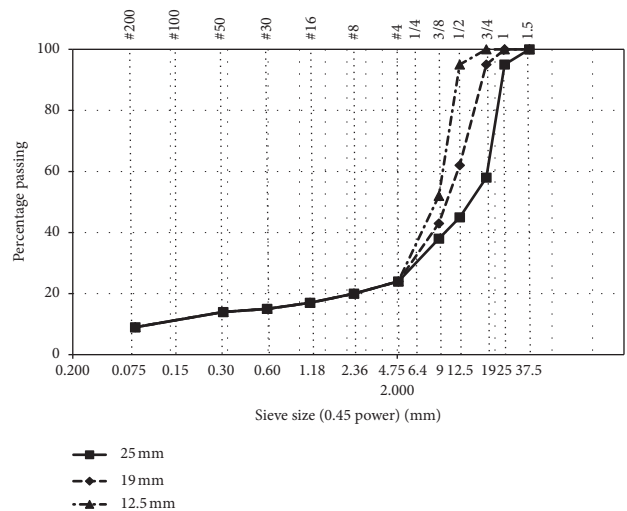


FIGURE 2: Gradation plot for SMA mixtures.

TABLE 1: Mix volumetric analysis of SMA mixtures.

Parameters	Mixtures			Range
	25 mm	19 mm	12.5 mm	
Asphalt content (%)	5.30	5.80	6.30	5–7.5
Air voids (%)	5.60	4.90	4.00	4–7
VMA (%)	19.81	18.78	18.01	Min.: 17
VFA (%)	71.73	73.90	78.01	65–80



FIGURE 3: Cellulose fiber pellets used in SMA mixtures.

a higher asphalt content, thick film coating, high mix stability, improve strength, and less drainage. The optimal quantity of cellulose fiber is based on appropriate quantity of binder and fiber content.

4.1.1. Specimen Preparation. For all performance testing, a superpave gyratory compactor was used to fabricate specimens. The specimens were placed in an oven for short-term aging of 2 hours prior to compaction. The cylindrical specimens with 100 mm diameter were taken from compacted 150 mm diameter gyratory specimens as per the AASHTO standard [31]. The height to diameter ratio of the specimen was kept 1.5 for all tests.

4.2. Performance Testing. Asphalt mixture performance tester (AMPT), which is commonly known as simple performance tester (SPT), is used for $|E^*|$, FN, and FT tests. The equipment has an environmental chamber that manages temperature from 4 to 60°C and confining pressure up to 210 kPa. The $|E^*|$ test is performed at four different temperatures (4.4, 21.1, 37.8, and 54.4°C) and six frequencies (0.1–25 Hz). After completion of the test, the data are acquired from software and employed for development of stress-dependent master curves and fatigue parameter.

AMPT was also used to conduct FN and FT tests. These tests were carried out at a single effective temperature of 54.4°C and deviator stress of 210 kPa. In case of the FN test, the prepared specimens were subjected to a repeated axial haversine compressive loading pulse of 0.1 seconds followed by a rest period of 0.9 seconds. However, for the FT test, the preconditioned specimens were subjected to a constant axial load until it fails, and permanent deformation was measured with respect to the loading time. This test was set to be terminated at 10,000 cycles or until maximum accumulated permanent strain in specimen reached 5%, or whichever came first [32].

5. Results and Discussion

5.1. Dynamic Modulus, $|E^*|$. The $|E^*|$ testing was performed in accordance with AASHTO TP 62-07 [16], which recommends that $|E^*|$ should be evaluated at four different temperatures and six different frequencies in order to develop master curves. The results obtained from the $|E^*|$ test suggest that, for a given loading frequency, an increase in temperature (from 21.1 to 37.8°C), translated into 41, 55, and 26% drop in $|E^*|$ values on average for 25, 19, and 12.5 mm mixtures, respectively. However, for a given temperature and an increase in loading frequency (from 0.1 to 25 Hz), 76, 85, and 74% of the variation in $|E^*|$ values on average were attributed for 25, 19, and 12.5 mm mixtures, respectively.

Since AASHTO TP 62 recommends the development of master curves, it has a few advantages: it allows the comparison of linear viscoelastic materials that are tested at diverse stress rate (loading frequency) and test temperatures, and it can predict $|E^*|$ even at lower temperatures that cannot be obtained from laboratory equipment due to its inability. The average test results are taken for each

temperature and used while developing a master curve for average $|E^*|$ at a reference temperature of 21°C using the time-temperature superposition principle, in which each temperature $|E^*|$ value is shifted to a reference temperature to obtain a smooth uniform curve. Microsoft Excel© sheet was used to develop master curves that works on the basis of minimization of error sum of squares to fit the curve. The generic form of the sigmoid function used to construct master curves is given by the following equation:

$$\log|E^*| = \delta + \frac{\alpha}{1 + e^{\beta + \gamma(\log f_r)}}, \quad (1)$$

where $\log(|E^*|)$ is the log of dynamic modulus, δ is the minimum modulus value, f_r is the reduced frequency, α is the span of the modulus value, and β and γ are shape parameters.

The maximum stiffness of a mix is a function of the binder at a lower temperature, while at higher temperatures, aggregate interlock overpowers the binder effect and becomes the indicator of mix stiffness. Figure 4 represents master curves for SMA mixtures, which indicated that 25 mm SMA mix has highest $|E^*|$ values at all frequencies while 12.5 mm mixture has lowest $|E^*|$ values.

The $|E^*|$ test values are further employed to derive fatigue parameter that estimates the fatigue resistance of asphalt mixtures [18, 33]. The fatigue parameter is a product of $|E^*|$ and viscoelastic behavior of mix, i.e., phase angle (φ), and can be estimated using equation (2). The fatigue parameter value is inversely proportional to resistance to fatigue cracking. A higher value of the fatigue parameter yields lower resistance to fatigue cracking and vice versa:

$$\text{fatigue parameter} = (|E^*| \times \sin \varphi), \quad (2)$$

where $|E^*|$ is the dynamic modulus (MPa) and φ is the phase angle (degree). The fatigue parameter evaluates the fatigue resistance of asphalt similar to $|G^* \times \sin \delta|$ for asphalt binders. Figure 5 shows the fatigue behavior and resistance to cracking by various SMA gradations, employing the principles of $|E^*|$ and phase angle at a temperature of 21°C. The 25 mm SMA mix shows the highest value for fatigue parameter that translates into minimum resistance to fatigue, whereas the 12.5 mm SMA mix performs relatively better among the tested gradations and exhibits higher resistance to fatigue cracking.

5.2. Flow Tests. The flow number (FN) test was performed in accordance with AASHTO TP 79 [31, 34] and defined as the loading cycle number where tertiary deformation starts. The FN is analogous to field conditions since the loading to the pavement is not continuous. The FN attempts to identify the resistance of a mixture to permanent deformation by measuring the shear deformation that occurs because of haversine loading. The most important output of the FN test is the curve of accumulated strain against the number of loading cycles, which describes the rutting resistance of mixtures (Figure 6). The relationship between the accumulated strain and loading cycles is based on the rutting mechanisms, densification, and shear flow. Figure 6

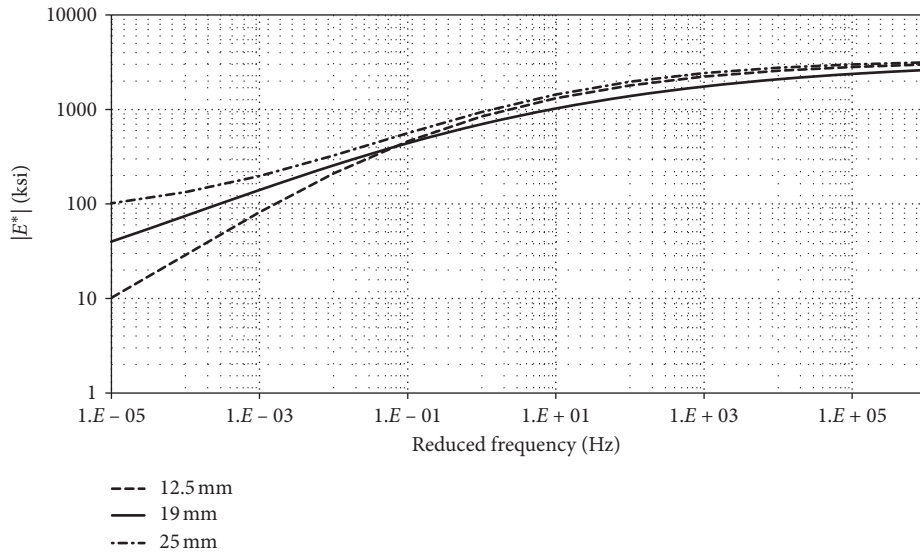


FIGURE 4: Master curves for SMA mixtures.

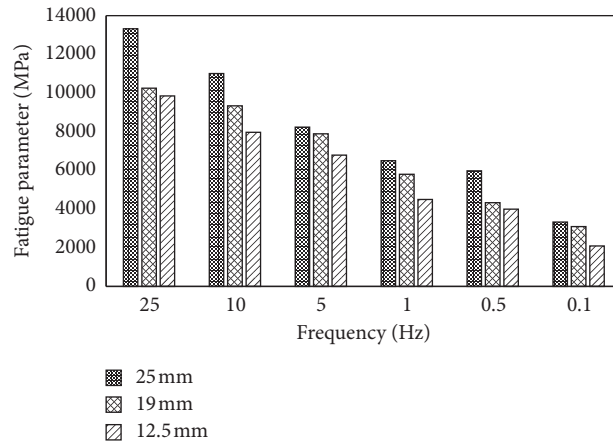


FIGURE 5: Fatigue parameter of SMA mixtures at 21°C.

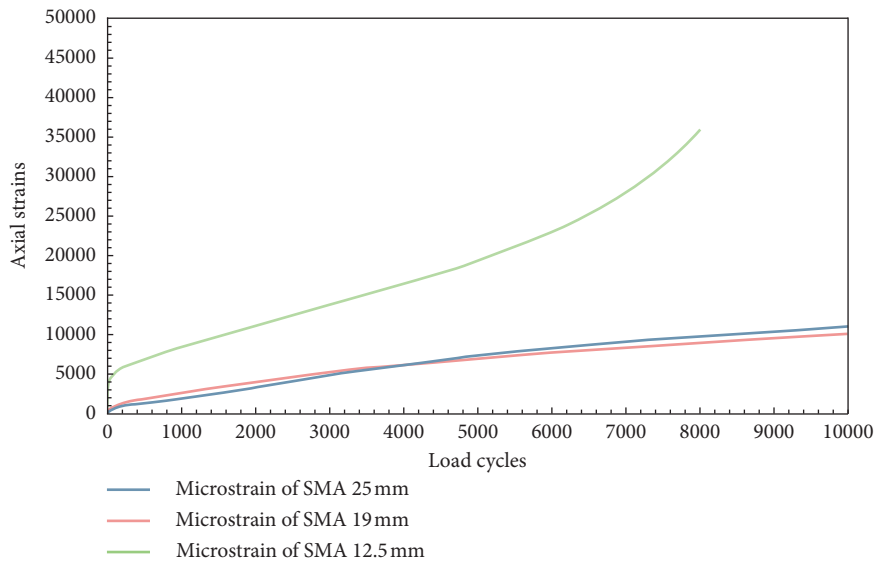


FIGURE 6: Load cycles versus axial strains.

indicates that only 12.5 mm mix has attained tertiary flow among the tested mixtures. The mixtures do not experience tertiary flow stage; therefore, the number of cycles for the completion of the test is regarded as flow number (FN) of these specimens.

The tertiary flow indicates that the strain rate again increases with loading cycles. When a specimen attains the tertiary stage, the data obtained from AMPT equipment software contain resonance that leads to false FN. In order to remove the noise/resonance from data, data smoothing technique, i.e., five-point moving average, is used to obtain corrected FN (Figure 7). The strain rate, against a designated cycle, is obtained by half of the difference of adjacent cycles. The FN is the start point of the tertiary deformation zone and can be reported as the lowest point in the relationship of rate of change of compliance to loading time. In order to confirm FN value visible as lowest on a curve, the equation is solved by putting y equal to zero as stated by Witczak [31] that theoretically FN is the cycle number corresponding to a rate of change of permanent strain equal to zero. Table 2 illustrates the FN and accumulated strains of SMA, and it is quite clear that 25 mm sustains more loading repetitions than any other tested gradations and less susceptible to rutting. However, other two mixtures experience more strains in short interval of time which make them less resistant to rutting.

The termination of FN is set to achieve any one of the two conditions, i.e., permanent strain of 5% or 10,000 loading cycles. Therefore, it requires more time to complete the test than the usual. The data obtained from the extensive lab testing were employed to develop a statistical model to predict pavement performance. This study used two different nonlinear formulations to predict axial strains from loading cycles. The general form of the model is given in the following equation:

$$\text{strain} = f(\text{load cycles}). \quad (3)$$

The data obtained from FN tests were subjected to initial scrutiny that suggests the power and polynomial (2nd order) formulation can best suit such a type of data. The generic form of these models is given in the following equation:

$$\begin{aligned} (\text{power functional form}) Y &= \alpha \times X_i^{\beta_i}, \\ (\text{power functional form}) Y &= \alpha + \beta \times X + \gamma \times X^2. \end{aligned} \quad (4)$$

This functional form can be rewritten for this study as follows:

$$\begin{aligned} \varepsilon_p &= \alpha \times N^\beta, \\ \varepsilon_p &= \alpha + \beta \times N + \gamma \times N^2, \end{aligned} \quad (5)$$

where ε_p is the permanent strain, N is the loading cycles (10,000), and α , β , and γ are regression coefficients.

The model summary and statistics are presented in Table 3. t -Statistics of all variables are higher than t -critical ($|t^*| = 2.30$) at 95% confidence level, which implies that model variables are significant in predicting permanent strain. The coefficient of determination (R^2) is 0.99 and 0.91

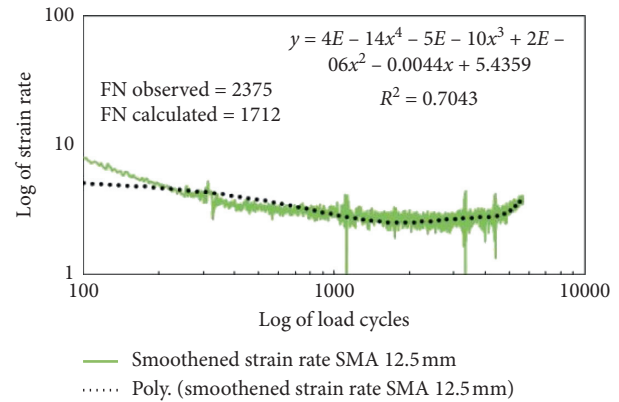


FIGURE 7: Data smoothing applied to 12.5 mm mix.

TABLE 2: FN test results.

Mixtures	FN value (seconds)	Accumulated strain@ FN (microstrains)	
	Corrected	AMPT	AMPT
25 mm	—	10000	11044
19 mm	—	10000	10194
12.5 mm	1712	2375	35819

for the power and polynomial model, respectively, which indicates that 99% and 91% of the variation in permanent strain is attributed to change in loading cycles.

The predictive capability of the developed model was assessed using mean absolute percentage error. It can be defined as the average of the absolute difference between the actual and predicted value:

$$\text{MAPE} = \frac{1}{n} \sum_{i=1}^n |PE_i|, \quad (6)$$

where $PE_i = 100 \times (X_i - P_i)/X_i$ is the percentage error for observation i of actual X_i and predicted P_i . X_i = actual/observed value. P_i = predicted value.

The MAPE value for the power and polynomial model is 0.19 and 0.20, respectively. A MAPE value of 0.19 (power model) represents on average, the predictions underestimate or overestimate the true values by 19%. The MAPE values closer to zero signify better accuracy.

The FT test was performed in accordance with NCHRP reports [35, 36] in which the preconditioned specimen is subjected to a constant axial load until it fails, and permanent deformation is measured with respect to the load time. The results indicate that, no any SMA mixture attained tertiary flow stage. Thus, no any data smoothing technique was required, and data acquired from AMPT software are used for comparison of accumulated strain at the time of termination of the test. The FT results suggest that all mixtures passed maximum cycles of 10,000, and mixtures are compared on the basis of accumulated strains. Table 4 indicates that, at time of termination, SMA 25 mm mix has a relatively small accumulated strain which suggests that this mix has relatively higher resistance to permanent deformation.

TABLE 3: Summary statistics of developed models.

Parameter	Estimate	Std. error	<i>t</i> -Statistics	<i>N</i>	<i>R</i> ²	95% CI	
						Lower	Upper
Power Model							
α	19.956	0.155	128.75	200	0.99	19.653	20.26
β	0.69	0.001	690			0.689	0.692
Polynomial Model							
α	-955.831	26.25	-36.41	200	0.91	-1007.3	-904.37
β	0.452	0.0002	2260			0.448	0.455
γ	125	2.787	44.85			119.155	130.083

TABLE 4: Accumulated strain values at termination.

Mixtures	Cycles (seconds)	Accumulated strain
SMA 25 mm	≥10000	5711
SMA 19 mm	≥10000	4868
SMA 12.5 mm	≥10000	9912

The results from this study—dynamic modulus, flow number, and flow time—would provide a foundation for evaluating pavement performance using M-EPDG. This design procedure entails both mechanistic and empirical procedure; dynamic modulus is used as a basic design input parameter at the first level of design in M-EPDG, which is mechanistic in nature. While for empirical evaluation, results from flow tests are used to develop flow models that predict pavement performance and serve as input to the second level of design in M-EPDG.

6. Summary and Conclusions

This paper presents the dynamic modulus testing of SMA mixtures at various temperatures (4.4–54.4°C) and frequencies (0.1–25 Hz) and flow number and flow time at a single effective temperature of 54°C. Given the tested SMA gradations/mixtures using limestone aggregate and 60/70 penetration grade, the dynamic modulus test reveals that, for a given loading frequency, an increase in temperature (from 21.1 to 37.8°C) translated into 41, 55, and 26% drop in $|E^*|$ values on average for 25 mm, 19 mm, and 12.5 mm mixtures, respectively. However, for a given temperature, an increase in loading frequency (from 0.1 to 25 Hz), 76, 85, and 74% of the variation in $|E^*|$ values on average was attributed for 25 mm, 19 mm, and 12.5 mm mixtures, respectively. Stress-dependent master curves were developed for each mix, and results indicated that 25 mm mix is relatively stiffer than other given mixtures. Resistance to fatigue cracking was evaluated using fatigue parameter, which shows that NMAAS of 12.5 mm with a binder content of 5.3% has shown relatively better resistance to fatigue cracking. Statistical models were also developed to express permanent strain as a function of loading cycles. Also, flow test results showed that the SMA mixture with coarser gradation (NMAAS 25 mm) having appropriate stone-to-stone contact exhibits excellent strength against rutting characteristics.

Data Availability

The gradation data, volumetric parameters, flow number, flow time test data, accumulated strain data, etc. used to support the findings of this study are included within the article. The master curve data, statistical parameter data, etc. used to support the findings of this study may be released upon application to Dr. Muhammad Irfan or Yasir Ali, who can be contacted via mirfan@mce.nust.edu.pk (Dr. Irfan) and yasirali@nit.nust.edu.pk (Yasir Ali).

Conflicts of Interest

The authors declare that they have no conflicts of interest.

Acknowledgments

The authors gratefully acknowledge the contribution of the National University of Sciences and Technology (NUST) laboratory support staff in preparing the samples for the research study.

References

- [1] R. Bonaquist, D. Christensen, and W. Stump, "Simple performance tester for superpave mix design development and evaluations," NCHRP Report 513, Transportation Research Record, Washington, DC, USA, 2003.
- [2] R. F. Bonaquist, *Refining the Simple Performance Tester for Use in Routine Practice*, Transportation Research Board, Washington, DC, USA, 2008.
- [3] J. Judycki, "Influence of low-temperature physical hardening on stiffness and tensile strength of asphalt concrete and stone mastic asphalt," *Construction and Building Materials*, vol. 61, pp. 191–199, 2014.
- [4] R. Muniandy, N. A. B. C. M. Akhir, S. Hassim, and D. Moazami, "Laboratory fatigue evaluation of modified and unmodified asphalt binders in stone mastic asphalt mixtures using a newly developed crack meander technique," *International Journal of Fatigue*, vol. 59, pp. 1–8, 2014.
- [5] E. İskender, "Rutting evaluation of stone mastic asphalt for basalt and basalt–limestone aggregate combinations," *Composites Part B: Engineering*, vol. 54, pp. 255–264, 2013.
- [6] T. B. Moghaddam, M. R. Karim, and T. Syammaun, "Dynamic properties of stone mastic asphalt mixtures containing waste plastic bottles," *Construction and Building Materials*, vol. 34, pp. 236–242, 2012.
- [7] E. Ahmadinia, M. Zargar, M. R. Karim, M. Abdelaziz, and P. Shafiq, "Using waste plastic bottles as additive for stone

- mastic asphalt," *Materials & Design*, vol. 32, no. 10, pp. 4844–4849, 2011.
- [8] A. Behnood and M. Ameri, "Experimental investigation of stone matrix asphalt mixtures containing steel slag," *Scientia Iranica*, vol. 19, no. 5, pp. 1214–1219, 2012.
- [9] C. E. Sengul, S. Oruc, E. Iskender, and A. Aksoy, "Evaluation of SBS modified stone mastic asphalt pavement performance," *Construction and Building Materials*, vol. 41, pp. 777–783, 2013.
- [10] A. Khodaii, H. F. Haghshenas, H. Kazemi Tehrani, and M. Khedmati, "Application of response surface methodology to evaluate stone matrix asphalt stripping potential," *KSCE Journal of Civil Engineering*, vol. 17, no. 1, pp. 117–121, 2013.
- [11] W. Cao, S. Liu, and Z. Feng, "Comparison of performance of stone matrix asphalt mixtures using basalt and limestone aggregates," *Construction and Building Materials*, vol. 41, pp. 474–479, 2013.
- [12] M. Pasetto and N. Baldo, "Performance comparative analysis of stone mastic asphalts with electric arc furnace steel slag: a laboratory evaluation," *Materials and Structures*, vol. 45, no. 3, pp. 411–424, 2012.
- [13] A. L. Lyne, P. Redelius, M. Collin, and B. Birgisson, "Characterization of stripping properties of stone material in asphalt," *Materials and Structures*, vol. 46, no. 1-2, pp. 47–61, 2013.
- [14] M. Irfan, M. Saeed, S. Ahmed, and Y. Ali, "Performance evaluation of elvaloy as a fuel-resistant polymer in asphaltic concrete airfield pavements," *Journal of Materials in Civil Engineering*, vol. 29, no. 10, article 04017163, 2017.
- [15] J. Gao, H. Wang, Z. You, M. R. M. Hasan, Y. Lei, and M. Irfan, "Rheological behavior and sensitivity of wood-derived bio-oil modified asphalt binders," *Applied Sciences*, vol. 8, no. 6, p. 919, 2018.
- [16] Y. Ali, M. Irfan, S. Ahmed, and S. Ahmed, "Permanent deformation prediction of asphalt concrete mixtures—a synthesis to explore a rational approach," *Construction and Building Materials*, vol. 153, pp. 588–597, 2017.
- [17] Y. Ali, M. Irfan, S. Ahmed, and S. Ahmed, "Empirical correlation of permanent deformation tests for evaluating the rutting response of conventional asphaltic concrete mixtures," *Journal of Materials in Civil Engineering*, vol. 29, no. 8, article 04017059, 2017.
- [18] Y. Ali, M. Irfan, S. Ahmed, S. Khanzada, and T. Mahmood, "Sensitivity analysis of dynamic response and fatigue behaviour of various asphalt concrete mixtures," *Fatigue & Fracture of Engineering Materials & Structures*, vol. 38, no. 10, pp. 1181–1193, 2015.
- [19] Y. Ali, M. Irfan, S. Ahmed, S. Khanzada, and T. Mahmood, "Investigation of factors affecting dynamic modulus and phase angle of various asphalt concrete mixtures," *Materials and Structures*, vol. 49, no. 3, pp. 857–868, 2016.
- [20] Y. Ali, M. Irfan, M. Zeeshan, I. Hafeez, and S. Ahmed, "Revisiting the relationship of dynamic and resilient modulus test for asphaltic concrete mixtures," *Construction and Building Materials*, vol. 170, pp. 698–707, 2018.
- [21] M. Irfan, Y. Ali, S. Ahmed, and I. Hafeez, "Performance evaluation of crumb rubber-modified asphalt mixtures based on laboratory and field investigations," *Arabian Journal for Science and Engineering*, vol. 43, no. 4, pp. 1795–1806, 2018.
- [22] M. Irfan, Y. Ali, S. Iqbal, S. Ahmed, and I. Hafeez, "Rutting evaluation of asphalt mixtures using static, dynamic, and repeated creep load tests," *Arabian Journal for Science and Engineering*, vol. 43, no. 10, pp. 5143–5155, 2018.
- [23] M. Irfan, A. S. Waraich, S. Ahmed, and Y. Ali, "Characterization of various plant-produced asphalt concrete mixtures using dynamic modulus test," *Advances in Materials Science and Engineering*, vol. 2016, Article ID 5618427, 12 pages, 2016.
- [24] M. Junaid, M. Irfan, S. Ahmed, and Y. Ali, "Effect of binder grade on performance parameters of asphaltic concrete paving mixtures," *International Journal of Pavement Research and Technology*, vol. 11, no. 5, pp. 435–444, 2018.
- [25] I. Hafeez and M. A. Kamal, "Creep compliance: a parameter to predict rut performance of asphalt binders and mixtures," *Arabian Journal for Science and Engineering*, vol. 39, no. 8, pp. 5971–5978, 2014.
- [26] Y. Kim, J. Lee, C. Baek, S. Yang, S. Kwon, and Y. Suh, "Performance evaluation of warm-and hot-mix asphalt mixtures based on laboratory and accelerated pavement tests," *Advances in Materials Science and Engineering*, vol. 2012, Article ID 901658, 9 pages, 2012.
- [27] C. Kai, X. Wenyuan, C. Dan, and F. Huimin, "High-and low-temperature properties and thermal stability of silica fume/SBS composite-modified asphalt mortar," *Advances in Materials Science and Engineering*, vol. 2018, Article ID 1317436, 8 pages, 2018.
- [28] M. A. Gul, M. Irfan, S. Ahmed, Y. Ali, and S. Khanzada, "Modelling and characterising the fatigue behaviour of asphaltic concrete mixtures," *Construction and Building Materials*, vol. 184, pp. 723–732, 2018.
- [29] E. Brown and L. Cooley, "Designing of SMA for rut resistant pavements," NCHRP Report 425, National Cooperative Highway Research Program, Washington, DC, USA, 1999.
- [30] E. R. Brown and J. E. Haddock, "Method to ensure stone-on-stone contact in stone matrix asphalt paving mixtures," *Transportation Research Record*, vol. 1583, no. 1, pp. 11–18, 1997.
- [31] A. T. 62-07, *Standard Method of Test for Determining Dynamic Modulus of Hot-Mix Asphalt Concrete Mixture*, American Association of State Highway and Transportation Officials (AASHTO), Washington, DC, USA, 2006.
- [32] M. Witczak, "Specification criteria for simple performance tests for rutting," NCHRP Report 580, National Cooperative Highway Research Program, Washington, DC, USA, 2007.
- [33] Q. Ye, S. Wu, and N. Li, "Investigation of the dynamic and fatigue properties of fiber-modified asphalt mixtures," *International Journal of Fatigue*, vol. 31, no. 10, pp. 1598–1602, 2009.
- [34] M. Witczak, K. Kaloush, T. Pellinen, M. El-Basyouny, and H. Von Quintus, "Simple performance test for superpave mix design," NCHRP Report 465, Transportation Research Board, Washington, DC, USA, 2002.
- [35] R. F. Bonaquist, *Ruggedness Testing of the Dynamic Modulus and Flow Number Tests with the Simple Performance Tester*, NCHRP Report 629, Transportation Research Board, Washington, DC, USA, 2008.
- [36] M. Witczak, D. Andrei, and W. Houston, *Guide for Mechanistic-Empirical Design of New and Rehabilitated Pavement Structures*, Transportation Research Board of the National Research Council, Washington, DC, USA, 2004.

Research Article

Size Effects of Finite Element Model for Three-Dimensional Microstructural Modeling of Asphalt Mixture

Kuanghuai Wu,¹ Qingzi Deng,² Naiming Deng,² Xu Cai ,³ and Wenke Huang ⁴

¹Professor, School of Civil Engineering, Guangzhou University, Guangzhou 510006, China

²Postgraduate, School of Civil Engineering, Guangzhou University, Guangzhou 510006, China

³Associate Professor, School of Civil Engineering, Guangzhou University, Guangzhou 510006, China

⁴Lecturer, School of Civil Engineering, Guangzhou University, Guangzhou 510006, China

Correspondence should be addressed to Wenke Huang; 846247234@qq.com

Received 30 July 2018; Revised 8 December 2018; Accepted 14 January 2019; Published 3 March 2019

Guest Editor: Munir Nazzal

Copyright © 2019 Kuanghuai Wu et al. This is an open access article distributed under the Creative Commons Attribution License, which permits unrestricted use, distribution, and reproduction in any medium, provided the original work is properly cited.

Asphalt mixture is a particulate composite material consisting of aggregate, mastic, and air voids. The computed tomography (CT) image-based finite element approach is used as an effective method to simulate micromechanical response of asphalt mixture. For finite element analysis, the accuracy of the finite results is determined by the size of the finite element. In this paper, a voxel-based three-dimensional (3D) digital reconstruction model of asphalt mixture with the CT images after being processed was proposed. In this 3D model, the aggregate phase was considered as elastic materials while the asphalt mastic phase was considered as linear viscoelastic material. Four micromechanical digital models were generated, whose voxel sizes were 0.5 mm, 0.67 mm, 1.0 mm, and 2.0 mm, respectively. The four digital models were used to conduct uniaxial creep test for predicting creep stiffness modulus to investigate the effect of voxel size. Simulation results showed that the voxel sizes had a significant effect on creep stiffness modulus. For the creep simulation test, the most appropriate voxel size whose creep stiffness modulus changes within 2.5% is 1.0 mm with regard to time steps, computational time, aggregate, and mastic shape representations.

1. Introduction

1.1. Background. Asphalt mixture is the most widely used road construction material in the paving industry. The traditional trial and error approach in industrial practice has focused on empirical experiments that develop correlations between the macro phenomena and the material characteristics. However, this traditional approach does not provide information that can be used to explain why certain mixtures perform better than others. And also this approach is cost intensive, high-resource consuming, and time consuming. To overcome these shortcomings, some microstructural methods and numerical techniques are developed to gain insight into the performance of asphalt mixture.

The composition of asphalt mixture can be considered to be included in three phases: the mastic phase (asphalt cement with a filler that is smaller than 2.36 mm in size), the

aggregate phase, and the air voids. The mechanical behavior of asphalt mixture is complex due to the heterogeneity of the asphalt composite material. Several research studies have investigated the internal properties and performance of asphalt mixture at microstructural scale using the non-destructive X-ray CT technique [1–9]. There have also been a number of recent attempts to use X-ray CT images to reconstruct a three-dimensional (3D) finite element specimen to predict the mechanical properties of asphalt mixture [10–14]. The majority of these microstructure numerical samples for asphalt mixture face challenges with regard to accurate geometry of different phases. The geometry accuracy and volume composition of aggregate and mastic phases are directly affected by the resolutions of CT image for asphalt mixture. But most of the previous image-based finite element approaches are limited to low precision numerical models in order to reduce the time steps and

computational time [15–17]. However, it is not sufficient enough to consider the quantitative effects of finite element dimensions on asphalt mixture simulation results.

1.2. Objective. The objective of this study is to investigate size effects of finite element model for three-dimensional microstructural modeling of asphalt mixture. Four image-based microstructure models with different finite element dimensions for asphalt mixture were established in order to quantify the size effects of finite element model for three-dimensional microstructural modeling. Firstly, the non-destructive industrial X-ray CT technique was used to capture the internal microstructure of the asphalt mixture specimen. The grayscale thresholds for dividing aggregate, asphalt mastic, and air voids were chosen based on the Otsu method. A morphological multiscale algorithm was applied to segment the coarse aggregate adhesion images. Then, four voxel-based 3D digital reconstruction models of the asphalt mixture specimen is constructed based on the X-ray CT images. After that, the parameters of the asphalt mastic phase are obtained using the dynamic shear rheometer (DSR) test. Finally, the image-based numerical specimens are applied to conduct the creep simulations in order to investigate size effects of finite elements on creep stiffness.

2. Three-Dimensional Microstructural Reconstruction

2.1. CT Image Processing. At present, there is no image analysis software especially for material segmentation of CT slice images of asphalt mixture. The usual method involves segmentation of the internal materials according to the gray distribution characteristics of asphalt mixture. The most widely used approach is the Otsu method [18–20].

Because the difference of material density is not very obvious in the areas where the particles are in close contact with each other, cohesion of aggregate particles occurs when using the Otsu method to segment the aggregate and asphalt mastic phases. So, the adhesive aggregates are identified as individual particles by computer in the subsequent mechanical simulation, resulting in a calculation result which is inconsistent with the actual situation. Therefore, before constructing the numerical model, adhesive aggregates in the images must be separated. At present, coarse aggregate adhesive separation is mainly based on manual processing, which is convenient for single image processing [21–23]. However, it is not conducive for rapid and efficient image processing if the number of images is too large. Therefore, an automatic separation algorithm for adhesive aggregates is necessary.

This section presents a morphological multiscale separation algorithm for adhesive aggregates based on different structural element radius. The algorithm first classifies the binary CT image in MATLAB before eroding in order to prevent smaller aggregates from being filtered out in the subsequent segmentation process. Then, structural element with a minimum size is applied to perform ultimate erosion on all the labeled binary images. In the ultimate erosion

process, if two or more divided objects appeared in the binary image, then they are classified as possible adhesive aggregates for the next analysis step. If two or more split objects are not observed, then the object could be considered as independent aggregate. Structural elements with different sizes are then selected as the ultimate erosion structural elements for the morphological algorithm of the adhesion particle binary map. According to the adhesive separation map based on morphological algorithm under different structural elements, the separation number with the largest number of division lines is taken as the actual separation of the binary image, and the separation image corresponding to the smallest structural element is taken as the actual separation image. Finally, all the separated marked images are superimposed to form a complete glue separation image. The algorithm flow chart is shown in Figure 1, which was implemented in the MATLAB.

2.2. Numerical Model Reconstructing Method. The three-dimensional microstructural reconstruction of asphalt mixture based on voxel is a reconstruction of complete asphalt mixture specimen from a series of asphalt mixture CT images. This reconstruction is a reverse solution process. For an $M \times N$ binary image, the basic constituent unit is a pixel. The expansion of a pixel in three dimensions is a voxel, as shown in Figure 2. A voxel is the most basic unit in the reconstruction of three-dimensional numerical samples.

After CT scanning of the asphalt mixture specimen, a series of continuous CT images can be obtained. These continuous pseudocolor CT images were converted into a matrix of gray images, and the adjacent images were superimposed on each other, thereby expanding into three-dimensional space to form a three-dimensional gray unit space network, as shown in Figure 3.

For finite element mesh models, the element, node number, and node coordinates must be specified. For a series of consecutive CT images, the unit and node number of the gray pixel matrix of the first CT image were defined as shown in Figure 4(a), and the unit and node number of the gray pixel matrix of no. k CT image were defined as shown in Figures 4(b). Figure 5 shows a diagram of an initial three-dimensional numerical model obtained in accordance with the above algorithm.

Figure 5 is a numerical model containing the background and mixture. The background, void, asphalt mastic, and aggregate of the CT image were segmented according to the relevant method in Sections 2.1 and 2.2. The segmentation process is shown in Figure 6.

2.3. Reconstruction of Numerical Model of AC-16 Asphalt Mixture. In this paper, an AC-16 asphalt mixture test specimen was used for analysis. According to the above numerical modeling method, four microstructure numerical models with voxel lengths of 0.5 mm, 0.67 mm, 1 mm, and 2 mm, respectively, were reconstructed for AC-16 asphalt mixture. The numerical models of four different voxel lengths for AC-16 asphalt mixture are shown in Figure 7. The eight-node 3D solid reduction integration elements

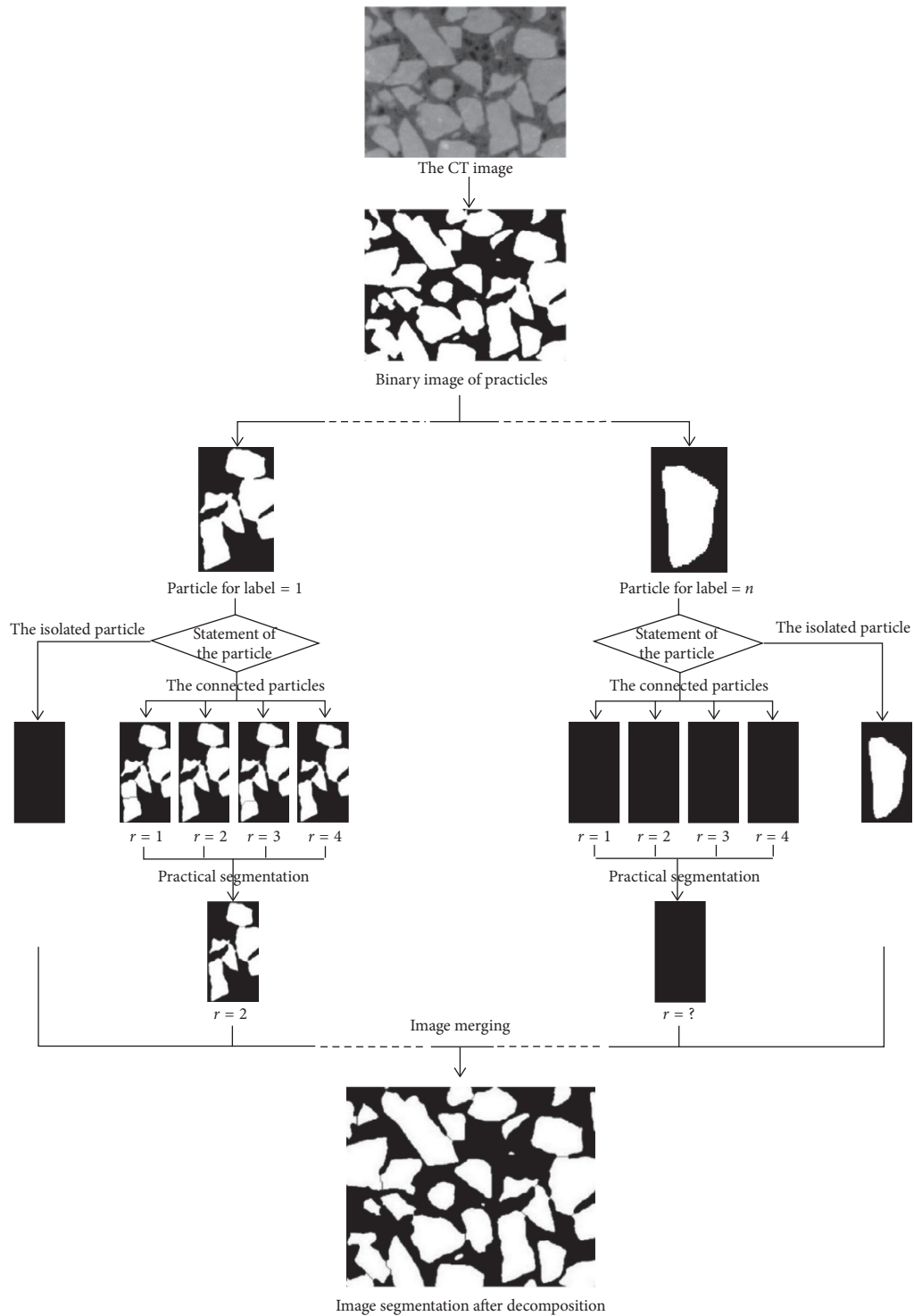


FIGURE 1: The algorithm flow chart.

(C3D8R) were adopted in constructing the mesh for the four types of numerical models. Numbers of units and nodes are shown in Table 1.

3. Material Parameters

Material properties are required for numerical modeling before simulation. The coarse aggregate can be considered to

be linear elastic material due to its small deformation. In this paper, modulus and Poisson's ratio of the coarse aggregate were assumed to be 25 GPa and 0.25, respectively. Asphalt mastic was set as a linear viscoelastic material, and the generalized Maxwell model is often used as its constitutive model [24–26]. The material properties of asphalt mastic in this numerical model adopted the 8-element generalized Maxwell model, and the parameters were obtained by

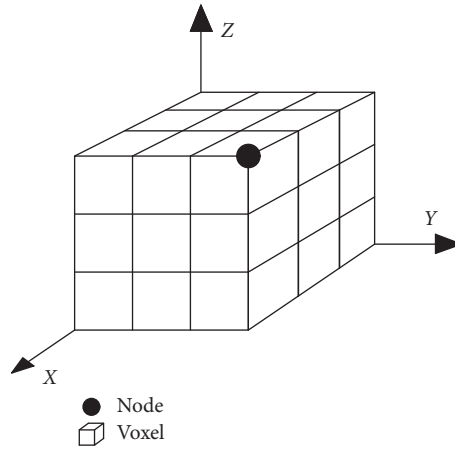


FIGURE 2: Definition of voxel.

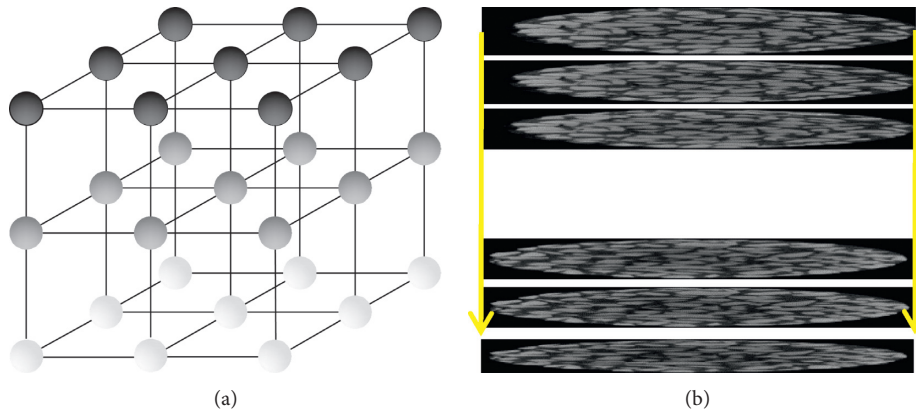


FIGURE 3: Three-dimensional unit net of CT gray image.

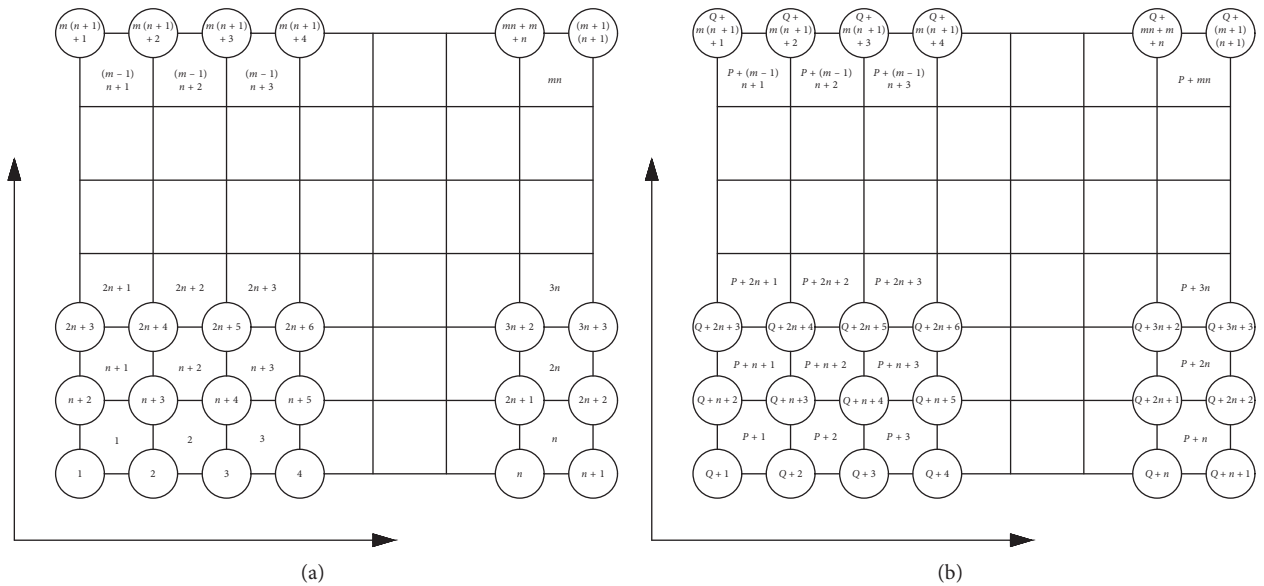


FIGURE 4: (a) Element and node label for the first CT image pixel matrix; (b) element and node label for no. k CT image pixel matrix.

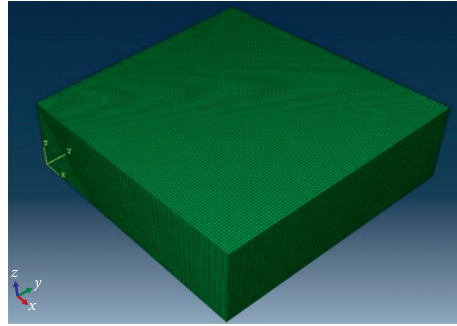


FIGURE 5: Initial three-dimensional numerical model.

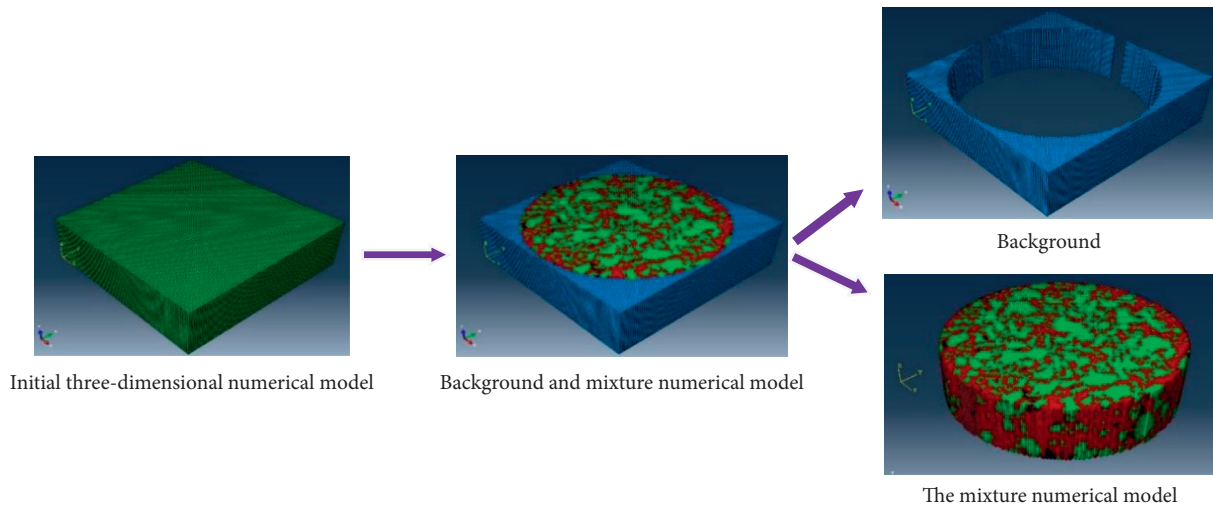


FIGURE 6: Flow chart of numerical modeling for asphalt mixture.

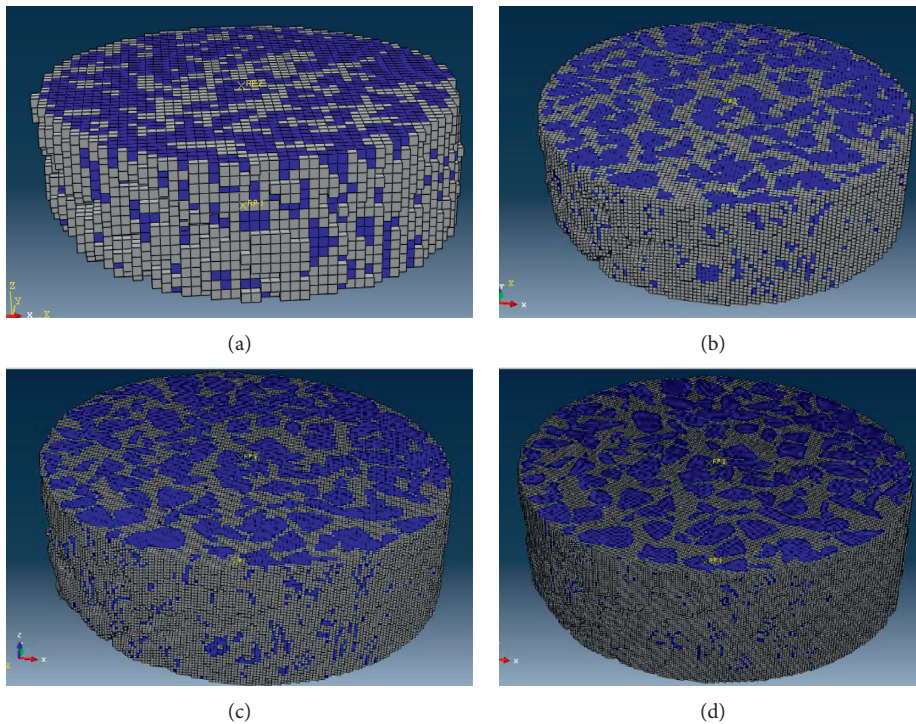


FIGURE 7: Numerical models of four different voxels for AC-16: (a) voxel edge length = 2 mm; (b) voxel edge length = 1 mm; (c) voxel edge length = 0.67 mm; (d) voxel edge length = 0.5 mm.

TABLE 1: Four types of numerical model element and node information.

Voxel edge length (mm)	0.5	0.67	1.0	2.0
Number of element	1723315	724557	213526	26305
Number of node	1780183	756418	227639	29853

dynamic shear rheological test. Initially, the dynamic shear rheometer (DSR) test was performed at five temperatures (15, 40, 50, 60, and 70°C), and the shear strain level was controlled within 0.15%. Then, the Williams–Landel–Ferry (WLF) equation was applied to shift the measured shear modulus at test temperature to the reference temperature (25°C in this study). The curve of the real part of the complex modulus can be described by the sigmoidal mathematical model:

$$\log_{10}(|G'|) = \delta + \frac{\alpha}{1 + e^{\beta + \gamma \cdot \log_{10} t_r}}, \quad (1)$$

where G' is the real part of the complex modulus; δ , α , β , and γ are the parameters of the equation; and t_r is the loading time at the reference temperature.

The real part of the complex modulus data was fitted by equation (1), as shown in Figure 8. The generalized Maxwell model parameters can be obtained (Table 2) according to the Prony series representation of the real part of the complex modulus as shown in equation (2) using the collocation method.

$$G'(\omega) = G_e + \sum_{i=1}^m \frac{\omega^2 \rho_i^2 G_i}{\omega^2 \rho_i^2 + 1}, \quad (2)$$

where m is the number of elements of the generalized Maxwell model; G_e is the equilibrium modulus; G_i is the relaxation strength of no. i ; and ρ_i is the shear relaxation time.

Given that the viscoelastic material was set to the generalized Maxwell model, which was the line viscoelastic constitutive, the load magnitude did not affect the analysis results. Therefore, the uniaxial creep simulation test was carried out with a dead load of 80 kPa. The displacement-based boundary conditions were applied to the asphalt mixture digital sample. The test specimen was completely fixed at one end to prevent the rigid body from being displaced, and the load was applied to the other end of the test specimen. For simplicity, the rigid body was used to simulate the loading plates at top and bottom of the specimen. A rigid body is a collection of nodes and elements whose motion is governed by the motion of a reference node. In this study, the dead load was imposed to the reference node, and the rigid body distributed the concentrated load on the top surface of the asphalt mixture digital model. The viscoelastic analysis step was used in this paper. The total analysis step time was 10 and the incremental step time was 0.1.

4. Numerical Simulation and Result Analysis

4.1. Computational Time Analysis. As can be seen in Table 1, the length of voxel became smaller; the number of elements

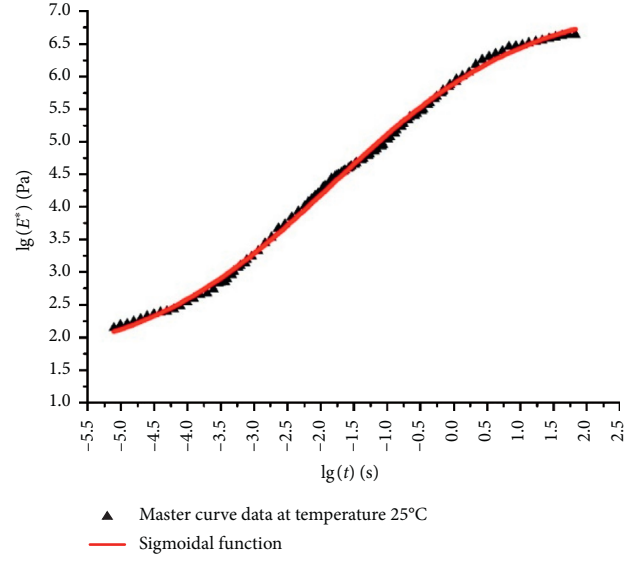


FIGURE 8: Fitting of the sigmoidal function.

TABLE 2: Prony series constants computed for the shear modulus.

i	ρ_i (s)	The standardized parameters G_i (kPa)	The normalized parameters g_i
1	0.0001	1927.8	0.15398
2	0.001	2918.2	0.23308
3	0.01	3555.1	0.28395
4	0.1	2834.0	0.22636
5	1	1072.2	0.08564
6	10	189.4	0.01513
7	100	19.4	0.00155
8	1000	3.4	0.00027
		$G_e = 12519.5$	

of the model and the number of nodes increased. Taking a model of about 1.7 million elements as an example, the minimum memory required for computer access is approximately 244 GB. So, it is difficult for a PC or a workstation computer to conduct the simulation. Therefore, using supercomputer for massive parallel simulation is necessary. Simulation and analysis of the four numerical models in this study were based on the supercomputer Milkyway-2 in the National Supercomputer Center in Guangzhou. In this paper, massive parallel simulation experiments were conducted on the numerical models with a total of 5 nodes having cumulative capacity of 120 processors and 600 GB of memory.

The computational time of each numerical model is shown in Table 3. The computational time consumed by different voxel length models varied greatly, and the maximum calculation time was 225.92 min. Thus, the computational time can be greatly reduced by increasing the number of applied nodes.

4.2. Creep Stiffness Modulus Analysis. Creep stiffness modulus was used as the result analysis index in this paper. The

TABLE 3: Calculating time of different models.

Voxel edge length (mm)	0.5	0.67	1.0	2.0
Calculating time (min)	225.92	107.43	32.88	7.7

creep stiffness modulus of the four numerical models is shown in Figure 9. When the voxel lengths were 0.5, 0.67, and 1 mm, the creep stiffness modulus curves were very close.

Since Figure 9 cannot clearly demonstrate differences among the four numerical models' creep stiffness modulus, stiffness ratios were used to quantify their differences. The ratio of the creep stiffness modulus for each numerical model shown in equation (3) is defined as a fraction of the reference creep stiffness modulus (creep stiffness modulus with a voxel length of 0.5 mm). This is taken as a variation in the evaluation of each creep stiffness modulus curve, as shown in Figure 10.

Ratio of stiffness modulus

$$= \frac{\text{Variation of stiffness modulus}}{\text{Stiffness modulus of the voxel side length of 0.5 mm}} \quad (3)$$

Figure 10 shows that a longer length of the voxel results in a higher rate of variation. When the length of the voxel was 0.67 mm, the ratio of the creep stiffness modulus from the first second to the tenth second was 0.55%–1.86%. When the length of the voxel was 1 mm, the ratio of the creep stiffness modulus from the first second to the tenth second was 2.14%–4.15%. When the length of the voxel was 2 mm, the ratio of the creep stiffness modulus from the first second to the tenth second was 6.56%–15.58%. Thus, when the accuracy of the CT image of the asphalt mixture reached a certain level, that is, when the length of the voxel is less than or equal to 1 mm, the ratio of the creep stiffness modulus within 10 s is less than 5%, that is, the length of the voxel had no significant effect on the creep test results. When the length of the voxel was 2 mm, the creep stiffness modulus curve was different from the other dimensions, with the maximum change of 15.58%. A smaller voxel size provides more accurate angular information of the aggregate. Voxel size has a great influence on the three-dimensional visualization of the asphalt mixture and the simulation results at local mesolevel. However, remarkably small voxel size showed no significant influence on the creep result. To reduce the computational time of simulation, a numerical model reconstructed with a pixel size of 1 mm can be recommended as an analytical model when performing the creep numerical simulation test.

5. Conclusions and Future Work

5.1. *Summary and Conclusions.* The size effect of finite elements in the three-dimensional microstructural numerical model of asphalt mixture was studied in this paper. Firstly, the industrial X-ray CT technique was used to obtain the CT image of the internal composition of the asphalt mixture. The Otsu method was used to segment the CT image material phases, and a morphological multiscale segmentation

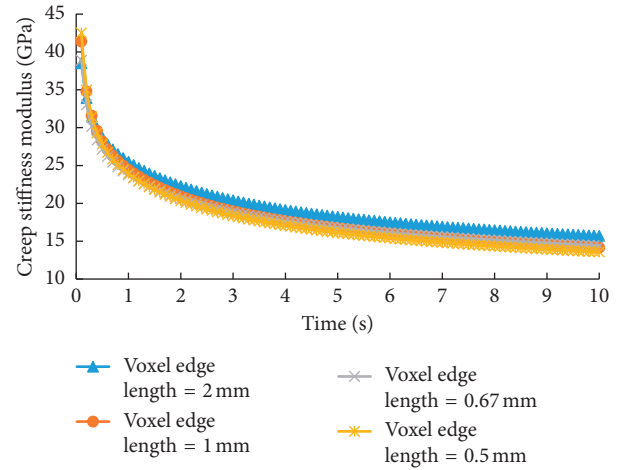


FIGURE 9: Creep stiffness modulus for four kinds of numerical model.

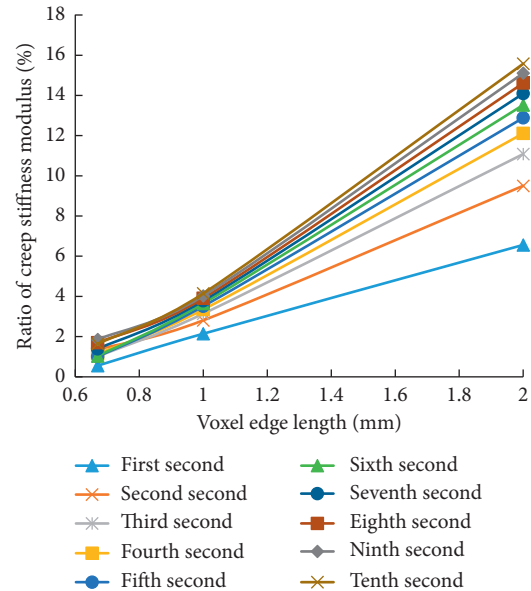


FIGURE 10: Relationship between ratio of creep stiffness modulus and voxel edge length.

algorithm was proposed to separate the adhesive aggregates after material classification. Finally, a three-dimensional numerical model reconstruction method for asphalt mixture based on voxel was proposed from a series of discrete asphalt mixture CT images. Four microstructural numerical models with voxel lengths of 0.5, 0.67, 1, and 2 mm were reconstructed. Uniaxial creep virtual test was implemented on the numerical model with four voxel sizes using the supercomputer Milkyway-2 in the National Supercomputer Center in Guangzhou to analyze the influence of the size effect on the simulation results, and the following conclusions were obtained:

- (1) A morphological multiscale algorithm for ultimate erosion of coarse aggregate adhesion image of asphalt mixture was proposed based on structural

elements with different sizes. The algorithm can effectively separate adhesive aggregate particles.

- (2) A voxel-based three-dimensional numerical model of AC-16 asphalt mixture reconstruction method was proposed. Numerical model was successfully reconstructed based on CT images of asphalt mixture processed by the Otsu method and morphological multiscale algorithm.
- (3) The numerical models with four different voxel sizes varied greatly in terms of the computational time when performing the creep numerical simulation test, and the maximum computational time was 225.92 min. Thus, more cumulative capacity of processors and memory can remarkably reduce the computational time.
- (4) When the length of the voxel was less than 1 mm, the creep stiffness modulus changed within 2.5%. This finding suggests that when the voxel size is less than 1 mm, the influence of the voxel size on creep stiffness modulus is not significant. Moreover, voxel size mainly affects the computational time and the angular information of the aggregate. A numerical model reconstructed with 1 mm voxel size is recommended as the analytical model.

5.2. Recommendations for Future Work

- (1) Many researchers have developed the low-resolution digital samples to simulate the behavior of asphalt mixture subjected to specific loading conditions, and this approach has been verified as a relatively reliable method to conduct the virtual test compared with the experimental test results. It is vital to validate the high-resolution simulation results with a series of experimental tests, and it will be the focus in our future papers.
- (2) The aggregate-mastic interface is a very challenging task in the asphalt mixture virtual simulation. For simplicity, the mastic phase was assumed to be perfectly bonded to the aggregate phase ignoring the internal cohesive behavior of the two phases in this paper. In order to obtain a more accurate digital sample, the interfacial conditions will be considered as part of our ongoing modeling efforts.
- (3) Asphalt mixture is a highly heterogeneous material consisting of aggregate, mastic, and air voids. The asphalt mastic has very complex temperature-, time-, and rate-dependent three-dimensional viscoelastic property. In this paper, the mastic is considered as a one-dimensional linear viscoelastic material. The under-way paper will be focused on a three-dimensional viscoelastic constitutive model developed for asphalt mastic.

Data Availability

The data used to support the findings of this study are available from the corresponding author upon request.

Conflicts of Interest

The authors declare that there are no conflicts of interest regarding the publication of this paper.

Acknowledgments

This study was supported by the Science and Technology Program of Guangzhou (no. 201804010231) and National Natural Science Foundation of China (no. 51878193). The authors thank all those who contributed in the X-ray CT image technique and the experimental part of this study. In addition, the authors acknowledge the National Super-computer Center in Guangzhou (NSCC) for providing computing resources useful in conducting the research reported in this paper.

References

- [1] E. Masad, "X-ray computed tomography of aggregates and asphalt mixes," *Materials Evaluation*, vol. 62, no. 7, pp. 775–783, 2004.
- [2] L. Wang, H. S. Paul, T. Harman, and J. D. Angelo, "Characterization of aggregates and asphalt concrete using X-ray computerized tomography a state of the art report," *Association of Asphalt Paving Technologies*, vol. 73, pp. 467–500, 2004.
- [3] K. Gopalakrishnan, H. Ceylan, and F. Inanc, "Using X-ray computed tomography to study paving materials," *Proceedings of the Institution of Civil Engineers-Construction Materials*, vol. 160, no. 1, pp. 15–23, 2007.
- [4] E. Coleri, J. T. Harvey, K. Yang, and J. M. Boone, "A micromechanical approach to investigate asphalt concrete rutting mechanisms," *Construction and Building Materials*, vol. 30, pp. 36–49, 2012.
- [5] I. Onifade, D. Jelagin, A. Guarin, B. Birgisson, and N. Kringos, "Asphalt internal structure characterization with X-ray computed tomography and digital image processing," in *Multi-Scale Modeling and Characterization of Infrastructure Materials*, pp. 139–158, Springer, Dordrecht, Netherlands, 2013.
- [6] J. Hu, P. F. Liu, D. Wang, M. Oesera, and Y. Tan, "Investigation on fatigue damage of asphalt mixture with different air-voids using microstructural analysis," *Construction and Building Materials*, vol. 125, no. 30, pp. 936–945, 2016.
- [7] M. Z. Hanif Mahmud, N. Abdul Hassan, M. R. Hainin, and C. R. Ismail, "Microstructural investigation on air void properties of porous asphalt using virtual cut section," *Construction and Building Materials*, vol. 155, no. 30, pp. 485–494, 2017.
- [8] D. Lo Presti, R. Khan, N. Abdul Hassan, A. Gordon, and A. Collop, "Laboratory mix design of asphalt mixture containing reclaimed material," *Advances in Materials Science and Engineering*, vol. 2014, Article ID 507082, 11 pages, 2014.
- [9] J. Hu, P. Liu, D. Wang, and M. Oeser, "Influence of aggregates' spatial characteristics on air-voids in asphalt mixture," *Road Materials and Pavement Design*, vol. 19, no. 4, pp. 837–855, 2017.
- [10] P. Liu, J. Hu, D. Wang et al., "Modelling and evaluation of aggregate morphology on asphalt compression behavior," *Construction and Building Materials*, vol. 133, no. 15, pp. 196–208, 2017.

- [11] Q. Dai, "Two- and three-dimensional micromechanical viscoelastic finite element modeling of stone-based materials with X-ray computed tomography images," *Construction and Building Materials*, vol. 25, no. 2, pp. 1102–1114, 2011.
- [12] H. Ying, M. Elseifi, L. Mohammad, and M. Hassan, "Heterogeneous finite-element modeling of the dynamic complex modulus test of asphalt mixture using X-ray computed tomography," *Journal of Materials in Civil Engineering*, vol. 26, no. 9, article 04014052, 2013.
- [13] T. You, R. Al-Rub, E. Masad, E. Kassem, and D. Little, "Three-dimensional microstructural modeling framework for dense-graded asphalt concrete using a coupled viscoelastic, viscoplastic, and viscodamage model," *Journal of Materials in Civil Engineering*, vol. 26, no. 4, pp. 607–615, 2014.
- [14] T. Schüler, R. Jänicke, and H. Steeb, "Nonlinear modeling and computational homogenization of asphalt concrete on the basis of XRCT scans," *Construction and Building Materials*, vol. 109, pp. 96–108, 2016.
- [15] Z. G. Ghauch, H. Ozer, and I. L. Al-Qadi, "Micromechanical finite element modeling of moisture damage in bituminous composite materials," *Construction and Building Materials*, vol. 80, pp. 9–17, 2015.
- [16] M. Shakiba, M. K. Darabi, R. K. Abu Al-Rub, E. A. Masad, and D. N. Little, "Microstructural modeling of asphalt concrete using a coupled moisture–mechanical constitutive relationship," *International Journal of Solids and Structures*, vol. 51, no. 25–26, pp. 4260–4279, 2014.
- [17] R. Khan, J. Grenfell, and A. Collop, "Micromechanical modelling of typical dense bitumen macadam (DBM) from laboratory testing and X-ray computed tomography (CT)," *Construction and Building Materials*, vol. 77, pp. 1–6, 2015.
- [18] Y. Zhang, W. Verwaal, M. F. C. van de Ven, A. A. A. Molenaar, and S. P. Wu, "Using high-resolution industrial CT scan to detect the distribution of rejuvenation products in porous asphalt concrete," *Construction and Building Materials*, vol. 100, pp. 1–10, 2015.
- [19] C. Zhang, H. Wang, Z. You, and X. Yang, "Compaction characteristics of asphalt mixture with different gradation type through superpave gyratory compaction and X-Ray CT scanning," *Construction and Building Materials*, vol. 129, pp. 243–255, 2016.
- [20] S. Wu, J. Yang, R. Yang, J. Zhu, S. Liu, and C. Wang, "Investigation of microscopic air void structure of anti-freezing asphalt pavement with X-ray CT and MIP," *Construction and Building Materials*, vol. 178, pp. 473–483, 2018.
- [21] E. Coleri, J. T. Harvey, K. Yang, and J. M. Boone, "Investigation of asphalt concrete rutting mechanisms by X-ray computed tomography imaging and micromechanical finite element modeling," *Materials and Structures*, vol. 46, no. 6, pp. 1027–1043, 2012.
- [22] M. Emin Kutay, E. Arambula, N. Gibson et al., "Three-dimensional image processing methods to identify and characterize aggregates in compacted asphalt mixtures," *International Journal of Pavement Engineering*, vol. 11, no. 6, pp. 511–528, 2010.
- [23] T. You, R. K. Abu Al-Rub, M. K. Darabi, E. A. Masad, and D. N. Little, "Three-dimensional microstructural modeling of asphalt concrete using a unified viscoelastic–viscoplastic–viscodamage model," *Construction and Building Materials*, vol. 28, no. 1, pp. 531–548, 2012.
- [24] H. Wang, J. Wang, and J. Chen, "Micromechanical analysis of asphalt mixture fracture with adhesive and cohesive failure," *Engineering Fracture Mechanics*, vol. 132, pp. 104–119, 2014.
- [25] A. Hamim, N. I. M. Yusoff, H. Ceylan, S. A. P. Rosyidi, and A. El-Shafie, "Comparative study on using static and dynamic finite element models to develop FWD measurement on flexible pavement structures," *Construction and Building Materials*, vol. 176, pp. 583–592, 2018.
- [26] H. K. Shanbara, F. Ruddock, and W. Atherton, "Predicting the rutting behavior of natural fiber-reinforced cold mix asphalt using the finite element method," *Construction and Building Materials*, vol. 167, pp. 907–917, 2018.

Research Article

Effect of Recycling Agents on Rheological and Micromechanical Properties of SBS-Modified Asphalt Binders

Meng Guo ¹, Yiqiu Tan,² Daisong Luo,^{2,3} Yafei Li,³ Asim Farooq ⁴, Liantong Mo,⁵
and Yubo Jiao¹

¹The Key Laboratory of Urban Security and Disaster Engineering of Ministry of Education, Beijing University of Technology, Beijing 100124, China

²School of Transportation Science and Engineering, Harbin Institute of Technology, Harbin 150090, China

³Research & Consulting Department of Road Structure & Materials Research Center, China Academy of Transportation Sciences, Beijing 100029, China

⁴University of Science and Technology Beijing, Beijing 100083, China

⁵State Key Lab of Silicate Materials for Architectures, Wuhan University of Technology, Wuhan 430070, China

Correspondence should be addressed to Meng Guo; mguo@ustb.edu.cn

Received 14 August 2018; Accepted 21 November 2018; Published 30 December 2018

Guest Editor: Ghazi G. Al-Khateeb

Copyright © 2018 Meng Guo et al. This is an open access article distributed under the Creative Commons Attribution License, which permits unrestricted use, distribution, and reproduction in any medium, provided the original work is properly cited.

Individual effect of aging and rejuvenator recycling on basic properties of asphalt is readily recognized, but there is only limited understanding about whether the recycling of SBS- (styrene-butadiene-styrene-) modified asphalt is an inverse process of aging or not. To compare the effects of aging and rejuvenator on microproperties and molecular composition of SBS-modified asphalt, comprehensive performance tests and physical-chemistry experiments were conducted. The results of infrared spectroscopy tests demonstrate that the reticular crosslinking structure of asphalt was destroyed and SBS's modification effect was gradually lost after aging. This can cause the strengthening of high-temperature performance and reduction of the low-temperature anticrack property of SBS-modified asphalt. Scanning electron microscope shows that the island structure of SBS-modified asphalt disappeared after aging. Energy spectrum analysis shows that the C (carbon) content of aged SBS-modified asphalt has decreased, while the O (oxygen) content and S (sulfur) content have increased obviously. Results of the fluorescence microscope, SEM, and rheological tests show that the epoxy functional group compounds of aliphatic glycidyl ether resin had high reactivity; the triblock molecular structure of SBS and the mechanical performance of SBS-modified asphalt were recovered.

1. Introduction

Traffic flow has been growing with the rapid development of China's highway construction, and many of the asphalt pavements built early in China have been damaged under heavy traffic pressure. Many high-grade road highways have approached or entered their maintenance period according to their design life and actual use conditions. It is estimated that, from now on, about 12% of asphalt pavement will need overhauling every year. At the same time, faced with the resourceful provinces' rising demand for transport capacity of the high-grade highway, China has been carrying out the reconstruction and widening project of the high-grade

highways in recent years. Both the overhaul and medium maintenance and reconstruction and widening of asphalt pavement produce a lot of reclaimed asphalt pavement (RAP). According to statistics, more than 35 million cubic meters of RAP are produced in overhaul and medium maintenance and widening of highways in China, and the figure grows at a rate of 15% per year and will reach 100 million cubic meters in ten years. The stacking, discarding, and degradation of such a huge amount of waste materials will aggravate the increasing serious environment pressure and resource problems. Therefore, using the RAP more efficiently is one big challenge in the field of highway construction.

Researchers have done a lot of research works, respectively, in the aspects of the physical properties decay law, component change law, and molecular structure changes. However, these were mainly done through indoor aging tests, and many factors affecting asphalt aging remain to be studied further, such as influence mechanism of water on asphalt aging, the relationship, and the difference between simulated and natural aging. Therefore, we also need to further study the asphalt aging performance and mechanism using advanced modern analytical test methods and various aging test methods to provide a theoretical basis for asphalt pavement recycling [1–7]. Zhang et al. studied the three types of aging methods on the performance of SBS- (styrene-butadiene-styrene-) modified asphalt, including thin film oven test (TFOT), pressure aging vessel (PAV), and ultraviolet (UV) radiation. They found that SBS-modified asphalt with penetration 90 had a higher retained penetration and ductility as well as the lower viscosity aging index compared to SBS-modified asphalt with penetration 70 [8].

At present, no definitive conclusion has been drawn from the mechanism of interaction between the recycling agent, aged asphalt, and new asphalt. For example, the measured data of some recycling projects show that the stiffness of recycled asphalt pavement is lower than the designed value. One explanation for this phenomenon is that the recycling agent fails to diffuse into the reclaimed asphalt. Therefore, it is of great significance for the asphalt recycling technology to study the law of recycling agent's diffusion into asphalt and recycling agent's peptization effect on asphalt and reveal the microproperties of recycling asphalt [9–15]. Xiao et al. studied the low-temperature performance characteristics of RAP mortars containing sieved RAP and soft binders at three aged states; they found that RAP mortar with a higher old binder content had a higher minimum low temperature regardless of the RAP source [16]. RAP mortars with virgin soft binder had the best low-temperature resistance followed by the RAP mortars with RTFO and PAV binders. However, it is still in doubt whether SBS-modified asphalt is recyclable. Supporters believe that SBS-modified asphalt is produced only by physical modification of base asphalt, while asphalt recycling involves more chemical reactions than a physical reaction. Therefore, SBS-modified asphalt recycling is only the recycling of aged asphalt and does not have effect on the SBS copolymer [17, 18]. Opponents believe that the aging process of SBS-modified asphalt includes the aging of both asphalt and SBS copolymer. Therefore, the recycling of SBS-modified asphalt inevitably includes the recycling of the SBS copolymer. To this end, recycling agents developed by researchers have different application scopes, and it is unknown whether they can be used for SBS-modified asphalt recycling [19–23]. In view that SBS-modified asphalt is adopted for surface and middle courses of most high-grade highways in China, it is of great practical significance to find a recycling agent applicable to SBS-modified asphalt.

The objective of this study was to investigate the mechanisms of aging and recycling of SBS-modified asphalt by conducting comprehensive performance tests and

physical-chemistry experiments and further to demonstrate whether the two processes were an inverse or not.

2. Materials and Methods

2.1. Materials. SBS-modified asphalt was used in this research. Two typical rejuvenators were selected to recover the aged asphalt binder in this research. The molecular structural formulas of rejuvenator A and rejuvenator B and the curing agents used in this research are shown in Figure 1.

2.2. Laboratory Tests. In this research, both conventional and advanced tests have been conducted. The conventional tests are used to evaluate the effect of the aging-recycling cycle on rheology of SBS-modified asphalt at the macrolevel. The advanced tests are used to investigate the mechanism of effect of the aging-recycling cycle on rheology of SBS-modified asphalt at the microlevel.

2.2.1. Penetration. Penetration is a widely used method in the world to measure asphalt stiffness. The smaller the stiffness, the greater the penetration would be. The greater the stiffness, the smaller the penetration would be. It is sure that stiffness change can reflect not only the asphalt aging but also the effect of SBS modification. Three replicates were tested in this research, and the data shown in this paper were the average of the three replicates.

2.2.2. Softening Point. The softening point is the temperature at which a material softens beyond some arbitrary softness. A ring and ball apparatus can also be used for the determination of the softening point of bituminous materials. Two replicates were tested in this research, and the data shown in this paper were the average of the two replicates.

2.2.3. Ductility. Ductility is a solid material's ability to deform under tensile stress. The ductility of the bituminous material is defined as the distance in centimeters, to which it will elongate before breaking when two ends of a briquet specimen of the material are pulled apart at a specified speed and a specified temperature. Three replicates were tested in this research, and the data shown in this paper were the average of the three replicates.

2.2.4. Viscosity. The rotational viscometer was used to measure binder viscosity at 135°C. First, a sample was placed in a chamber that was heated to the test temperature. Second, the sample viscosity was measured by rotating the spindle immersed in the binder. The rotational speed was set at 20 revolutions per minute (RPM), and the viscosity reading was recorded in units of centipoise. Two replicates were tested in this research, and the data shown in this paper were the average of the two replicates.

2.2.5. Gel Permeation Chromatography (GPC). Gel permeation chromatography (GPC) has low requirements for flow

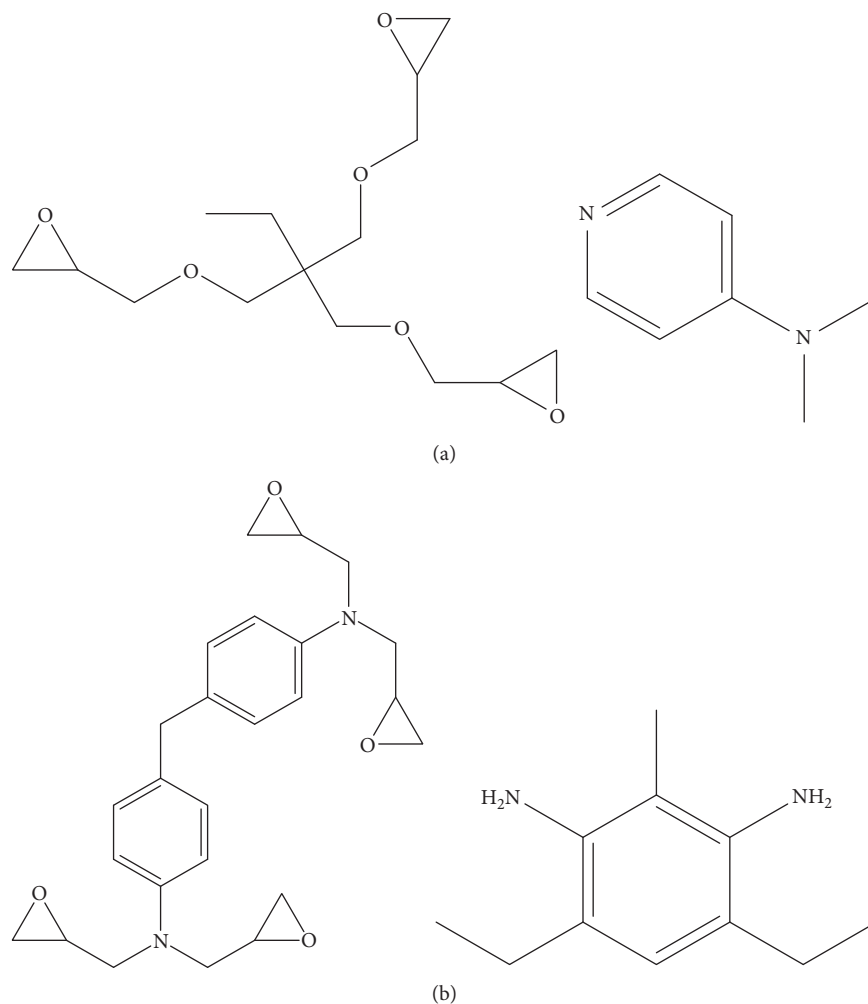


FIGURE 1: Molecular structural formulas of rejuvenators and the curing agents. (a) Rejuvenator A: fat glycidyl ether epoxy resin (left) and its curing agent (right). (b) Rejuvenator B: glycidyl amine epoxy resin (left) and its curing agent (right).

phase and features moderate test conditions, good repeatability, and fast analysis speed. It is currently the most widely used method for determining the molecular weight distribution of high polymer materials. Its separation basis is different hydrodynamic volumes of solute molecules in solution. The molecular elution volume of the solute depends on the physical parameters such as molecular dimension, filler aperture, porosity, and column volume. Two replicates were tested in this research, and the data shown in this paper were the average of the two replicates.

2.2.6. Thermogravimetric Analysis (TGA). To further reveal the changes before and after SBS-modified asphalt aging, the thermogravimetric (TG) test was conducted on SBS-modified asphalt and aged SBS-modified asphalt to analyze the thermal gravimetric property. Q600SDT TGA produced by TA Instruments was adopted for the TG test, with a temperature range of room temperature to 1500°C, a sensitivity of 0.1 μg , and a temperature accuracy higher than 2%. The test was conducted in a nitrogen atmosphere at a temperature rise rate of 10°C/min and at a temperature range from room

temperature to 1,000°C. Samples were made with SBS-modified asphalt before and after aging, respectively, and put in TGA for comprehensive thermal gravimetric analysis. Two replicates were tested in this research, and the data shown in this paper were the average of the two replicates.

2.2.7. Hydrogen Nuclear Magnetic Resonance (1HNMR) Spectrometry. Hydrogen nuclear magnetic resonance (1HNMR) spectrometry is conducted with Bruker AV-400 MHz NMR, with CDCl_3 as the solvent, TMS as the internal reference, and a test temperature of 25°C. Two replicates were tested in this research, and the data shown in this paper were the average of the two replicates.

2.2.8. Scanning Electron Microscope (SEM). Scanning electron microscope (SEM) is a method observing micro properties. It can be directly used for microimaging of the matter properties of the sample surface material. In principle, SEM scans the sample with a very thinly focused high-energy electron beam to stimulate various physical

information, which is received, amplified, and imaged to get the observation results of the sample surface.

2.2.9. Energy Dispersive Spectrometer (EDS). Energy dispersive spectrometer is used for analyzing the types and content of microarea elements of the material, which is used together with an electronic microscope and transmission electron microscope. Different elements have their own characteristic wavelengths of X-ray, which depend on the characteristic energy ΔE released during energy transition. Energy spectrometer conducts composition analysis according to different characteristic energies of X-ray photons of different elements.

When X-ray photons enter the detector, they will stimulate a certain number of electron-hole pairs in the Si (Li) crystal. The minimum average energy ϵ for producing an electron-hole pair is constant (3.8 eV at low temperature), and the number of electron-hole pairs produced by one X-ray photon is $N = \Delta E/\epsilon$. Therefore, the greater energy the incident X-ray photons have, the bigger the N will be. Biases installed on both ends of the crystal are used to collect electron-hole pairs, which are converted to current pulses by the preamplifier. The height of current pulses depends on the size of N . Current pulses are then converted into voltage pulses by the main amplifier and enter the multichannel pulse height analyzer, which classified and counted the pulses by height. Thus, a diagram of X-ray distribution according to energy is obtained. Two replicates were tested in this research, and the data shown in this paper were the average of the two replicates.

3. Results and Discussion

3.1. Aging of SBS-Modified Asphalt. In order to find the role of SBS-modified asphalt aging, the laboratory adopted I-D modified asphalt meeting the requirements of Technical Specification for Construction of Highway Asphalt Pavements (JTG E20-2011) as a sample and put it in an RTFOT at 163°C for aging for 16h and then put the asphalt aged by RTFOT in a PAV at 100°C for aging for 20h. Finally, the changes in performance indicators, functional groups, components, and molecular weight of the aged SBS-modified asphalt were analyzed.

3.1.1. Effects of Aging on the Thermodynamic Performance of SBS-Modified Asphalt. Figure 2 presents TG curves before and after SBS-modified asphalt aging. This figure shows that the thermal weight loss of SBS-modified asphalt in a nitrogen atmosphere had one phase. Little residue carbon is left at 540°C, and combustion is completed. The thermogravimetric processes are consistent before and after SBS-modified asphalt aging, indicating that the aging effect is weak.

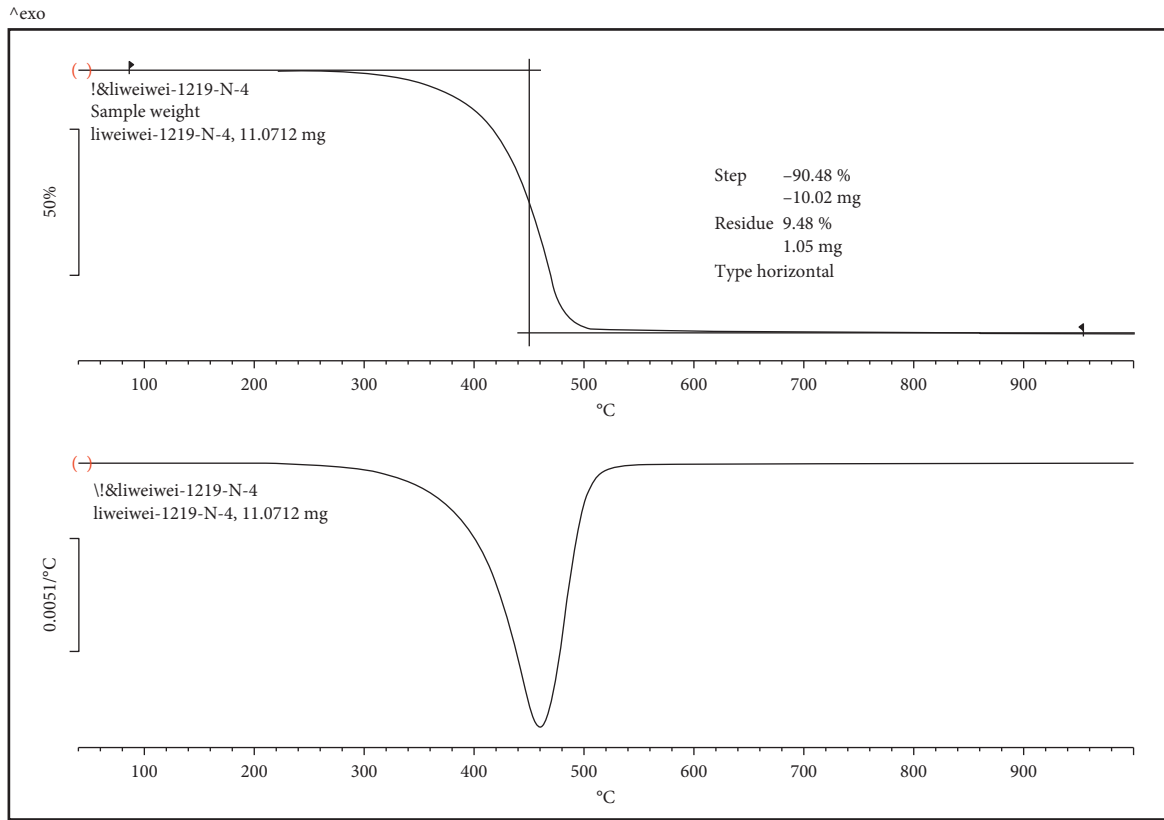
3.1.2. Effects of Aging on the Chemical Properties of SBS-Modified Asphalt

(1) FTIR Tests. The aging process of SBS-modified asphalt is essentially a slow process of chemical reaction. A shift of

functional groups inevitably accompanies the chemical reaction of organic matters. In the infrared spectrogram, the absorption band spectra shown are also different. Figure 3 contains the infrared spectrograms of SBS-modified asphalt before and after aging in room temperature conditions.

In general, the stretching vibration absorption peak of hydroxyl is at 3450 cm^{-1} , mainly characterized by a wide peak and that the higher degree of association, the closer the peak to low wavenumber; the stretching vibration absorption peak of alkyl hydrocarbon bonds is at 2800 cm^{-1} ~3000 cm^{-1} , including $-\text{CH}_3$, $-\text{CH}_2$, and $-\text{CH}$; carbonyl absorption peaks in ketone and carboxylic acid are near 1600 cm^{-1} . When the carbonyl group and a benzene vibrate, the absorption peak moves towards the low wavenumber. The bending vibration absorption peak of alkyl hydrocarbon bonds is at 1350 cm^{-1} ~1480 cm^{-1} , including $-\text{CH}_3$ (1370 cm^{-1} and 1450 cm^{-1}), $-\text{CH}_2$ (1465 cm^{-1}), and $-\text{CH}(\text{CH}_3)_2$ (1365 cm^{-1} ~1385 cm^{-1}); the stretching vibration absorption peak of organic sulfoxide and sulphone is at 1120 cm^{-1} ~1160 cm^{-1} and 1030 cm^{-1} ~1070 cm^{-1} ; the C-H bond out-of-plane bending vibration absorption peak of olefins (polybutadiene) is at 900 cm^{-1} ~950 cm^{-1} ; the C-H bond out-of-plane bending vibration absorption peak of a series of heteroaromatic compounds is at 650 cm^{-1} ~810 cm^{-1} , whereas the C-H bond out-of-plane bending vibration absorption peak of benzene rings of styrene and fatty aldehyde is at 700 cm^{-1} . Asphalt mainly consists of elemental carbon, hydrogen, oxygen, nitrogen, and sulfur. The infrared spectrogram shows that, with the increase of the aging period, the absorption intensity of different groups has different degrees of increase and decrease. These long-chain polymers often contain carbon-carbon double bonds and carbon-carbon triple bonds, which are very unstable and easily have addition reaction or oxidation reaction to produce hydroxyl groups and carbonyl groups. Some hydroxyl groups, due to the chain end effect, will be further oxidized to produce ketone or carboxylic acid.

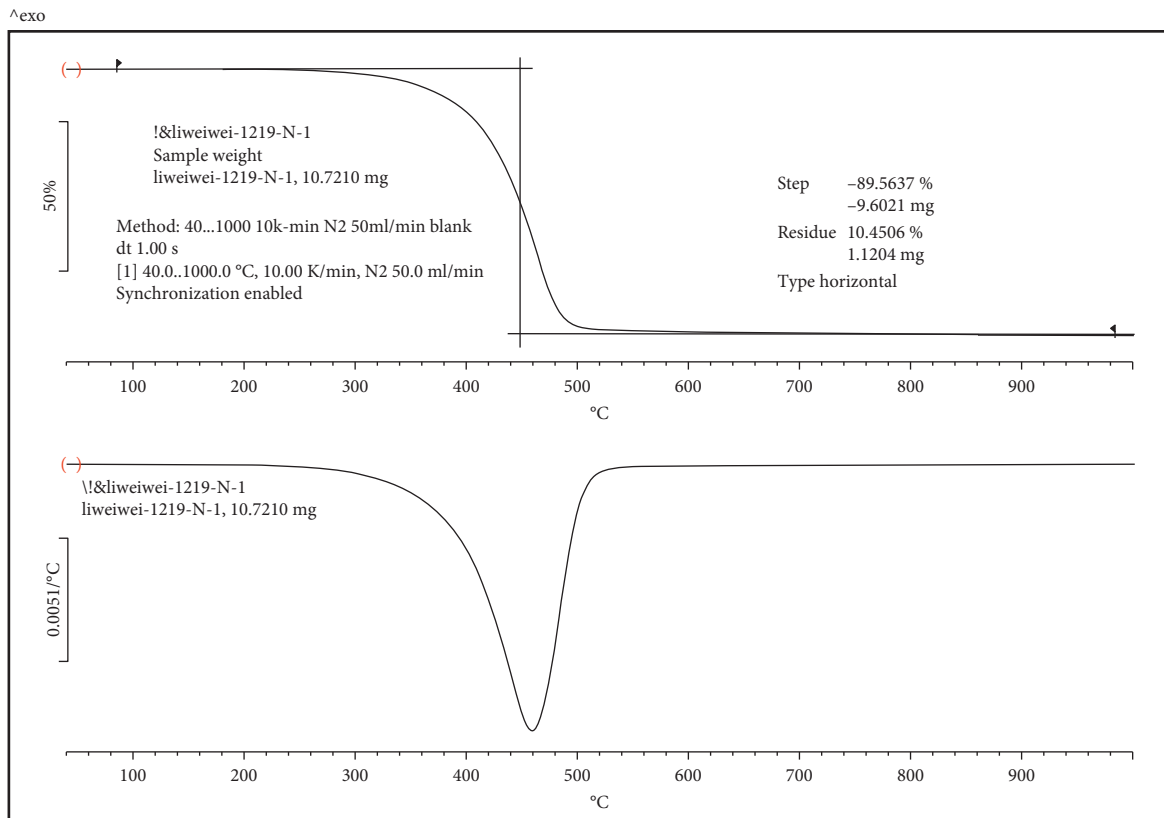
After aging of SBS-modified asphalt, a new absorption peak appears at 1120 cm^{-1} ~1160 cm^{-1} and 1030 cm^{-1} ~1070 cm^{-1} . This is because elemental sulfur in the modified asphalt is oxidized to sulfoxide (S=O) and sulphone (O=S=O). The absorption intensity of the two absorption peaks increases with the aging time of asphalt. Sulfur mainly exists in the form of sulfur ether and mercaptan in asphalt molecules. Peroxide easily oxidizes sulfur ether and mercaptan into sulfoxide base, a sulfur atom which still has a pair of lone electrons. In the case of sufficient oxygen, sulfoxide groups will be further oxidized into sulfonates. In addition to such polar functional groups as ketones, aldehydes, and carboxyl, a series of heteroaromatic compounds are also produced in the aging of SBS-modified asphalt. These heteroaromatic compounds are from the cleavage oxidation and local cleavage polymerization of SBS polystyrene chain segments. The deeper the asphalt is aged, the higher the heteroaromatic compound's absorption intensity is, indicating a higher decomposition degree of polystyrene.



Lab: METTLER

STAR® SW 14.00

(a)



Lab: METTLER

STAR® SW 14.00

(b)

FIGURE 2: TG curve of aged SBS-modified asphalt. (a) Before aging. (b) After aging.

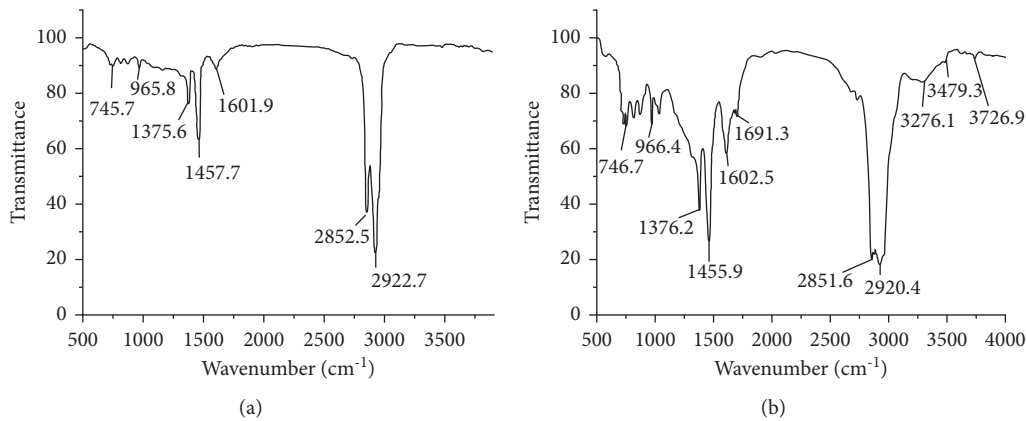


FIGURE 3: Infrared spectrogram of SBS-modified asphalt. (a) Before aging. (b) After aging.

Infrared spectroscopy shows that the reason for the embrittlement and hardening of SBS-modified asphalt after aging is SBS failure and the generation of a large number of polar groups. Polar groups have strong intermolecular interaction, and some form an association body, which reduces asphalt ductility and increases stiffness modulus.

(2) *NMR Tests.* Figure 4 shows the nuclear magnetic resonance spectrograms of SBS-modified asphalt before and after aging. The peak at 1 ppm-2 ppm belongs to hydrogen on methyl in the sample, and the one at 3.7 ppm belongs to hydrogen on methene (alkene) and methine (alkyne). Comparison between the two figures shows that the characteristic peaks of methene and methine at 3.7 ppm have disappeared in the nuclear magnetic resonance spectrogram of SBS-modified asphalt after aging. The reason is that, with the progress of aging, the double bonds of SBS polybutadiene segments are opened when oxidation occurs. Some double bonds are oxidized into alcoholic hydroxyl groups, carbonyl groups, or carboxyl groups, and some are added to produce saturated carbon bonds; some small molecules may also have mutual addition to producing macromolecules with unsaturated carbon-carbon bonds, namely, alkyl produced by alkene or alkyne through hydrogenation (generally oxygen addition).

In the nuclear magnetic resonance spectrogram of SBS-modified asphalt after aging, the characteristic peaks of methene and methine at 3.7 ppm have disappeared, indicating that SBS decomposition and degradation have completed.

3.1.3. Effects of Aging on the Surface Microtopography of SBS-Modified Asphalt. The SEM images of SBS-modified asphalt before and after aging are shown in Figures 5(a) and 5(b).

Figure 5(a) shows that the SBS asphalt is uniform. It indicates that modifier SBS can be evenly distributed in asphalt to form a subhomogeneous island structure; namely, styrene-butadiene-styrene triblock forms a network structure in the base asphalt. Figure 5(b) shows the SEM image of SBS-modified asphalt after aging. Observed under SEM, it is

very homogeneous, with few impurities in local parts, and the subhomogeneous island structure has disappeared. It is inferred that SBS has had severe cracking and decomposition and produced small molecules, or has had oxygen absorption reaction and produced highly polar substances. This coincides with the results of the GPC test above.

3.1.4. Effects of Aging on the Elementary Composition of SBS-Modified Asphalt. The analysis results of the SEM-EDS of SBS-modified asphalt before and after aging are shown in Table 1.

As shown in Table 1, the C content of aged SBS-modified asphalt has decreased compared with that of original SBS-modified asphalt, while the O content and S content have increased obviously. According to analysis, the reason is that, with the deepening of aging, sulfur elements in modified asphalt were oxidized into sulfoxide (S=O) and sulphone (O=S=O). In addition to such polar functional groups as ketones, aldehydes, and carboxyl, a series of heteroaromatic compounds are also produced in the aging of SBS-modified asphalt. These heteroaromatic compounds are from the cleavage oxidation and local cleavage polymerization of SBS polystyrene chain segments. The deeper the asphalt is aged, the higher the heteroaromatic compound's absorption intensity is, indicating a higher decomposition degree of polystyrene. These long-chain polymers often contain carbon-carbon double bonds and carbon-carbon triple bonds, which are very unstable and easily have addition reaction or oxidation reaction to produce hydroxyl groups and carbonyl groups. Some hydroxyl groups, due to the chain end effect, will be further oxidized to produce ketone or carboxylic acid.

3.2. Recycling of Aged SBS-Modified Asphalt

3.2.1. Effects of Rejuvenators on the Basic Properties of Aged SBS-Modified Asphalt. In this section, the effect of the two rejuvenators on the macroproperties of aged SBS-modified asphalt was explored. The contents of rejuvenators were 6%, 8%, 10%, 12%, and 14% of base asphalt binder by mass.

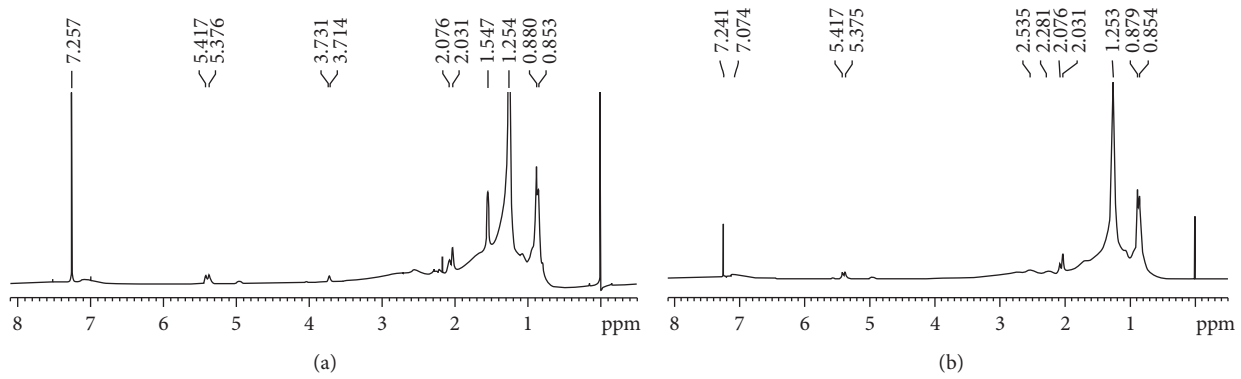


FIGURE 4: Nuclear magnetic resonance spectrograms of SBS-modified asphalt. (a) Before aging. (b) After aging.

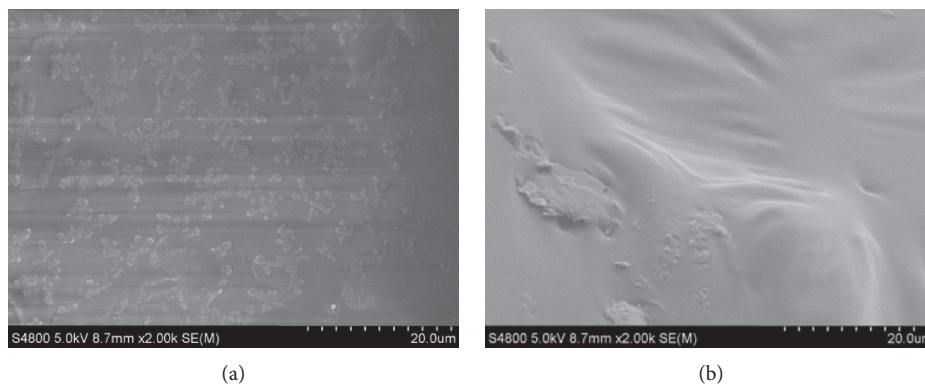


FIGURE 5: SEM images of SBS-modified asphalt. (a) Before aging. (b) After aging.

TABLE 1: Effects of aging on the elementary composition of SBS-modified asphalt.

Element type	Element content of SBS-modified asphalt (%)	
	Before aging	After aging
C	90.0	62.2
O	7.4	22.5
S	0.8	1.1

(1) *Viscosity*. Figure 6 shows the changes in the viscosity of aged SBS-modified asphalt after epoxy resin rejuvenators A and B are added. According to the figure, the viscosity of aged SBS-modified asphalt decreases with the increase of the additive amount of the epoxy resin rejuvenators A and B. This is because these two rejuvenators contain both low-viscosity catalytic cracking oil slurry and epoxy functional group compounds, whose viscosity is lower than that of SBS-modified asphalt, and it makes the viscosity of recycled SBS-modified asphalt decreases with the increasing additive amount of rejuvenator. The rejuvenators A and B have different effects on the viscosity of aged SBS-modified asphalt. The viscosity of asphalt modified by rejuvenator A is lower than that modified by rejuvenator B. According to the molecular structures of the two rejuvenators, the molecular backbone of rejuvenator A is a flexible aliphatic, while that of rejuvenator B is a rigid benzene ring structure. It leads to that

viscosity of asphalt modified by rejuvenator A is lower than that modified by rejuvenator B.

(2) *Penetration*. Figure 7 shows the penetration improvement of the aged SBS-modified asphalt after the epoxy resin recycling agents A and B are added. According to the figure, the penetration of recycled SBS-modified asphalt increased with the increase of the content of the recycling agent. We speculate that the reason is that these two recycling agents contain both low-viscosity catalytic cracking oil slurry and epoxy functional group compounds, whose viscosity is lower than that of SBS-modified asphalt, and it makes the penetration of recycled SBS-modified asphalt decreases with the increasing additive amount of recycling agent.

Regarding the molecular structure, the molecular backbone of recycling agent A is a flexible aliphatic, while that of recycling agent B is a rigid benzene ring structure. However, recycling agent B does not recover to the triblock molecular chain structure of SBS, so the effect of recycling agent B on the penetration of aged SBS-modified asphalt is not as evident as that of recycling agent A.

(3) *Ductility*. Figure 8 shows the effects of recycling agents A and B on the ductility of aged SBS-modified asphalt.

It can be seen from Figure 8 that the ductility of aged SBS-modified asphalt increased with the increasing additive amount of recycling agent A. The possible reason was that

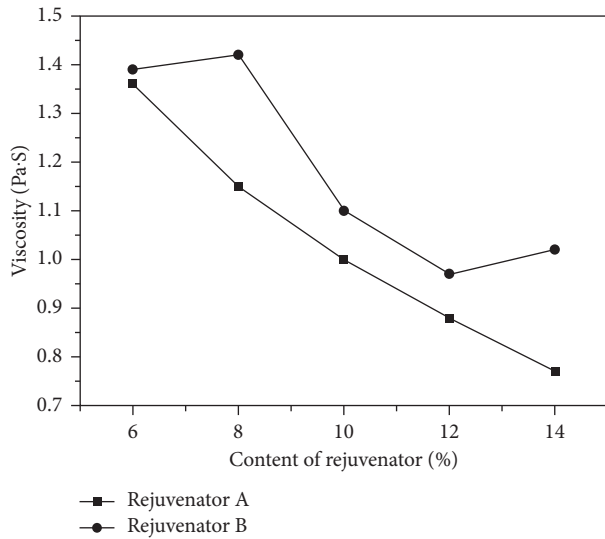


FIGURE 6: Effect of rejuvenators A and B on a viscosity of aged SBS-modified asphalt binder.

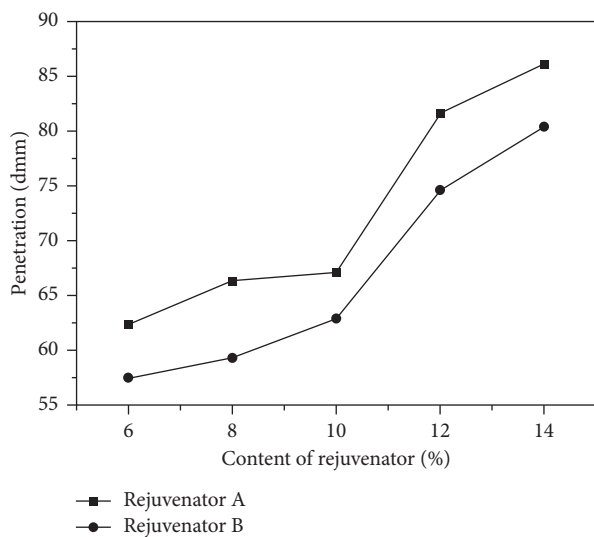


FIGURE 7: Effect of rejuvenators A and B on the penetration of aged SBS-modified asphalt binder.

the epoxy functional groups of recycling agent A reacted with the cracked carboxyl at the SB molecular chain end. It made biblock copolymer SB re-crosslinked into triblock copolymer SBS by epoxy resin molecular chains. That is, the triblock molecular structure of SBS was recovered, with the macro performance that the ductility of aged SBS-modified asphalt was obviously recovered. Recycling agent B did not have the recovered triblock molecular chain structure of SBS, so the addition of recycling agent B had an insufficient effect on the ductility of aged SBS-modified asphalt.

(4) *Softening Point.* The softening point improvement of the aged SBS-modified asphalt after the epoxy resin recycling agents A and B are added is shown in Figure 9.

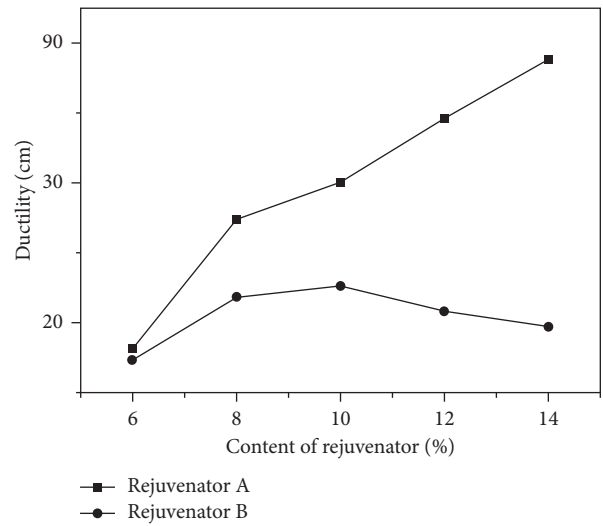


FIGURE 8: Effect of rejuvenators A and B on the ductility of aged SBS-modified asphalt binder.

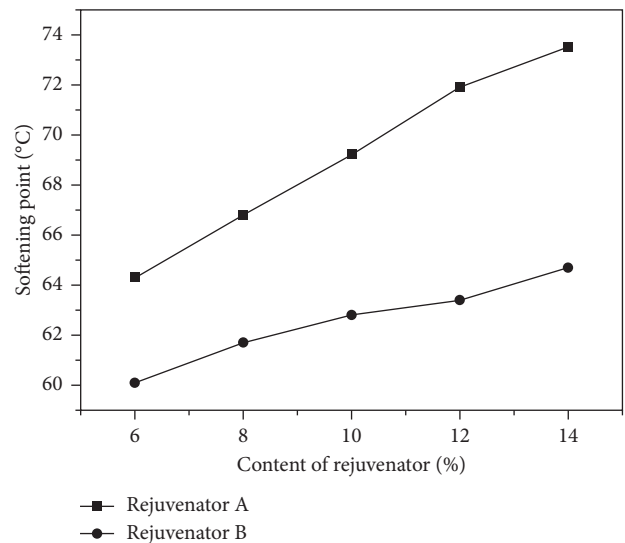


FIGURE 9: Effect of rejuvenators A and B on the softening point of aged SBS-modified asphalt binder.

According to Figure 9, the softening point of recycled SBS-modified asphalt rises with the increasing additive amount of recycling agent. Compared with recycling agent B, the softening point rises more sharply by adding recycling agent A because recycling agent A recovers the triblock molecular structure of SBS and accelerates the rising trend of the softening point. Although recycling agent B has a low-viscosity component, it does not recover the molecular chain structure of SBS, resulting in a very limited increase of softening point.

3.2.2. *Effects of Rejuvenators on the Molecular Weight Distribution of Aged SBS-Modified Asphalt.* The GPC graphs of SBS-modified asphalt after rejuvenators A and B are added are shown in Figure 10.

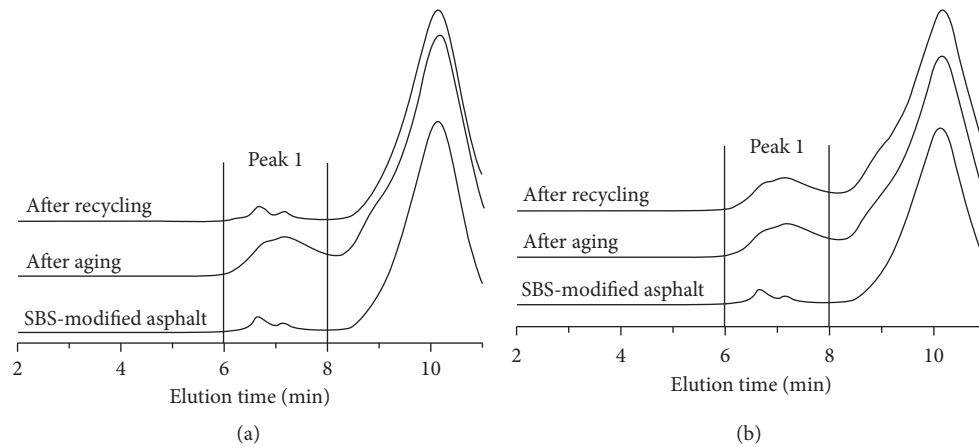


FIGURE 10: Effect of aging and recycling on molecular weight distribution of SBS-modified asphalt binder. (a) Rejuvenator A. (b) Rejuvenator B.

According to Figure 10, the SBS molecular chain cracks after the aging of SBS-modified asphalt, which is characterized by the trailing in the macromolecular part at Peak 1 of the GPC curve. After recycling agent A is added, the GPC curve at Peak 1 has migrated overall; that is, the previous macromolecular chain is recovered. It is inferred that the epoxy functional groups of recycling agent A react with the cracked carboxyl at the SB molecular chain end, which makes diblock copolymer SB re-crosslinked into triblock copolymer SBS by epoxy resin molecular chains. That is, the triblock molecular structure of SBS is recovered. After recycling agent B is added, the GPC curve at Peak 1 has no noticeable change. It indicates that epoxy functional groups of recycling agent B did not have coupling reaction with the SB molecular chain end, resulting in the very limited effect on the recycling of SBS-modified asphalt.

3.2.3. Effects of Rejuvenators on the Microstructure of Aged SBS-Modified Asphalt

(1) *Fluorescence Microscope*. Figures 11(a) and 11(b) show the microscopic morphology of SBS-modified asphalt recycled by adding the epoxy resin recycling agents A and B, respectively. Under a fluorescence microscope, SBS is the bright area in the figure. In Figure 11(b), there are very few particles in the bright area, and it is inferred that serious chain fracture occurred in the SBS triblock copolymer after asphalt aging, indicating serious aging of SBS. Figures 11(a)–(C) show the aged SBS-modified asphalt after recycling agent A is added. According to the figure, the distribution of bright area has been obviously improved and is close to that before aging. It indicates that the recycling agent A has obviously restored the SBS distribution and thus improved the aging degree of SBS-modified asphalt. Figures 11(b)–(C) show that SBS distribution has no obvious changes after recycling agent B is added, indicating very limited recycling effect. The microproperties are consistent with the molecular weight result tested by GPC.

Therefore, the recycling agent A has an obviously better recycling effect than the recycling agent B.

(2) *SEM*. The microscopic morphologies of SBS-modified asphalt recycled by adding the epoxy resin recycling agents A and B are shown in Figures 12(a) and 12(b), respectively.

It can be seen from Figures 12(a)–(A) and 12(b)–(A) that SBS is distributed in the base asphalt, which can be called the island structure in the SEM image. With the progress of aging, serious chain fracture occurs in the SBS triblock copolymer, which is manifested by the missing of islands in Figure 12(a)–(B). Figure 12(a)–(C) shows the aged SBS-modified asphalt after recycling agent A is added. According to the figure, the islands are recovered and similar to those before aging. It indicates that the rejuvenator A has obviously restored the SBS triblock structure and thus improved the aging degree of SBS-modified asphalt. Figure 12(a)–(A) shows that the SEM image has no obvious changes after rejuvenator B is added, indicating a very limited recycling effect. The microproperties are consistent with the molecular weight result tested by GPC and fluorescence microscopy results. The rejuvenator A has higher reactivity and better recycling effect than rejuvenator B.

4. Conclusions

Based on the testing and analysis presented in this paper, the conclusions of the study are summarized as follows:

- (1) Infrared spectrogram analysis results show that, with the aging progress of asphalt, the area of the carbonyl absorption peak and carbonyl content increase continuously; sulfur compounds in asphalt react with oxygen to produce sulfoxide base functional groups during asphalt aging. The butadiene absorption peak gradually disappears, indicating that base asphalt components and SBS copolymer age simultaneously during asphalt aging; with the degradation of the SBS copolymer, the reticular

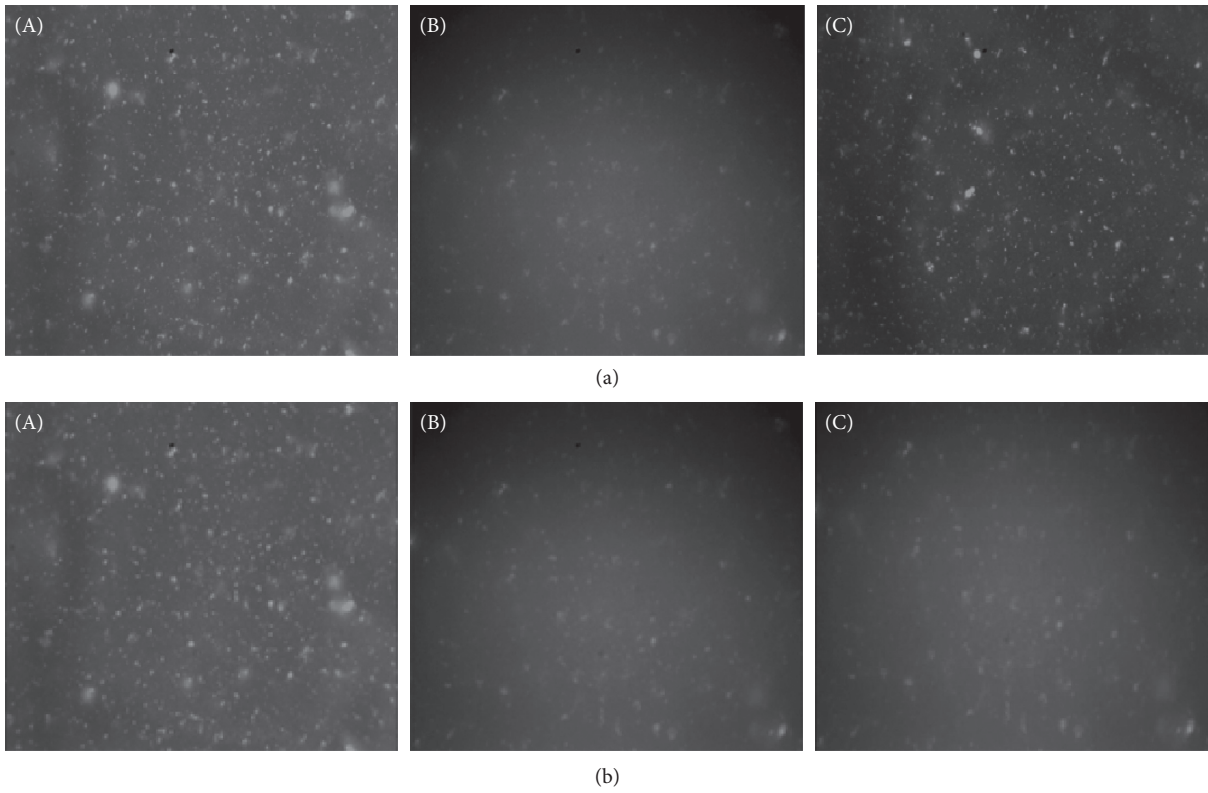


FIGURE 11: Effect of rejuvenators on microstructure of aged SBS-modified asphalt binder by fluorescence microscope (measuring scale is 1 : 10000): (A) SBS-modified asphalt, (B) aged SBS-modified asphalt, and (C) recycled SBS-modified asphalt of (a) rejuvenator A and (b) rejuvenator B.

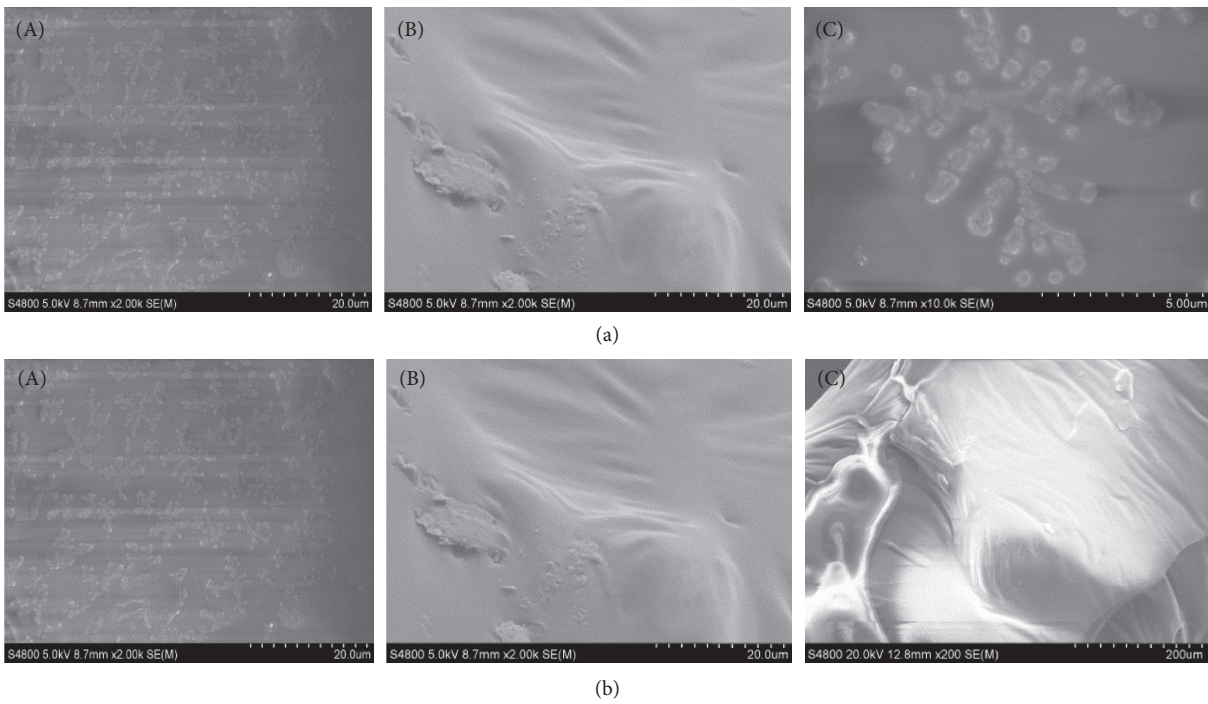


FIGURE 12: Effect of rejuvenators on microstructure of aged SBS-modified asphalt binder by SEM: (A) SBS-modified asphalt, (B): aged SBS-modified asphalt, and (C): recycled SBS-modified asphalt of (a) rejuvenator A and (b) rejuvenator B.

crosslinking structure of asphalt is destroyed and SBS's modification effect is gradually lost. The increase of polar functional groups of SBS-modified asphalt and the decomposition and failure of the SBS modifier are the immanent causes for continuous change in viscosity, strengthening of high-temperature performance, and reduction of low-temperature anticrack property.

- (2) According to the SEM analysis results, modifier SBS can be evenly distributed in asphalt to form a sub-homogeneous island structure; namely, styrene-butadiene-styrene triblock forms a network structure in the base asphalt. According to the SEM image of SBS-modified asphalt after aging, observed under SEM, it is very homogeneous, with few impurities in local parts, and the subhomogeneous island structure has disappeared. It is inferred that SBS has had severe cracking and decomposition and produced small molecules, or has had oxygen absorption reaction and produced highly polar substances. Energy spectrum analysis shows that, with the progress of aging, the C content of aged SBS-modified asphalt has decreased compared with that of original SBS-modified asphalt, while the O content and S content have increased obviously.
- (3) Fluorescence microscope and SEM were used to observe the changes in molecular structure and distribution of the SBS modifier before and after recycling. It shows that the epoxy functional group compounds of aliphatic glycidyl ether resin have high reactivity, and the triblock molecular structure of SBS is recovered. The pavement performance of recycled SBS-modified asphalt also shows that it has a good recycling effect. GPC demonstrated that epoxy functional groups of recycling agent B did not have coupling reaction with the SB molecular chain end, resulting in the very limited effect on the recycling of SBS-modified asphalt.

Based on the findings of this research, chemical-related tests are recommended conducting to select one proper rejuvenator for the aged SBS-modified asphalt. This can increase recycling efficiency.

Data Availability

The data used to support the findings of this study are included within the article.

Conflicts of Interest

The authors declare no conflicts of interest.

Authors' Contributions

Meng Guo and Daisong Luo conceived and designed the experiments. Meng Guo performed the experiments. Liantong Mo and Meng Guo analyzed the data. Yiqiu Tan

and Yafei Li contributed reagents/materials/analysis tools. Yubo Jiao and Asim Farooq wrote the paper.

Acknowledgments

This study was supported by the Beijing Natural Science Foundation (8174071) and National Natural Science Foundation of China (51808016).

References

- [1] S. Kim, S. H. Lee, O. Kwon, J. Y. Han, Y. S. Kim, and K. W. Kim, "Estimation of service-life reduction of asphalt pavement due to short-term ageing measured by GPC from asphalt mixture," *Road Materials and Pavement Design*, vol. 17, no. 1, pp. 153–167, 2015.
- [2] J.-Y. Yu, P.-C. Feng, H.-L. Zhang, and S.-P. Wu, "Effect of organo-montmorillonite on aging properties of asphalt," *Construction and Building Materials*, vol. 23, no. 7, pp. 2636–2640, 2009.
- [3] Y. F. Li, J. Chen, J. Yan, and M. Guo, "Influence of buton rock asphalt on the physical and mechanical properties of asphalt binder and asphalt mixture," *Advances in Materials Science and Engineering*, vol. 2018, Article ID 2107512, 7 pages, 2018.
- [4] S.-p. Wu, L. Pang, L.-t. Mo, Y.-c. Chen, and G.-j. Zhu, "Influence of aging on the evolution of structure, morphology and rheology of base and SBS modified bitumen," *Construction and Building Materials*, vol. 23, no. 2, pp. 1005–1010, 2009.
- [5] Y. Tan and M. Guo, "Interfacial thickness and interaction between asphalt and mineral fillers," *Materials and Structures*, vol. 47, no. 4, pp. 605–614, 2013.
- [6] M. Guo, A. Motamed, Y. Tan, and A. Bhasin, "Investigating the interaction between asphalt binder and fresh and simulated RAP aggregate," *Materials & Design*, vol. 105, pp. 25–33, 2016.
- [7] D. S. Luo, M. Guo, Y. Q. Tan, and Y. F. Li, "Study on effects of aging on SBS modified asphalt based on GPC and rheological methods," in *RILEM 252-CMB Symposium. RILEM 252-CMB 2018. RILEM Bookseries*, L. Poulikakos, A. Cannone Falchetto, M. Wistuba, B. Hofko, L. Porot, and H. Di Benedetto, Eds., Springer, Cham, Switzerland, 2019.
- [8] D. Zhang, H. Zhang, and C. Shi, "Investigation of aging performance of SBS modified asphalt with various aging methods," *Construction and Building Materials*, vol. 145, pp. 445–451, 2017.
- [9] M. Mohajeri, A. A. A. Molenaar, and M. F. C. Van de Ven, "Experimental study into the fundamental understanding of blending between reclaimed asphalt binder and virgin bitumen using nanoindentation and nano-computed tomography," *Road Materials and Pavement Design*, vol. 15, no. 2, pp. 372–384, 2014.
- [10] C. Castorena, S. Pape, and C. Mooney, "Blending measurements in mixtures with reclaimed asphalt: use of scanning electron microscopy with X-ray analysis," *Transportation Research Record: Journal of the Transportation Research Board*, vol. 2574, pp. 57–63, 2018.
- [11] S. Zhao, B. Huang, X. Shu, and M. E. Woods, "Quantitative evaluation of blending and diffusion in high RAP and RAS mixtures," *Materials & Design*, vol. 89, pp. 1161–1170, 2016.
- [12] H. Qiu and M. Bousmina, "New technique allowing the quantification of diffusion at polymer/polymer interfaces using rheological analysis: theoretical and experimental results," *Journal of Rheology*, vol. 43, no. 3, pp. 551–568, 1999.

- [13] H. Qiu and M. Bousmina, "Determination of mutual diffusion coefficients at nonsymmetric polymer/polymer interfaces from rheometry," *Macromolecules*, vol. 33, no. 17, pp. 6588–6594, 2000.
- [14] Y. He, Z. Alavi, J. Harvey, and D. Jones, "Evaluating diffusion and aging mechanisms in blending of new and age-hardened binders during mixing and paving," *Transportation Research Record: Journal of the Transportation Research Board*, vol. 2574, pp. 64–73, 2018.
- [15] F. Y. Rad, N. R. Sefidmazgi, and H. Bahia, "Application of diffusion mechanism," *Transportation Research Record: Journal of the Transportation Research Board*, vol. 2444, pp. 71–77, 2018.
- [16] F. Xiao, R. Li, H. Zhang, and S. Amirkhanian, "Low temperature performance characteristics of reclaimed asphalt pavement (RAP) mortars with virgin and aged soft binders," *Applied Sciences*, vol. 7, no. 3, p. 304, 2017.
- [17] C. Zhu, H. Zhang, D. Zhang, and Z. Chen, "Influence of base asphalt and SBS modifier on the weathering aging behaviors of SBS modified asphalt," *Journal of Materials in Civil Engineering*, vol. 30, no. 3, article 04017306, 2018.
- [18] H. Zhang, Z. Chen, G. Xu, and C. Shi, "Evaluation of aging behaviors of asphalt binders through different rheological indices," *Fuel*, vol. 221, pp. 78–88, 2018.
- [19] X. Liu, F. Cao, F. Xiao, and S. Amirkhanian, "BBR and DSR testing of aging properties of polymer and polyphosphoric acid-modified asphalt binders," *Journal of Materials in Civil Engineering*, vol. 30, no. 10, article 04018249, 2018.
- [20] P. Cong, W. Luo, P. Xu, and H. Zhao, "Investigation on recycling of SBS modified asphalt binders containing fresh asphalt and rejuvenating agents," *Construction and Building Materials*, vol. 91, pp. 225–231, 2015.
- [21] Y. H. Nie, S. H. Sun, Y. J. Ou, C. Y. Zhou, and K. L. Mao, "Experimental investigation on asphalt binders ageing behavior and rejuvenating feasibility in multicycle repeated ageing and recycling," *Advances in Materials Science and Engineering*, vol. 2018, Article ID 5129260, 11 pages, 2018.
- [22] D. Sun, T. Lu, F. Xiao, X. Zhu, and G. Sun, "Formulation and aging resistance of modified bio-asphalt containing high percentage of waste cooking oil residues," *Journal of Cleaner Production*, vol. 161, pp. 1203–1214, 2017.
- [23] L. Sun, Y. Wang, and Y. Zhang, "Aging mechanism and effective recycling ratio of SBS modified asphalt," *Construction and Building Materials*, vol. 70, pp. 26–35, 2014.

Research Article

Study on Cooling Effect and Pavement Performance of Thermal-Resistant Asphalt Mixture

Jiarong Wang,¹ Zhengqi Zhang ,¹ Datong Guo,² Cheng Xu,¹ and Ke Zhang³

¹Key Laboratory for Special Area Highway Engineering of Ministry of Education, Chang'an University, Xi'an, Shaanxi 710064, China

²The Northwest Subsidiary Company of CACC, Xi'an, Shaanxi 710075, China

³Fuyang Normal University, Fuyang, Anhui 236000, China

Correspondence should be addressed to Zhengqi Zhang; z_zhengqi@126.com

Received 29 May 2018; Accepted 26 November 2018; Published 24 December 2018

Guest Editor: Syed W. Haider

Copyright © 2018 Jiarong Wang et al. This is an open access article distributed under the Creative Commons Attribution License, which permits unrestricted use, distribution, and reproduction in any medium, provided the original work is properly cited.

To reduce the temperature of asphalt pavement and improve the antirutting performance of asphalt mixture, a thermal-resistant asphalt mixture (TRAM) was produced, in which a certain proportion of mineral aggregate was replaced by ceramic (CE) or floating beads (FB) featuring low thermal conductivity. Firstly, a parallel plate test was developed to test the thermal conductivity of asphalt mixture added with different thermal-resistant materials. Secondly, the illumination test system was designed to study the visual cooling effect of different TRAM by imitating the natural environment. Finally, the effect of different thermal-resistant materials on asphalt pavement performance was evaluated. The results show that the addition of thermal-resistant materials can reduce the thermal conductivity and the temperature of asphalt mixture. The cooling effect of CE75 and CE100 (coarse aggregate substituted by 75% and 100% CE, respectively) is superior to other aggregates. The temperature reduction rates of CE75 and CE100 reached 6.6°C and 6.8°C, respectively. For FB50 and FB75 (fine aggregate substituted with 50 and 75% FB, respectively), the cooling effect of them reached 3.9°C and 4.5°C, respectively. In addition, the CE and FB can improve the antirutting performance of asphalt mixture by reducing the temperature inside the pavement. The high-temperature performance of CE75 and FB75 is the best. With the increase of thermal resistance materials, the low-temperature cracking resistance of asphalt mixture decreases gradually. The failure strain of mixture added with 100% thermal resistance materials is close to the lower limit of Chinese specification. The water stability of different TRAM changes with various test methods. Taking into account the results of pavement performance and the cooling effect, the substitution proportion of CE and FB for TRAM is proposed as 50%~75%, respectively.

1. Introduction

Asphalt mixture is a kind of black material, which highly absorbs solar radiation [1]. The temperature of asphalt pavement is higher than atmospheric temperature, leading to the occurrence of high-temperature deformation. In addition, the absorption of heat energy in asphalt pavement not only leads to the raising of pavement temperature but also releases a lot of heat to the surrounding environment, which results in rutting disease of pavement and “urban heat island effect” [2–10]. Therefore, improving the temperature field of asphalt pavement structure is of great advantage for pavement rutting resistance and mitigation of “heat island effect.” Due to the low thermal conductivity,

the thermal-resistant materials used in asphalt mixture have drawn more and more attention. The heat absorption and storage of asphalt pavement can be decreased, and thus, the pavement temperature is reduced.

Heat-reflective layer and thermal resistance technology have been used to lower the pavement temperature [11]. A heat-reflective layer improves the reflectivity and radiation efficiency of pavement surface and then lowers the pavement temperature by preventing external heat from transferring into pavement structure [12–19]. But, the application of coating has been limited due to the defects in cost, technology, and durability. The thermal resistance technology for reducing the pavement temperature is adding thermal resistance material, which could reduce the temperature of

pavement effectively. The thermal resistance materials include ceramic, pottery sand, diatomite, bauxite, and refractory stone [20–24].

Feng and Yi [25] made a kind of thermal-resistant seal layer by adding ceramic or diatomite; the two seal layers showed obvious cooling effect after strong light exposure for 3 h. The results showed that the ceramic seal layer specimen can reduce the temperature by 2~3°C. Zhang [26] added the ceramic into the asphalt wear layer, and the results showed that, as the aggregates whose diameter varies from 9.5 mm to 4.75 mm are replaced by the equal volume of 20% ceramic, the thermal conductivity of mixture decreases by 31.8% and the specific heat capacity increases by 212.9%. Khan and Mrawira [27] found that the thermal conductivity of asphalt pavement could be improved by adding lightweight aggregate ceramic. Ren [28] studied the thin wear layer of ceramic asphalt mixture with different contents of ceramic waste. The study showed that when the wear layer is 5 cm thick, the cooling effect can reach more than 10°C. The water stability and high-temperature stability of the mixture decrease rapidly when the proportion of ceramic waste is more than 60%; it was found that the optimal content of ceramic waste is 40%~60%.

Li [29] used calcined bauxite to replace the coarse aggregate of AC-13C mixture. The results showed that the incorporation of calcined bauxite would decrease the temperature of asphalt mixture effectively. The optimum content of calcined bauxite for asphalt mixture was proposed as 80%. Cong et al. [30] studied the pavement surface temperature and the relationship between pavement permeability coefficient and mixture porosity. The results showed that the pavement temperature is related to the porosity and connectivity of the mixture. The pavement with 10% porosity can reduce the temperature by 5°C.

Although there have been considerable researches related to the cooling effect of asphalt mixture added with different materials, at present, many studies just describe the cooling effect of thermal resistance materials on pavement, and the test methods cannot simulate the actual working environment of asphalt pavement. Only some studies relate the influence of cooling effect of different thermal resistance materials on pavement performance. In this paper, the test method, imitating the real temperature environment of asphalt pavement, was designed to evaluate the thermal conductivity and antirutting performance of two kinds of TRAM. Firstly, the thermal conductivity was measured by a parallel plate test. Secondly, the indoor and outdoor illumination tests were developed to evaluate the cooling effect of TRAM by imitating the natural environment. Finally, the effect of different thermal-resistant materials on asphalt mixture pavement performance was also studied.

2. Materials and Methods

2.1. Materials

2.1.1. Raw Materials. SK-70# asphalt was used in the TRAM. The coarse basalt aggregate, fine limestone aggregate, and limestone powder were selected. Thermal-resistant materials

were shale ceramic (CE) and fly ash floating beads (FE). CE is a mineral material which is produced through the process of burning up and foaming. It is a spherical material with smooth surface and honeycomb porous. In this paper, CE was used to replace the coarse aggregate to produce a thermal-resistant asphalt mixture due to its larger particle size. The shale ceramic was adopted in this paper, and the particle size was between 5 and 15 mm [31]. The physical properties of CE are shown in Table 1.

Floating beads (FB) [32] is a fly ash material, derived from power plant fly ash. It is a material with following features such as lightweight, heat insulation, sound insulation, high-temperature resistance, high wear resistance, low thermal conductivity, and good mobility. The use of FB in asphalt mixture can reduce pavement temperature. In addition, its application is helpful in the resources recycling [33]. The physical properties of FB are shown in Table 2.

2.1.2. Design of TRAM. In this paper, AC-13C which was widely used in the upper layer of asphalt pavement was used to analyze the thermal resistance effect of CE and FB. The gradation composition is detailed in Table 3.

(1) Optimal Asphalt Content of CE. The aggregate was replaced by CE with an equal volume proportion in the asphalt mixture. CE was used to replace three sizes of coarse aggregate (13.2 m, 9.5 mm, and 4.75 mm) in AC-13C asphalt mixture. The substitution proportions were 0, 25, 50, 75, and 100% respectively, and the five ratios were represented by CE0, CE25, CE50, CE75, and CE100. The replacement mass can be calculated using the following formula [34]:

$$M_{R-i} = \frac{M_{A-i} \cdot P_i \cdot \rho_{R-i}}{\rho_{A-i}}, \quad (1)$$

where M_{R-i} is the quantity of the thermal-resistant material that replaces the aggregate in size i , g; M_{A-i} is the quantity of the aggregate in size i of the specimen, g; P_i is the proportion of the thermal-resistant material of aggregate in size i , %; and ρ_{A-i} and ρ_{R-i} are, respectively, the apparent density of the aggregate in size i and the thermal-resistant material, g/cm³.

According to the Marshall test, the optimal asphalt content of CE (CE0, CE25, CE50, CE75, and CE100) can be determined. The results are shown in Table 4.

(2) Optimal Asphalt Content of FB. FB was used to replace the fine aggregate due to its small particle size. Appropriate particle size of FB was chosen to replace the fine aggregate (0.6 mm, 0.3 mm, 0.15 mm, and 0.07 mm), and the substitution proportions were 0, 25, 50, 75, and 100%, respectively. The five substitution ratios were represented by FB0, FB25, FB50, FB75, and FB100. Formula (1) is also used in the calculation of the replacement mass of FB. According to the Marshall test, the optimal asphalt content and volume parameters of the mixture with different proportion FB were determined as shown in Table 5.

TABLE 1: The physical properties of CE.

Technical index	Unit	Measured value	Norms requirement
Crushing value	%	30.1	≤26
Los Angeles wear rate	%	26	≤28
Polished value	PSV	50	≥42
Average particle size coefficient	%	0.9	≤1.6
Adhesion	—	4 grade	≥4 grade
Water absorption	%	5.3	≤3

TABLE 2: Major performance indexes of FB used in the test.

Technical index	Unit	Floating beads	Fly ash
Refractory temperature	°C	1500	1400
True density	g/cm ³	0.721	1.95
Specific surface area	cm ² /g	2516	3120
SiO ₂ content	%	55–59	1.3–65
Particle-size distribution	μm	0–600	0–300
Thermal conductivity	W/(m·K)	0.058	0.110

TABLE 3: Aggregate gradation used for AC-13C mixture.

Mineral aggregate gradation	Passing ratio (by mass) (%)									
	16	13.2	9.5	4.75	2.36	1.18	0.6	0.3	0.15	0.075
AC-13C	100	96.5	80.0	53.7	37.0	25.2	17.5	11.8	9.0	5.4

TABLE 4: Results of the mixture with different CE proportions.

Mixture type	Optimal asphalt content (%)	Gross volume density (g/cm ³)	Maximum theoretical relative density	VV (%)	VMA (%)	VFA (%)	MS (kN)	FL (0.1 mm)
CE0	4.7	2.384	2.493	4.4	16.1	73.00	11.58	3.24
CE25	4.8	2.214	2.320	4.6	17.0	73.12	11.44	3.37
CE50	4.8	2.059	2.156	4.5	16.8	71.10	10.77	3.17
CE75	5.2	1.956	2.052	4.7	21.7	78.44	10.43	2.96
CE100	5.5	1.817	1.902	4.5	26.9	83.30	10.31	3.52

TABLE 5: Results of the mixture with different FB proportions.

Mixture type	Optimal asphalt content (%)	Gross volume density (g/cm ³)	Maximum theoretical relative density	VV (%)	VMA (%)	VFA (%)	MS (kN)	FL (0.1 mm)
FB0	4.7	2.384	2.493	4.4	16.1	73.00	11.58	3.24
FB25	4.8	2.331	2.425	3.9	16.7	76.79	10.32	2.46
FB50	4.6	2.320	2.415	3.9	12.6	68.74	9.73	2.33
FB75	4.4	2.273	2.368	4.0	10.8	62.99	9.39	2.05
FB100	4.3	2.225	2.326	4.1	8.2	51.24	9.28	1.44

2.2. Test Methods

2.2.1. Thermal Conductivity Test. The thermal resistance material was applied to reduce pavement temperature due to its low thermal conductivity. To verify the thermal conductivity of thermal resistance materials, the parallel plate test was developed. The schematic diagram is shown in Figure 1.

The test device is mainly composed of three parts: heating and temperature control system, temperature acquisition system, and insulation system. The test specimens were 300 mm × 300 mm × 50 mm in dimensions. In order to accurately control and measure the heat passing through

the specimen, the electric heating plate was sandwiched between two slab specimens; the constant-temperature water tank was controlled by a thermostatic circulation system which was arranged on the outside of the two specimens so that the heat passes through the specimens from the inside to the outside and gradually forms a stable gradient temperature field through which the thermal conductivity state can be reached. The probes of the temperature collector were arranged on both sides of the specimen. Thus, the collector can accurately measure the surface temperature on both sides, and then, the data were imported and stored in a multichannel temperature data acquisition instrument.

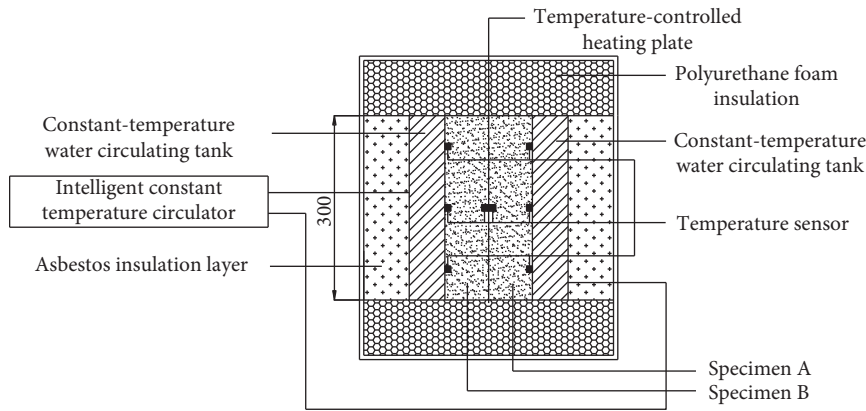


FIGURE 1: Schematic diagram of the test system.

2.2.2. Cooling Effect Test

(1) *Indoor Illumination Test.* The cooling effect of asphalt mixture was evaluated by the indoor illumination system developed by Chang'an University. The slab specimen with the dimension of $30\text{ cm} \times 30\text{ cm} \times 5\text{ cm}$ was formed with rolling wheel compaction and placed in the testing apparatus, as shown in Figure 2. To prevent heat from getting out and improve the measurement accuracy, a test board around was sealed by using a 5 cm thick foam plate. The testing apparatus consists of a lighting system (xenon lamps, wire, and bracket), a temperature acquisition system (a temperature sensor, a temperature recorder, and a computer), and a transparent glass box with top opening. The illumination intensity of 788 W/m^2 of the illumination system was adopted according to the equivalent conversion for the total solar illumination intensity of the pavement.

The temperature sensors were installed in the middle of top and bottom surface of the slab specimen, respectively. The temperature of the specimens was measured by using the multichannel automatic temperature recorder at the intervals of 30 min. In the procedure, the specimen was exposed to the lighting system at least 5 hours in the test.

(2) *Outdoor Illumination Test.* To verify the accuracy of the indoor illumination test, the outdoor illumination test was also designed. The test was conducted using the same specimen that was used in the indoor test. The test system is the same as of the indoor test as described, as shown in Figure 3. To reduce environment disturbance, the specimen around was insulated by clay.

2.2.3. *Pavement Performance Test.* To evaluate the influence of asphalt mixture with different thermal-resistant materials on pavement performance, the asphalt mixture with different contents of CE and FB was subjected to the illumination rutting test, the little beam bending test, the freeze-thaw splitting test, and the Hamburg wheel tracking device (HWTDD) test.

At present, the rutting test is a widely used method for evaluating the high-temperature performance of mixture. In the rutting test, the specimen is conditioned at 60°C for 5

hours in the environment box. By this insulated condition process, the top and bottom of the specimen reaches a thermal equilibrium; the cooling effect of the thermal-resistant material cannot work in the rutting test. Therefore, the test method of illumination rutting was developed to evaluate the high-temperature performance of different thermal resistance asphalt mixtures. In the environment box, the temperature change of the asphalt mixture is close to its regularity under natural illumination during actual use so that the rutting resistance of the thermal resistance asphalt mixture was evaluated more objectively. The illumination rutting test system operates as shown in Figure 4.

(1) *Illumination Rutting Test System.* In the illumination rutting test system, the illumination heating was used instead of the traditional air bath heating. The system consists of three parts: a rolling system, an illumination system, and temperature acquisition system. The kilowatts iodine tungsten lamp was used as the illumination source. The lamp heating equipment was fixed above the slab specimen, and the illumination intensity was set to 788 W/m^2 . One four-channel temperature recorder was used for temperature acquisition with the recording frequency of 15 min/times. Two temperature sensor probes were set on the top and bottom of the slab specimen parallel to the rolling direction, and the probes were positioned at the two sides for 3 cm from the wheel track.

(2) *Test Process.* The rolling times were counted as the illumination system turned on, and at that time, the room temperature was measured; then, as the temperature at the top of the specimen was 60°C , the rutting test was ended and the rolling times were recorded.

The addition of thermal-resistant material causes the change of the temperature field in pavement structure under the illumination and ultimately affects the antirutting ability of the pavement.

3. Results and Discussion

3.1. *Results of Thermal Conductivity Test.* It can be seen from Figure 5 that the thermal conductivity of asphalt mixture decreases as the content of thermal resistance materials

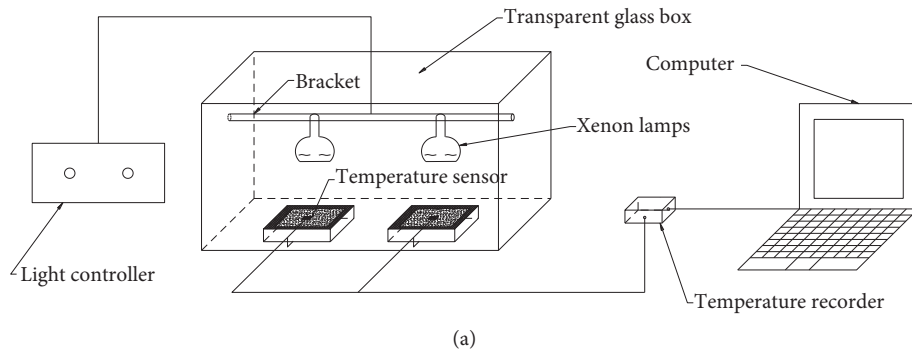


FIGURE 2: Test system of indoor illumination. (a) Schematic diagram of the illumination test and (b) light testing apparatus.



FIGURE 3: Test system of outdoor illumination.

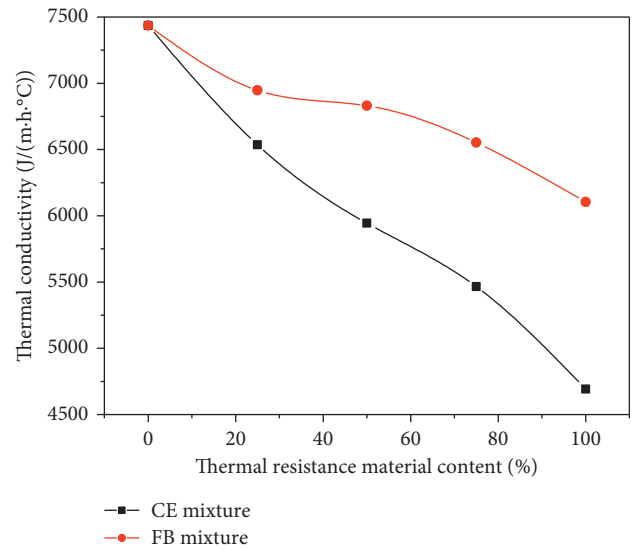


FIGURE 5: Results of the thermal conductivity test.



FIGURE 4: Illumination rutting test system.

increases; the reason may be that the thermal conductivity of CE and FB is much smaller than that of mineral aggregate. Adding thermal resistance materials into aggregate will decrease thermal conductivity of the mixture. And with

more thermal-resistant materials, the decreasing amplitude becomes larger gradually; it is because more and more thermal-resistant materials connect the heat transfer path in the mixture, so the effect of thermal resistance is superimposed and enhanced [35, 36]. By comparison, it can be seen that thermal conductivity of CE mixture is smaller than that of FB mixture under the same amount of admixture.

3.2. Results of Cooling Effect

3.2.1. Indoor Illumination Test. The slab specimens of CE and FB mixtures were subjected to the indoor illumination

test, and the results are shown in Figure 6 and Table 6. It can be seen from Figure 6 that the test results of CE mixture and FB mixture show similar trends, where the temperatures at the top and bottom of the slab specimens gradually increase with the illumination time during 5 hours lighting; it accords the change law of temperature of asphalt pavement in the natural environment. But, with the addition of more CE and FB, the maximum temperature of top surface increases and that of bottom surface decreases. This is due to that the increasing of thermal resistance materials lead to the decrease of thermal conductivity of mixture, and it can effectively impede heat transfer downward, resulting in more accumulation of heat near the top surface and the temperature of lower layer in pavement to reduce. Table 6 shows that when the substitution proportion of CE is 25, 50, 75, and 100%, the effect of cooling is 2.6, 4.2, 6.6, and 6.8°C, respectively. This shows that the cooling effect increases with more addition of CE, but the rate of increase slows down because the increase rate of top surface temperature also increases with more CE, which weakens the cooling effect of the whole pavement structure. With the more addition of FB, the effect of cooling is 3.1, 3.9, 4.5, and 2.2°C respectively. FB can reduce the temperature of the pavement, but the cooling effect of FB does not correspond with the proportion strictly, which does not mean that the more the FB, the better the cooling effect. When the substitution proportion is more than 75%, its cooling effect is relatively poor. That may be caused by the less asphalt content which results in inadequate compaction of asphalt mixture. The heat insulation effect of asphalt mixture gets poorer when the aggravate structure is loose, so the proportion of FB should not be too large.

For the mixture added with CE, the order of their cooling effect is as follows: 100, 75, 50, 25, and 0%, while for the mixture added with FB, the order is as follows: 75, 50, 25, 100, and 0%; the cooling effect of specimen CE100 and specimen FB75 reaches 6.8°C and 4.5°C, respectively. By comparison, the cooling effect of CE is better than that of FB.

3.2.2. Outdoor Illumination Test. In order to verify the accuracy of the indoor illumination test, the outdoor illumination test of CE was carried out in this study. The results are shown in Figure 7 and Table 7. Figure 7 shows that the maximum temperature at the top surface of specimens changes little. However, the maximum temperature at the bottom reduces gradually with the increase of thermal-resistant materials, which is different from the indoor test. The reason is that the outdoor test was carried out in the air environment in which the air flows freely. This makes the radiant heat dissipate out and results in that the rise of top surface temperature is not obvious. Furthermore, in the outdoor test, the illumination intensity and the incident angle are changing with time. The illumination is weak both in morning and evening, and it is just strong at noon, which inevitably results in that the pavement temperature will not vary greatly. As can be seen in Table 7, the cooling effect of specimen CE is

slightly better than the results from the indoor test. When the substitution proportions of CE are 25, 50, 75, and 100%, the effect of cooling is 4.3, 5.2, 6.7, and 6.8°C, respectively. But, the cooling trend of CE as a thermal resistance material in the asphalt mixture is the same under two different test conditions; that is, the cooling effect increases with the larger proportion of CE. What is more, the mixture added with 100% proportion of CE is exposed to both indoor and outdoor illuminations, which has the same cooling effect of 6.8°C. This indicates that the indoor illumination test has limitation, but it can still be used to evaluate the cooling effect of thermal resistance asphalt mixture.

3.3. Results of Road Performance

3.3.1. Evaluation of High-Temperature Performance. As can be seen from Figure 8 that as the temperature of the top of the specimen reached 60°C, the rutting depth of CE mixture declines first and then increases slightly with the increase of CE. In the rutting depths of CE0, the CE25, CE50, CE75, and CE100, the decrease rates are 17.4%, 30.8%, 36.5%, and 32.9%, respectively. As for the deformation rate, it declines first and then increases. Because the temperature field of the slab specimen changes with the addition of CE, the anti-rutting performance improves. It must be noted that, with the addition of porous materials, the mechanical properties of the mixture may decrease. When the amount of CE is more than 75%, the performance degradation is larger than the performance improvement caused by temperature decrease, so the deformation rate of the specimen will increase. However, the performance of CE mixture is still better than ordinary hot mix in general.

For FB mixture, the change laws of rutting depth and deformation rate are similar to the CE mixture as a whole. With the increasing of FB, compared with FB0, the decrease rates are 8.5% (FB25), 20.1% (FB50), 25.1% (FB75), and 16.5% (FB100). The reason for the change of rutting depth and deformation rate is similar to that of CE mixture.

Under the same proportion of admixture, the anti-rutting performance of FB mixture is worse than that of CE mixture. Moreover, the cooling effect of CE mixture is also better than that of FB mixture, and the same conclusions are achieved in the thermal conductivity test and cooling effect test. The order of CE mixture performance is conducted as follows: 75, 100, 50, 25, and 0%. It can be seen that the high-temperature performance order of mixture with 75% and 100% CE is not consistent with the cooling effect order. The reason is that hollow ceramic makes the strength of mixture to decrease and the content of asphalt will increase due to more porous materials in the mixture. These two factors comprehensively make the high-temperature performance decrease, so the content of CE in the mixture should be controlled. While for the mixture with FB, the order of anti-rutting performance is as follows: 75, 50, 100, 25, and 0%, which is not consistent with the cooling effect order of the mixture with 25% and

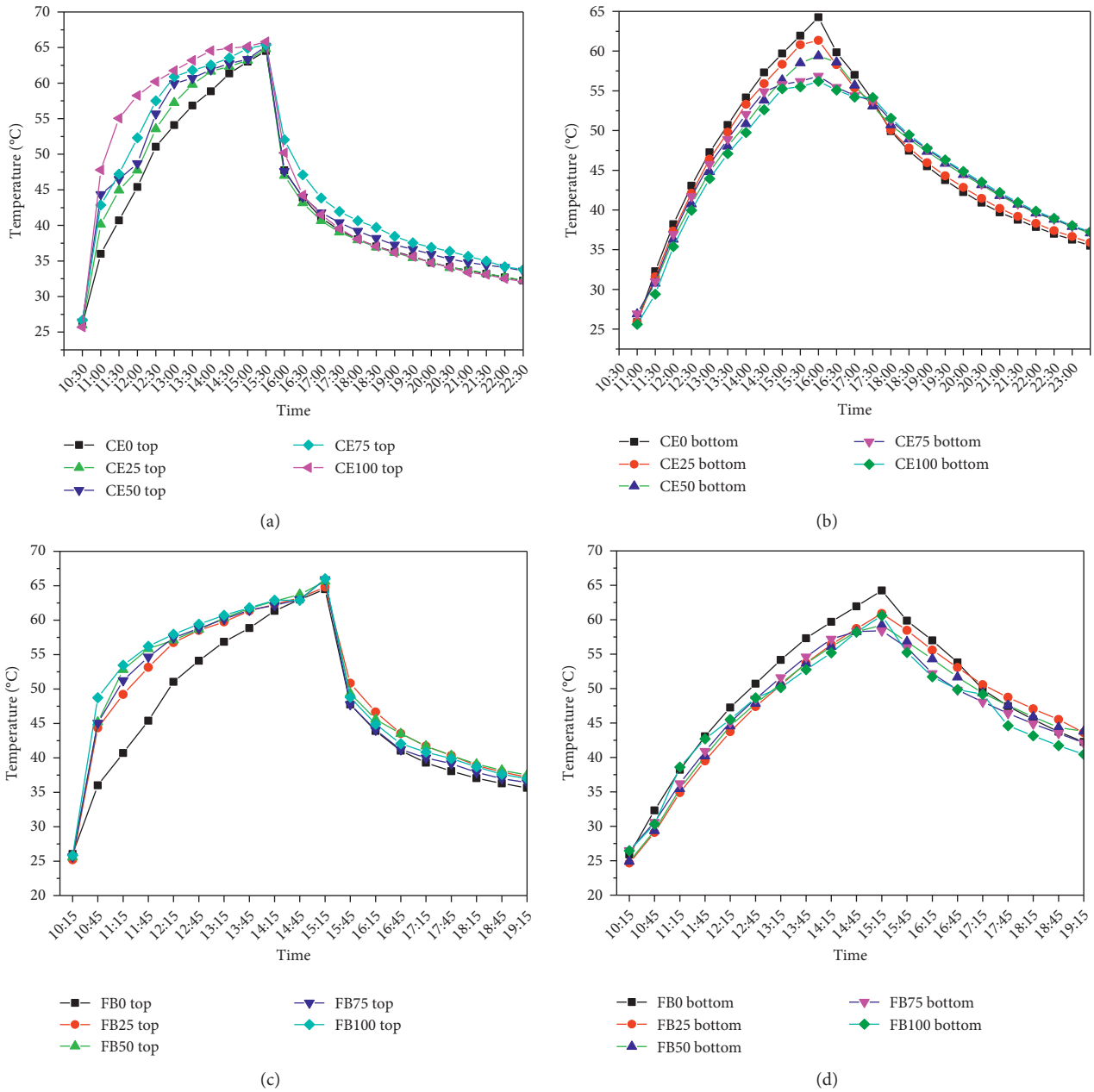


FIGURE 6: Temperature variation of the indoor illumination test (°C). (a) The top surface for CE type, (b) the bottom surface for CE type, (c) the top surface for FB type, and (d) the bottom surface for FB type.

TABLE 6: Results of the indoor cooling effect for TRAM.

Mixture type	Top surface maximum temperature (°C)	Bottom surface maximum temperature (°C)	Temperature difference (°C)	Cooling effect (°C)
CE0	64.5	64.3	0.3	—
CE25	64.8	61.4	3.4	2.6
CE50	65.2	59.4	5.8	4.2
CE75	65.35	56.85	8.5	6.6
CE100	65.8	56.2	9.6	6.8
FB0	64.5	64.3	0.2	—
FB25	64.8	60.9	3.9	3.1
FB50	65.7	59.2	6.5	3.9
FB75	65.9	58.4	7.5	4.5
FB100	66.0	60.6	5.4	2.2

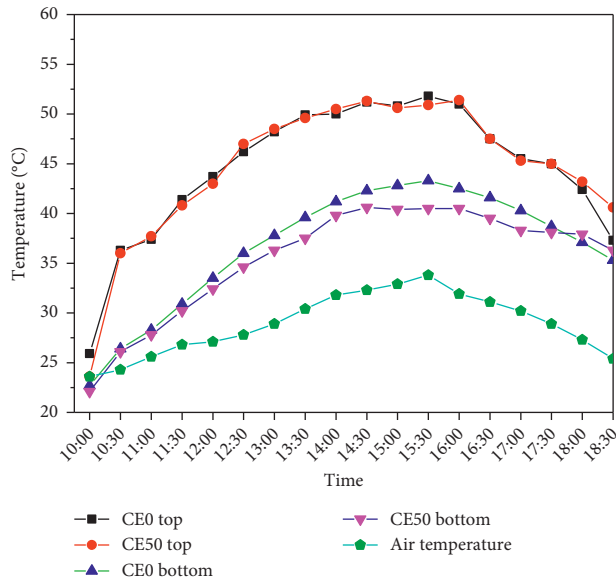


FIGURE 7: Temperature variation of the outdoor illumination test (°C).

TABLE 7: Results of outdoor cooling effect for CE.

Mixture type	Top surface maximum temperature (°C)	Bottom surface maximum temperature (°C)	Temperature difference (°C)	Cooling effect (°C)
CE0	51.8	45.3	6.5	—
CE25	51.6	41.2	10.4	4.3
CE50	51.3	40.6	10.7	5.2
CE75	51.5	38.9	12.6	6.7
CE100	51.8	38.5	13.3	6.8

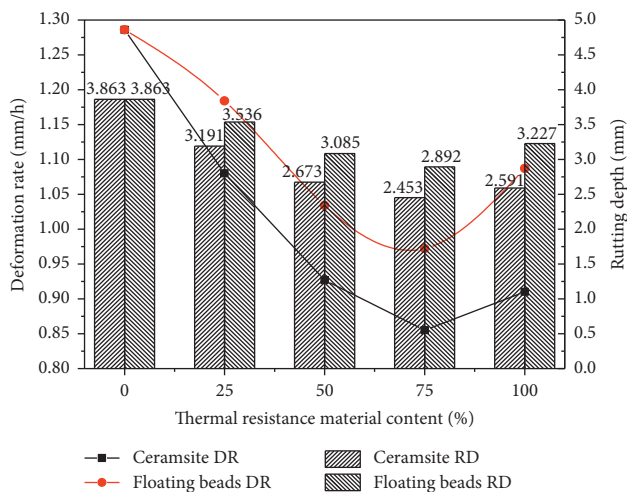


FIGURE 8: Results of the illumination rutting test.

100% FB. This is because when the substitution proportion of FB reaches 100%, the spherical shape of FB makes the asphalt mixture easily to be compacted and less optimum

asphalt content, which improves the high-temperature performance to some extent.

3.3.2. Evaluation of Low-Temperature Anticracking Performance. The low-temperature anticracking performance of mixture added with different contents of CE and FB was evaluated by the beam bending test, respectively. The results are shown in Figure 9.

As shown in Figure 9, with the increase of thermal resistance materials, the ultimate flexural strength and failure strain of the mixture decrease gradually, and the stiffness modulus increases. The results show that the addition of thermal resistance materials reduces the low-temperature cracking resistance of the mixture, the failure strain of CE100 and FB100 reaches 2938.6 $\mu\epsilon$ and 2812.3 $\mu\epsilon$, respectively. Obviously, when the proportion of thermal resistance materials reaches 100%, the failure strain of the mixture is close to the lower limit of Chinese specification. So, the replacement of two thermal resistance materials in the mixture should be less than 100%.

3.3.3. Evaluation of Water Stability Performance. As can be seen from Figure 10 and Table 8, the results of freeze-thaw splitting test for CE mixture are similar to those of HWTD. That is, a small amount of CE reduces the water stability of the mixture. But, with the increase of CE, the water stability performance increases first and then decreases. The reason is that the addition of low crushing value of CE reduces the overall strength of asphalt mixture. As CE dosage continues to increase, the porous structure of CE forms connected void in the mixture, and the space is reserved for the frost heave of water. Furthermore, CE can absorb light oil. CE plays the role of wedging and anchoring in the mixture. So, with the increase of CE, the water stability performance has a small increase. When the content of CE is more than 75%, its low mechanical strength is the main factor affecting the decline of water stability, thus causing the TSR of CE100 near the lower limit of specification. But, the water stability of CE mixture can still meet the requirements of Chinese standard JTG F40-2004.

For the mixture with FB, the TSR of asphalt mixture gradually drops as the proportion of FB increases. When the substitution proportion of FB reaches 100%, water stability of asphalt mixture cannot meet the requirements of specification. In the HWTD test, the order of water stability performance is as follows: 75, 50, 25, 0, and 100%. This means that the conclusions about the water stability evaluation of the mixture with FB are concerned with different test methods. The reason is that the freeze-thaw splitting test is used to evaluate short-term water stability, and the test loading mode of asphalt mixture is different from reality, causing the relatively low result reliability. In comparison, the dynamic loading is used in the HWTD test to simulate real load action which can imitate the effect of dynamic water on adhesion between asphalt and aggregate, so the result is more credible.

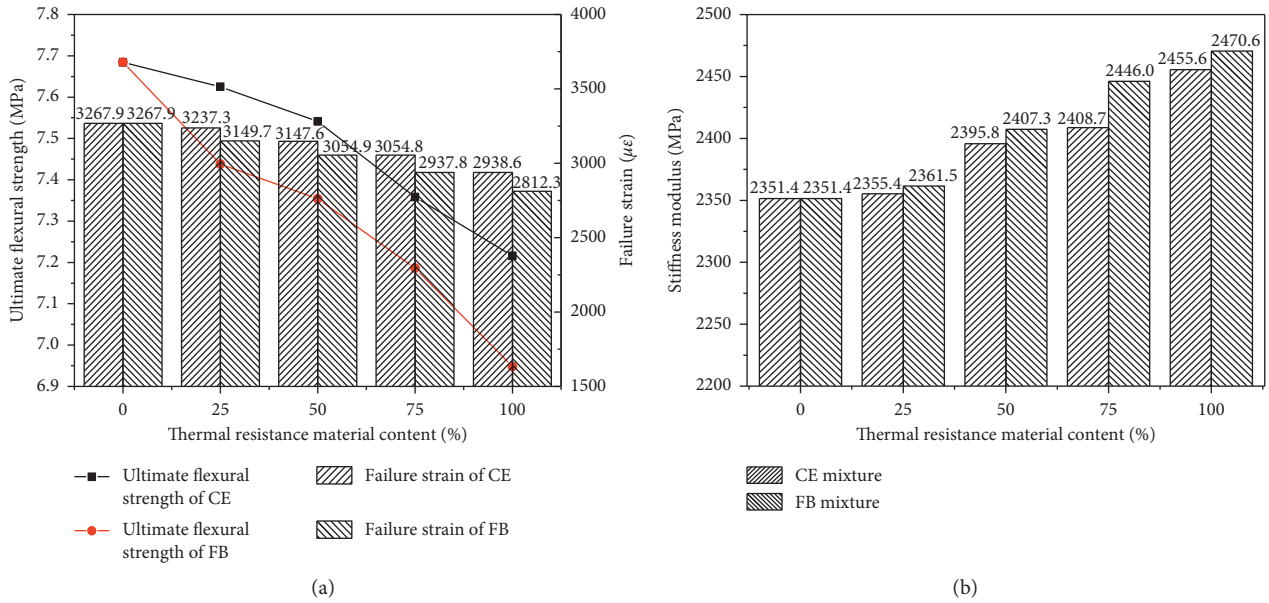


FIGURE 9: Results of the little beam bending test. (a) Ultimate flexural strength and failure strain and (b) stiffness modulus.

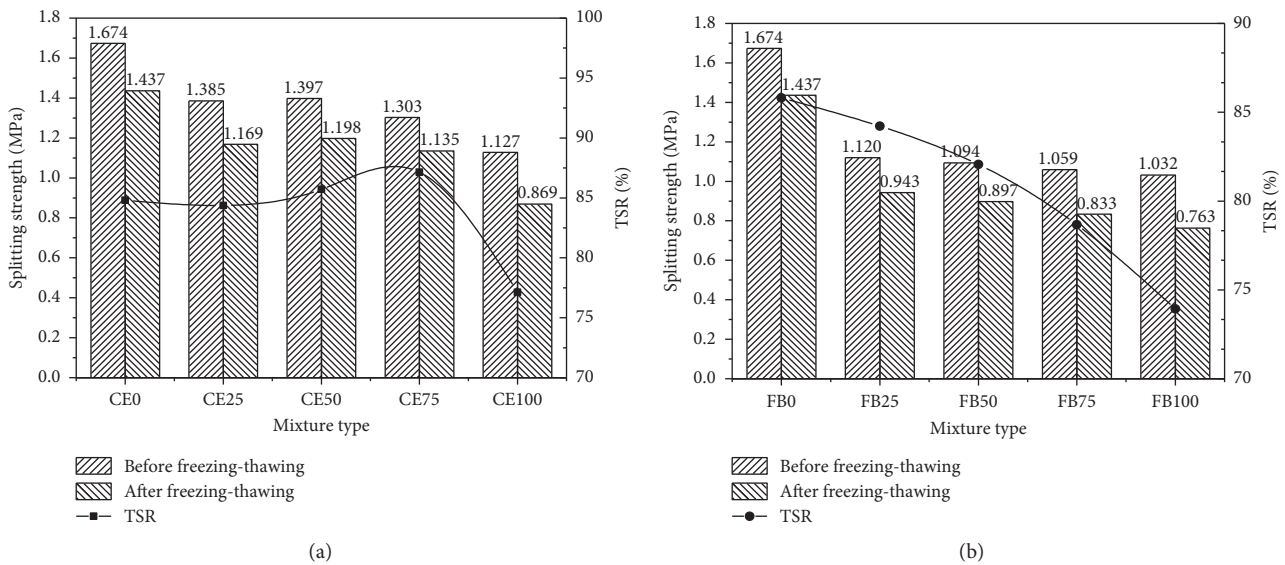


FIGURE 10: Results of the freeze-thaw splitting test. (a) CE type. (b) FB type.

TABLE 8: Results of HWTD.

Mixture type	Loading times (times)	Rut depth (mm)	Sip (times)	Strip slope
HMA	20000	19.4	11800	450.3
CE25	20000	18.9	9800	576.4
CE50	20000	17.3	12160	858.5
CE75	20000	15.6	12710	999.7
CE100	20000	18.0	7360	835.9
FB25	20000	15.6	12920	995.5
FB50	20000	16.4	13250	910.2
FB75	20000	16.5	13900	751.7
FB100	20000	19.2	8130	703.3

4. Conclusions

In this study, the cooling effect of two kinds of thermal resistance materials was studied through indoor and outdoor illumination tests. The road properties of the mixture, such as high-temperature performance, low-temperature performance, and water stability performance, added with thermal resistance materials were investigated. The main conclusions are summarized as follows:

- (1) The thermal conductivity of asphalt mixture decreases as the proportion of thermal resistance material increases. The thermal conductivity of CE mixture is smaller than that of FB mixture under the same proportion of admixture.
- (2) For CE mixture, the cooling effect increases gradually with the increase of CE content. The temperature of the mixture added with 75% and 100% CE drops to 6.6 and 6.8°C, respectively. And, for FB mixture, the cooling effect increases first and then decreases as the proportion of FB increases. The temperature drops to 3.9°C and 4.5°C, respectively, for the mixture added with 50% and 75% FB. The cooling effect of CE is better than that of FB.
- (3) The high-temperature performance of the mixture added with CE and FB increases first and then decreases. When the proportion of CE and FB is 75%, the mixture obtains the best high-temperature performance. The antirutting performance of FB mixture is worse than that of CE mixture. With the increase of two thermal resistance materials, the low-temperature cracking resistance of cooling mixture decreases. The failure strain of CE100 and FB100 is close to the lower limit of Chinese specifications, so the replacement of two thermal resistance materials in the mixture should be less than 100%. The water stability of different TRAM varies with the test methods.
- (4) Based on the results of pavement performance and the cooling effect, the substitution proportion of CE and FB for the TRAM is proposed as 50%~75%.

Data Availability

We confirm that the data submitted in this manuscript are available. All the data provided in the manuscript were obtained from the experiments performed at the Key Laboratory for Special Area Highway Engineering of Ministry of Education of Chang'an University.

Conflicts of Interest

The authors declare that they have no conflicts of interest.

Acknowledgments

This work was supported by the Key Project of Natural Science Research of Anhui Provincial Department of Education (KJ2018A0668) and Demonstration Experiment

Training Center (2018FXJS01). The authors gratefully acknowledge their financial support. And special thanks also are due to the Key Laboratory for Special Area Highway Engineering of Ministry of Education.

References

- [1] Z. Ma, Z. Tan, and C. Qian, "Study on the distribution of temperature field of asphalt pavement," *China Journal of Highway and Transport*, vol. 143, no. 4, pp. 9–15, 2014.
- [2] X. Feng, X. Zha, W. Wang et al., "Study on new mix design method for balancing anti-rutting and anti-cracking," *Journal of Wuhan University of Technology*, vol. 33, no. 5, pp. 86–89, 2011.
- [3] W. Yang, H. Gu, and Y. Shan, "Influence of pavement temperature on urban heat island," *Journal of Highway and Transport Research and Development*, vol. 25, no. 3, pp. 147–150, 2008.
- [4] Q. Zhu, W. Wang, S. Wang et al., "Unilateral heat-transfer asphalt pavement for permafrost protection," *Cold Regions Science and Technology*, vol. 71, pp. 129–138, 2012.
- [5] D. Feng, W. Hu, and F. Yu, "Influence of thermal properties of materials on temperature field for asphalt pavement," *Journal of Highway and Transport Research and Development*, vol. 28, no. 11, pp. 12–19, 2011.
- [6] W. Yang, H. Gu, and Y. Shan, "Influence of road surface temperature on urban heat island," *Journal of Highway and Transportation Research and Development*, vol. 25, no. 3, pp. 147–152, 2008.
- [7] Y. Lei, *Study on Asphalt Mixture of Automobile Exhaust Degradation and Ease of Urban Heat Island Effect*, Chang'an University, Xi'an, China, 2014.
- [8] W. Huang, S. Bao, and M. Gong, "Study on performance of cooling concrete pavement brick based on relieving urban heat island effect," *Journal of China & Foreign Highway*, vol. 37, no. 1, pp. 234–237, 2017.
- [9] Y. Guo, H. Zhang, J. Wang et al., "Influence of urban heat island on temperature field and mechanical properties of asphalt pavement," *Journal of Chongqing Jiaotong University (Natural Science)*, vol. 29, no. 4, pp. 548–551, 2010.
- [10] H. Takebayashi and M. Moriyama, "Study on surface heat budget of various pavements for urban heat island mitigation," *Advances in Materials Science and Engineering*, vol. 2012, Article ID 523051, 11 pages, 2012.
- [11] L. Doulos, M. Santamouris, and I. Livada, "Passive cooling of outdoor urban spaces. The role of materials," *Solar Energy*, vol. 77, no. 2, pp. 231–249, 2004.
- [12] K. L. Uemoto, N. M. N. Sato, and V. M. John, "Estimating thermal performance of cool colored paints," *Energy and Buildings*, vol. 42, no. 1, pp. 17–22, 2010.
- [13] C. S. S. Kumar, S. Suresh, L. Yang et al., "Flow boiling heat transfer enhancement using carbon nanotube coatings," *Applied Thermal Engineering*, vol. 65, no. 1-2, pp. 166–175, 2014.
- [14] M. Zheng, L. Han, F. Wang, H. Mi, Y. Li, and L. He, "Comparison and analysis on heat reflective coating for asphalt pavement based on cooling effect and anti-skid performance," *Construction and Building Materials*, vol. 93, pp. 1197–1205, 2015.
- [15] M. Zheng, L. He, X. Gao et al., "Performance analysis of thermal reflective coating on asphalt pavement," *Journal of Traffic and Transportation Engineering*, vol. 13, no. 5, pp. 10–16, 2013.

- [16] C. Wang, Y. Wang, X. Sun et al., "Development and performance evaluation of road cooling coating materials," *China Journal of Highway and Transport*, vol. 28, no. 8, pp. 14–21, 2015.
- [17] M. Zheng, C. Cheng, Y. Wang et al., "Study on asphalt pavement cooling technology based on improving pavement albedo," *The Journal of Highway and Transportation Research and Development*, vol. 8, no. 9, pp. 63–66, 2012.
- [18] W. Su, *Study on Thermal Reflective Waterborne Coating Material for Asphalt Pavement*, Southeast University, Nanjing, China, 2016.
- [19] H. Wang, *Study on Performance and Application of Thermal Reflection Coating for Asphalt Pavement*, Harbin Institute of Technology, Harbin, China, 2013.
- [20] B. González-Corrochano, J. Alonso-Azcárate, M. Rodas, J. F. Barrenechea, and F. J. Luque, "Microstructure and mineralogy of lightweight aggregates manufactured from mining and industrial wastes," *Construction and Building Materials*, vol. 25, no. 8, pp. 3591–3602, 2011.
- [21] B. Huang, Q. Dong, and E. G. Burdette, "Laboratory evaluation of incorporating waste ceramic materials into Portland cement and asphaltic concrete," *Construction and Building Materials*, vol. 23, no. 12, pp. 3451–3456, 2009.
- [22] R. B. Mallick, F. P. Hooper, S. O'Brien, and M. Kashi, "Evaluation of use of synthetic lightweight aggregate in hot-mix asphalt," *Transportation Research Record: Journal of the Transportation Research Board*, vol. 1891, no. 1, pp. 1–7, 2018.
- [23] E. B. Pancar, "Using recycled glass and zeolite in concrete pavement to mitigate heat island and reduce thermal cracks," *Advances in Materials Science and Engineering*, vol. 2016, Article ID 8526354, 8 pages, 2016.
- [24] J. Ren, B. Ma, W. Si, X. Zhou, and C. Li, "Preparation and analysis of composite phase change material used in asphalt mixture by sol-gel method," *Construction and Building Materials*, vol. 71, pp. 53–62, 2014.
- [25] D. Feng and J. Yi, "Study on mechanism and performance of asphalt pavement thermal resistance adhesive seal," *Journal of Highway and Transportation Research and Development*, vol. 26, no. 5, pp. 1–5, 2009.
- [26] X. Zhang, *Study on Cooling Mechanism and Application of Thermal Reflection and Thermal Resistance Technology for Asphalt Pavement*, Harbin Institute of Technology, Harbin, China, 2011.
- [27] A. Khan and D. Mrawira, "Investigation of the use of lightweight aggregate hot-mixed asphalt in flexible pavements in frost susceptible areas," *Journal of Materials in Civil Engineering*, vol. 22, no. 2, pp. 171–178, 2010.
- [28] Y. Ren, *Study on Performance of Ceramic Waste Material Used for Asphalt Pavement Insulation Mixture*, South China University of Technology, Guangzhou, China, 2011.
- [29] Y. Li, *Study on Properties of Calcined Bauxite Thermal Resistance of Asphalt Mixture*, Changsha University of Science and Technology, Changsha, China, 2014.
- [30] L. Cong, Y. Zhang, F. Xiao, and Q. Wei, "Laboratory and field investigations of permeability and surface temperature of asphalt pavement by infrared thermal method," *Construction and Building Materials*, vol. 113, pp. 442–448, 2016.
- [31] S. Yang and F. Yang, "Analysis of ceramsite raw materials," *Science and Technology*, vol. 7, pp. 45–55, 2010.
- [32] L. Luo and J. Sun, "Determination of some physicochemical properties for fly ash floating beads," *China Mining*, vol. 16, no. 12, pp. 111–115, 2007.
- [33] Z. Yang, Y. Liu, and Z. Yang, "The physical and chemical properties and its comprehensive utilization of fly ash," *Mineral Resources Protection and Utilization*, vol. 5, pp. 48–51, 2002.
- [34] Y. Zhang, *Construction Technology and Quality Control of Asphalt Pavement*, China Communications Press, Beijing, China, 2011.
- [35] Z. Yao and R. Wang, *Heat Transfer Science*, Beijing Institute of Technology Press, Beijing, China, 2003.
- [36] D. Xu, *Study on Heat Transfer of Asphalt Mixture*, Chang'an University, Xi'an, China, 2012.

Research Article

Comparative Study on the Axial Compression and Bearing Capacity of Reactive Powder Concrete-Filled Circular Steel Tube

Mingyang Chen  and Xiaomeng Hou

Department of Civil Engineering, Harbin Institute of Technology, Harbin, China

Correspondence should be addressed to Mingyang Chen; chenmy08@163.com

Received 29 May 2018; Accepted 4 December 2018; Published 19 December 2018

Guest Editor: Munir Nazzal

Copyright © 2018 Mingyang Chen and Xiaomeng Hou. This is an open access article distributed under the Creative Commons Attribution License, which permits unrestricted use, distribution, and reproduction in any medium, provided the original work is properly cited.

Reactive powder concrete (RPC) was confined by the circular steel tube to obtain the required ductility. The axial compression test results of 139 columns from different scholars were collated and compared to study the axial compression and bearing capacity of a reactive powder concrete-filled circular steel tube, of which the confining coefficient is 0.057–2.312 and the RPC strength is 76.6–178.2 MPa. Load-displacement curves have been categorized into four stages: (1) elastic; (2) elastic-plastic; (3) descending; and (4) strengthening. The failure mode can be divided into three types according to the different confining coefficients as (1) wall buckling; (2) diagonal shear; and (3) drum-shaped. The confining coefficient, core RPC strength, steel fiber volume, steel tube D/t ratio, and loading mode on the ultimate bearing capacity were analyzed. The results showed the confining coefficient to be the main factor affecting ultimate bearing capacity. The equation for determining ultimate bearing capacity was established based on the limit equilibrium theory, with the lateral confining coefficient of RPC (k) determined to be 2.86, less than that of normal concrete at 4.1. Based on the experimental analysis results and China's "Design and Construction Code for Concrete-Filled Steel Tube Structure" (CECS 28-2012), the design proposal for an RPC-filled steel tube was recommended.

1. Overview of Experiments

Reactive powder concrete (RPC) is the direction for further development of high-strength concrete (HSC) and ultrahigh performance concrete (UHPC), with a relatively new type of cement-based composite material successfully developed by Richard in 1993, which has ultrahigh strength, good volume stability, and excellent durability [1, 2]. The science behind the development of RPC is mature, and many studies have focused on its mechanical properties for further broad application in engineering [3–5]. However, RPC is very dense and uniform since it does not contain coarse aggregate; therefore, the pinning effect provided by coarse aggregates in normal concrete (NC) is weakened or even absent in RPC, and most RPCs are "explosive" and are destroyed by top-down longitudinal splitting after compression [5]. Measures to decrease brittleness and increase ductility of RPC are used for structures with ductile seismic performance requirements. RPC has been used in concrete-filled steel tubes

(RPCFTs) [6]. The steel tube restrains transverse deformation of the core RPC to allow the superior compressive performance of RPC to be fully utilized and its ductility to meet the requirements of the column design. The successful application of steel tube RPC in the construction of the Sherbrooke Bridge, Quebec, Canada, demonstrated its superior mechanical properties and economic benefits [7]. Although both RPC and NC are cement-based composite materials, their water/binder ratios, composition of raw materials, and mechanical properties differ considerably [8]. Therefore, the theory and method for calculating the ultimate bearing capacity of CFT cannot be directly applied to RPCFT.

The present study aimed at analyzing the axial compressive mechanical behavior and ultimate bearing capacity of RPCFTs. Many studies have focused on the experimental determination of the axial compression performance and ultimate bearing capacity of RPCFTs. The present study collated the experimental results of past studies on the axial

compression performance of 139 RPCFTs during 2003 to 2016, including Meng Shiqiang [8], Zhang Jing [9], Yang Wusheng [10], Wu Yanhai [11], Feng Jianwen [12], Yan Zhigang [13], Luo Hua [14], Yang Guojing [15], and Jian Wei [16]. Among the studies, tube diameter, wall thickness, and strength varying between 102 mm and 273 mm, 1 mm and 12 mm, and 210 MPa and 425 MPa, respectively, were considered to cause variation of the steel tube confining coefficient (ξ) in the range of 0.057–2.312. RPC strengths in the range of 76.6 MPa–178.2 MPa were affected by the RPC water/binder ratio (0.16–0.26), RPC steel fiber content (0%–2%), and curing methods (standard curing, 90°C steam curing, and curing in an autoclaved reactor with a maximum temperature and pressure of 200°C and 1.3 MPa, respectively). The main parameters are shown in Table 1.

2. Test Results

2.1. Load-Displacement Relationship. A review of the 139 RPCFT axially compressed experiments conducted in past studies found that the vertical stress and strain of the steel tube and core RPC gradually increased with increasing axial load due to pressure, and the core RPC was compressed in three directions because of constraints placed by the steel tube. The RPC peak strain under pressure varied from 0.0035 to 0.008 and increased by 3% to 32%, respectively. The ultimate bearing capacity of RPCFT increased between 2% and 58% over the sum of the bearing capacity of the steel tube and RPC, and brittle failure of the core RPC was not found with effective restraint, plastic deformability of the components was gradually reduced, and the integrity of samples with larger confining coefficients remained after sizeable deformations of 5%, thereby demonstrating excellent ductility. Figure 1 shows the load-displacement curve of the specimen. The mechanical characteristics of RPCFT could be divided into four stages: (1) elasticity; (2) elastic-plastic; (3) descending; and (4) strengthening.

2.1.1. Elastic Stage (OA). Vertical deformation of the steel tube and RPC increased proportionally with increased load, and no significant deformation of the steel tube surface was observed. The proportional ultimate load of RPCFT ranged from 85% to 95% of the ultimate bearing capacity, whereas the value of CFT was 70%, smaller than that of RPCFT, thereby explaining the disproportionately high strength of RPC in relation to NC. RPC had a uniform and denser internal structure, with mechanical properties closer to elastic material. RPC remained elastic at the ultimate load of 80–95% with no significant volume expansion and maintained Poisson's ratio at 0.2–0.4. CFT at 40% of the ultimate load experienced rapid expansion of the cracks in the interface between aggregate and cementite, with sharp increases in deformation and significant expansion of volume, resulting in the appearance of the Lüder J slip line. Figure 2 compares the longitudinal and transverse strains between RPC and NC.

2.1.2. Elastic-Plastic Stage (AB). With the increasing axial load, yielding of the steel tube occurred due to compression

and redistribution of internal force between RPC and steel tube. Thus, there were sharp increases in RPC compressive stress and internal microcracks emerged. In addition, there was continuous expansion of the widths and lengths of cracks, along with increases in transverse volume expansion deformation. The overall stiffness was degraded and the load-deformation curve showed a significant nonlinearity. Since RPC does not contain coarse aggregates, the fracture surface was relatively smooth, the steel fiber at the fracture surface was almost broken, and cracks were filled with powdery material. After the steel tube was extruded, the surface was partially convex, the rust began to peel off, and the Lüder J slip line appeared.

2.1.3. Descending Stage (BC). At the attainment of the ultimate load, a large amount of internal energy accumulated inside the core of RPC due to compression deformation being suddenly released. Internal cracks rapidly expanded to form a fracture surface. When the steel fiber was almost broken at the fracture surface, the strain energy was rapidly released and the sample broke into pieces. A sound of a sudden splitting failure could then be heard, indicating a load-deformation curve on the decline in the bearing capacity (BC). The sudden drop of bearing capacity involved a process where strain energy was rapidly released, which was dependent on the confining coefficient. RPCFT with a small confining coefficient experienced a small confining force provided by the steel tube. After reaching the ultimate load, the drop in longitudinal stress in the steel tube was higher than that of the restraining effect on the RPC strength provided by the steel tube. There was a marked drop in bearing capacity, and the slope ratio of the descending segment became almost equal to the RPC. An increasing confining coefficient resulted in a significant increase in the confinement effect of the steel tube on the core RPC, and the load-deformation curve showed that the load amplitude did not descend obviously or no obvious decrease after reaching the ultimate bearing capacity was evident. Taking specimens XG1-1 and G1 of Wu Yanhai [11] as examples, the confining coefficient of XG1-1 was small; thus, the steel tube had little restraining effect on RPC and the specimen emitted a bursting sound after reaching the ultimate load. The bearing capacity then drastically dropped and the remaining bearing capacity became only 65% of the ultimate load. The specimen showed significant brittle failure, whereas G1 had a large confining coefficient, the steel tube had a strong constraint on the RPC and the ultimate load bearing capacity descended slowly. The remaining bearing capacity reached as high as 95% of the ultimate load, the curve of the descending section was gentle, and the specimen underwent ductile failure.

2.1.4. Strengthening Stage (CD). The steel tube entered the strengthening stage after the plastic flow stage under a sufficiently thick steel tube wall, and the strong restraint provided by the steel tube continued to slow down the decline in the core RPC bearing capacity. The entire test bearing capacity entered a rebound state when the increased

TABLE 1: The main parameters of the axial compression experiments of reactive powder concrete-filled steel tubes (RPCFTs)

Index	Section	f_{cu} (MPa)	f_y (MPa)	ξ	Fiber (%)	N_u (kN)
1	100 × 4.5 × 200	141.5	210	0.434	2.00	2178
2	100 × 4.5 × 200	141.5	210	0.434	0.00	2070
3	100 × 4.5 × 200	141.5	210	0.434	2.00	2121
4	125 × 1 × 438	155.4	250	0.057	0.00	1700
5	125 × 1 × 438	155.4	250	0.057	0.00	2000
6	125 × 1 × 438	155.4	250	0.057	0.00	1840
7	127 × 2 × 445	155.4	245	0.113	0.00	1930
8	127 × 2 × 445	155.4	245	0.113	0.00	1790
9	127 × 2 × 445	155.4	245	0.113	0.00	1850
10	133 × 3.5 × 465	155.4	289	0.231	0.00	2420
11	133 × 3.5 × 465	155.4	289	0.231	0.00	2360
12	133 × 3.5 × 465	155.4	289	0.231	0.00	2490
13	133 × 5 × 465	155.4	319	0.378	0.00	2450
14	133 × 5 × 465	155.4	319	0.378	0.00	2480
15	133 × 5 × 465	155.4	319	0.378	0.00	2350
16	133 × 3.5 × 465	167.1	289	0.221	0.00	2180
17	133 × 3.5 × 465	167.1	289	0.221	0.00	2480
18	133 × 3.5 × 465	167.1	289	0.221	0.00	2440
19	133 × 3.5 × 400	167.1	289	0.221	0.00	2430
20	133 × 3.5 × 400	167.1	289	0.221	0.00	2500
21	133 × 3.5 × 400	167.1	289	0.221	0.00	2565
22	102 × 1 × 324	148	328	0.101	0.00	1310
23	102 × 1 × 324	172	328	0.088	1.20	1335
24	104 × 2 × 416	172	328	0.178	1.20	1463
25	104 × 2 × 416	172	328	0.178	1.20	1486
26	106 × 3 × 378	172	328	0.27	1.20	1780
27	106 × 3 × 378	172	328	0.27	1.20	1853
28	106 × 3 × 378	172	328	0.27	1.20	1760
29	121 × 5 × 484	172	350	0.439	1.20	2608
30	121 × 5 × 484	172	350	0.439	1.20	2576
31	121 × 5 × 484	172	350	0.439	1.20	2612
32	128 × 2 × 466	172	315	0.138	1.20	2256
33	128 × 2 × 466	172	315	0.138	1.20	2228
34	128 × 2 × 466	172	315	0.138	1.20	2218
35	128 × 2 × 466	172	315	0.138	1.20	2224
36	128 × 2 × 466	148	315	0.158	0.00	2190
37	128 × 2 × 466	148	315	0.158	0.00	2213
38	130 × 3 × 455	172	315	0.208	1.20	2496
39	130 × 3 × 455	172	315	0.208	1.20	2510
40	130 × 3 × 455	172	315	0.208	1.20	2523
41	130 × 3 × 455	172	315	0.208	1.20	2508
42	130 × 3 × 455	172	315	0.208	1.20	2489
43	130 × 3 × 455	172	315	0.208	1.20	2467
44	133 × 3 × 400	122.4	290	0.257	0.00	2000
45	133 × 3 × 400	122.4	290	0.257	0.00	2005
46	133 × 3 × 400	172.2	290	0.182	0.00	2300
47	133 × 3 × 400	172.2	290	0.182	0.00	2350
48	133 × 4.5 × 400	122.4	318	0.439	0.00	2250
49	133 × 4.5 × 400	122.4	318	0.439	0.00	2200
50	133 × 4.5 × 400	172.2	318	0.311	0.00	2700
51	133 × 4.5 × 400	172.2	318	0.311	0.00	2750
52	133 × 6.5 × 400	122.4	318	0.666	0.00	2300
53	133 × 6.5 × 400	122.4	318	0.666	0.00	2350
54	133 × 6.5 × 400	172.2	318	0.472	0.00	2950
55	133 × 6.5 × 400	172.2	318	0.472	0.00	2950
56	133 × 8.5 × 400	122.4	290	0.837	0.00	2500
57	133 × 8.5 × 400	122.4	290	0.837	0.00	2550
58	133 × 8.5 × 400	172.2	290	0.592	0.00	2950
59	133 × 8.5 × 400	172.2	290	0.592	0.00	2960
60	133 × 10 × 400	122.4	376	1.329	0.00	3200

TABLE 1: Continued.

Index	Section	f_{cu} (MPa)	f_y (MPa)	ξ	Fiber (%)	N_u (kN)
61	133 × 10 × 400	122.4	376	1.329	0.00	3100
62	133 × 10 × 400	172.2	376	0.941	0.00	3450
63	133 × 10 × 400	172.2	376	0.941	0.00	3450
64	133 × 12 × 400	172.2	336	1.067	0.00	3500
65	133 × 12 × 400	172.2	336	1.067	0.00	3650
66	110 × 5 × 300	133.9	310	0.562	0.00	1580
67	113 × 6.5 × 300	133.9	321	0.768	0.00	2076
68	113 × 6.5 × 300	133.9	321	0.768	0.00	2048
69	110 × 5 × 300	125.5	310	0.552	0.50	1620
70	110 × 5 × 300	125.5	310	0.552	0.50	1621
71	110 × 5 × 300	125.5	320	0.57	0.50	1645
72	110 × 5 × 300	125.5	320	0.57	0.50	1709
73	110 × 5 × 300	125.5	320	0.57	0.50	1655
74	113 × 6.5 × 300	125.5	321	0.754	0.50	2096
75	113 × 6.5 × 300	125.5	321	0.754	0.50	2172
76	113 × 6.5 × 300	163	321	0.65	0.00	2379
77	113 × 6.5 × 300	163	321	0.65	0.00	2415
78	108 × 6 × 300	170	391	0.72	1.00	2141
79	108 × 6 × 300	170	391	0.72	1.00	2146
80	110 × 5 × 300	178.2	320	0.464	2.00	1693
81	110 × 5 × 300	178.2	320	0.464	2.00	1641
82	110 × 5 × 300	178.2	320	0.464	2.00	1734
83	110 × 5 × 300	125.5	310	0.552	0.50	1789
84	110 × 5 × 300	125.5	310	0.552	0.50	1730
85	110 × 5 × 300	125.5	320	0.57	0.50	1865
86	110 × 5 × 300	125.5	320	0.57	0.50	1745
87	110 × 5 × 300	178.2	320	0.464	2.00	1886
88	110 × 5 × 300	178.2	320	0.464	2.00	1745
89	110 × 5 × 300	133.9	310	0.562	0.00	1789
90	110 × 5 × 300	125.5	310	0.552	0.50	1760
91	110 × 5 × 300	125.5	310	0.552	0.50	1780
92	108 × 6 × 300	170	391	0.72	1.00	2127
93	108 × 6 × 300	170	391	0.72	1.00	2170
94	108 × 6 × 300	170	391	0.72	1.00	2034
95	108 × 6 × 300	170	391	0.72	1.00	2090
96	152 × 5 × 500	87.4	314	0.595	0.00	2704
97	152 × 5 × 500	87.4	314	0.595	0.00	2679
98	152 × 5 × 500	87.4	314	0.595	0.00	2799
99	152 × 5 × 500	76.6	314	0.639	0.00	2287
100	152 × 5 × 500	76.6	314	0.639	0.00	2306
101	121 × 6 × 450	85.4	316	0.979	0.00	1907
102	121 × 6 × 450	85.4	316	0.979	0.00	1902
103	102 × 4 × 450	85.4	291	0.689	0.00	1183
104	102 × 4 × 450	85.4	291	0.689	0.00	1140
105	152 × 5 × 450	85.4	322	0.625	0.00	2833
106	152 × 5 × 450	85.4	322	0.625	0.00	3057
107	121 × 6 × 450	113.6	316	0.734	0.00	2165
108	121 × 6 × 450	113.6	316	0.734	0.00	2173
109	102 × 4 × 450	113.6	291	0.517	0.00	1326
110	102 × 4 × 450	113.6	291	0.517	0.00	1275
111	152 × 5 × 450	113.6	322	0.469	0.00	2961
112	152 × 5 × 450	113.6	322	0.469	0.00	2870
113	133 × 4.5 × 400	96.8	351	0.621	0.00	1817
114	133 × 4.5 × 400	96.8	351	0.621	0.00	1814
115	133 × 4.5 × 400	96.8	351	0.621	0.00	1837
116	133 × 4.5 × 400	96.8	351	0.621	0.00	1843
117	133 × 6 × 400	96.8	330	0.808	0.00	2039
118	133 × 6 × 400	96.8	330	0.808	0.00	2128
119	133 × 6 × 400	96.6	330	0.808	0.00	1966
120	133 × 6 × 400	96.6	330	0.808	0.00	1978

TABLE 1: Continued.

Index	Section	f_{cu} (MPa)	f_y (MPa)	ξ	Fiber (%)	N_u (kN)
121	133 × 8 × 400	96.6	338	1.162	0.00	2550
122	133 × 8 × 400	96.6	338	1.162	0.00	2552
123	133 × 8 × 400	96.6	338	1.162	0.00	2430
124	133 × 8 × 400	96.6	338	1.162	0.00	2512
125	133 × 10 × 400	96.8	313	1.419	0.00	2890
126	133 × 10 × 400	96.8	313	1.419	0.00	2894
127	133 × 10 × 400	96.8	313	1.419	0.00	2583
128	133 × 10 × 400	96.8	313	1.419	0.00	2510
129	133 × 12 × 400	96.8	402	2.312	0.00	3374
130	133 × 12 × 400	96.8	402	2.312	0.00	3396
131	133 × 12 × 400	96.6	402	2.312	0.00	3260
132	133 × 12 × 400	96.6	402	2.312	0.00	3262
133	219 × 8 × 657	118	450	0.737	2.00	6569
134	219 × 10 × 657	118	430	0.908	2.00	7095
135	219 × 12 × 657	118	375	0.98	2.00	7318
136	245 × 8 × 735	118	425	0.615	2.00	7747
137	245 × 12 × 735	118	383	0.877	2.00	8761
138	273 × 8 × 819	118	412	0.529	2.00	9211
139	273 × 10 × 819	118	380	0.625	2.00	9666

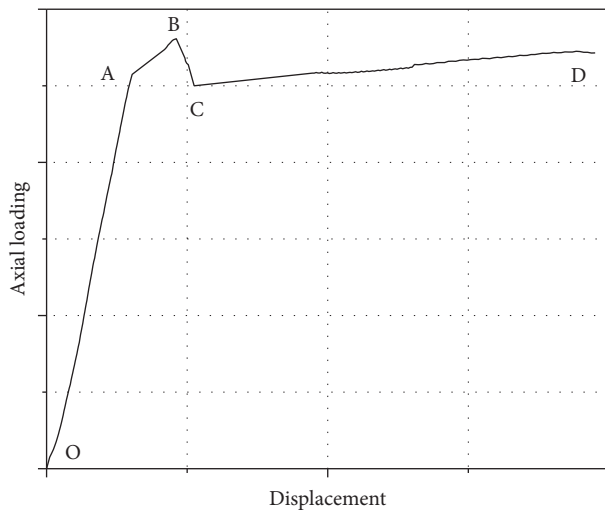


FIGURE 1: Load-displacement curve of the reactive powder concrete-filled steel tube (RPCFT).

bearing capacity of the steel tube was sufficient to offset the decline of the core RPC bearing capacity, with the amplitude of its rebound dependent on the confining coefficient of the specimen itself. The larger the confining coefficient, the greater the magnitude of the rebound. Yang Wusheng [10] obtained a similar conclusion when analyzing these test results, namely, under a confining coefficient < 0.4 , the bearing capacity of the specimen did not rebound and the curve was flat or continued to decrease, whereas when the bearing capacity was > 1.3 , the curve enhancement segment could experience sustainable growth.

2.2. Failure Mode. It was found that the failure modes of the 139 RPCFTs could be categorized into three types, as showed in Figure 3.

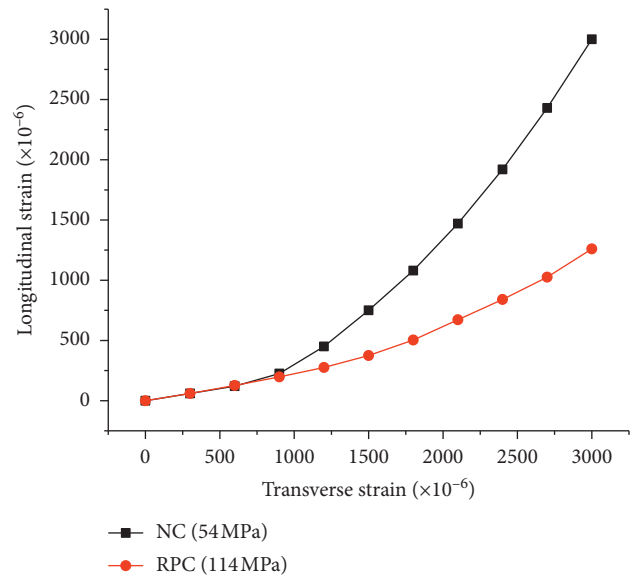


FIGURE 2: The transverse strain versus longitudinal strain of reactive powder concrete (RPC) and normal concrete (NC).

2.2.1. Steel Tube Buckling Failure. The CFT research results showed that under a large steel tube diameter-thickness ratio (D/t), the straight steel tube underwent a “bowstring effect” under the axial pressure, and the specimen formed a “string” buckling instability by brittleness failure when the ultimate bearing capacity was reached. The CFT design specification of every country provides the D/t limit, and China’s “Technical Specification for CFT” (GB50936-2014) stipulates D/t to be: $(20 \sim 135)(235/f_y)$. However, Zhang Jing [9] studied A1-1 specimens with a diameter of 125 mm and a wall thickness of 1 mm, and Yang Wusheng [10] studied specimens of a diameter of 104 mm and a wall thickness of 1 mm, with D/t of 125 and 104, respectively, thereby meeting the requirements of the technical specifications for CFT.

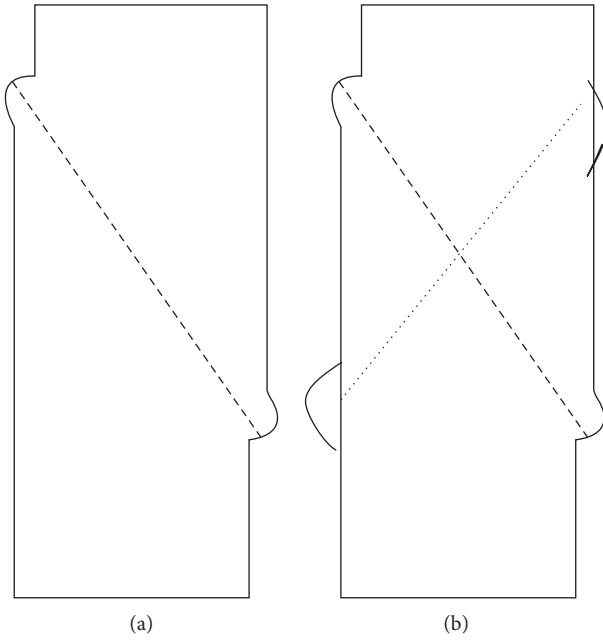


FIGURE 3: (a) Oblique shear failure and (b) waist drum-shaped failure of reactive powder concrete-filled steel tube (RPCFT).

However, “string” buckling instability remained, mainly because deformation of NC increased rapidly reaching 40% of the ultimate load, and the volume of the core concrete expanded significantly, thereby playing a certain role in supporting the steel tube wall. The transverse strain and volume expansion of RPCFT did not markedly change before reaching the ultimate load. The core concrete cannot support or restrain the tube wall. Therefore, it is recommended that the D/t ratio of RPCFT be determined in accordance with the “Code for Design and Construction of CFT” (CECS 28:90) as $(20 \sim 80)(235/f_y)$.

2.2.2. Oblique Shear Failure. The internal energy accumulated in the core RPC was suddenly released to form a fracture surface after the RPC reached the ultimate strength. The fracture surface generated a misalignment and formed two wedge blocks above and below, which were able to slide along the shear surface, resulting in local convexity of the steel tube. However, the increase in the confining coefficient resulted in a strengthening of the restraining effect of the steel tube, an increased restriction of sliding, a slowing down of the development speed of the internal shear crack, and a decrease in the bearing capacity of the steel tube RPC. Yang Wusheng [10] observed a significant shear slip plane after cutting the specimen with shear failure. An inclination angle of $25^\circ \sim 31^\circ$ was evident; the steel fiber at the shear failure surface was removed, and powdery particles were observed at the RPC contact surface.

2.2.3. Drum-Shaped Failure. Under a large confining coefficient, although the upper and lower wedge blocks of core RPC were able to slide to form a shear slip plane, slide was prevented because the wedge block was placed under a large

lateral constraint. The core RPC formed a second shear plane in the opposite direction, thereby increasing the transverse deformation of the specimen to form a partially roughened portion, eventually forming a multifold shear failure, i.e., drum bending in the position of the top and bottom roofs of the bearing capacity. The RPC was severely crushed and could be peeled off by hand. For NC, Zhang Sumei [17] found that CFT with a confining coefficient of approximately 0.8 would suffer from drum-type damage. The characteristics of RPC material and the results of 139 RPCFT showed that the critical confining coefficient is suggested to occur in oblique shear failure and waist drum failure.

3. Analysis of Factors Affecting RPCFT Axial Compression Bearing Capacity

3.1. Confining Coefficient. The confining coefficient (ξ) is a comprehensive index that reflects the extent to which the core RPC is constrained by the steel tube and is the key factor affecting the ultimate bearing capacity and failure mode of the RPCFT. The fitting curve between ξ and $N_u/A_c f_c$ by the test results of 87 RPCFT without steel fibers in Table 1 is shown in Figure 4.

Figure 4 shows that ξ is proportional to $N_u/A_c f_c$, and the proportional factor is 1.394; however, the factors for HSC and NC were 1.8 and 2, respectively. The factor decreased with increasing strength due to the weakened confining coefficients of HSC and RPC. This was mainly because when NC was loaded to 40% of the ultimate load, expansion of microcracks in the transition zone between cement stone and coarse aggregate caused discontinuity of the displacement field, resulting in a rapid increase of the transverse deformation coefficient of the concrete. The large sum exceeded Poisson’s ratio of the steel tube, and a large confining force was formed after the steel tube was extruded. The water-binder ratio was smaller, and the internal structure was denser for HSC or RPC. RPC was in particular close to an elastic material. Poisson’s ratio of RPC did not change much before the RPC was loaded 80%–90% of the ultimate load. The transversal strain and vertical strain ratio developed proportionally. The lateral deformation coefficient of RPC struggled to exceed Poisson’s ratio of the steel tube, and the confining force of the steel tube was difficult to initiate:

$$\frac{N_u}{A_c f_c} = 1.394\xi + 1.103. \quad (1)$$

3.2. Diameter to Thickness Ratio of Steel Tube. When applying a fixed steel tube outer diameter (D), the confining coefficient increased with increasing steel tube thickness (t) and the ultimate bearing capacity continued to increase. Figures 5 and 6 show the fit of the relationship between D/t and $N_u/A_c f_c$ from the results of Yang Guojing [15] and Wu Yanhai [11], respectively. From the figures, it is evident that, under a relatively small D/t , the change in D/t had a greater influence on the ultimate bearing capacity, whereas under a larger D/t , variation of D/t had little effect on the ultimate bearing capacity, and the critical D/t ratio was 25–30.

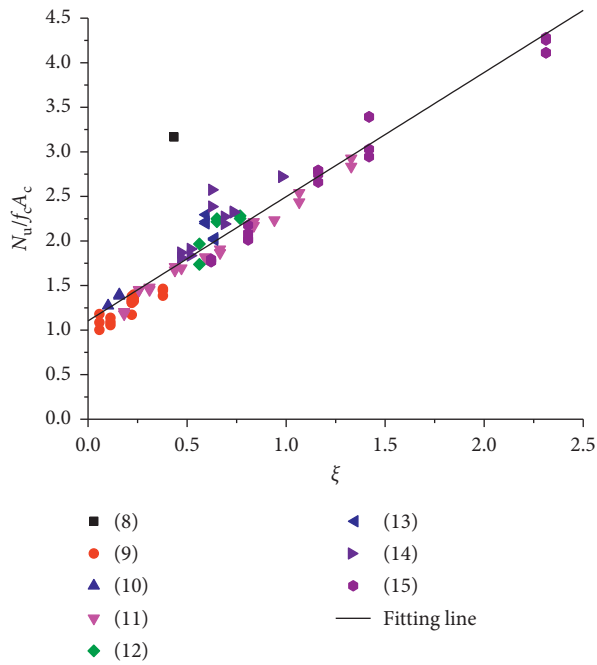


FIGURE 4: Relationship between ξ and $N_u/A_c f_c$ by RPCFT without steel fiber.

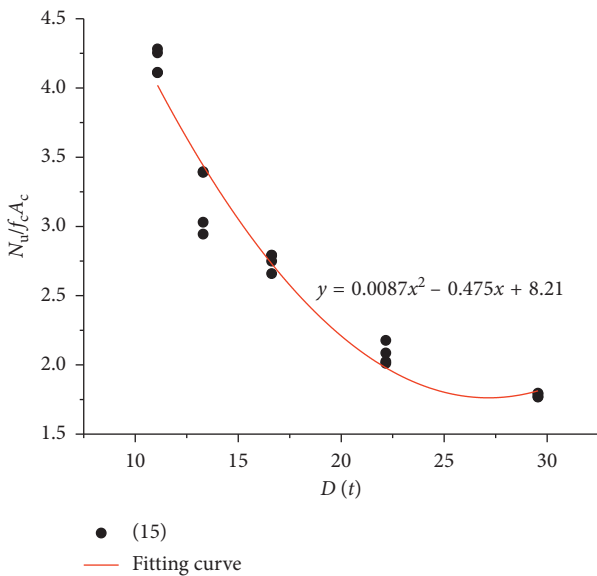


FIGURE 5: The relationship between D/t and $N_u/A_c f_c$ provided by Yang Guojing [15].

3.3. Core RPC Strength. Figure 7 shows the fitting relationship between ξ and $N_u/A_c f_c$ by Yang Guojing [15] using the results of 20 RPCFT with an RPC strength of 96.6 MPa. Figure 8 shows the above relationship from the study of Zhang Jing [9] and Wu Yanhai [11] with RPC strengths of 167.1 MPa and 172.1 MPa, respectively. Evident from Figures 7 and 8 is that the scale factor between ξ and $N_u/A_c f_c$ under a strength of 96.6 MPa is 1.43 and under the strengths of 167.1 MPa and 172.2 MPa is 1.37. Therefore, with an increase of RPC strength, the effect of the steel tube on RPC restraint was further weakened, and its proportional

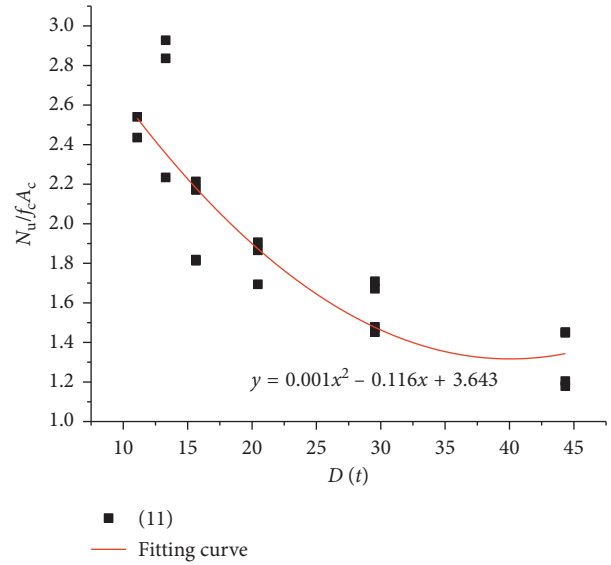


FIGURE 6: The relationship between D/t and $N_u/A_c f_c$ provided by Wu Yanhai [11].

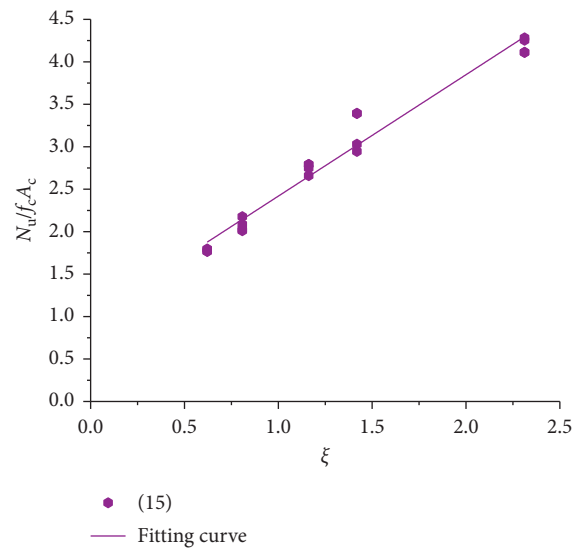


FIGURE 7: Relationship between ξ and $N_u/A_c f_c$ provided by Yang Guojing [15].

coefficient was reduced from 1.43 to 1.37. However, the change was merely 4.2%, which can be neglected for practical applications.

3.4. Steel Fiber Content in RPC. Table 2 shows the effect of steel fiber content on the ultimate bearing capacity of RPCFT. It is evident from Table 2 that, for a steel fiber content of 1.2%, RPC axial compressive strength increased by 15%, and the total axial compressive strength of RPC and steel tube should be increased by approximately 10%, whereas the actual ultimate load of the test samples were increased by an almost negligible amount of 0.7% to 3.8%. The axial compressive strength of RPC increased by 25% under a steel fiber content of 2%. Considering the contribution of RPC to strength, the theoretical ultimate capacity of

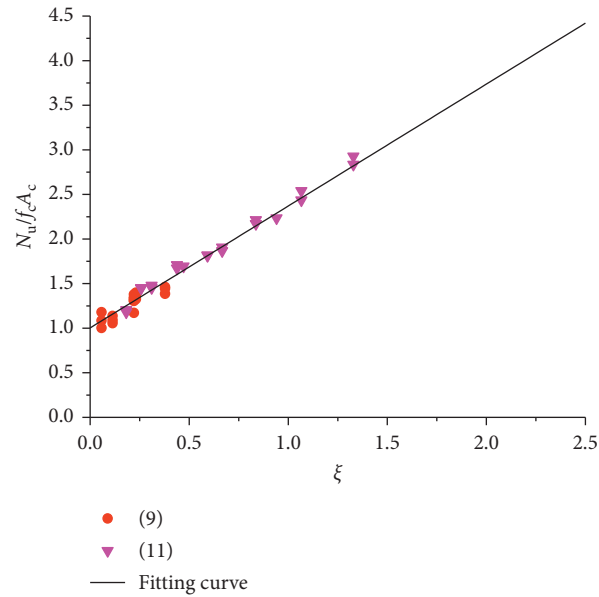


FIGURE 8: The relationship between ξ and $N_u/A_c f_c$ provided by Zhang Jing [9].

TABLE 2: The effect of the ultimate bearing capacity by the fiber ratio in reactive powder concrete (RPC).

Reference	Sample no.	Steel fiber (%)	f_c	A_c	N_u	f'/f (%)	$(f'_c - f_c)A_c/N_u$ (%)	$N'_u - N_u/N_u$ (%)
[8]	B21	0	141	6504	2070			
	B22	2	—	6504	2121			2.4
[10]	L-1	0	131	7854	1310			
	H-1	1.2	150	7854	1335	115	11	1.9
	L-2A	0	131	12076	2190			
	H-8A	1.2	150	12076	2256	115	10	3.0
	L-2B	0	131	12076	2213			
[12]	H-8B	1.2	150	12076	2228	115	10	0.7
	CFT1	0	116	7854	1580			
	CFT8-2	2	145	7854	1641	125	14	3.8

RPCFT resulting from an increase of the axial compressive strength of RPC increased by approximately 14%, whereas the ultimate load bearing capacity of the actual test increased by merely from 2.4% to 3.8%. Almost no effect on the ultimate bearing capacity could be expected. Therefore, although the steel fiber content could increase the axial compressive strength of RPC, the contribution to the ultimate bearing capacity of RPCFT was negligible, consistent with the conclusion of Dallaier [18], mainly because of differences in the action mechanism between steel fibers and steel tubes in RPC. The main role of steel fiber was to withstand some of the tensile stress placed on the RPC principal stress section, thereby increasing the strength of RPC. However, the core RPC confined by the steel tube was compressed in three directions, and the principal compressive stress failure was found when the ultimate load reached. Therefore, the addition of steel fiber to steel tube RPC did not contribute considerably to the bearing capacity. To reduce costs, the addition of steel fiber to RPCFT is not recommended.

3.5. Loading Method. The most commonly used loading methods for CFT as shown in Figure 9 include full-section

load and core-loaded concrete. Table 3 compares the ultimate bearing capacity from the study of Yang Guojing [15] under different loading methods. The differences in bearing capacities under both loading modes were within 5%. It can be considered that the loading method was applied to the mechanical properties of the axially compressed short columns of steel tube RPC. The impact could be regarded as negligible.

4. Analysis of RPCFT-Bearing Capacity Based on Limit Equilibrium Theory

Methods of determining the ultimate bearing capacity of CFT can be divided into two categories: (1) numerical analysis methods and (2) limit analysis methods [19]. A numerical analysis method analyzes the material stress-strain relationship to simulate the load history and process, thereby determining the force and deformation characteristics of the entire process from elasticity to failure. The limit analysis method is based on the force balance relationship evident when components are in a limit bearing capacity state. This method can calculate the ultimate bearing capacity and is independent of the loading history and the deformation process. At present, research on the

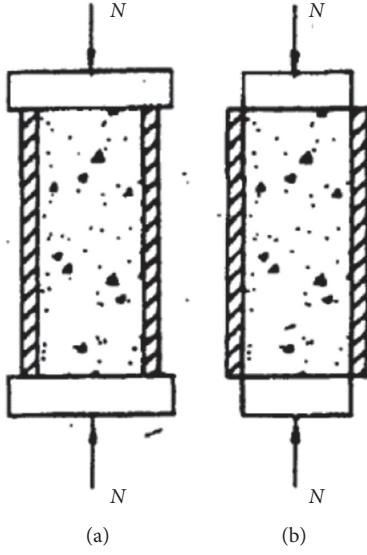


FIGURE 9: Loading pattern of the RPC-filled circular tube used in the experiment. (a) Loading on the reactive powder concrete (RPC) and tube. (b) Loading only on the reactive powder concrete (RPC).

TABLE 3: Effect of the ultimate bearing capacity according to the loading pattern.

Sample no.	Loading pattern	ξ	N_u	$N_u(A)/N_u(B)$ (%)
A-4.1	A	0.621	1817	99
A-4.2	A	0.621	1814	
B-4.1	B	0.621	1837	
B-4.2	B	0.621	1843	
A-6-1	A	0.808	2039	106
A-6-2	A	0.808	2128	
-6-1	B	0.808	1966	
B-6-2	B	0.808	1978	
A-8-1	A	1.162	2550	103
A-8-2	A	1.162	2552	
B-8-1	B	1.162	2430	
B-8-2	B	1.162	2512	
A-12-1	A	2.312	3374	104
A-12-2	A	2.312	3396	
B-12-1	B	2.312	3260	
B-12-2	B	2.312	3262	

stress-strain relation of RPC remains inadequate, and no constitutive relationship is available to form a widely accepted constraint for RPC. Thus, this method does not meet the conditions for numerical analysis. Therefore, the limit analysis method was used to explore the ultimate bearing capacity of steel RPCFT axially compressed short columns.

The parameters are shown in Figure 10 so that the RPC core area and steel tube area are

$$A_c = \frac{\pi d_c^2}{4}, \quad (2)$$

$$A_s = \frac{\pi(D^2 - d_c^2)}{4} \approx \pi d_c t. \quad (3)$$

According to the internal force balance, the relationship between annular tension and confining force of the steel tube is

$$\sigma_r d_c = -2\sigma_2 t. \quad (4)$$

Synthesis (equations (2)–(4)) can be obtained:

$$\sigma_2 = -\frac{\sigma_r d_c}{2t} = -\sigma_r \frac{2A_c}{A_s}. \quad (5)$$

The steel tube conforms to the von Mises yield criterion, which is

$$\sigma_1^2 + \sigma_2^2 - \sigma_1 \sigma_2 = f_y^2. \quad (6)$$

Equation (6) can be solved as follows:

$$\sigma_1 = \sqrt{f_y^2 - \frac{3}{4}\sigma_2^2} + \frac{\sigma_2}{2}. \quad (7)$$

The study of confined concrete showed that there is a linear relationship between confined concrete strength and confining force:

$$f_3 = f_c + k\sigma_r. \quad (8)$$

Therefore,

$$\begin{aligned} N &= \sigma_c A_c + \sigma_1 A_s, \\ &= f_c \left(1 + k \frac{\sigma_r}{f_c}\right) A_c + \left(\sqrt{f_y^2 - \frac{3}{4}\sigma_2^2} + \frac{\sigma_2}{2}\right) A_s, \\ &= f_c A_c + k\sigma_r A_c + \sqrt{f_y^2 - \frac{3}{4}\left(-\sigma_r \frac{2A_c}{A_s}\right)^2} - \left(-\sigma_r \frac{A_c}{A_s}\right) A_s, \\ &= [f_c + (k-1)\sigma_r] A_c + \sqrt{f_y^2 A_s^2 - 3\sigma_r^2 A_c^2}. \end{aligned} \quad (9)$$

When N reached the ultimate bearing capacity:

$$\frac{dN}{d\sigma_r} = 0. \quad (10)$$

That is, under equation (10), when the ultimate bearing capacity was reached, the confining force was:

$$\sigma_r = \frac{f_y A_s}{A_c} \frac{k-1}{\sqrt{9+3(k-1)^2}}. \quad (11)$$

Substituting confining force into equation (9):

$$\begin{aligned} N &= f_c A_c + f_y A_s \frac{(k-1)^2 + 3}{\sqrt{9+3(k-1)^2}} = f_c A_c \\ &\quad + f_y A_s \sqrt{\frac{(k-1)^2 + 3}{3}}, \end{aligned} \quad (12)$$

replaced in (12),

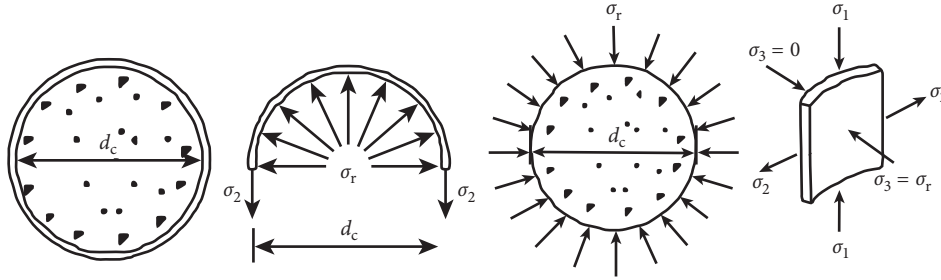


FIGURE 10: The internal stress of RPC-infilled circular tube.

$$N_u = f_c A_c \left(1 + \sqrt{\frac{(k-1)^2 + 3}{3}} \xi \right). \quad (13)$$

5. Calculation of Bearing Capacity of RPCFT

By referring to the “Technical Specifications for Concrete-Filled Steel Tubular Structures” (GB50936-2014) and the analysis results presented in Figure 4 and Equation (13), it is recommended that the value of RPC should be 1.394. The equation for calculating the bearing capacity of RPCFT is

$$N = 0.9 A_c f_c (1 + 1.394 \xi). \quad (14)$$

6. Conclusion

Circular steel tube-confined RPC is an effective method to increase ductility, and the following conclusions could be drawn from the results obtained for the analyzes:

- (1) Results for a total of 139 RPCFT axial compression columns showed that the load-displacement curves can be divided into four stages: (1) elastic; (2) elastic-plastic; (3) descending; and (4) strengthening. Moreover, the elastic limit could reach the ultimate limit of 90%. The failure modes could be divided into three categories: (1) wall buckling instability failure; (2) oblique shear failure; and (3) waist drum damage. It was suggested that the D/t ratio of RPCFT should be kept below $80(235/f_y)$ to avoid buckling and brittle failure of the tube wall. Oblique shear failure and drum-type damage could both result in ductile failure, and it was recommended that the critical confining coefficient be set to 1.
- (2) The larger the confining coefficient, the greater the increase in bearing capacity of RPCFT. The core RPC strength, loading method, and steel fiber content of RPC had little effect on the RPC bearing capacity of the steel tube. To reduce cost, it was recommended that no steel fiber be added to the steel tube RPC.
- (3) Steel tube has less of a constraining effect on RPC than NC and HSC. The increase in the coefficient of steel tube-constrained RPC was 1.394. The equation for the ultimate bearing capacity of the steel tube

RPC was proposed in reference to the “Technical Specifications for Concrete-Filled Steel Tube Structure” (GB50936-2014).

Data Availability

The data used to support the findings of this study are available from the corresponding author upon request.

Conflicts of Interest

The authors declare that there are no conflicts of interest regarding the publication of this paper.

Acknowledgments

The author also would like to acknowledge the support provided by the National Natural Science Foundation of China (no. 51678190) for partially funding this research. All staff and laboratory technicians are thanked for their kind assistance during the research.

References

- [1] P. Richard and M. Cheyrezy, “Composition of reactive powder concretes,” *Cement and Concrete Research*, vol. 25, no. 7, pp. 1501–1511, 1995.
- [2] P. Richard and M. Cheyrezy, “Reactive powder concretes with high ductility and 200–800 MPa compressive strength,” *ACI Spring Conversion*, vol. 114, pp. 507–518, 1994.
- [3] W. Zheng and L. Li, “Preparation and mix proportion calculation of reactive powder concrete,” *Journal of Hunan University (Science)*, vol. 36, no. 2, pp. 13–17, 2009.
- [4] W. Zheng and LV. XueYuan, “Literature review of reactive powder concrete,” *Journal of Building Structures*, vol. 36, no. 10, pp. 44–58, 2015.
- [5] X. Hou, S. Cao, Q. Rong, W. Zheng, and G. Li, “Effects of steel fiber and strain rate on the dynamic compressive stress-strain relationship in reactive powder concrete,” *Construction and Building Materials*, vol. 170, pp. 570–581, 2018.
- [6] L. Han, *Structure of Concrete Filled Steel Tube*, Science Press, Beijing, China, 2004.
- [7] P. Y. Blais and M. Couture, “Precast, prestressed pedestrian Bridge world’s first reactive powder concrete structure,” *PCI Journal*, vol. 44, no. 5, pp. 60–71, 1999.
- [8] M. Shiqiang, “Preliminary study of reactive powder concrete filled steel tube,” *China Concrete and Cement Products*, vol. 1, no. 1, pp. 5–8, 2003.

- [9] J. Zhang, *Experimental Investigation On Behavior Of Reactive Powder Concrete Filled Steel Tube*, Fuzhou University, Fuzhou, China, 2003.
- [10] W. Yang, *The Mechanic Property and Ultimate Bearing Capacity of Reactive Powder Concrete Filled Steel Tube*, Hunan University, Changsha, China, 2003.
- [11] Y. Wu and L. Yao, "Experimental study of axial compressive performance of reactive powder concrete filled steel tube," *Building Structure: China*, vol. 39, no. 1, pp. 821–823, 2009.
- [12] J. Feng, *Study on Mechanical Behavior of Reactive Powder Concrete Filled Steel Tubular Columns*, Tsinghua University, Beijing, China, 2008.
- [13] Z. Yan, W. Zhang, and A. Mingzhe, "The analysis of reactive powder concrete filled steel tubular columns ultimate bearing capacity," *Journal of Beijing University of Technology*, vol. 37, no. 3, pp. 361–367, 2011.
- [14] H. Luo, *Research on Behavior of Reactive Powder Concrete-Filled Circular Steel Tube Stub Columns under Aixel Compression*, Beijing Jiatong University, Beijing, China, 2011.
- [15] G. Yang, *Research on Behavior and Ultimate Bearing Capacity of Reactive Powder Concrete-Filled Steel Tube Columns under Axial Compression*, Beijing Jiatong University, Beijing, China, 2013.
- [16] W. Jian, *Experiment Research and analysis on Behavior of Reactive Powder Concrete-filled Circular, Steel Tube Columns under Axial Compression*, Harbin Institute of Technology, Harbin, China, 2013.
- [17] S. Zhang, "Failure modes of short columns of high-strength concrete-filled steel tubes," *China Civil Engineering Journal*, vol. 37, no. 9, pp. 1–10, 2004.
- [18] H. Musha, H. Ohkuma, and T. Kitamura, *Innovative UFC Structures in Japan, International Symposium on Ul-tra-High Performance Fibre-Reinforced Concrete*, RILEM Publications, Mar-seille, France, 2013.
- [19] S. Zhong, *Structure of Concrete Filled Steel Tube*, Tsinghua University Press, Beijing, China, 2003.

Research Article

Superposed Incremental Deformations of an Elastic Solid Reinforced with Fibers Resistant to Extension and Flexure

Chun IL Kim 

Department of Mechanical Engineering, University of Alberta, Edmonton, Alberta T6G 1H9, Canada

Correspondence should be addressed to Chun IL Kim; cikim@ualberta.ca

Received 12 July 2018; Revised 15 November 2018; Accepted 21 November 2018; Published 13 December 2018

Guest Editor: Syed W. Haider

Copyright © 2018 Chun IL Kim. This is an open access article distributed under the Creative Commons Attribution License, which permits unrestricted use, distribution, and reproduction in any medium, provided the original work is properly cited.

A comprehensive linear model for an elastic solid reinforced with fibers resistant to extension and flexure is presented. This includes the analysis of both unidirectional and bidirectional fiber-reinforced composites subjected to in-plane deformations. Within the prescription of the superposed incremental deformations, the fiber kinematics are approximated and used to determine the Euler equilibrium equations. The constraints of bulk incompressibility and admissible boundary conditions are also discussed for completeness. In particular, the complete systems of differential equations are obtained for the cases of Neo-Hookean and Mooney–Rivlin types of materials from which analytical solutions can be obtained.

1. Introduction

The mechanics of microstructured solids have consistently been the subject of intense research [1–5] for their practical importance in materials science and engineering. In particular, a considerable amount of attention is committed to the development of continuum models and analyses in an effort to predict the mechanical responses of fiber-matrix systems subjected to external forces and/or induced deformations (see, for example, [6, 7] and references therein). Continuum-based approaches postulate continuous distribution of fibers within the matrix materials so as to establish the idealized description of homogenized fiber-matrix composites. This is framed in the setting of anisotropic elasticity where the response function depends on the first gradient of deformations, typically augmented by the constraints of bulk incompressibility and/or fiber inextensibility. The latter condition often results highly constrained prediction models so that the corresponding deformation fields are essentially kinematically determinate, especially that arises in fibers [6, 7]. The approach has clear advantages in the prediction of deformation profiles of the system via the deformation mapping of an individual fiber, yet rather insufficient in the estimation of overall material properties of the

fiber-matrix system. Nonetheless, the aforementioned models have been widely adopted in the analysis of composite materials for their merit in the continuum description and the associated mathematical framework [5–7]. For the estimation of resultant properties, one may also consider multiscale modeling method which integrates the material properties of continua assigned in different length scales by means of the Cauchy–Born rule. Examples of such practice can be found in the works of Shahabodini et al. [8, 9].

A considerable advance in the continuum theory of fiber-reinforced solids was made in recent years. This includes the incorporation of the bending resistance of fibers into the models of deformations where elastic resistance is assigned to changes in curvature of the fibers [10–12]. More precisely, the fibers are regarded as convected curves so that the bending deformation of fibers can be formulated via the second gradient of deformations explicitly [13]. The concept has been successfully adopted in a wide range of problems arising in materials science [14–17], and the mathematical perspective of the subject is discussed in [18–20]. The authors in [21] proposed a general theory for the mechanics of an elastic solids with fibers resistant to flexure, stretch, and twist within the simplified setting of the Cosserat theory of nonlinear elasticity [10, 22].

Further, the second gradient theory of elasticity for the mechanics of meshed structures is presented in [23–25]. To this end, the authors in [26–29] developed continuum-based models in the analysis of fiber-reinforced composites, where the extension and bending resistance of fibers are incorporated via the computations of the first and second gradient of deformations. The majority of the aforementioned studies address nonlinear continuum theory of fiber composites so that little has been devoted to the development of compatible linear models describing the mechanics of an elastic medium reinforced with fibers.

In the present work, we present comprehensive linear theory of the strain gradient elasticity for the mechanics of fiber-reinforced composites with fibers resistant to bending and extension. The kinematics of fibers is approximated with the prescription of the superposed incremental deformations. We formulate, in cases of Neo-Hookean types of materials, complete expressions of the linearized Piola stresses from which the Euler equilibrium equations and the admissible boundary conditions are obtained. Bidirectional fiber composites are accommodated via the decomposition of the deformation gradient tensor along the directions of fibers. In addition, the reduction of simultaneous differential equations into a single differential equation is demonstrated by utilizing the compatibility conditions of the response function. More importantly, we show that, even with the introduction of the second gradient of deformations, two different bases (referential and current coordinate) do indeed merge for “small” deformations superposed in large. Lastly, Mooney–Rivlin types of materials are elaborated where we show that the resulting Euler equilibrium equations are of the same form as those obtained from the Neo-Hookean model. The corresponding Piola stresses, on the other hand, are distinguished in that they demonstrate clear dependency on both the first and second invariant of the deformations gradient tensor. The obtained model can be easily adopted in the study of composite structures subjected to small in-plane deformations. For example, in the design stage of crystalline nanocelluloses (CNCs) composite, the overall responses and deformation profiles can be pre-determined by utilizing the proposed model. In addition, the underlined theory can also be extended to the deformation analysis of lipid membranes (e.g., budding and thickness distension) [30–32], where phospholipids (microstructure) are aligned to the normal direction of the membrane, and therefore, their deformations can be mapped and computed using the proposed model.

Throughout the paper, we make use of a number of well-established symbols and conventions such as A^T , A^{-1} , A^* , and $\text{tr}(A)$. These are the transpose, the inverse, the cofactor, and the trace of a tensor A , respectively. The tensor product of vectors is indicated by interposing the symbol \otimes , and the Euclidian inner product of tensors \mathbf{A} and \mathbf{B} is defined by $\mathbf{A} \cdot \mathbf{B} = \text{tr}(\mathbf{A}\mathbf{B}^T)$; the associated norm is $|\mathbf{A}| = \sqrt{\mathbf{A} \cdot \mathbf{A}}$. The symbol $|\cdot|$ is also used to denote the usual Euclidian norm of three vectors. Latin and Greek indices take values in $\{1, 2\}$ and, when repeated, are summed over their ranges. Lastly, the notation \mathbf{F}_A stands for the tensor-valued derivatives of a scalar-valued function $\mathbf{F}(\mathbf{A})$.

2. Incremental Elastic Deformations and Equilibrium Equations

The incremental deformation is defined by (see, for example, [33] and the references therein) the following equation:

$$\chi = \chi_o + \varepsilon \dot{\chi}, \quad |\varepsilon| \ll 1, \quad (1)$$

where $(*)_o$ denotes configurations of $*$ evaluated at $\varepsilon = 0$ and $(\dot{*}) = \partial(*)/\partial\varepsilon$. In the forthcoming derivations, we define $\dot{\chi} = (\partial\chi/\partial\varepsilon) = \mathbf{u}$ for the sake of convenience and clarity. From equation (1), the gradient of the deformation function $\chi(\mathbf{X})$ can be approximated up to the leading order as shown in the following equation:

$$\mathbf{F} = \frac{\partial(\chi_o + \varepsilon \dot{\chi})}{\partial \mathbf{X}} = \mathbf{F}_o + \varepsilon \nabla \mathbf{u}, \quad (2)$$

where $\dot{\mathbf{F}} = (\partial\dot{\chi}/\partial\mathbf{X}) = \nabla \mathbf{u}$.

In the above equation, we assume that the body is initially undeformed and stress free at $\varepsilon = 0$, that is, $\mathbf{F}_o = \mathbf{I}$ and $\mathbf{P}_o = 0$, where \mathbf{P} is the Piola stress. Thus, equation (2) becomes the following equation:

$$\mathbf{F} = \frac{\partial(\chi_o + \varepsilon \dot{\chi})}{\partial \mathbf{X}} = \mathbf{I} + \varepsilon \nabla \mathbf{u}, \quad (3)$$

and successively yields

$$\mathbf{F}^{-1} = \mathbf{I} - \varepsilon \nabla \mathbf{u} + o(\varepsilon), \quad (4)$$

which can be found by using the identity $\mathbf{F}\mathbf{F}^{-1} = \mathbf{I}$. The determinant of \mathbf{F} can be approximated similarly as

$$J = J_o + \varepsilon \dot{J} + o(\varepsilon), \quad (5)$$

where we evaluate $\dot{J} = (J_F)_o \cdot \dot{\mathbf{F}} = J_o \text{tr}(\mathbf{F}_o^{-1} \dot{\mathbf{F}})$ and $\dot{\mathbf{F}} = (\text{gradu})\mathbf{F}_o$. Since $\text{tr}(\mathbf{F}_o^{-1} \dot{\mathbf{F}}) = \text{tr}(\text{gradu}) = \text{div} \mathbf{u}$, we obtain from equation (5) that

$$J = 1 + \varepsilon \text{div} \mathbf{u} + o(\varepsilon). \quad (6)$$

In addition, the Euler equilibrium equation can be expanded as the following equation:

$$\text{Div}(\mathbf{P}) = \text{Div}(\mathbf{P}_o)1 + \varepsilon \text{Div} \dot{\mathbf{P}} + o(\varepsilon) = 0. \quad (7)$$

Dividing the above equation by ε and letting $\varepsilon \rightarrow 0$, we obtain

$$\text{Div} \dot{\mathbf{P}} = 0, \quad (8)$$

which serves as the linearized Euler equilibrium equation. The expression of Piola stresses in the case of fiber composites reinforced with fibers resistant to flexure is given by [27]:

$$\mathbf{P} = W_F - p\mathbf{F}^* - C\text{Div}(\mathbf{g} \otimes \mathbf{D} \otimes \mathbf{D}), \quad (9)$$

where W , p , and C are the energy density function, Lagrange multiplier, and material constant of fibers ($C = \text{constant}$), respectively. Also, \mathbf{g} is the geodesic curvature of fibers' trajectory (i.e., $\mathbf{g} = \mathbf{G}(\mathbf{D} \otimes \mathbf{D})$) and \mathbf{D} is the initial director filed of fibers' where $\mathbf{D} = (\partial\mathbf{X}(S))/\partial S$. Here, S is the arc length parameter on the reference configuration. In general, most of fibers are straight prior to deformations. Even slightly curved fibers can be regarded as “fairly straight”

fibers, considering their length scales with respect to that of matrix materials. Thus, from here and forthcoming derivations, it is assumed that

$$\begin{aligned}\frac{\partial \mathbf{D}}{\partial \mathbf{X}} &= 0, \\ \dot{\mathbf{D}} &= \frac{\partial \mathbf{D}}{\partial \boldsymbol{\varepsilon}} = 0.\end{aligned}\quad (10)$$

Accordingly, we find $\text{Div}(\mathbf{D}) = 0$ and thereby reduce equation (10) to the following equation:

$$\mathbf{P} = W_{\mathbf{F}} - p\mathbf{F}^* - C\nabla\mathbf{g}(\mathbf{D} \otimes \mathbf{D}), \quad (11)$$

where the last term of the above equation is obtained by using the identity $g_{i,B}D_AD_B(\mathbf{e}_i \otimes \mathbf{E}_A) = \nabla\mathbf{g}(\mathbf{D} \otimes \mathbf{D})$. Thus, from equation (11), \mathbf{P} can be evaluated as the following equation:

$$\begin{aligned}\dot{\mathbf{P}} &= (W_{\mathbf{F}})' - (p\mathbf{F}^*)' - [C\nabla\mathbf{g}(\mathbf{D} \otimes \mathbf{D})]' \\ &= W_{\mathbf{FF}} \cdot \dot{\mathbf{F}} - \dot{p}\mathbf{F}_o^* - p_o\dot{\mathbf{F}}^* - C\nabla\dot{\mathbf{g}}(\mathbf{D} \otimes \mathbf{D}).\end{aligned}\quad (12)$$

In the case of an incompressible Neo-Hookean material, the energy density function is given by the following equation:

$$W(\mathbf{F}) = \frac{\mu}{2}(\mathbf{F} \cdot \mathbf{F} - 3), \quad (13)$$

and we find

$$\dot{\mathbf{P}} = \mu\dot{\mathbf{F}} - \dot{p}\mathbf{F}_o^* - p_o\dot{\mathbf{F}}^* - C\nabla\dot{\mathbf{g}}(\mathbf{D} \otimes \mathbf{D}), \quad \therefore W_{\mathbf{FF}} = \mu. \quad (14)$$

In view of equations (8) and (14), the linearized Euler equilibrium equation then satisfies

$$\text{Div}(\mu\dot{\mathbf{F}}) - \text{Div}(\dot{p}\mathbf{F}_o^*) - \text{Div}(p_o\dot{\mathbf{F}}^*) - C\text{Div}(\nabla\dot{\mathbf{g}}(\mathbf{D} \otimes \mathbf{D})) = 0. \quad (15)$$

The evaluation of equation (15) is essential to extract boundary value problems (BVPs); nonetheless, the details are often heavily omitted in the literature (see, for example, [26–29]). To see this, we first compute the following equation:

$$\text{Div}(\mu\dot{\mathbf{F}}) = \text{Div}(\mu\nabla\mathbf{u}) = \mu u_{i,AA}\mathbf{e}_i. \quad (16)$$

In the above equation, caution needs to be taken, in which $\nabla(*)$ and $\text{div}(*)$ are the operators in the reference frame. Although, there are no clear distinction between the reference and current configurations for “small” incremental deformations, the mathematical procedure should reasonably address their connections especially when dealing with tensors with mixed bases (e.g., $\nabla\mathbf{u}$, \mathbf{F}). The collapse of bases for the present problem will be discussed in the later sections. The second term in equation (15) becomes

$$\begin{aligned}\text{Div}(\dot{p}\mathbf{F}_o^*) &= \text{Div}[\dot{p}(\mathbf{F}_o^*)_{iA}\mathbf{e}_i \otimes \mathbf{E}_A] = [\dot{p}(\mathbf{F}_o^*)_{iA}]_A\mathbf{e}_i \\ &= \dot{p}_A(\mathbf{F}_o^*)_{iA}\mathbf{e}_i = \dot{p}_i\mathbf{e}_i,\end{aligned}\quad (17)$$

where we use the Piola identity (i.e., $\mathbf{F}_{i,A}^* = 0$) and $(\mathbf{F}_o^*)_{iA} = \delta_{iA}$. Similarly, it can be easily shown that

$$\text{Div}(p_o\dot{\mathbf{F}}^*) = [(p_o)_A\dot{\mathbf{F}}_{iA}^* + p_o(\dot{\mathbf{F}}^*)_{iA,A}]\mathbf{e}_i = (p_o)_A\dot{\mathbf{F}}_{iA}^*\mathbf{e}_i. \quad (18)$$

However, in order to recover the initial stress free state at $\boldsymbol{\varepsilon} = 0$, we require from equations (11) and (13) that

$$\mathbf{P}_o = \mu\mathbf{F}_o - p_o\mathbf{F}_o^* - C\nabla\mathbf{g}_o(\mathbf{D} \otimes \mathbf{D}) = \mu\mathbf{I} - p_o\mathbf{I} = 0, \quad (19)$$

and thus find $p_o = \mu = \text{constant}$. Therefore, equation (18) becomes

$$\begin{aligned}\text{Div}(p_o\dot{\mathbf{F}}^*) &= \mu_A\dot{\mathbf{F}}_{iA}^*\mathbf{e}_i + \mu(\text{Div}(\mathbf{F}^*))' = 0, \\ \therefore (p_o)_A &= (\mu)_A = 0,\end{aligned}\quad (20)$$

and $\text{Div}(\mathbf{F}^*) = 0$ (Piola’s identity). Also, $\text{Div}(\nabla\dot{\mathbf{g}}(\mathbf{D} \otimes \mathbf{D}))$ can be evaluated as

$$\begin{aligned}\text{Div}[\dot{g}_{i,B}D_AD_B(\mathbf{e}_i \otimes \mathbf{E}_A)] &= (\dot{g}_{i,B}D_AD_B)_A\mathbf{e}_i \\ &= \dot{G}_{iAB,CD}D_AD_BD_CD_C\mathbf{e}_i,\end{aligned}\quad (21)$$

where $g_i = G_{iAB}D_AD_B$ (see [27]) and $\mathbf{G} = G_{iAB}(\mathbf{e}_i \otimes \mathbf{E}_A \otimes \mathbf{E}_B)$ is the second gradient of deformations (i.e., $\nabla\mathbf{F} = \mathbf{G}$). Consequently, by substituting equations (16), (17), (20), and (21) into equation (15), the linearized Euler equation can be obtained as follows:

$$\begin{aligned}(\mu u_{i,AA} - \dot{p}_i - C u_{i,ABCD}D_AD_BD_CD_D)\mathbf{e}_i &= 0\mathbf{e}_i, \\ \therefore \dot{G}_{iAB} &= \dot{\mathbf{F}}_{i,AB} = u_{i,AB}.\end{aligned}\quad (22)$$

For a single family of fibers (i.e., $\mathbf{D} = \mathbf{E}_1$, $D_1 = 1$, $D_2 = 0$), equation (22) reduces to

$$(\mu(u_{i,11} + u_{i,22}) - \dot{p}_i - C u_{i,1111})\mathbf{e}_i = 0\mathbf{e}_i. \quad (23)$$

3. Boundary Conditions and Solution to the Linearized System

The corresponding boundary conditions are given by [27]

$$\begin{aligned}\mathbf{t} &= \mathbf{PN} - \frac{d}{ds} [C\mathbf{g}(\mathbf{D} \cdot \mathbf{T})(\mathbf{D} \cdot \mathbf{N})], \\ \mathbf{m} &= C\mathbf{g}(\mathbf{D} \cdot \mathbf{N})^2,\end{aligned}\quad (24)$$

$$\mathbf{f} = C\mathbf{g}(\mathbf{D} \cdot \mathbf{T})(\mathbf{D} \cdot \mathbf{N}),$$

where \mathbf{t} , \mathbf{m} , and \mathbf{f} are, respectively, the expressions of edge tractions, edge moments, and the corner forces. Further, \mathbf{N} and \mathbf{T} are unit normal and tangent to the boundary. The “small” increment of boundary forces are then computed as follows:

$$\begin{aligned}\dot{\mathbf{t}} &= \dot{\mathbf{P}}\mathbf{N} - \frac{d}{ds} [C\dot{\mathbf{g}}(\mathbf{D} \cdot \mathbf{T})(\mathbf{D} \cdot \mathbf{N})], \\ \dot{\mathbf{m}} &= C\dot{\mathbf{g}}(\mathbf{D} \cdot \mathbf{N})^2,\end{aligned}\quad (25)$$

$$\dot{\mathbf{f}} = C\dot{\mathbf{g}}(\mathbf{D} \cdot \mathbf{T})(\mathbf{D} \cdot \mathbf{N}).$$

The expression of $\dot{\mathbf{P}}$ can be obtained from equation (14) that

$$\begin{aligned}\dot{\mathbf{P}} &= \dot{\mathbf{P}}_{iA}(\mathbf{e}_i \otimes \mathbf{E}_A) \\ &= [\mu u_{i,A} - \dot{p}(\mathbf{F}_{iA}^*)_{\circ} - p_{\circ} \dot{\mathbf{F}}_{iA}^* - C \dot{g}_{i,B} D_A D_B](\mathbf{e}_i \otimes \mathbf{E}_A),\end{aligned}\quad (26)$$

$$\dot{g}_i \mathbf{e}_i = \dot{G}_{iAB} D_A D_B \mathbf{e}_i = \dot{\mathbf{F}}_{iA,B} D_A D_B \mathbf{e}_i = u_{i,AB} D_A D_B \mathbf{e}_i. \quad (27)$$

In order to apply boundary tractions (e.g., $\dot{\mathbf{P}}_{11}$), it is necessary to compute equation (26) as a function of $\mathbf{u} = \mathbf{u}(X_1, X_2)$. For the purpose, we first find the following equation:

$$(\mathbf{F}_{iA}^*)_{\circ} = J_{\circ} (\mathbf{F}_{iA}^T)_{\circ}^{-1} = (\delta_{iA})^{-1} = \delta_{iA}, \quad (28)$$

where $(\mathbf{F}_{iA}^*)_{\circ} = \delta_{iA}$ at $\varepsilon = 0$. Also, to compute $\dot{\mathbf{F}}_{iA}^*(\mathbf{e}_i \otimes \mathbf{E}_A)$, we use the chain rule in the form of the following equation:

$$\begin{aligned}\dot{\mathbf{F}}_{iA}^*(\mathbf{e}_i \otimes \mathbf{E}_A) &= (\mathbf{F}_{\mathbf{F}}^*)_{\circ} [\dot{\mathbf{F}}] = \left(\frac{\partial \mathbf{F}_{iA}^*}{\partial \mathbf{F}_{jB}} \right)_{\circ} \dot{\mathbf{F}}_{kC}(\mathbf{e}_i \otimes \mathbf{E}_A \otimes \mathbf{e}_j \otimes \mathbf{E}_B)(\mathbf{e}_k \otimes \mathbf{E}_C) \\ &= \left(\frac{\partial \mathbf{F}_{iA}^*}{\partial \mathbf{F}_{jB}} \right)_{\circ} u_{j,B}(\mathbf{e}_i \otimes \mathbf{E}_A).\end{aligned}\quad (29)$$

Here, the expression of $(\partial \mathbf{F}_{iA}^* / \partial \mathbf{F}_{jB})$ can be found via the connection [34]:

$$J \left(\frac{\partial \mathbf{F}_{iA}^*}{\partial \mathbf{F}_{jB}} \right) = \mathbf{F}_{iA}^* \mathbf{F}_{jB}^* - \mathbf{F}_{jA}^* \mathbf{F}_{iB}^*. \quad (30)$$

Thus, at $\varepsilon = 0$, we have from the above equation that

$$\left(\frac{\partial \mathbf{F}_{iA}^*}{\partial \mathbf{F}_{jB}} \right)_{\circ} = \delta_{iA} \delta_{jB} - \delta_{jA} \delta_{iB}, \quad (\delta_{iA}: \text{Kronecker delta}), \quad (31)$$

and thereby obtain

$$\left(\frac{\partial \mathbf{F}_{iA}^*}{\partial \mathbf{F}_{jB}} \right)_{\circ} u_{j,B} = (\delta_{iA} \delta_{jB} - \delta_{jA} \delta_{iB}) u_{j,B} = \delta_{iA} (\text{Div} \mathbf{u}) - u_{A,i}. \quad (32)$$

Consequently, substituting equations (27), (28), and (32) into equation (26) furnishes

$$\begin{aligned}\dot{\mathbf{P}}_{iA}(\mathbf{e}_i \otimes \mathbf{E}_A) &= \left[\mu u_{i,A} - \dot{p} \delta_{iA} - p_{\circ} (\delta_{iA} (\text{Div} \mathbf{u}) - u_{A,i}) \right. \\ &\quad \left. - C u_{i,BCD} D_A D_B D_C D_D \right] (\mathbf{e}_i \otimes \mathbf{E}_A),\end{aligned}\quad (33)$$

from which the expression of boundary tractions is completely determined in terms of \mathbf{u} .

Remark 1. In the above equation, $\delta_{iA} \delta_{jB} u_{j,B}$ is interpreted as $\delta_{iA} u_{B,B}$ resulting $\delta_{iA} \delta_{jB} u_{j,B} = \delta_{iA} \text{Div} \mathbf{u}$ in the reference configuration (Eulerian). However, one may also find $\delta_{iA} \delta_{jB} u_{j,B} = u_{j,j}$ and thus obtain $\delta_{iA} \delta_{jB} u_{j,B} = \delta_{iA} \text{div} \mathbf{u}$ in the current configuration (Lagrangian). This confirms the well-known result from the linear elasticity theory that the bases collapse in the event of small deformations superposed on large (i.e., $\text{Div} \mathbf{u} = \text{div} \mathbf{u}$ and $\mathbf{E}_A = \mathbf{e}_i$). In the present problem, the result allows one to formulate linearized Euler equations without conflicting bases mismatch especially

when operating linear transform of mixed basis tensors. Although there are no clear distinctions between the current and deformed configurations, caution needs to be taken that the Euler equation ($\text{Div} \dot{\mathbf{P}}$) is, in principal, defined in the reference frame together with the boundary conditions.

Now, in view of equations (5) and (6), the constraints of bulk incompressibility reduce to the following equation:

$$(J - 1)_{\cdot} = \dot{J} = \mathbf{F}_{\circ}^* \cdot \dot{\mathbf{F}} = \text{tr}(\mathbf{F}_{\circ}^{-1} \dot{\mathbf{F}}) = \text{tr}(\text{grad} \mathbf{u}) = \text{div} \mathbf{u} = 0. \quad (34)$$

Equation (34) serves as the linearized bulk incompressibility condition (i.e., $u_{i,i} = 0$), which needs to be solved together with equation (23). In addition, since $\text{Div} \mathbf{u} = \text{Div} \mathbf{u}$ for small deformations (see Remark 1), we find $\text{Div} \mathbf{u} = \text{div} \mathbf{u} = 0$ and thereby reduce equation (33) to the following equation:

$$\begin{aligned}\dot{\mathbf{P}}_{iA}(\mathbf{e}_i \otimes \mathbf{E}_A) &= \left[\mu u_{i,A} - \dot{p} \delta_{iA} + p_{\circ} u_{A,i} \right. \\ &\quad \left. - C u_{i,BCD} D_A D_B D_C D_D \right] (\mathbf{e}_i \otimes \mathbf{E}_A),\end{aligned}\quad (35)$$

which serves as an explicit form of the linearized Piola stress for elastic solids reinforced with single family of fibers. In particular, if the fibers' directions are either normal or tangential to the boundary (i.e., $(\mathbf{D} \cdot \mathbf{T})(\mathbf{D} \cdot \mathbf{N}) = 0$), equation (25) becomes

$$\begin{aligned}\mathbf{t} &= \dot{\mathbf{P}} \mathbf{N}, \\ \dot{\mathbf{m}} &= C \dot{g}(\mathbf{D} \cdot \mathbf{N})^2, \\ \dot{\mathbf{f}} &= 0,\end{aligned}\quad (36)$$

and therefore, we compute, for example,

$$\begin{aligned}\mathbf{t}_i \mathbf{e}_i &= (\mu u_{i,A} - \dot{p} \delta_{iA} + p_{\circ} u_{A,i} - C u_{i,111} \delta_{1A} D_1 D_1 D_1)(\mathbf{e}_i \otimes \mathbf{E}_A) \mathbf{E}_1 \\ &= (\mu u_{i,1} - \dot{p} \delta_{i1} + p_{\circ} u_{1,i} - C u_{i,111}) \mathbf{e}_i,\end{aligned}\quad (37)$$

where \mathbf{N} is assumed to be parallel to the fiber's director field (i.e., $\mathbf{N} = \mathbf{D} = \mathbf{E}_1$). Lastly, from equations (27) and (36), the expression of boundary moments are obtained by

$$\dot{m}_i \mathbf{e}_i = C u_{i,AB} D_A D_B \mathbf{e}_i. \quad (38)$$

3.1. Solutions to the Linearized System. In the case of single family of fibers (i.e., $\mathbf{D} = \mathbf{E}_1$), the linearized system of partial differential equations (PDEs) is given by

$$\begin{aligned}(\mu(u_{i,11} + u_{i,22}) - \dot{p}_i - C u_{i,1111}) \mathbf{e}_i &= 0, \\ u_{i,i} &= 0.\end{aligned}\quad (39)$$

The second one in the above equation can be automatically satisfied by introducing the following scalar field φ :

$$\begin{aligned}\mathbf{u} &= \mathbf{k} \times \nabla \varphi, \quad \mathbf{k}(\text{unit normal}), \\ u_i &= \varepsilon_{\lambda i} \varphi_{\lambda},\end{aligned}\quad (40)$$

so that $u_{1,1} + u_{2,2} = \varphi_{12} - \varphi_{21} = 0$. Now, we recast the first one of equation (39) and thereby find the following equation:

$$\dot{p}_i \mathbf{e}_i = [\mu \varepsilon_{\lambda i} (\varphi_{\lambda 11} + \varphi_{\lambda 22}) - C \varepsilon_{\lambda i} \varphi_{\lambda 1111}] \mathbf{e}_i. \quad (41)$$

In addition, using the compatibility conditions of p_i (i.e., $\dot{p}_{ij} = \dot{p}_{ji}$), the first one of equation (41) becomes

$$\dot{p}_{21} - \dot{p}_{12} = \mu (\varphi_{1111} + 2\varphi_{1122} + \varphi_{2222}) - C (\varphi_{11} + \varphi_{22})_{1111} = 0. \quad (42)$$

Consequently, equation (42) further reduces to

$$\begin{aligned} \nabla H - \alpha H_{1111} &= 0, \quad \text{where } H = \Delta \varphi, \\ \alpha &= \frac{C}{\mu} > 0. \end{aligned} \quad (43)$$

An analytical solution of the above exists (see [27]) and is completely determined by imposing admissible boundary conditions as discussed in equation (25). For example, the symmetric bending can be imposed as

$$\dot{\mathbf{m}} = \dot{m}_1 \mathbf{e}_1 + \dot{m}_2 \mathbf{e}_2 = C u_{1,11} \mathbf{e}_1 + 0 \mathbf{e}_2 = -C \varphi_{112} \mathbf{e}_1, \quad (44)$$

which serves as the boundary conditions for the equation (42).

4. Extensible Fibers

The Piola stress in the case of initially straight and extensible fibers is given by Zeidi and Kim [28]:

$$\mathbf{P} = W_{\mathbf{F}} + \frac{E}{2} (\mathbf{F}\mathbf{D} \cdot \mathbf{F}\mathbf{D} - 1) (\mathbf{F}\mathbf{D} \otimes \mathbf{D}) - p \mathbf{F}^* - C \nabla \mathbf{g} (\mathbf{D} \otimes \mathbf{D}), \quad (45)$$

where E is the elastic modulus of fibers (extension). Further, the fibers' stretch λ can be computed as

$$\lambda^2 = \mathbf{F}\mathbf{D} \cdot \mathbf{F}\mathbf{D}. \quad (46)$$

In the case of Neo-Hookean type materials (see equation (13)), equation (45) becomes

$$\mathbf{P} = \mu \mathbf{F} + \frac{E}{2} (\mathbf{F}\mathbf{D} \cdot \mathbf{F}\mathbf{D} - 1) (\mathbf{F}\mathbf{D} \otimes \mathbf{D}) - p \mathbf{F}^* - C \nabla \mathbf{g} (\mathbf{D} \otimes \mathbf{D}). \quad (47)$$

Thus, equations (1) and (47) can be approximated as

$$\begin{aligned} \dot{\mathbf{P}} &= \mu \dot{\mathbf{F}} + E (\dot{\mathbf{F}}\mathbf{D} \cdot \mathbf{F}_0 \mathbf{D}) (\mathbf{F}_0 \mathbf{D} \otimes \mathbf{D}) \\ &+ \frac{1}{2} E (\mathbf{F}_0 \mathbf{D} \cdot \mathbf{F}_0 \mathbf{D} - 1) (\dot{\mathbf{F}}\mathbf{D} \otimes \mathbf{D}) - p_0 \dot{\mathbf{F}}^* \\ &- \dot{p} \mathbf{F}_0^* - C \nabla \dot{\mathbf{g}} (\mathbf{D} \otimes \mathbf{D}). \end{aligned} \quad (48)$$

Since $\mathbf{F}_0 = \mathbf{F}_0^* = \mathbf{I}$, the above equation further reduces to the following equation:

$$\dot{\mathbf{P}} = \mu \dot{\mathbf{F}} + E (\dot{\mathbf{F}}\mathbf{D} \cdot \mathbf{D}) (\mathbf{D} \otimes \mathbf{D}) - p_0 \dot{\mathbf{F}}^* - \dot{p} \mathbf{I} - C \nabla \dot{\mathbf{g}} (\mathbf{D} \otimes \mathbf{D}), \quad (49)$$

where $\mathbf{F}_0 \mathbf{D} \cdot \mathbf{F}_0 \mathbf{D} = \mathbf{D} \cdot \mathbf{D} = 1$. To obtain the desired expression, it is required to compute the following equation:

$$\mathbf{D} = \delta_{iA} (\mathbf{e}_i \otimes \mathbf{E}_A) D_B \mathbf{E}_B = \delta_{iA} \delta_{AB} D_B \mathbf{e}_i = D_i \mathbf{e}_i. \quad (50)$$

In the above equation, the initial director field (\mathbf{D}) is represented by the current frame (i.e., \mathbf{e}_i). However, \mathbf{D} is, in principal, a vector in the reference coordinate (i.e., $\mathbf{D} = D_A \mathbf{E}_A$). This is due to the collapse of bases as discussed in Remark 1. Caution needs to be taken when applying the Einstein summation. Thus, we obtain from equations (32), (34), (49), and (50) that

$$\begin{aligned} \dot{\mathbf{P}}_{iA} (\mathbf{e}_i \otimes \mathbf{E}_A) &= \left[\mu u_{i,A} + E u_{j,B} D_i D_j D_A D_B + p_0 u_{A,i} \right. \\ &\left. - \dot{p} \delta_{iA} - C u_{i,BCD} D_A D_B D_C D_D \right] (\mathbf{e}_i \otimes \mathbf{E}_A), \end{aligned} \quad (51)$$

where $\dot{\mathbf{F}}\mathbf{D} \cdot \mathbf{D} = \dot{\mathbf{F}}_{jB} D_j D_B = u_{j,B} D_j D_B$. Equation (51) can be used as the expression of boundary tractions in the case of extensible fibers. For example, if $\mathbf{D} = \mathbf{E}_1$ (single family of fibers), the above equation yields the following equation:

$$\begin{aligned} \dot{\mathbf{P}}_{iA} (\mathbf{e}_i \otimes \mathbf{E}_A) &= \left[\mu u_{i,A} + E u_{1,1} \delta_{i1} \delta_{A1} + p_0 u_{A,i} \right. \\ &\left. - \dot{p} \delta_{iA} - C u_{i,111} \delta_{A1} \right] (\mathbf{e}_i \otimes \mathbf{E}_A). \end{aligned} \quad (52)$$

Further, from equations (8) and (49), the corresponding equilibrium equation then satisfies the following equation:

$$\begin{aligned} \text{Div}(\dot{\mathbf{P}}) &= \text{Div}(\mu \dot{\mathbf{F}}) - \text{Div}(\dot{p} \mathbf{F}_0^*) + \text{Div}(E (\dot{\mathbf{F}}\mathbf{D} \cdot \mathbf{D}) (\mathbf{D} \otimes \mathbf{D})) \\ &- \text{Div}(p_0 \dot{\mathbf{F}}^*) - C \text{Div}(\nabla \dot{\mathbf{g}} (\mathbf{D} \otimes \mathbf{D})) = 0. \end{aligned} \quad (53)$$

The evaluation of the above equation is well discussed through equations (16)–(21) except the stretch term which is now equated as

$$\begin{aligned} \text{Div}(E (\dot{\mathbf{F}}\mathbf{D} \cdot \mathbf{D}) (\mathbf{D} \otimes \mathbf{D})) &= \text{Div}(E u_{j,B} D_i D_j D_A D_B (\mathbf{e}_i \otimes \mathbf{E}_A)) \\ &= E u_{j,AB} D_i D_j D_A D_B \mathbf{e}_i. \end{aligned} \quad (54)$$

Therefore, we obtain the following equation:

$$\begin{aligned} \mu u_{i,AA} - \dot{p}_i + E u_{j,AB} D_i D_j D_A D_B \\ - C u_{i,ABCD} D_A D_B D_C D_D \mathbf{e}_i &= 0. \end{aligned} \quad (55)$$

The linearized boundary conditions in the case of extensible fibers remain intact (see [28]), except the expression of $\dot{\mathbf{P}}$ where the explicit expression is obtained in equation (52). Thus, for example, in the case of unidirectional fiber composed where a boundary vector \mathbf{N} is parallel to the fiber's director field (i.e., $\mathbf{N} = \mathbf{D} = \mathbf{E}_1$), the complete set of equations can be found as

$$\begin{aligned} (\mu u_{i,11} - \dot{p}_i + E u_{1,11} \delta_{i1} - C u_{i,1111}) \mathbf{e}_i &= 0, \\ u_{i,i} &= 0. \end{aligned} \quad (56)$$

Also, the corresponding boundary conditions are given by

$$\begin{aligned}\dot{\mathbf{t}}_i \mathbf{e}_i &= \dot{\mathbf{P}} \mathbf{E}_1 = \dot{\mathbf{P}}_{i1} \mathbf{e}_i, \\ \dot{\mathbf{m}}_i \mathbf{e}_i &= C \dot{\mathbf{g}} (\mathbf{E}_1 \cdot \mathbf{E}_1)^2 = C u_{i,11} \mathbf{e}_i, \\ \dot{\mathbf{f}}_i \mathbf{e}_i &= 0 \mathbf{e}_i,\end{aligned}\quad (57)$$

where from equation (52), $\dot{\mathbf{P}}_{iA} = [\mu u_{i,A} + E u_{1,1} D_i D_A - p_o (\delta_{iA} u_{1,1} - u_{A,i}) - \dot{p} \delta_{iA} - C u_{i,11} D_A] (\mathbf{e}_i \otimes \mathbf{E}_A)$. Lastly, we note here that the value of p_o , in the case of extensible fibers, can be obtained by evaluating the corresponding stresses (see equation (47)) at $\varepsilon = 0$ which is again found to be $p_o = \mu$. By applying the similar scheme as applied in Section 3.1, we rearrange equation (56) and thereby obtain

$$\dot{p}_{21} - \dot{p}_{12} = \Delta \left[\Delta \varphi - \frac{C}{\mu} \varphi_{1111} \right] + \frac{E}{\mu} \varphi_{1122} = 0. \quad (58)$$

The solution of equation (58) is not accommodated by conventional methods such as the separation of variables method, Fourier transform, and polynomial solutions. Instead, a particular form of solution ($\varphi = X(x) \sin(my)$) can be proposed, inspired by the modified Helmholtz equation.

5. Extensible Bidirectional Fibers

In the forthcoming derivations, we confine our attention to the case of initially orthogonal fiber families. The bidirectional fibers can be accommodated by using the following decompositions of the deformation gradient:

$$\begin{aligned}\mathbf{F} &= \lambda l \otimes \mathbf{L} + \gamma m \otimes \mathbf{M}, \\ \mathbf{M} \cdot \mathbf{L} &= 0,\end{aligned}\quad (59)$$

where \mathbf{L} and \mathbf{M} are the director fields of each fiber family in the reference configuration and l and m are their counterparts in the current configuration. The fibers' stretches are computed similarly as in equation (46) that

$$\begin{aligned}\lambda^2 &= \mathbf{F} \mathbf{L} \cdot \mathbf{F} \mathbf{M}, \\ \gamma^2 &= \mathbf{F} \mathbf{M} \cdot \mathbf{F} \mathbf{M}.\end{aligned}\quad (60)$$

Equations (59) and (60) complete the deformation mapping, for example, $\mathbf{L} = L_A \mathbf{E}_A$ and $\mathbf{I} = l_i \mathbf{e}_i$ to yield

$$\begin{aligned}\lambda l_i \mathbf{e}_i &= \mathbf{F} \mathbf{L} = \mathbf{F}_{iA} L_A \mathbf{e}_i, \\ \therefore \mathbf{M} \cdot \mathbf{L} &= 0 \text{ for orthogonal fiber families.}\end{aligned}\quad (61)$$

Further, by employing the variational principles, the Piola stress for the bidirectional and extensible fiber composites can be found as

$$\begin{aligned}\mathbf{P} &= W_{\mathbf{F}} + \frac{E_1}{2} ((\mathbf{F} \mathbf{L} \cdot \mathbf{F} \mathbf{L} - 1) (\mathbf{F} \mathbf{L} \otimes \mathbf{L})) \\ &+ \frac{E_2}{2} ((\mathbf{F} \mathbf{M} \cdot \mathbf{F} \mathbf{M} - 1) (\mathbf{F} \mathbf{M} \otimes \mathbf{M})) - C_1 \nabla \mathbf{g}_1 (\mathbf{L} \otimes \mathbf{L}) \\ &- C_2 \nabla \mathbf{g}_2 (\mathbf{M} \otimes \mathbf{M}) - p \mathbf{F}^*,\end{aligned}\quad (62)$$

where E_i and C_i are the material constants of fiber families, respectively, to extension and flexure. Applying the similar

scheme as in Section 4, we approximate equation (62) and successively obtain

$$\begin{aligned}\dot{\mathbf{P}}_{iA} (\mathbf{e}_i \otimes \mathbf{E}_A) &= \left[\mu u_{i,A} + E_1 u_{j,B} L_i L_j L_A L_B + E_2 u_{j,B} M_i M_j M_A M_B \right. \\ &- C_1 u_{i,BCD} L_A L_B L_C L_D - C_2 u_{i,BCD} M_A M_B M_C M_D \\ &\left. + p_o u_{A,i} - \dot{p} \delta_{iA} \right] (\mathbf{e}_i \otimes \mathbf{E}_A).\end{aligned}\quad (63)$$

Therefore, equations (8) and (63) furnish

$$\begin{aligned}0 \mathbf{e}_i &= \dot{\mathbf{P}}_{iA,A} \mathbf{e}_i = \mu u_{i,AA} - \dot{p}_i + E_1 u_{j,AB} L_i L_j L_A L_B \\ &+ E_2 u_{j,AB} M_i M_j M_A M_B - C_1 u_{i,ABCD} L_A L_B L_C L_D \\ &- C_2 u_{i,ABCD} M_A M_B M_C M_D \mathbf{e}_i,\end{aligned}\quad (64)$$

where we evaluate

$$\begin{aligned}\text{Div} [p_o u_{A,i} (\mathbf{e}_i \otimes \mathbf{E}_A)] &= p_o u_{A,iA} \mathbf{e}_i = p_o (u_{A,A})_i \mathbf{e}_i = 0, \\ \therefore u_{A,A} &= 0 \text{ (bulk incompressibility),}\end{aligned}\quad (65)$$

$$\text{Div} [\dot{p} \delta_{iA} (\mathbf{e}_i \otimes \mathbf{E}_A)] = \dot{p}_A \delta_{iA} \mathbf{e}_i = \dot{p}_i \mathbf{e}_i.$$

Compatible results can be also found directly from equations (17) and (20) (i.e., $\text{Div}(\dot{p} \mathbf{F}_o^*) = \dot{p}_i \mathbf{e}_i$ and $\text{Div}(p_o \mathbf{F}^*) = 0$). In the case of bidirectional and extensible fibers, the corresponding boundary conditions are given by (see [26]) the following equation:

$$\begin{aligned}\mathbf{t} &= \mathbf{P} \mathbf{N} - \frac{d}{ds} [C_1 \mathbf{g}_1 (\mathbf{L} \cdot \mathbf{T}) (\mathbf{L} \cdot \mathbf{N}) + C_2 \mathbf{g}_2 (\mathbf{M} \cdot \mathbf{T}) (\mathbf{M} \cdot \mathbf{N})], \\ \mathbf{m} &= C_1 \mathbf{g}_1 (\mathbf{L} \cdot \mathbf{N})^{2+} + C_2 \mathbf{g}_2 (\mathbf{M} \cdot \mathbf{N})^2, \\ \mathbf{f} &= C_1 \mathbf{g}_1 (\mathbf{L} \cdot \mathbf{T}) (\mathbf{L} \cdot \mathbf{N}) + C_2 \mathbf{g}_2 (\mathbf{M} \cdot \mathbf{T}) (\mathbf{M} \cdot \mathbf{N}).\end{aligned}\quad (66)$$

Now, we approximate the above boundary conditions and thus obtain

$$\begin{aligned}\dot{\mathbf{t}} &= \dot{\mathbf{P}} \mathbf{N} - \frac{d}{ds} [C_1 \dot{\mathbf{g}}_1 (\mathbf{L} \cdot \mathbf{T}) (\mathbf{L} \cdot \mathbf{N}) + C_2 \dot{\mathbf{g}}_2 (\mathbf{M} \cdot \mathbf{T}) (\mathbf{M} \cdot \mathbf{N})], \\ \dot{\mathbf{m}} &= C_1 \dot{\mathbf{g}}_1 (\mathbf{L} \cdot \mathbf{N})^{2+} + C_2 \dot{\mathbf{g}}_2 (\mathbf{M} \cdot \mathbf{N})^2, \\ \dot{\mathbf{f}} &= C_1 \dot{\mathbf{g}}_1 (\mathbf{L} \cdot \mathbf{T}) (\mathbf{L} \cdot \mathbf{N}) + C_2 \dot{\mathbf{g}}_2 (\mathbf{M} \cdot \mathbf{T}) (\mathbf{M} \cdot \mathbf{N}).\end{aligned}\quad (67)$$

If the fibers' directions are aligned with the axes of Cartesian coordinates (i.e., $\mathbf{L} = \mathbf{E}_1$ and $\mathbf{M} = \mathbf{E}_2$) and are either normal or tangential to the boundary (i.e., $(\mathbf{L} \cdot \mathbf{T}) (\mathbf{L} \cdot \mathbf{N}) = (\mathbf{M} \cdot \mathbf{T}) (\mathbf{M} \cdot \mathbf{N}) = 0$), equations (64) and (67) further reduces to the following equation:

$$\begin{aligned}[\mu u_{i,AA} - \dot{p}_i + E_1 u_{1,11} \delta_{i1} + E_2 u_{2,22} \delta_{i2} \\ - C_1 u_{i,1111} - C_2 u_{i,1111}] \mathbf{e}_i &= 0, \\ \dot{\mathbf{t}} &= \dot{\mathbf{P}} \mathbf{N}, \\ \dot{\mathbf{m}} &= C_1 \dot{\mathbf{g}}_1 (\mathbf{L} \cdot \mathbf{N})^2 + C_2 \dot{\mathbf{g}}_2 (\mathbf{M} \cdot \mathbf{N})^2, \\ \dot{\mathbf{f}} &= 0,\end{aligned}\quad (68)$$

which together with the incompressibility condition ($u_{,i} = 0$) constitutes the complete set of the PDEs system to solve the final deformation profiles. Similarly, equation (63) now becomes

$$\begin{aligned} \dot{\mathbf{P}}_{iA}(\mathbf{e}_i \otimes \mathbf{E}_A) &= [\mu u_{,iA} + E_1 \overrightarrow{u}_{1,1} \delta_{i1} \delta_{A1} + E_2 u_{,2,2} \delta_{i2} \delta_{A2} \\ &\quad - C_1 u_{,i,111} \delta_{A1} - C_2 u_{,i,222} \delta_{A2} \\ &\quad + p_o u_{A,i} - \dot{p} \delta_{iA}] (\mathbf{e}_i \otimes \mathbf{E}_A). \end{aligned} \quad (69)$$

For example, if the unit normal of a boundary is $\mathbf{N} = \mathbf{E}_1$, the boundary traction can be computed as follows:

$$\begin{aligned} \dot{\mathbf{t}}_i \mathbf{e}_i &= \dot{\mathbf{P}} \mathbf{E}_1 = [\mu u_{,iA} + E_1 u_{,1,1} \delta_{i1} \delta_{A1} + E_2 \overrightarrow{u}_{2,2} \delta_{i2} \delta_{A2} \\ &\quad - C_1 u_{,i,111} \delta_{A1} - C_2 u_{,i,222} \delta_{A2} + p_o u_{A,i} - \dot{p} \delta_{iA}] (\mathbf{e}_i \otimes \mathbf{E}_A) \mathbf{E}_1 \\ &= (\mu u_{,i1} + E_1 u_{,1,1} \delta_{i1} - C_1 u_{,i,111} + p_o u_{1,i} - \dot{p} \delta_{i1}) \mathbf{e}_i. \end{aligned} \quad (70)$$

Again, by introducing the scalar field φ (see equation (40)) and employing the compatibility conditions (i.e., $\dot{p}_{ij} = \dot{p}_{ji}$), we reduce the above equation to the following equation:

$$\begin{aligned} \dot{p}_{21} - \dot{p}_{12} &= \Delta \left[\Delta \varphi - \frac{C_1}{\mu} \varphi_{1111} - \frac{C_2}{\mu} \varphi_{2222} \right] \\ &\quad + \left(\frac{E_1}{\mu} - \frac{E_2}{\mu} \right) \varphi_{1122} = 0. \end{aligned} \quad (71)$$

A complete analytical solution for equation (71) is available via the methods of iterative reduction and the principle of eigenfunction expansion (see, more details, [35–37]). Figures 1–4 illustrate the deformation profiles for the cases discussed through Sections 3–5. As the equations become mathematically compact, the corresponding deformation fields experience less oscillatory behaviors. This is clearly demonstrated by the results in Figures 3–4, bi-directional cases, which show a close agreement with the predictions from nonlinear models. We also mention here that equation (71) reduces to equations (42) and (58) in the limit of vanishing C_2 and E_2 , respectively. This, in turn, suggests that unidirectional cases can be assimilated within the systems of equation (71) by setting $C_2 = E_2 = 0$ (see Figure 5). In fact, the latter model is recommended to use, since the bidirectional and extension fibers case is the most general and compact form (with minimal singular behaviors) and therefore produces more accurate prediction results.

To elaborate the proposed model, we present comparisons with the experimental data obtained from the 3-point bending test of CNC fiber composite ($C = 150$ GPa, $\mu = 1$ GPa). This is a particular case of the proposed model, when $C/\mu = 150$ and vanishing E (i.e., equation (20)). Using the method presented in Section 3.1, we find the solution of equation (20) as

$$\begin{aligned} \varphi(x, y) &= \sum_{m=1}^{\infty} \left[\left\{ e^{a_m x} (-C_m \cos b_m x + D_m \sin b_m x) \right. \right. \\ &\quad \left. \left. + e^{-a_m x} (C_m \cos b_m x + D_m \sin b_m x) \right\} \times \sin \left(\frac{\pi}{2d} \right) y \right], \end{aligned} \quad (72)$$

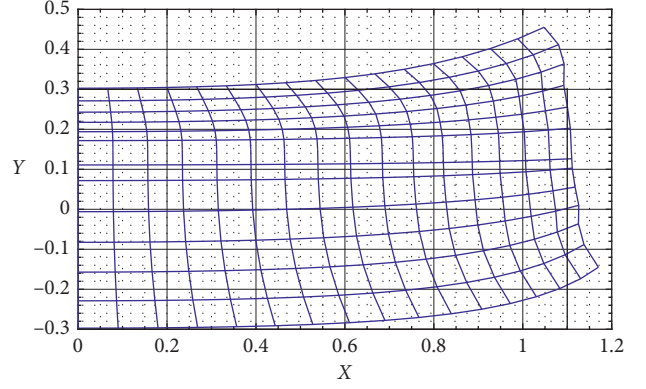


FIGURE 1: Unidirectional fibers.

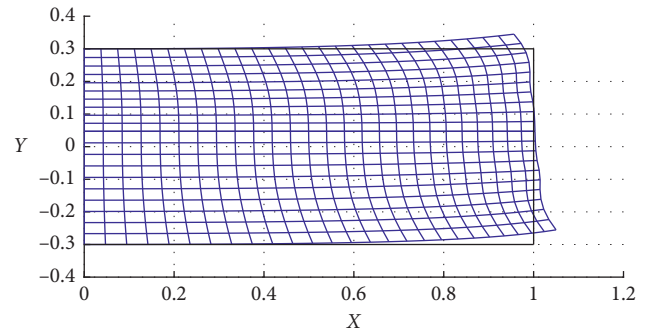


FIGURE 2: Unidirectional extensible fibers.

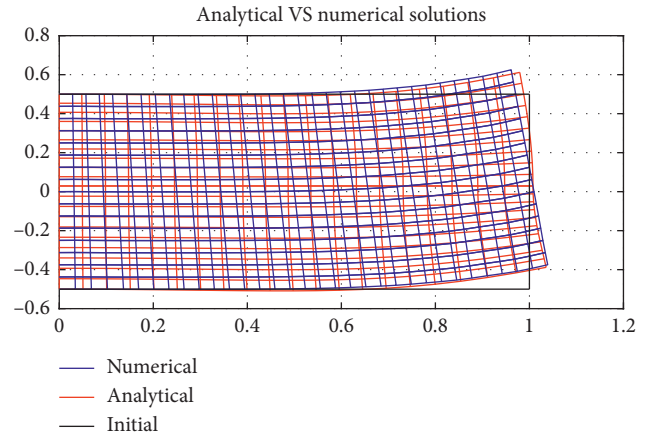


FIGURE 3: Bidirectional fibers.

where

$$\begin{aligned} m &= \frac{\pi n}{2d}, \\ \alpha &= \frac{C}{\mu}, \\ a_m &= \frac{\sqrt{2m\sqrt{\alpha} + 1}}{2\sqrt{\alpha}}, \\ b_m &= \frac{\sqrt{2m\sqrt{\alpha} - 1}}{2\sqrt{\alpha}}, \end{aligned} \quad (73)$$

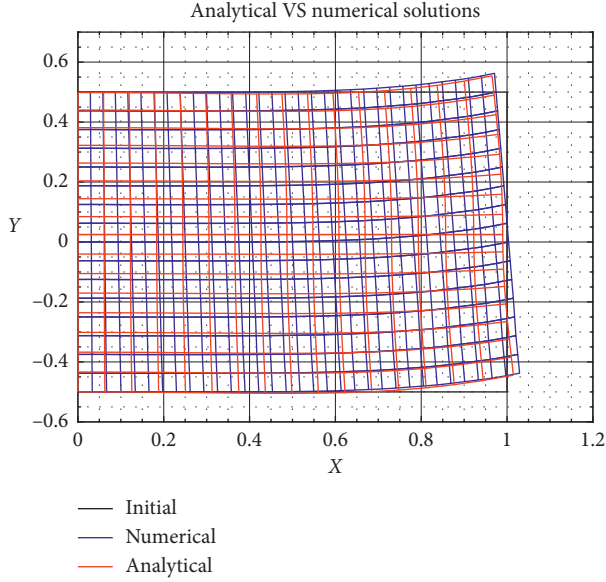
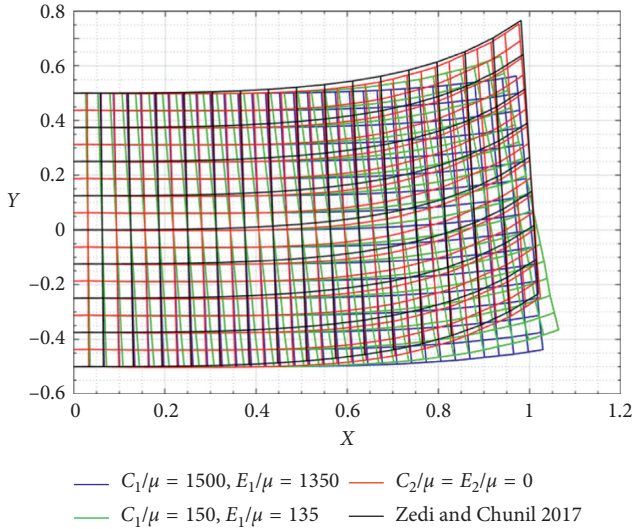


FIGURE 4: Bidirectional extensible fibers.

FIGURE 5: Reduction of solutions in the limit of $C_2 = E_2 = 0$.

and the unknowns C_m and D_m can be determined via the applied moment in the form of Fourier expansion; i.e.,

$$\dot{m}_1 = C u_{1,11} = -\varphi_{211} = \sum_{n=1}^{30} \frac{20}{\pi n} (-1)^{n-1/2} \cos\left(\frac{\pi n}{2d}\right) y. \quad (74)$$

Using equation (74), we compute the maximum deflections of the CNC composite and illustrate the results in Figure 6. It is shown in Figure 6 that the proposed model successfully predicts the normal deflections of the CNC composite strip. Since the slope of the graph in Figure 6 indicates the moduli of the composite (when divided by the corresponding length scale), it can also be used in the estimation of the overall material properties of the composite. However, due to the paucity of available data, we are not able to provide the quantitative analysis other than

those presented in Figure 6 at this time. The study is currently underway, and our intention is to present elsewhere when ready. We also mention here that the overall responses of composite materials can also be estimated using multiscale modeling methods (see, for example, Shahabodini et al. [8, 9]).

Lastly, we assimilate the case of single family of fiber composites subjected to the axial tension. The linear solution obtained from equation (56) demonstrates good agreement with the compatible nonlinear model [28] for small deformations superposed on large, while it shows discrepancies in the prediction of large deformations (See Figure 7). It is also noted here that we reserve the details in solving the corresponding differential equations (equation (56)) for the sake of conciseness. However, the procedures for the particular case of the present example can be found in [28].

6. Further Considerations

For the analysis of soft materials-based composites, such as carbon rubber-fiber composites and polymer composites, a different type of energy potential may be suggested instead of the Neo-Hookean model discussed in the previous sections. The Mooney–Rivlin model is one of the most commonly used energy potentials for the aforementioned cases (see, for example, [33]). In the forgoing development, we present a compatible linear model for the Mooney–Rivlin types of materials for the desired applications. The expression of the Mooney–Rivlin potential is given by the following equation:

$$W(\mathbf{F}) = \frac{\mu}{2} (\mathbf{F} \cdot \mathbf{F} - 3) + \frac{\lambda}{2} \left[\frac{1}{2} (\text{tr} \mathbf{F})^2 - \text{tr}(\mathbf{F}^2) \right], \quad \mu, \lambda > 0. \quad (75)$$

The derivative of equation (75) with respect to the deformation gradient tensor then yields the following equation:

$$W_{\mathbf{F}} = \mu \mathbf{F} + \lambda \mathbf{F} [(\mathbf{F} \cdot \mathbf{F}) \mathbf{I} - \mathbf{F}^T \mathbf{F}]. \quad (76)$$

Substituting equation (76) into equation (9) furnishes the following expression of the Piola stresses:

$$\mathbf{P} = \mu \mathbf{F} + \lambda \mathbf{F} [(\mathbf{F} \cdot \mathbf{F}) \mathbf{I} - \mathbf{F}^T \mathbf{F}] - p \mathbf{F}^* - C \text{Div}(\mathbf{g} \otimes \mathbf{D} \otimes \mathbf{D}). \quad (77)$$

Now, by applying the same schemes as adopted in the previous sections, we find the following equation:

$$\dot{\mathbf{P}} = \mu \dot{\mathbf{F}} - [\lambda \mathbf{F} \{(\mathbf{F} \cdot \mathbf{F}) \mathbf{I} - \mathbf{F}^T \mathbf{F}\}] - \dot{p} \mathbf{F}_o^* - p_o \dot{\mathbf{F}}^* - C \nabla \dot{\mathbf{g}}(\mathbf{D} \otimes \mathbf{D}), \quad (78)$$

where the second term of the right side of equation (78) can be evaluated at $\varepsilon = 0$ as

$$\begin{aligned} [\lambda \mathbf{F} \{(\mathbf{F} \cdot \mathbf{F}) \mathbf{I} - \mathbf{F}^T \mathbf{F}\}] &= \lambda \dot{\mathbf{F}} \{(\mathbf{F}_o \cdot \mathbf{F}_o) \mathbf{I} - \mathbf{F}_o^T \mathbf{F}_o\} \\ &\quad + \lambda \mathbf{F}_o \{2(\dot{\mathbf{F}} \cdot \mathbf{F}_o) \mathbf{I}_o - \dot{\mathbf{F}}^T \mathbf{F}_o - \mathbf{F}_o^T \dot{\mathbf{F}}\}. \end{aligned} \quad (79)$$

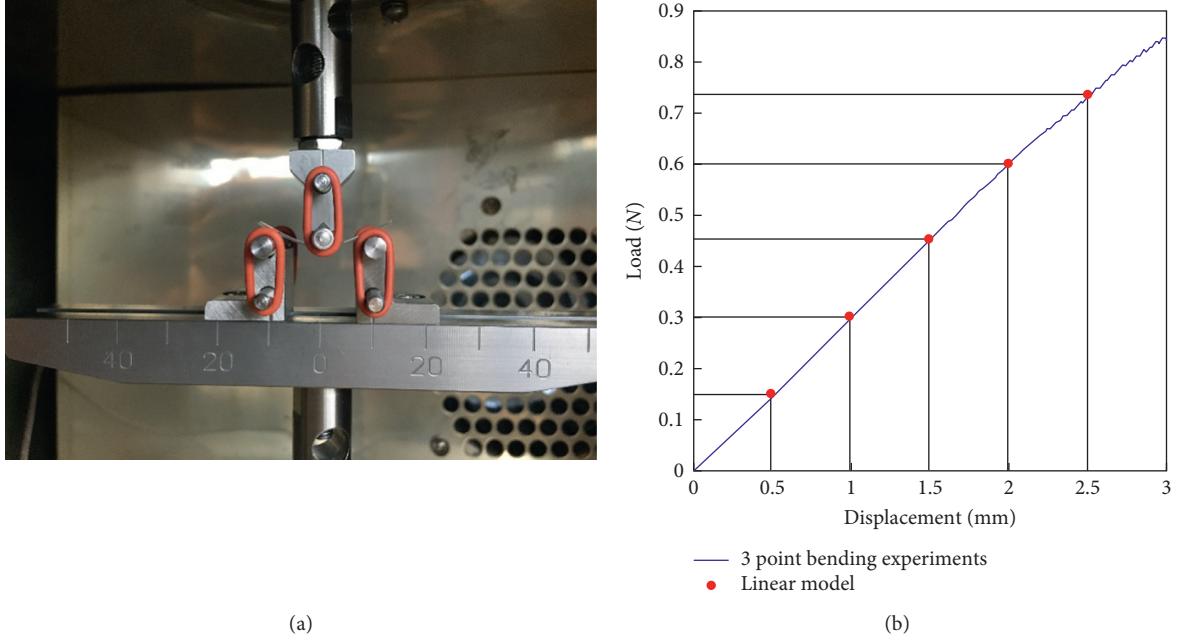


FIGURE 6: (a) Experimental setting. (b) Experiment vs theoretical prediction.

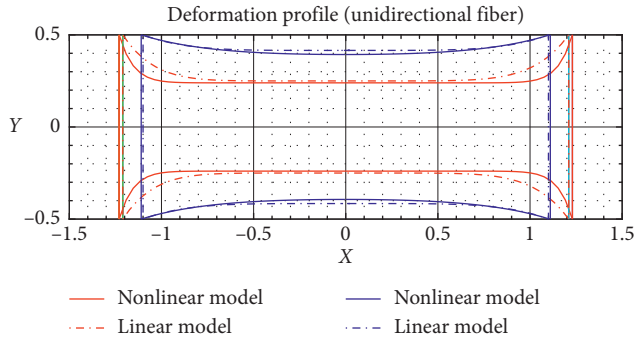


FIGURE 7: Deformation profiles of unidirectional fiber composites under axial tension.

Since $\mathbf{F}_0^T = \mathbf{F}_0 = \mathbf{I}$, the above equation becomes the following equation:

$$\begin{aligned} & \lambda \dot{\mathbf{F}}(\delta_{AA} - 1) + \lambda \left\{ 2(\dot{\mathbf{F}} \cdot \mathbf{I})\mathbf{I} - \dot{\mathbf{F}}^T - \dot{\mathbf{F}} \right\} \\ & = (\lambda \dot{\mathbf{F}}_{iA} + 2\lambda \dot{\mathbf{F}}_{BB} \delta_{iA} - \lambda \dot{\mathbf{F}}_{Ai} - \lambda \dot{\mathbf{F}}_{iA}) (\mathbf{e}_i \otimes \mathbf{E}_A), \quad \delta_{AA} = 2. \end{aligned} \quad (80)$$

Thus, from the results in equations (2), (27), (28), (33), (78), and (80), we find the following stress expression for the cases of unidirectional fiber composites as

$$\begin{aligned} \dot{\mathbf{P}}_{iA} (\mathbf{e}_i \otimes \mathbf{E}_A) & = \left[\mu u_{i,A} - \dot{p} \delta_{iA} + p_0 u_{A,i} \right. \\ & \left. - C u_{i,BCD} D_A D_B D_C D_D \right] (\mathbf{e}_i \otimes \mathbf{E}_A), \end{aligned} \quad (81)$$

where $\dot{\mathbf{F}}_{BB} = u_{B,B} = 0$ from the conditions of bulk incompressibility (see equation (34)). Consequently, the corresponding Euler equilibrium equation satisfies the following equation:

$$\begin{aligned} \text{Div}(\dot{\mathbf{P}}) & = \lambda u_{A,i} [\mu u_{i,AA} - \lambda u_{A,iA} - p_i + p_0 u_{A,iA} \\ & - C u_{i,ABCD} D_A D_B D_C D_D] \mathbf{e}_i = 0 \mathbf{e}_i. \end{aligned} \quad (82)$$

Using the compatibility condition of $u_{A,iA}$ (i.e. $u_{A,iA} = u_{A,Ai}$) and the constraints of bulk incompressibility, we find that $u_{A,Ai} = (u_{A,A})_i = 0$ and thereby reduce equation (83) to the following equation:

$$(\mu u_{i,AA} - p_i - C u_{i,ABCD} D_A D_B D_C D_D) \mathbf{e}_i = 0 \mathbf{e}_i. \quad (83)$$

The resulting equilibrium equation (equation (83)) implies that there is no clear distinction between the Neo-Hookean model and Mooney–Rivlin model as far as the superposed incremental deformations with the augmented bulk incompressibility conditions are considered. This is due to the fact that the divergence of high-strain terms identically vanishes upon the imposition of linearized bulk incompressibility conditions (i.e., $\text{Div} \mathbf{u} = \text{div} \mathbf{u} = 0$). However, the expressions of Piola stresses are affected by the introduction of Mooney–Rivlin type materials (see equations (33) and (81)). Thus, for example, if $\mathbf{N} = \mathbf{D} = \mathbf{E}_1$, we compute from equation (25) that

$$\begin{aligned} \dot{t}_i \mathbf{e}_i & = \dot{\mathbf{P}} \mathbf{E}_1 = \mu u_{i,A} - \lambda u_{A,i} - \dot{p} \delta_{iA} + p_0 u_{A,i} \\ & - C u_{i,111} \delta_{iA} D_1 D_1 D_1 (\mathbf{e}_i \otimes \mathbf{E}_A) \mathbf{E}_1 \\ & = (\mu u_{i,1} - \lambda u_{1,i} - \dot{p} \delta_{i1} + p_0 u_{1,i} - C u_{i,111}) \mathbf{e}_i, \end{aligned} \quad (84)$$

which is the boundary tractions for the case of the Mooney–Rivlin energy potential. Lastly, from equation (77), we find at $\varepsilon = 0$ that

$$\mathbf{P}_0 = \mu \mathbf{I} + \lambda \mathbf{I} [\mathbf{I} - \mathbf{I}] - p_0 \mathbf{I} - C \text{Div}(\mathbf{I} \otimes \mathbf{D} \otimes \mathbf{D}) = 0, \quad (85)$$

and thereby obtain $\mu = p_0$. Equation (83) together with the imposed boundary conditions (i.e., equations (25) and (84))

constitutes a complete set of PDEs system which can be solved using the similar schemes as presented in Section 3.1. Further, because the resulting equilibrium equations are of the same form (see equations (22) and (84)), equations (81) and (84) may be used in the determination of the parameters associated with high-strain terms (λ) by comparing stresses in equations (33) and (81). Investigations in this respect (including the implementations of the developed linear theory) are currently underway. Our intention is to report elsewhere.

7. Conclusions

We present complete linear models for the mechanics of an elastic solid reinforced with fibers resistant to flexure and extension. Within the prescription of the superposed incremental deformations, the first and second gradient of deformations is approximated through which the kinematics of fibers is explicitly determined. The linearized Euler equilibrium equations and the Piola stress are then formulated for the Neo-Hookean types of materials. We also derive the corresponding boundary conditions and the conditions of bulk incompressibility for the sake of completeness. In addition, the cases of the bidirectional fiber composites are considered via the fiber decomposition of the deformation gradient tensor. It is found that the systems of PDEs for the bidirectional and extensible fibers reduce to those from single family of fibers in the limit of vanishing material parameters of fibers.

In particular, we demonstrate the well-known result from the linear theory of elasticity that the merging of the bases remains valid even with the incorporation of fibers' bending and extension into the models of deformations. A Mooney–Rivlin material is also elaborated, where we show that there is no clear distinctions in the resulting Euler equations obtained from the two different strain energy models (i.e., Neo-Hookean and Mooney–Rivlin) as long as the small deformations are concerned. However, the resulting Piola stresses are of different forms in that the one from the Mooney–Rivlin model demonstrates clear dependency on both the first and second invariant of deformation gradient tensors, whereas the Piola stress, in the case of the Neo-Hookean model, depends only on the first invariant. Lastly, we mention here that the present model can be used in the approximation of the nonlinear theory of strain gradient elasticity arising in finite plane elastostatics.

Data Availability

The data used to support the findings of this study are available from the corresponding author upon request.

Conflicts of Interest

The authors declare that they have no conflicts of interest.

Acknowledgments

This work was supported by the Natural Sciences and Engineering Research Council of Canada via Grant #RGPIN

04742 and the University of Alberta through a start-up grant. The author would like to thank Dr. David Steigmann for many useful discussions.

References

- [1] J. E. Adkins, "Finite plane deformation of thin elastic sheets reinforced with inextensible cords," *Philosophical Transactions of the Royal Society A: Mathematical, Physical and Engineering Sciences*, vol. 249, no. 961, pp. 125–150, 1956.
- [2] J. L. Ericksen and R. S. Rivlin, "Large elastic deformations of homogeneous anisotropic materials," *Indiana University Mathematics Journal*, vol. 3, no. 3, pp. 281–301, 1954.
- [3] A. J. M. Spencer, *Deformations of Fibre-Reinforced Materials*, Oxford University Press, Oxford, UK, 1972.
- [4] A. C. Pipkin, "Stress analysis for fiber-reinforced materials," *Advances in Applied Mechanics*, vol. 19, pp. 1–51, 1979.
- [5] J. F. Mulhern, T. G. Rogers, and A. J. M. Spencer, "A continuum model for fibre-reinforced plastic materials," *Proceedings of the Royal Society A: Mathematical, Physical and Engineering Sciences*, vol. 301, no. 1467, pp. 473–492, 1967.
- [6] J. F. Mulhern, T. G. Rogers, and A. J. M. Spencer, "A continuum theory of a plastic-elastic fibre-reinforced material," *International Journal of Engineering Science*, vol. 7, no. 2, pp. 129–152, 1969.
- [7] A. C. Pipkin and T. G. Rogers, "Plane deformations of incompressible fiber-reinforced materials," *Journal of Applied Mechanics*, vol. 38, no. 3, 1971.
- [8] A. Shahabodini, R. Ansari, and M. Darvizeh, "Atomistic-continuum modeling of vibrational behavior of carbon nanotubes using the variational differential quadrature method," *Composite Structures*, vol. 185, pp. 728–747, 2018.
- [9] A. Shahabodini, R. Ansari, and M. Darvizeh, "Multiscale modeling of embedded graphene sheets based on the higher-order Cauchy-Born rule: nonlinear static analysis," *Composite Structures*, vol. 165, pp. 25–43, 2017.
- [10] R. A. Toupin, "Theories of elasticity with couple-stress," *Archive for Rational Mechanics and Analysis*, vol. 17, no. 2, pp. 85–112, 1964.
- [11] R. D. Mindlin and H. F. Tiersten, "Effects of couple-stresses in linear elasticity," *Archive for Rational Mechanics and Analysis*, vol. 11, no. 1, pp. 415–448, 1962.
- [12] W. T. Koiter, "Couple-stresses in the theory of elasticity," *Proceedings of the Koninklijke Nederlandse Akademie van Wetenschappen B*, vol. 67, pp. 17–44, 1964.
- [13] A. J. M. Spencer and K. P. Soldatos, "Finite deformations of fibre-reinforced elastic solids with fibre bending stiffness," *International Journal of Non-Linear Mechanics*, vol. 42, no. 2, pp. 355–368, 2007.
- [14] H. C. Park and R. S. Lakes, "Torsion of a micropolar elastic prism of square cross-section," *International Journal of Solids and Structures*, vol. 23, no. 4, pp. 485–503, 1987.
- [15] G. A. Maugin and A. V. Metrikine, *Mechanics of Generalized Continua: One Hundred Years after the Cosserats*, Springer, New York, NY, USA, 2010.
- [16] P. Neff, "A finite-strain elastic-plastic Cosserat theory for polycrystals with grain rotations," *International Journal of Engineering Science*, vol. 44, no. 8-9, pp. 574–594, 2006.
- [17] I. Munch, P. Neff, and W. Wagner, "Transversely isotropic material: nonlinear Cosserat vs. classical approach," *Continuum Mechanics and Thermodynamics*, vol. 23, no. 1, pp. 27–34, 2011.
- [18] P. Neff, "Existence of minimizers for a finite-strain micromorphic elastic solid," *Proceedings of the Royal Society of*

- Edinburgh: Section A Mathematics*, vol. 136, no. 5, pp. 997–1012, 2006.
- [19] S. K. Park and X. L. Gao, “Variational formulation of a modified couple-stress theory and its application to a simple shear problem,” *Zeitschrift für angewandte Mathematik und Physik*, vol. 59, no. 5, pp. 904–917, 2008.
- [20] E. Fried and M. E. Gurtin, “Gradient nanoscale polycrystalline elasticity: intergrain interactions and triple-junction conditions,” *Journal of the Mechanics and Physics of Solids*, vol. 57, no. 10, pp. 1749–1779, 2009.
- [21] D. J. Steigmann, “Theory of elastic solids reinforced with fibers resistant to extension, flexure and twist,” *International Journal of Non-Linear Mechanics*, vol. 47, no. 7, pp. 734–742, 2012.
- [22] C. Truesdell and W. Noll, “The non-linear field theories of mechanics,” in *Handbuch der Physik*, III/3, S. Flugge, Ed., Springer, Berlin, Germany, 1965.
- [23] F. D. Isola, M. Cuomo, L. Greco, and A. Della Corte, “Bias extension test for pantographic sheets: numerical simulations based on second gradient shear energies,” *Journal of Engineering Mathematics*, vol. 103, no. 1, pp. 127–157, 2017.
- [24] F. D. Isola, A. Della Corte, L. Greco, and A. Luongo, “Plane bias extension test for a continuum with two inextensible families of fibers: a variational treatment with Lagrange multipliers and a perturbation solution,” *International Journal of Solids and Structures*, vol. 81, pp. 1–12, 2016.
- [25] E. Turco, “Non-standard coupled extensional and bending bias tests for planar pantographic lattices. Part I: numerical simulations,” *Zeitschrift für angewandte Mathematik und Physik*, vol. 67, no. 5, p. 122, 2016.
- [26] C. Kim and M. Zeidi, “Gradient elasticity theory for fiber composites with fibers resistant to extension and flexure,” *International Journal of Engineering Science*, vol. 131, pp. 80–99, 2018.
- [27] M. Zeidi and C. Kim, “Finite plane deformations of elastic solids reinforced with fibers resistant to flexure: complete solution,” *Archive of Applied Mechanics*, vol. 88, no. 5, pp. 819–835, 2017.
- [28] M. Zeidi and C. Kim, “Mechanics of fiber composites with fibers resistant to extension and flexure,” *Mathematics and Mechanics of Solids*, 2017.
- [29] M. Zeidi and C. Kim, “Mechanics of an elastic solid reinforced with bidirectional fiber in finite plane elastostatics: complete analysis,” *Continuum Mechanics and Thermodynamics*, vol. 30, no. 3, pp. 573–592, 2018.
- [30] M. Zeidi and C. Kim, “The effects of intra-membrane viscosity on lipid membrane morphology: complete analytical solution,” *Scientific Reprints. Nature*, vol. 8, no. 1, 2018.
- [31] T. Belay, C. I. Kim, and P. Schiavone, “Analytical solution of lipid membrane morphology subjected to boundary forces on the edges of rectangular membrane,” *Continuum Mechanics and Thermodynamics*, vol. 28, no. 1-2, pp. 305–315, 2015.
- [32] C. Kim and D. J. Steigmann, “Distension-induced gradient capillarity in lipid membranes,” *Continuum Mechanics and Thermodynamics*, vol. 27, no. 4-5, pp. 609–315, 2015.
- [33] R. W. Ogden, *Non-Linear Elastic Deformations*, Ellis Horwood Ltd., Chichester, England, 1984.
- [34] D. J. Steigmann, “Invariants of the stretch tensors and their application to finite elasticity theory,” *Mathematics and Mechanics of Solids*, vol. 7, no. 4, pp. 393–404, 2002.
- [35] W. W. Read, “Analytical solutions for a Helmholtz equation with dirichlet boundary conditions and arbitrary boundaries,” *Mathematical and Computer Modelling*, vol. 24, no. 2, pp. 23–34, 1996.
- [36] W. W. Read, “Series solutions for Laplace’s equation with nonhomogeneous mixed boundary conditions and irregular boundaries,” *Mathematical and Computer Modelling*, vol. 17, no. 12, pp. 9–19, 1993.
- [37] Y. Huang and X. Zhang, “General analytical solution of transverse vibration for orthotropic rectangular thin plates,” *Journal of Marine Science and Application*, vol. 1, no. 2, pp. 78–82, 2002.

Research Article

Study on Mechanics-Based Cracking Resistance of Semiflexible Pavement Materials

Duanyi Wang, Xiayi Liang , Danning Li , Hehao Liang , and Huayang Yu 

School of Civil Engineering and Transportation, South China University of Technology, Guangzhou 510641, China

Correspondence should be addressed to Huayang Yu; huayangyu@scut.edu.cn

Received 7 June 2018; Revised 10 September 2018; Accepted 31 October 2018; Published 21 November 2018

Guest Editor: Munir Nazzal

Copyright © 2018 Duanyi Wang et al. This is an open access article distributed under the Creative Commons Attribution License, which permits unrestricted use, distribution, and reproduction in any medium, provided the original work is properly cited.

Semiflexible mixture is a composite paving material combining the advantages of both asphalt and cement concrete materials. It consists of matrix asphalt skeleton and cement mortar. Due to the different volume characters between asphalt structure and cement mortar, stress concentration always happens in this semiflexible mixture, leading to internal cracking. The objective of this study is to alleviate the internal cracking concern of the semiflexible mixture by adjusting the material components. To this end, optimal material design and numerical simulation have been conducted. Matrix asphalt structures with four different air voids were incorporated with different dosages of cement mortar. The contraction strain and expansion strain of cement mortar as well as the indirect tensile strength of matrix asphalt structure were measured. The results were input into ABAQUS for numerical simulation. The results indicated that (1) the internal stress in this semiflexible mixture is mainly determined by the contraction of cement mortar, rather than expansion; (2) larger air void of matrix asphalt structure and less volumetric variation of cement mortar reduce the internal stress; (3) once the air void of matrix asphalt structure is decided, both maximum contraction and expansion deformations of cement mortar should meet specific requirement to ensure less internal cracking. This is a practical-ready paper that provides reference for the anticracking design of semiflexible pavement.

1. Introduction

Semiflexible pavement material is a composite pavement material, which consists of porous asphalt structure and cement mortar. The main advantages of semiflexible pavement include high carrying capacity, high wearing resistance, high shear resistance, high water stability, and driving comfort. Semiflexible pavement material has very bright application prospects and is suitable for intersection turner, gas station, parking, bus station, airport runways, and other sections [1–6]. However, the insufficient volume stability resulted from the defects in the material composition and structure of semiflexible pavement leads to frequent cracking. The cracks occurring in semiflexible pavement materials can be divided into three types based on their causes: fatigue cracking under the action of traffic load, temperature contraction cracking and dry contraction cracking caused by temperature and humidity variation, and reflection cracks of semirigid base cracking [7]. Fatigue crack

and reflection crack are mainly caused by traffic load. In addition, temperature contraction cracking and dry contraction crack result from the different volume stability of asphalt mixture matrix and cement mortar. The volume of cement mortar can be greatly changed when the water reaction period or ambient temperature varies greatly. Consequently, the volume deformation of the asphalt mixture matrix and cement mortar cannot be coordinated. This incoordination leads to the stress concentration in semiflexible pavement, which makes the pavement more prone to crack. Thus, internal stress control of semiflexible pavement is particularly critical for crack resistance.

The effects of asphalt, aggregate, and cement mortar on the volumetric stability and cracking resistance of semiflexible pavement were studied by Huang [7], who researched and developed an easy-to-pour small contraction deformation polymer cement mortar. Wang and Wu [8] evaluated the cracking resistance of semiflexible pavement materials based on the fracture toughness using the

J-integral theory and three-point bending semicircular beam test. Huang et al. [9] studied the cracking resistance of semiflexible pavement materials based on cement-emulsified asphalt mortar. At present, studies of the anticracking of semiflexible pavement have been mainly focused on controlling the volumetric stability of the cement mortar and the overall cracking resistance of semiflexible pavement materials. However, few researchers have mechanically studied the internal cracking resistance and anticrack design of semiflexible pavement. Therefore, to improve the cracking resistance of semiflexible pavement from the material composition, the control of the internal stress of the cement mortar and matrix asphalt mixture in semiflexible pavement is particularly critical. In other words, the prerequisite for the anticracking design of semiflexible pavement materials is that the expansion stress and contraction stress of the cement mortar must be lower than the ultimate tensile strength of the asphalt mixture matrix.

In this paper, the expansion strain and contraction strain of cement mortar and the matrix were determined firstly. The ultimate tensile strength of the asphalt mixture matrix was measured. Then digital images of semiflexible pavement cross section were collected using a CCD digital camera. The locations of the cement mortar, asphalt, aggregate, and voids were obtained using AutoCAD software. The finite element analysis method was employed for the mechanical analysis of the digital image results. Taking the internal stress peak as the control index, this paper put forward the standard of strain control of cement mortar, which can effectively control the cracking of semiflexible pavement materials.

2. Materials and Methods

2.1. Materials. The performance indicators of materials used to prepare the cement mortar and the matrix of semiflexible pavement are shown in Tables 1–4.

2.2. The Expansion Strain and Contraction Strain of Cement Mortar. The expansion strain and contraction strain of cement mortar are the main reasons for the internal stress in semiflexible pavement. In order to explore the anticracking performance of semiflexible pavement, this paper measured the maximum expansion strain and contraction strain of cement mortar.

Referring to “Explain for General Code of Asphalt Pavement Engineering” [10], the cement mortar fluidity, compressive strength, flexural strength, and amount of contraction were used as the evaluation index. Based on the orthogonal test method, taking water-cement ratio and dosage of mineral filler and sand as the influencing factors, the indoor relevant experimental study would be processed to measure the flow performance, bending resistance, and volume stability of cement mortar. Through the range analysis, the best mix ratio of cement mortar can be determined, which is shown in Table 5.

2.2.1. The Expansion Strain of Cement Mortar. It has been shown that the thermal expansion coefficient of cement

TABLE 1: Gradation of standard sand.

Sieve size (mm)	1.18	0.6	0.3	0.15	0.075	Content of clay (%)
Passing rate (%)	100	98.5	92.7	51.5	2.2	0.5

TABLE 2: Technical indexes of mineral filler.

Testing indexes	Expressway or first grade highway requirement	Other grade highway requirement	Value
Apparent relative density (g/cm^3)	≥ 2.50	≥ 2.45	2.761
Water content (%)	≤ 1	≤ 1	0.27
Hydrophilic coefficient (%)	< 1	< 1	0.33
Plasticity index	≤ 4	≤ 4	2.4

TABLE 3: Technical indexes of asphalt.

Testing indexes	Technical requirement	Value
Penetration 25°C, 100 g, 5 s, 0.1 mm	60–80	68
Softening point TR&B (°C) min	≥ 46	49.5
Ductility 5°C, 5 cm/min, cm	> 15	65
Ductility 15°C, 5 cm/min, cm	≥ 100	> 100
Solubility (%) min	≥ 99.5	99.6
Flash point (°C) min	≥ 260	285
Wax content (%)	≤ 2.2	1.8
Dynamic viscosity 60°C	≥ 180	215
	Quality change	± 0.8
Rotate the film to heat the test residue (163°C, 85 min)	Penetration ratio: 25°C	≥ 61
	Ductility: 10°C, cm/min	≥ 6
		25.2

TABLE 4: Technical indexes of aggregate.

Testing indexes	Value	Technical requirement
Crushing value (%)	11	≤ 26
Los Angeles wear value (%)	12	≤ 28
Stone polishing value (BPN)	55	≥ 42
Coarse aggregate ruggedness (%)	4	≤ 12
Coarse aggregate needle sheet content (%)	4	≤ 15
Sand equivalent (%)	53	≤ 65
Methylene blue value (g/kg)	1.1	≤ 2.0

TABLE 5: Optimal mix ratio of cement mortar.

Cement mortar indicators	Water-cement ratio	Dosage of mineral filler (%)	Dosage of sand (%)
Value	0.61–0.63	10	20

mortar is time-dependent, whose largest value is $48 \mu\epsilon/^\circ\text{C}$ during the initial setting [11]. After the initial setting, the coefficient of thermal expansion decreases and reaches the lowest value of approximately $11 \mu\epsilon/^\circ\text{C}$ during the final setting. As time goes by, the coefficient of thermal expansion will increase slowly to the second largest value of $13.6 \mu\epsilon/^\circ\text{C}$ and will then gradually stabilize at $13.1 \mu\epsilon/^\circ\text{C}$. Therefore, the thermal expansion deformation becomes the largest when the cement mortar undergoes a hydration reaction. According to the actual project time, semiflexible pavement is generally constructed during the summer. Using the most unfavorable climatic conditions as a reference, the maximum surface temperature difference in Guangdong Province of China is about 40°C in summer, and the maximum expansion strain of cement mortar may be 1.92×10^{-3} .

2.2.2. The Contraction Strain of Cement Mortar. Contraction deformation of cement mortar can be divided into dry contraction, temperature contraction, plastic contraction, self-contraction (hardening contraction), and carbonation contraction. Among them, dry contraction is not only the most common deformation type of cement mortar but also the main reason for the cracking of materials [12]. In this paper, the maximum contraction strain of cement mortar is determined by a contraction test. According to the optimal mix ratio of cement mortar described in Table 5, a triple-test-molded dry contraction specimen with a standard size of $25 \text{ mm} \times 25 \text{ mm} \times 250 \text{ mm}$ was created. After the specimen was formed, it was maintained for 24 hours in a curing room at a temperature of $20 \pm 3^\circ\text{C}$ and a relative humidity of 98%. Then, the specimens were removed and their initial lengths were measured. The specimens were moved into a box with constant temperature and humidity ($20 \pm 1^\circ\text{C}$ and relative humidity of $50 \pm 3\%$). The contraction deformations of the cement mortar were measured at 1, 3, 7, 14, 28, 35, 60, 90, 120, 150, and 180 days. The average contraction strains were calculated, and the results of which are shown in Figure 1.

As shown in Figure 1, the average contraction strain of cement mortar increases with time and finally tends to be stable. After 180 days of hardening, the maximum contraction strain is 1.33×10^{-3} .

2.3. The Expansion Strain and Contraction Strain of the Matrix. The expansion strain and contraction strain of the asphalt matrix can go a long way to influence the internal stresses of the semiflexible pavement and therefore must be accounted for in the study. According to prior research [13], the coefficients of thermal contraction and expansion of AC are nonlinear with temperature, as shown in Table 6.

According to data of Table 6, the largest coefficients of thermal contraction and expansion of AC were determined to be 31.1 and $31.2 \mu\epsilon/^\circ\text{C}$, respectively. Using the most unfavorable climatic conditions as a reference, the maximum surface temperature difference in Guangdong Province of China is about 40°C in summer, and the maximum contraction strain and expansion strain of AC may be 1.24×10^{-3} and 1.25×10^{-3} .

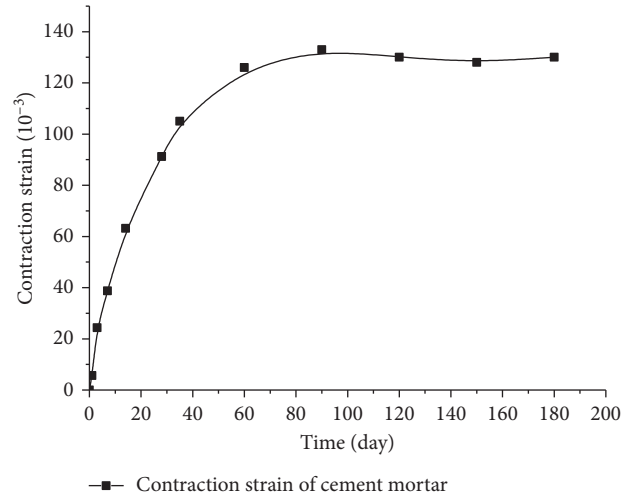


FIGURE 1: Contraction curve of cement mortar.

TABLE 6: Measured coefficients of thermal contraction and expansion at different temperature ranges.

Temperature range ($^\circ\text{C}$)	The coefficients of thermal contraction and expansion ($\mu\epsilon/^\circ\text{C}$)	
	The coefficient of thermal contraction	The coefficient of thermal expansion
-20 to -5	3.3	31.2
-5 to 10	19.2	28.1
10-25	29.4	23.8
25-40	31.1	25.6
40-55	25.7	26.3

Based on the research results [13], gradation of aggregate and air void of the sample do not affect the coefficients of thermal contraction and expansion significantly. Therefore, the maximum contraction strain and expansion strain of the asphalt matrix are referenced to 1.24×10^{-3} and 1.25×10^{-3} in this paper.

2.4. Indirect Tensile Test of the Matrix. This study adopted the multistage aggregate skeleton space-filling method [14, 15] to design the gradation of the matrix under the target air void (15%, 20%, 25%, and 30%) and combined the drainage test and the Cantabro test to determine the optimum asphalt content. The grading design results are shown in Table 7.

The ultimate tensile strength of the matrix is directly related to the cracking resistance of the semiflexible pavement materials. In this study, the MTS testing machine was used for the indirect tensile strength test to measure the indirect tensile strength of the matrix specimens with different air voids. Then, the splitting strength of the matrix would be calculated. This study used the indirect tensile strength of the matrix as the ultimate tensile strength. The ultimate tensile strength of the matrix is shown in Table 8.

TABLE 7: The grading design results of the asphalt mixture matrix with different target air voids.

Sieve size (mm)	Percent passing										Asphalt content (%)	
	19	16	13.2	9.5	2.36	1.18	0.6	0.3	0.15	0.075		
Air voids (%)	15	100	81.9	60.1	29.2	23.6	14.5	13.1	8.6	5.1	3.4	4.6
	20	100	78.7	57.3	25.4	19.4	13.6	12.5	8.4	4.8	3.2	4.2
	25	100	74.1	54.0	17.2	15.1	13.7	11.4	8.2	4.5	3.0	3.8
	30	100	71.4	51.4	15.2	13.7	12.4	10.6	7.6	4.2	2.7	3.4

TABLE 8: Ultimate tensile strength of the matrix.

The air void of the matrix (%)	Ultimate tensile strength of the matrix (MPa)
15	0.36
20	0.34
25	0.31
30	0.28

2.5. *Semiflexible Pavement Molding.* After the specimens were molded, they would be placed statically for 24 hours. The specimens were fixed to the vibration platform, and the cement mortar was poured into the matrix mixture until the surface voids were filled under multiple vibrations. The specimens were then stored in a curing box at constant temperature and humidity (temperature $20^{\circ}\text{C} \pm 3^{\circ}\text{C}$ and humidity $>90\%$) for 7 days. To identify the grouting depth of cement mortar, a small amount of Sudan dye was added to color the cement mortar.

The voids of the matrix can be divided into closed voids and connected voids. It is difficult to pour cement mortar into the closed voids. In order to ensure the accuracy, the amount of cement mortar grouting would be measured. As shown in the formula (1), the actual air void would be calculated to select the specimens whose actual air void is close to target air void. The density of cement mortar is 1.87 g/cm^3 . The test results are shown in Table 9.

$$V_{\text{actual air void}} = \frac{m}{\rho \times v}, \quad (1)$$

where $V_{\text{actual air void}}$ is the actual air void of the matrix, m is the amount of cement mortar grouting quantity, ρ is the density of cement mortar, $\rho = 1.87\text{ g/cm}^3$, and v is the volume of the specimen.

As shown in Table 9, by comparing the actual air void and target air void, the specimens 15-2, 15-3, 15-4, 20-2, 20-3, 20-6, 25-3, 25-4, 25-5, 30-2, 30-5, and 30-6 were selected for the follow-up study.

2.6. *Finite Element Simulation.* In this study, the semiflexible pavement structure was used as the simulation prototype, and the internal stress of the semiflexible pavement was analyzed by using the two-dimensional plane strain finite element method. The peak stress and stress level of the matrix were calculated considering the expansion and contraction deformations of the cement mortar. Asphalt mixture is a typical viscoelastic material, but in order to simplify the calculation, the linear elastic model is used to characterize the constitutive model of the asphalt mixture matrix and cement mortar in the semiflexible pavement structure. The basic assumptions are as follows:

TABLE 9: The quantity of grout to the asphalt mixture matrix.

Target air void (%)	Specimen number	Cement mortar grouting volume (g)	Actual air void (%)
15	15-1	124.16	13.2
	15-2	133.57	14.2
	15-3	134.51	14.3
	15-4	132.63	14.1
	15-5	126.04	13.4
	15-6	121.34	12.9
20	20-1	171.19	18.2
	20-2	181.54	19.3
	20-3	178.72	19.0
	20-4	167.43	17.8
	20-5	163.67	17.4
	20-6	177.78	18.9
25	25-1	217.28	23.1
	25-2	210.70	22.4
	25-3	225.75	24.0
	25-4	224.81	23.9
	25-5	227.63	24.2
	25-6	216.34	23.0
30	30-1	269.01	28.6
	30-2	273.72	29.1
	30-3	249.26	26.5
	30-4	259.61	27.6
	30-5	272.78	29.0
	30-6	272.78	29.0

- (1) The semiflexible pavement structure consists of the asphalt mixture matrix and cement mortar. The asphalt mixture matrix is a homogeneous and isotropic material.
- (2) As cement mortar and matrix asphalt mixture both produce contraction deformation and expansion deformation, in order to facilitate the finite element calculation, the volume of the matrix asphalt mixture is locked in the finite element model, and the volumetric deformation of cement mortar is defined as the relative volumetric deformation of the matrix asphalt mixture and cement mortar.
- (3) The influence of the road surface weight is not considered.
- (4) The adhesion between matrix and cement mortar is good, without any separation phenomenon.

To obtain a semiflexible pavement cracking resistance model, this study cut semiflexible pavement specimens with different air voids and then used a CCD digital camera to collect the screenshots of the specimens, as shown in Figure 2.

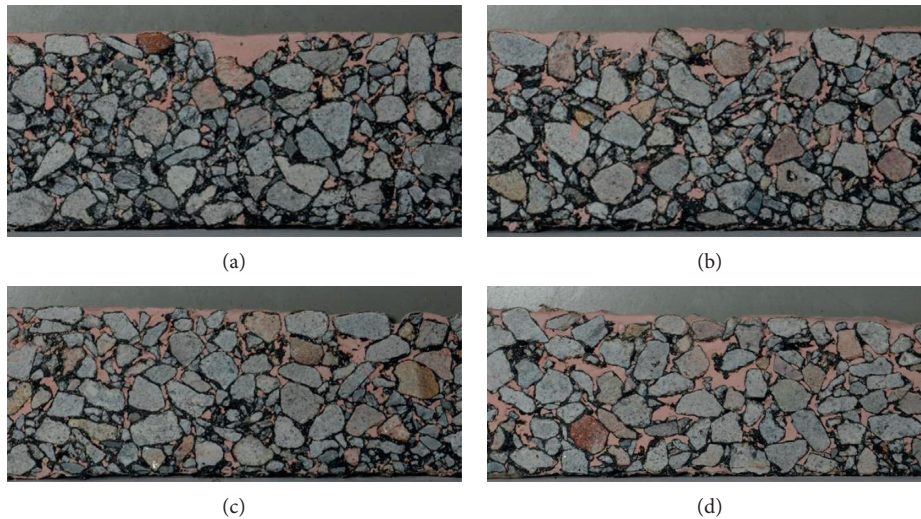


FIGURE 2: Cross-sectional images of semiflexible pavement. (a) 15% air void of the matrix; (b) 20% air void of the matrix; (c) 25% air void of the matrix; (d) 30% air void of the matrix.

The images of the semiflexible pavement were imported into AutoCAD software, and sectional information view was extracted to indicate the distributions of cement mortar, matrix, and air, as shown in Figure 3.

Taking the CAD images of the semiflexible pavement as the calculation model, the CAD images were imported into the finite element software. The material parameters were input, and the contact type was defined. For the boundary conditions, the upper boundary was bounded, the lower boundary was fixed ($U_1 = UR_1 = UR_2 = 0$), the left and right boundaries were horizontally constrained ($U_1 = UR_1 = UR_2 = 0$), the meshing partition was controlled using a triangular element (Tri), and the model had about 300,000 microcells. The meshing partition results are shown in Figure 4.

In Figure 4, the green part represents the aggregate, the white part indicates the cement mortar, and the red part is the asphalt. By changing the expansion and contraction of cement mortar, the stress distributions of aggregate and cement mortar were calculated. Due to the large size of the model, the computation takes a great deal of time. Therefore, five cross sections of each semiflexible pavement material with different air voids would be chosen to calculate the average value.

According to prior research [16–19], the material parameters of the semiflexible pavement were set up using the finite element analysis, as shown in Table 10.

Based on Sections 2.2 and 2.3, the contraction strain and expansion strain range of cement mortar is from -1.33×10^{-3} to 1.92×10^{-3} , and the contraction strain and expansion strain range of the matrix is from -1.24×10^{-3} to 1.25×10^{-3} . Therefore, the relative deformation range of the internal structure of the matrix and cement mortar is -2.58×10^{-3} to 3.16×10^{-3} . In this paper, the volume of the matrix was locked, and the volume deformation rate range of cement mortar during the finite element simulation was set from -4×10^{-3} to 4×10^{-3} , with an analysis calculation every 0.5×10^{-3} . The peak stress of the matrix was calculated under the conditions of contraction and expansion of the cement mortar.

Taking a 20% air void of the matrix as an example, the finite element analysis charts of the semiflexible pavement are as shown in Figure 5.

3. Results and Discussion

3.1. Stress Peak Analysis. The finite element simulation results show that the internal stress of the matrix mixture is related to the contraction and expansion deformations of cement mortar, as indicated in Figure 6.

Figure 6 shows the following:

- (1) Contraction and expansion deformations of the cement mortar both produce tensile stress in the matrix. In addition, the stress level of the contraction deformation is significantly higher than that of the expansion deformation. Taking a matrix mixture of 15% air void as an example, when the cement mortar shrinks by 0.2%, the internal stress of the matrix asphalt mixture is 0.46 MPa, but when the cement mortar expands by 0.2%, the internal stress of the matrix asphalt mixture is only 0.16 MPa; that is, the contraction stress is 2.8 times greater than the expansion stress. Meanwhile, the internal stress of the matrix mixture under the contraction of cement mortar grows obviously faster than that under the expansion deformation. It can be seen that the contraction deformation of cement mortar is the dominant factor that affects the stress growth of semiflexible pavement materials. Therefore, if the stress peak of semiflexible pavement is taken as an anticracking indicator, the cement mortar contraction stress should be controlled.
- (2) When the cement mortar expands, the internal stress of the matrix mixture has a good linear relationship with the expansion deformation. When the contraction deformation of the cement mortar is greater than 0.2%, the internal stress and contraction

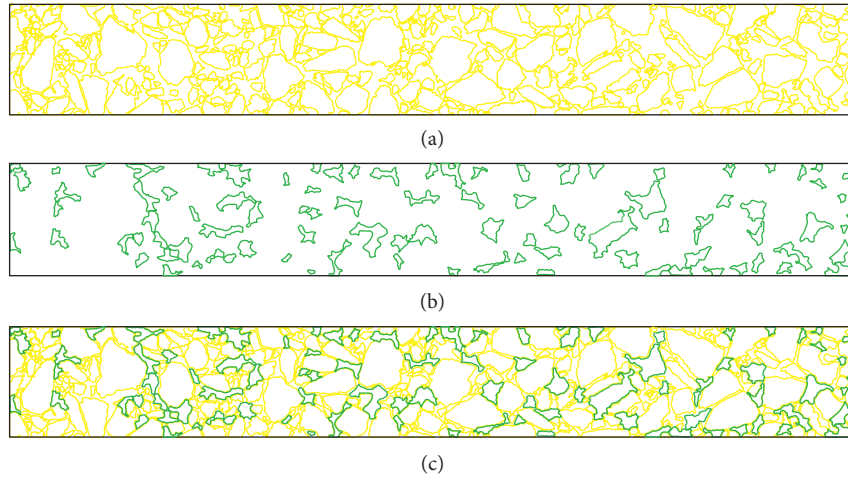


FIGURE 3: Sectional information view of the semiflexible pavement (15% air void). (a) Aggregate distribution; (b) cement mortar distribution; (c) distribution of materials.

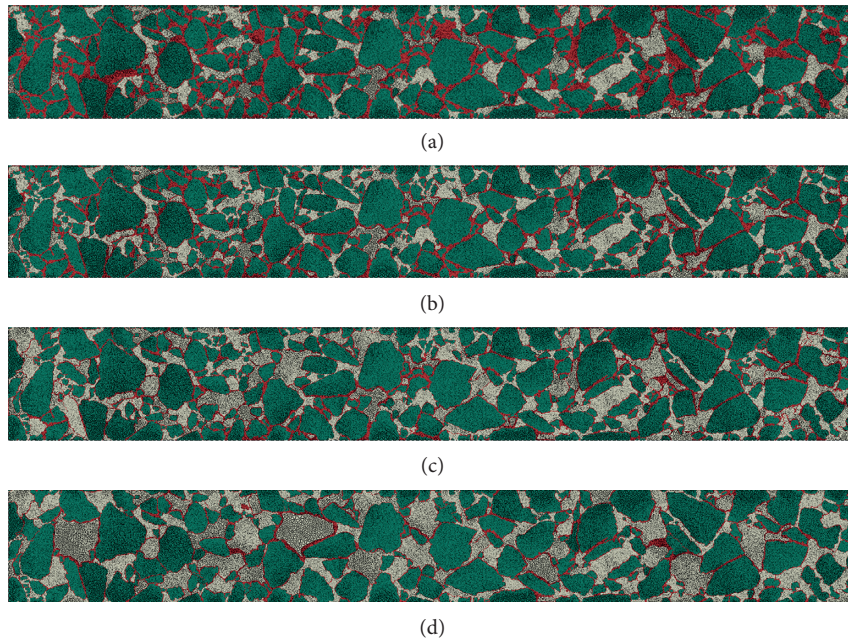


FIGURE 4: Finite element model of the semiflexible pavement. (a) 15% air void of the matrix; (b) 20% air void of the matrix; (c) 25% air void of the matrix; (d) 30% air void of the matrix.

TABLE 10: Material parameters of the semiflexible pavement.

Material	Poisson's ratio	Elastic modulus (MPa)
Asphalt (25°C)	0.35	1250
Aggregate (granite)	0.28	120000
Cement mortar	0.30	15000

deformation of the matrix mixture show a linear growth relationship. When the contraction deformation is less than 0.2%, the internal stress of the matrix mixture is a nonlinear growth model, and the internal stress growth rate decreases with the increase of the deformation amount. It is shown that

the matrix mixture is more sensitive to the change in stress when the contraction of the cement mortar is small.

When the cement mortar shrinks and expands, the relationship between air void of the matrix and stress level is as shown in Figure 7.

It can be seen from Figure 7 that the internal stress of the matrix increases with the increase of the contraction of cement mortar. And the air void of the matrix affects the growth rate of stress. Under the same deformation conditions, the smaller the air void of the matrix mixture is, the greater the stress and stress growth rate is. For example, the stress growth rate is about 1.7 MPa/% for 15% air void of the

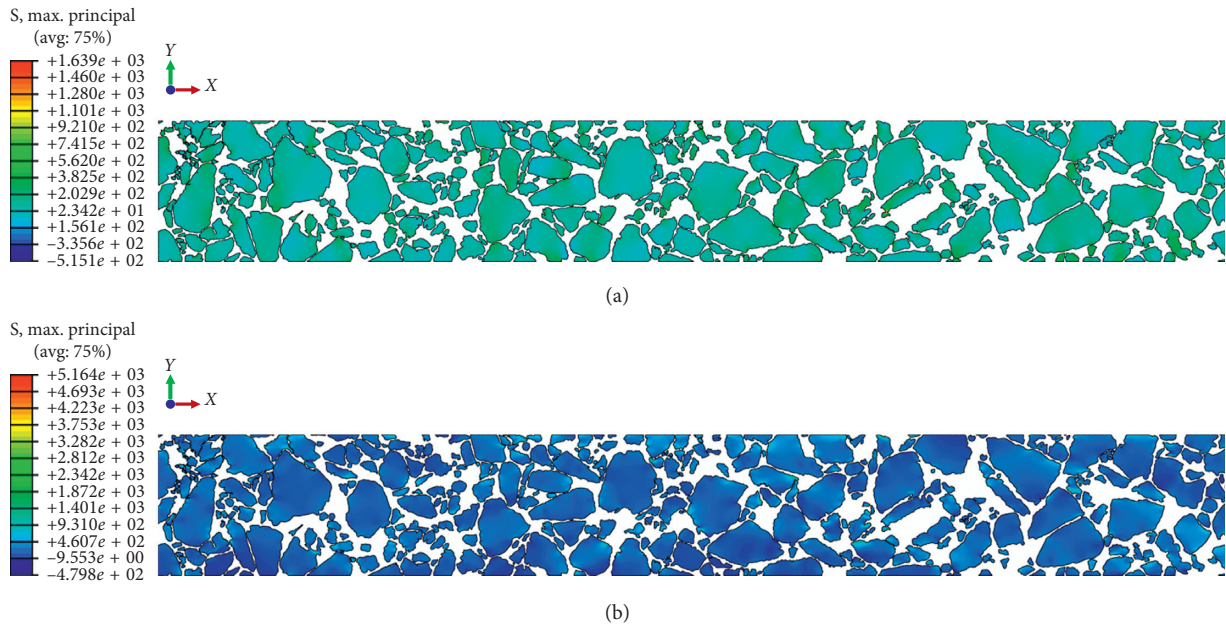


FIGURE 5: Matrix mixture stress cloud. (a) 20% air void, 0.2% expansion; (b) 20% air void, 0.2% contraction.

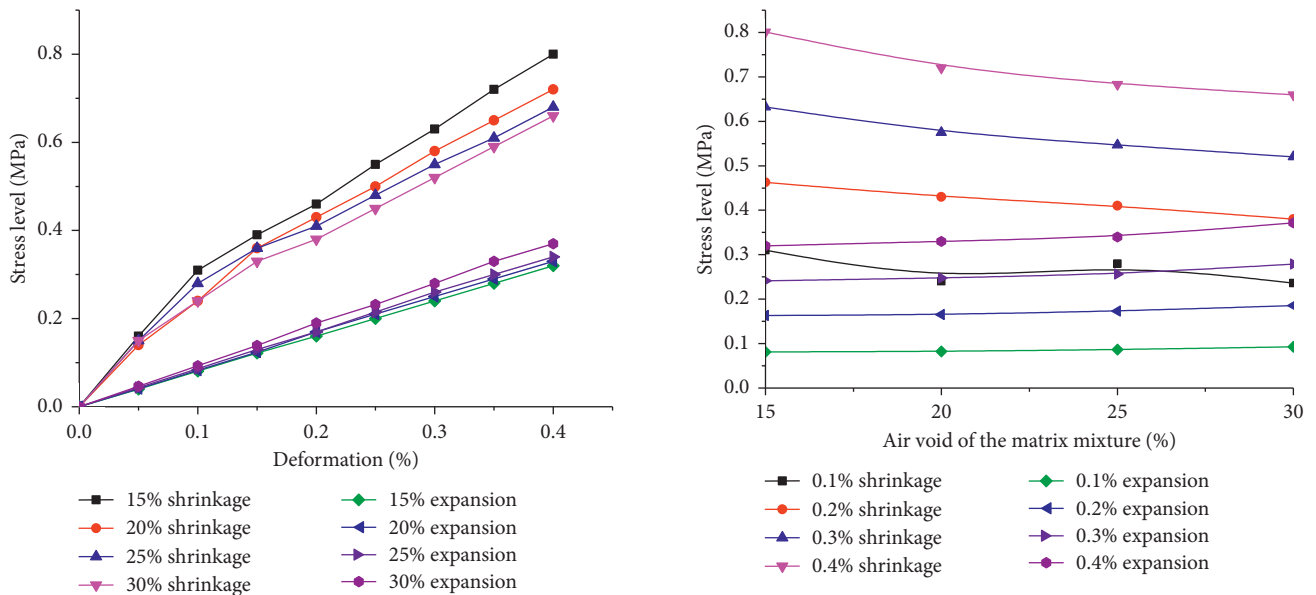


FIGURE 6: The relationship between internal stress of the matrix and deformation of cement mortar.

FIGURE 7: Relationship between air void and stress of the asphalt mixture matrix.

asphalt mixture matrix, whereas the stress growth rate is 1.3MPa/% for 30% air void of the asphalt mixture matrix. Thus, the lower the air void of the matrix mixture is, the more sensitive the stress generated by the contraction of the cement mortar becomes. It can be seen that an appropriate increase in the air void of the matrix, to a certain extent, can reduce the cracking caused by the contraction of cement mortar.

In contrast with the contraction of cement mortar, the larger the air void of the matrix mixture is, the higher the internal stress level under an expansion deformation

becomes. In addition, the internal stress produced by expansion deformation is much lower than that by contraction deformation. When the air void of the matrix is between 15% and 25%, the internal stress under the same deformation is basically the same. When the air void of the matrix asphalt mixture is more than 25%, the internal stress of the matrix mixture slowly increases. In general, an increase in the air void of the matrix has little effect on the internal stress growth caused by expansion deformation.

According to the analysis above, larger air void of matrix asphalt structure and less volumetric variation of cement mortar reduce the internal stress. In the actual

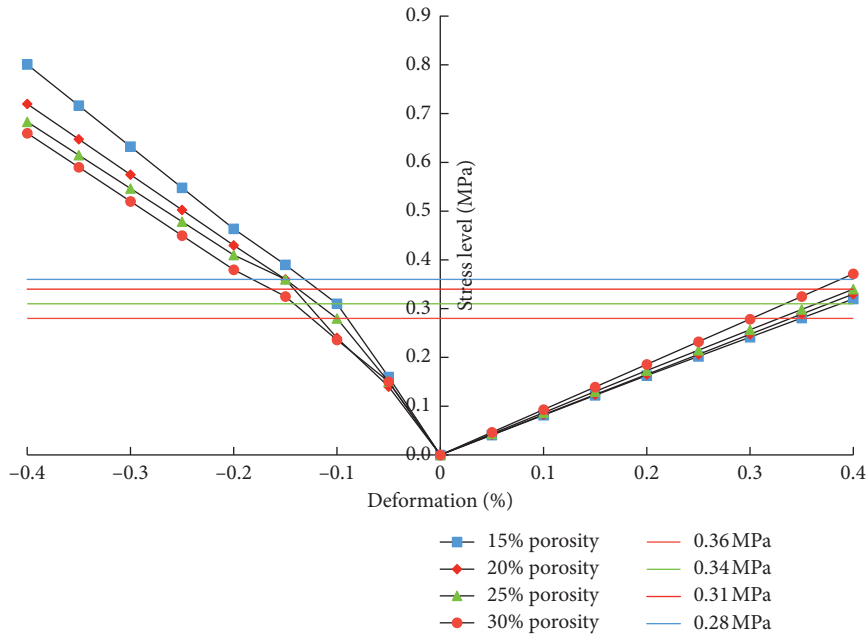


FIGURE 8: Relationship between stress and deformation of the matrix mixture.

project, after measuring the ultimate tensile strength of matrix asphalt structure with target air void, the cement mortar with suitable volume stability can be selected by the peak stress.

3.2. Strain Control Analysis of Cement Mortar. As a prerequisite for the anticracking design of semiflexible pavement materials, the contraction stress and expansion stress of cement mortar should be less than the ultimate tensile strength of the matrix asphalt mixture. Therefore, a threshold value of stress can be set to control the peak stress of cement mortar. As described in Table 7, the threshold value of the ultimate deformation of the cement mortar can be obtained by controlling the ultimate tensile strength of the matrix mixture. When the deformation is negative, it indicates a contraction deformation of the cement mortar, whereas a positive value indicates an expansion deformation.

The relationship between the stress curve caused by the contraction and expansion deformations of cement mortar under different air voids and the corresponding ultimate tensile strength is shown in Figure 8. The results calculated by the interpolation method show that when the air void of the matrix mixture is 15%, the maximum contraction of cement mortar should be less than 0.13%, and the maximum expansion should be less than 0.4%. When the air void of the matrix is 20%, the maximum contraction of cement mortar should be less than 0.14%, and the maximum expansion should be less than 0.4%. When the air void is 25%, the maximum contraction of cement mortar should be less than 0.12%, and the maximum expansion should be less than 0.38%. When the air void is 30%, the maximum contraction should be less than 0.12%, and the maximum expansion should be less than 0.31%.

Therefore, for the matrix and cement mortar used in this paper, the maximum allowable deformation values of cement mortar are summarized in Table 11.

According to the above analysis, this study proposes an anticracking design method of semiflexible pavement materials. Firstly, the ultimate tensile strength of matrix asphalt structure with target air void is measured, and the results are input into a mechanical model for numerical simulation to determine the maximum allowable strain of cement mortar. To avoid the cracking of semiflexible pavement, cement mortar whose maximum contraction strain and expansion strain are both below the maximum allowable strain is selected to alleviate the internal cracking concern of the semiflexible mixture.

4. Conclusions

This study proposed an anticracking design method of semiflexible pavement materials. The ultimate tensile strength of matrix asphalt structure with target air void was measured, and the results were input into a mechanical model for numerical simulation to determine the maximum allowable strain of cement mortar. Based on the laboratory test results and FEM simulation, the following findings were obtained:

- (1) Both contraction and expansion deformations of cement mortar produce tensile stress in the asphalt mixture matrix. The stress of cement mortar from contraction deformation is significantly higher than that from expansion deformation. The contraction deformation of cement mortar is the dominant factor causing internal stress in semiflexible pavement. In addition, the matrix mixture is more sensitive to the changes in stress when the less contraction deformation of the cement mortar occurs.

TABLE 11: The maximum allowable deformation values of cement mortar.

The air void of the matrix (%)	Maximum allowable contraction (%)	Maximum allowable expansion (%)
15	0.13	0.40
20	0.14	0.40
25	0.12	0.38
30	0.12	0.31

- (2) The expansion deformation of cement mortar shows a good linear relationship with the internal stress of the matrix, and the tensile stress produced by the expansion of cement mortar is much lower than that caused by contraction. In addition, the increase in air void of the matrix has little effect on the internal stress growth caused by expansion deformation.
- (3) Larger air void of matrix asphalt structure and less volumetric variation of cement mortar reduce the internal stress. For real projects, the ultimate tensile strength of the matrix with target air void can be measured and the peak stress can be used as the control index to select cement mortar with suitable volume stability.

This paper mainly puts forward the research method of semiflexible pavement internal crack resistance. As the deformation of asphalt matrix and cement mortar changes dynamically with temperature and time, and the variation trend is different, the relative deformation of cement mortar and asphalt matrix considered in this paper is not very accurate. In future research, the expansion strain and contraction strain-time curve of cement mortar and asphalt matrix will be further studied, and the expansion and contraction deformations of cement mortar and asphalt matrix will be simulated by the finite element method, and the stress change of semiflexible pavement internal structure will be accurately calculated.

Data Availability

No data were used to support this study.

Conflicts of Interest

The authors declare that there are no conflicts of interest regarding the publication of this paper.

Acknowledgments

The authors sincerely acknowledge the funding support from the National Natural Science Foundation of China (NSFC 51808228) and the Fundamental Research Funds for the Central Universities (2018MS92).

References

- [1] C. Pratelli, G. Betti, T. Giuffrè, and A. Marradi, "Preliminary in-situ evaluation of an innovative, semi-flexible pavement

wearing course mixture using fast falling weight deflectionometer," *Materials*, vol. 11, no. 4, p. 611, 2018.

- [2] G. Berardi and P. Di Mascio, "Le pavimentazioni aeroportuali in conglomerato bituminoso open grade intasato di Malta cementizia-open grade asphalt concrete filled with cement mortar for airport pavements," *Rassegna del Bitume*, vol. 61, pp. 29–36, 2009.
- [3] S. E. Zoorob, K. E. Hassan, and A. Setyawan, "Cold mix, cold laid semi-flexible Grouted Macadams mix design and properties," in *Proceedings of the Performance of Bituminous and Hydraulic Materials in Pavements*, CRC Press, Nottingham, UK, April 2002.
- [4] K. E. Hassan, A. Setyawan, and S. E. Zoorob, "Effect of cementitious grouts on the properties of semi-flexible bituminous pavements," in *Proceedings of the Performance of Bituminous and Hydraulic Materials in Pavements*, CRC Press, Nottingham, UK, April 2002.
- [5] D. V. Ramsamooj, J. Ramadan, and G. S. Lin, "Model prediction of rutting in asphalt concrete," *Journal of Transportation Engineering*, vol. 124, no. 5, pp. 448–456, 1998.
- [6] I. J. Huddleston, H. Zhou, and R. G. Hicks, "Evaluation of open-graded asphalt concrete mixtures used in Oregon," Transportation Research Record 1427TRB, National Research Council, Washington, DC, USA, 1993.
- [7] C. Huang, "Study on volume stability and crack resistance of semi-flexible pavement," M.S. thesis, Wuhan University of Technology, Wuhan, China, 2010.
- [8] W. Wang and K. Wu, "Study on crack resistance of semi-flexible pavement based on J-integral," *Highway*, vol. 61, no. 11, pp. 63–66, 2016.
- [9] C. Huang, J. P. Liu, J. X. Hong, and Z. F. Liu, "Improvement on the crack resistance property of semi-flexible pavement by cement-emulsified asphalt mortar," *Key Engineering Materials*, vol. 509, pp. 26–32, 2012.
- [10] Japan Association of Roads, *Explain for General Code of Asphalt Pavement Engineering*, Maruzen Co., Ltd., Tokyo, Japan, 1992.
- [11] D. Shen, J. Shen, J. Huang et al., "Study on thermal expansion coefficient of cement - based materials in early age and hardening stage," *Journal of Hydraulic Engineering*, vol. 43, no. 1, pp. 153–160, 2012.
- [12] S. Li, "Cement mortar contraction research," M.S. thesis, Nanjing University of Technology, Nanjing, China, 2004.
- [13] M. R. Islam and R. A. Tarefder, "Coefficients of thermal contraction and expansion of asphalt concrete in the laboratory," *Journal of Materials in Civil Engineering*, vol. 27, no. 11, article 04015020, 2015.
- [14] G. Lees, "The rational design of aggregate gradings for dense asphaltic compositions," in *Proceedings of Asphalt Paving Technologies*, pp. 60–90, Kansas City, MO, USA, 1970.
- [15] X. Cai, D. Wang, K. Wu, and G. Yang, "Design of anti-rutting asphalt mixture by simplified classification method," *Journal of Highway and Transportation Research and Development*, vol. 33, no. 3, pp. 13–17, 2016.
- [16] A. Epps, T. Ahmed, D. C. Little et al., "Performance assessment with the MMLS3 at WesTrack," *Asphalt Paving Technology: Association of Asphalt Paving Technologists Proceedings of the Technical Sessions*, vol. 70, pp. 509–542, 2002.
- [17] R. B. Mallick and J. A. Bergendahl, *An Evaluation of Rutting and Shoving Potential of, and Chloride Diffusion through Hot Mix Asphalt (HMA) with Rosphalt*, Civil and Environmental

Engineering Department, Worcester Polytechnic Institute,
Worcester, MA, USA, 2004.

- [18] L. Shao, S. Chi, and Y. Jia, "Mesoscopic simulation of large triaxial test of rockfill material," *Rock and Soil Mechanics*, vol. 30, no. S1, pp. 239–243, 2009.
- [19] X. Shao, M. Shao, Y. Bi et al., "Asphalt mixture Poisson's ratio test method," *Journal of Tongji University (Natural Science Edition)*, vol. 34, no. 11, pp. 1470–1474, 2006.

Research Article

Strength Characteristics and the Reaction Mechanism of Stone Powder Cement Tailings Backfill

Jianhua Hu ¹, Qifan Ren ², Quan Jiang,² Rugao Gao ¹, Long Zhang,²
and Zhouquan Luo¹

¹Professor, School of Resources and Safety Engineering, Central South University, Changsha, Hunan 410081, China

²Research Assistant, School of Resources and Safety Engineering, Central South University, Changsha, Hunan 410081, China

Correspondence should be addressed to Qifan Ren; qifanren@csu.edu.cn

Received 14 March 2018; Accepted 17 October 2018; Published 13 November 2018

Guest Editor: Syed W. Haider

Copyright © 2018 Jianhua Hu et al. This is an open access article distributed under the Creative Commons Attribution License, which permits unrestricted use, distribution, and reproduction in any medium, provided the original work is properly cited.

Stone powder cement (SPC) is widely used as a novel cement substitute material in concrete for its good gelling performance and low cost. In order to reduce the backfilling cost and assess the potential of SPC backfilling materials, a series of experiments were conducted to analyze the strength and hydration reaction mechanism of stone powder cement tailings backfill (SPCTB). The analysis was based on SPC and tailings, which were used as the gelling agent and the aggregate, respectively. The results showed that the strength of the backfill was greatly reduced at an early stage and slightly reduced in the final stages. The stone powder content was less than 15%, which met the requirement of mining procedure. The addition of stone powder reduced the content of adsorbed water and capillary water in the early stages, while it increased in the middle stages. The SiO₂ contained in stone powder reacted with the hydration products at later stages, which is the reason why the growth of strength is rapid between the groups with the addition of stone powder. The addition of stone powder improved the microstructure of backfill and produced a denser three-dimensional (3D) network structure; however, the plane porosities of Groups A and B gradually increased with the increase in the content of stone powder. The cement powder mixed appropriately with the stone powder could meet the strength requirement and reduce the cost of backfilling materials.

1. Introduction

When manufacturing crushed aggregate, the process creates a stone powder, which could be collected and used to produce SPC. The majority of particles of stone powder range from 1 μm to 100 μm, making them difficult to handle, transport, and recycle. The quantity of stone powder produced from crushed aggregate factories in China is approximately 10 million tons per year, most of which is dumped in soil. The disposal of stone powder is a major environmental problem, and therefore, there is a great interest to find solutions for its safe utilization [1]. Portland cement is used as a gelling agent in traditional backfill in mines, whereas the high cost of cement needs a suitable and sustainable low-cost substitute. In China, most of the mines are in mountainous areas surrounded by quarries where the stone powder is thrown out every year and causes a lot of

environmental pollution [2]. However, it can be collected and utilized in backfill. Figure 1 shows a quarry.

Al-Kheetan et al. [3, 4] introduced crystalline material along with a curing compound in fresh concrete to protect and extend its service life and developed hydrophobic concrete by adding dual-crystalline admixture during the mixing stage. Choi et al. [1] examined the microstructure and strength of alkali-activated systems using stone powder sludge, which had some water content as a replacement material in alkali-activated mixtures that strengthened the concrete's ability to withstand extreme variable temperatures and loads. Compared to ordinary concrete, other properties, including early gain in compressive strength, durability, and high acid and fire resistance, make it an appealing construction material. Compressive strengths of four different natural pozzolans with the replacement level of 10–25% at various ages were studied [5]. The results



FIGURE 1: Quarry around the mine.

showed that, with the increase in natural pozzolans content, natural pozzolans replacements reduced the compressive strengths of concrete due to reduction in cement content in the mixture. However the compressive strength increases with age. Several investigations [6, 7] showed that the compressive strength of mortars with different cements and incorporating 10% silica fume was about 30–50% higher than that of plain cements after 28 days. The strength of silica fume mortars depends on the water to binder ratio of the mixture. The compressive strength of mortars containing 10% silica fume decreases with the decrease in the fineness of parent Portland cement. However, it is always higher than the strength of plain Portland cement after 28 days. In addition, a previous study [7] showed the reduction of chloride penetration of silica fume mortars and concretes in rapid chloride penetration tests (RCPTS). However, there are a few materials used in mine backfilling, and the research on these materials is limited.

The results showed that the stone powder is not completely inert diluent for the cement. A chemical reaction between CaCO_3 , C_3A , and C_4AF generates $\text{C}_3\text{A}\cdot\text{X}\cdot\text{CaCO}_3\cdot 11\text{H}_2\text{O}$ and ettringite [8]. As the center of hydration process, stone powder can increase the early rate and degree of hydration [9]. In addition, SPC results in a smaller consumption of water than that of the cement of the same standard; when comparing the bleeding rate of SPC and ordinary cement, Albeck and Sutej [10–12] found that the bleeding rate of SPC is always less than that of the ordinary cement, and it also stops bleeding more quickly. According to El-Didamony et al. [13], the set time of cement decreases with the increase in the stone powder content, which means that the SPC has a high early strength. Consequently, as substituted minerals are added in the cement paste, stone powder can promote the hydration of cement, induce the crystallization of cement hydrate products, accelerate the hydration of cement, and participate in the hydration reactions [14]. Previous studies have found that the powder of silicate minerals could be used as sustainable replacements of cement. Abd Elmoaty et al. [15] used granite dust to replace cement with 5–15%, which could improve concrete's compressive strength and tensile strength. Kannan et al. [16] reported that high-performance concrete can be produced

with significant replacement of between 20% and 40% of Portland cement with ceramic waste powder. Berriel et al. and Akhlaghi et al. [17, 18] showed that a combination of calcined clay, limestone, and gypsum, used as the substitution of Portland cement for up to 50%, can provide economic benefits while maintaining the mechanical properties of the cement. However, if the stone powder content exceeds a certain value, the water demand of the cement paste will increase, and the fluidity will reduce. Therefore, in the current work, the possibility of reasonably using waste stone powder as a partial replacement for cement has been explored. The comprehensive use of stone powder having the same main ingredients as the mother rock conforms to the concept of green building materials and is conducive to sustainable developments in the construction industry [19, 20].

Based on the abovementioned properties of SPC, the experimental study of stone powder cement tailings backfill (SPCTB) can be developed. In this study, the physico-chemical properties and the particle-size distribution of stone powder and tailings were analyzed using X-ray fluorescence (XRF) and laser particle size analyzer (LPSA). In addition, the strength characteristics of backfill with different ratios were analyzed to evaluate the feasibility of SPC used as the cementitious material. The microscopic morphology, composition, water evolution, and pore changes of SPCTB at different ages were examined, and the reaction mechanism of SPCTB was studied using X-ray diffraction spectroscopy (XRD), scanning electron microscopy (SEM), and nuclear magnetic resonance (NMR). The use of SPC as the cementitious material not only reduces the backfilling costs for mountainous mines but also benefits the construction of “green mines” and achieves no-waste mining.

2. Experimental

2.1. Tailings, Stone Powder, and Cement. Tailings were obtained from Gaofeng mine in Guangxi Province, China, and were divided into two types (tailings A and tailings B). The types of tailings were produced by different beneficiation processes. The stone powder was obtained from the



(a) (b) (c)

FIGURE 2: Physical appearance of (a) tailings A, (b) tailings B, and (c) stone powder.

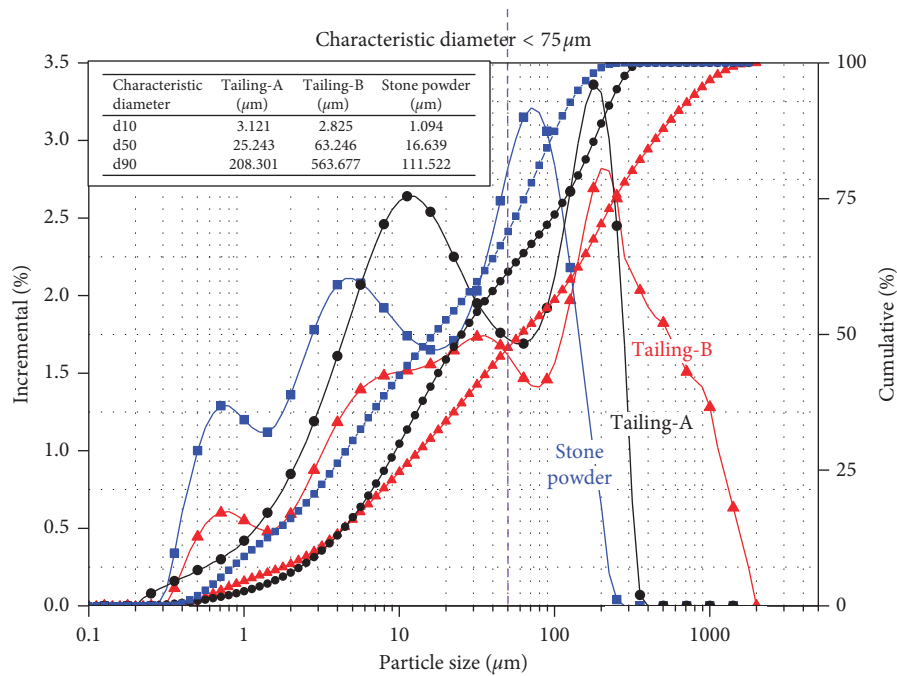


FIGURE 3: Particle-size distributions of tailings and stone powder (including incremental and cumulative values).

quarry around the Gaofeng mine (Figure 2). The particle-size distributions of the tailings and the stone powder were analyzed using a mastersizer 2000 obtained from Malvern Instruments Inc., UK (Figure 3). The characteristic median diameters d_{50} of tailings A and tailings B were $25.243 \mu\text{m}$ and $31.168 \mu\text{m}$, respectively, based on which the tailings could be considered as ultrafine tailings. The median diameter d_{50} of the stone powder was $16.639 \mu\text{m}$ due to which it belonged to the category of ultrafine particles. The nonuniformity coefficient (Cu) and the curvature coefficient (Cc) of tailings A and tailings B were (14.56, 0.72) and (40.02, 0.71), respectively, indicating that the gradation of tailings A was good, though the tailings B had a wider range.

The apparent density, the bulk density, and the contents of surface water of tailings and stone powder were analyzed

according to the standard GB/T 50080-2016 “Standard Test Method for Performance of Ordinary Concrete Mixtures.” The corresponding results are presented in Table 1. The elemental and chemical compositions of tailings and stone powder were obtained using XRF and XRD, and the respective results are provided in Table 2 and Figure 4. According to the chemical composition index [21], the alkaline coefficients of tailings A, tailings B, and stone powders were 3.21, 0.53, and 1.53, respectively. These results showed that tailings A belonged to the alkaline tailings and tailings B belonged to the acid tailings.

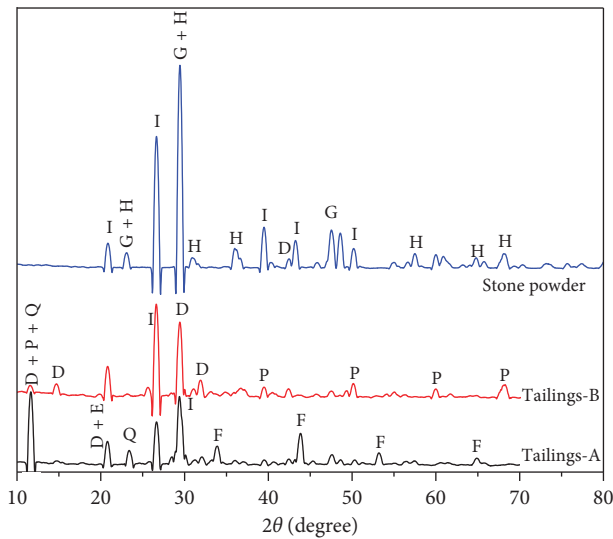
The cement from the Xinxing cement factory in Changsha, China, meets the national standard GB 175-2007 “Common Portland Cement.” The mineral composition of the cement is provided in Table 2. Furthermore, tap water was used for the experiments.

TABLE 1: Physical properties of the tailings and the stone powder.

Class	Apparent density	Packing density	Surface moisture content
Tailings A	3.49	1.24	0.128
Tailings B	2.77	1.17	0.135
Stone powder	2.89	0.99	0.162

TABLE 2: Elemental composition of the tailings and the stone powder along with the chemical composition of Portland cement (%).

Elemental composition	O	Fe	S	Ca	Si	Mg	Al
Tailings A	34.699	23.098	15.857	14.025	4.476	2.117	1.113
Tailings B	44.376	12.662	8.877	9.091	16.24	0.403	3.057
Stone powder	58.301	0.942	0.298	23.279	14.901	0.471	1.273
Chemical composition	3CaO·SiO ₂		2CaO·SiO ₂		3CaO·Al ₂ O ₃		4CaO·Al ₂ O ₃ ·Fe ₂ O ₃
Portland cement	52.8		20.7		11.5		8.8



D—gypsum
 E—brushite
 F—pyrrhotite
 G—magnesium calcite
 H—calcite
 I—SiO₂
 P—silicon sulfide
 Q—hydrotalcite

FIGURE 4: XRD patterns of the tailings and stone powder.

2.2. Specimen Preparation. In this work, SPC and the tailings were used as the cementitious material and the aggregate, respectively. The ratios between the two materials, which were tested in this work, are presented in Table 3. The SPC tailings ratio (SPCTR), the mass fractions, and the stone powder dosage of Group A using tailings A and those of Group B using tailings B were the same.

The SPCTB components, including stone powder, cement, tailings, and water, were weighted using a high-precision electronic scale having an accuracy of 0.01 g. Mixtures with 10 different formulations (mixing ratios) were mixed in the laboratory blenders for 5 min to ensure homogeneity. Then, the mixtures were casted in plastic cubical molds with the side length of 7.07 cm. A total of 180 sextuplicate specimens (three for UCT and three for NMR) were prepared (Figure 5). The specimens were cured in a humidity chamber at 20°C and 95% relative humidity for different

TABLE 3: Backfilling slurry of stone powder cement tailings ratio (SPCTR), mass fractions, stone powder content, and cement content.

Group	SPCTR	Mass fractions (%)	Stone powder content ^a (%)	Cement content (%)
A/B 1			0	100
A/B 2			10	90
A/B 3	1:4	70	15	85
A/B 4			20	80
A/B 5			100	0

^aThe proportion of stone powder in SPC.

durations (3, 7, and 28 days) until the prescribed age reached. After that, the samples were analyzed for their physicochemical properties.

2.3. Uniaxial Compressive Tests. The uniaxial compressive strength (UCS) at a given time is the most important parameter to evaluate the mechanical performance of SPC. Until the predetermined curing time, the SPCTB specimens were analyzed for USC using a computer-controlled universal pressure mechanical device (WDW-2000). The tests were performed following the procedure given in the standard *ASTM D2166/D2166M-16*. The specimens were loaded under a constant vertical displacement rate of 1 mm/min. To reduce the error, the tests were conducted in triplicates, and the average values were used to determine the UCS of SPCTB (accurate to 0.1 MPa) (Figure 6). The individual strengths of three specimens, molded with the same characteristics, should not deviate more than 15% from the mean strength.

2.4. NMR Analysis. During the hardening of backfilling slurry, the water, pore distribution, and strength of the backfilling slurry would change with age, and backfill is formed after hardening. The UCS of the backfill is closely related to the water content in different binding states. The NMR, performed using 1 H relaxation signal, can be used to

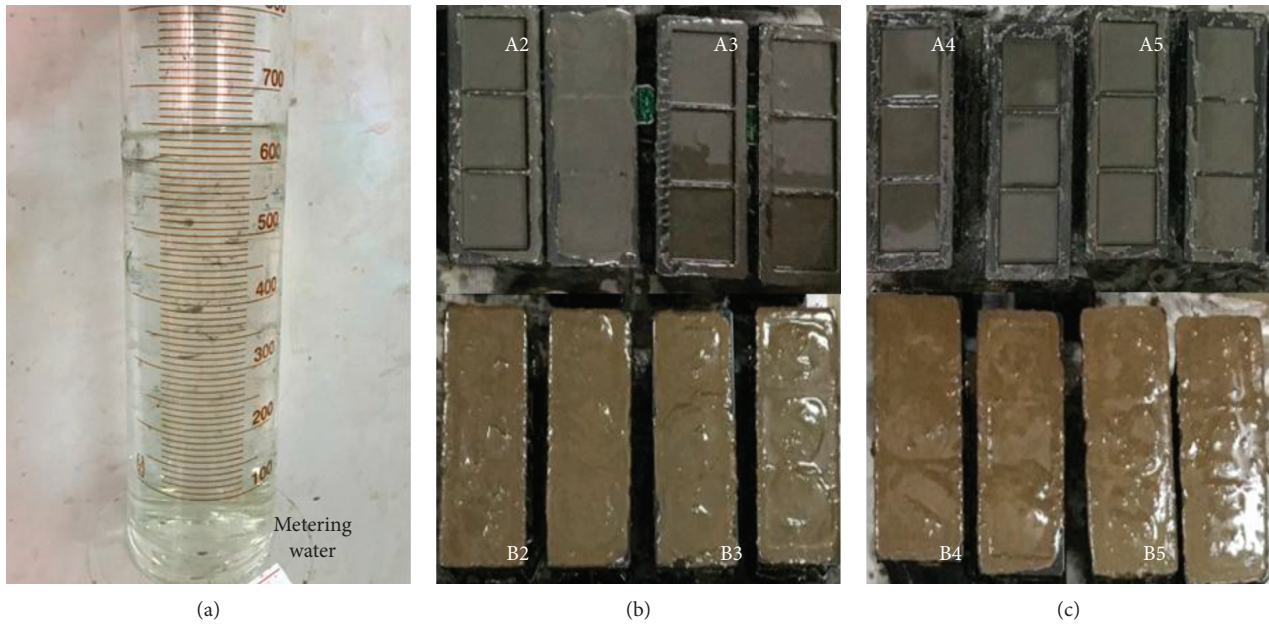


FIGURE 5: Production process for the backfill (including metering water and backfilling paste).



FIGURE 6: UCT and destruction process of a 28-day SPCTB specimen containing 10% stone powder.

measure the porous content in the slurry and the backfill. The T2 distribution can be used to analyze the variation in pore distribution, which has the advantages of non-destructive detection and good repeatability [22].

The NMR tests used the MiniMR-60 magnetic resonance imaging (MRI) analysis system, which was manufactured by Shanghai Newmai Co. Ltd., China. The main magnetic field of the device was 0.51 T, and the H proton resonance frequency was 21.7 MHz.

The analysis was performed in triplicates, and the average value for further analysis was calculated. After the SPCTB specimens reached the specified age (3 d, 7 d and 28 d), the SPCTB specimens were taken out from the constant temperature and constant humidity curing box and subjected to NMR relaxation measurements. During the tests, the SPCTB specimens were wrapped in a cling film to reduce the impact of water evaporation.

2.5. SEM and XRD Analyses. At the curing times of 3 d, 7 d, and 28 d, the SPCTB specimen of 1 mm² area was taken from the core of the specimen and dehydrated with absolute ethanol to stop the hydration. The specimen was dried at 45°C to constant weight and analyzed using XRD and SEM analyses. The experiments used a Siemens D500 X-ray diffractometer and a TESCAN MIRA3 field-emission scanning electron microscope for these analyses.

3. Strength Characteristics

The (statistical) average strength of each group of specimens and part of the stress-strain curves of these specimens are shown in Figures 7 and 8, respectively.

- (1) At the curing time of 3 days (d), the UCS of Group A was 0.4-0.5 MPa, while that of the Group B was

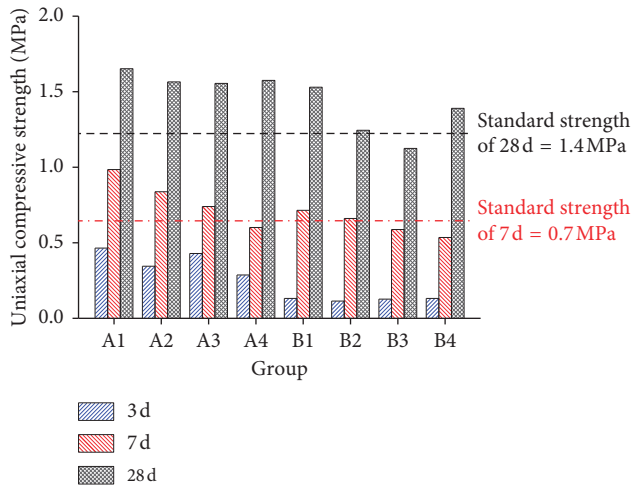


FIGURE 7: Uniaxial compressive strength of each group of specimens at the curing times of 3 d, 7 d, and 28 d (according to the mine information 7 d and 28 d compressive strengths need to reach 0.7 MPa and 1.4 MPa, respectively. A5 and B5 groups are not analyzed for compressive strength).

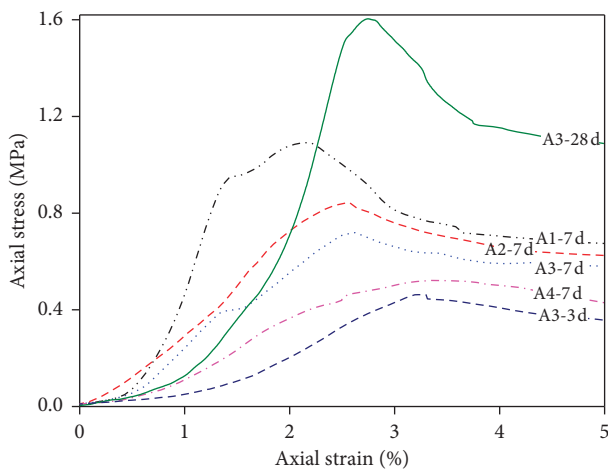


FIGURE 8: Stress-strain curves at the curing time of 7 d of Group A and at the curing times of 3 d and 28 d of Group A3.

0.2 MPa. At the curing time of 7 d, the USC of Group A was 0.6–1.0 MPa, whereas that of Group B was 0.6–0.7 MPa, which gradually decreased with the increase in the content of stone powder. At the curing time of 28 d, the USC of Group A was 1.6–1.7 MPa, while the USC of SPCTB specimens mixed with the stone powder was basically the same as 1.6 MPa. The USC of Group B was 1.2–1.6 MPa, which tended to decrease with the increase in stone powder's USC. In addition, the USC suddenly increased to 1.5 MPa at the stone powder content of 20%.

- (2) The minimum requirements for the backfill strength of mine stopes at the curing times of 3 d, 7 d, and 28 d were 0.25 MPa, 0.7 MPa, and 1.4 MPa, respectively. Group A met the 3 d backfill strength requirements, while the strength's value for Group B was too low. The content of stone powder in Group A was varied to

values of 0%, 10%, and 15%, while Group B1, which was not doped with stone powder, satisfied the requirements of 7 d backfill strength. While for the curing time of 28 d, only Groups B3 and B4 did not meet the backfill strength requirements. Furthermore, Groups A1, A2, and A3 met the requirements of the backfill strength with less than 15% of the stone powder content. The backfill strength of groups that met the requirements had a certain safety factor, which could be changed according to the actual conditions of the stopes and was based on the minimum requirements of the mine. The ratio of the backfill material and the content of the stone powder were adaptable to the environmental parameters of the stopes, which ensured that safe and efficient recovery of backfill material ratio parameters can be selected for the mine.

- (3) The intensity ratio after the curing times of 3 d, 7 d, and 28 d for Group A gradually changed from 1:2:4 to 1:2:6 with the increase in the content of stone powder. After the stone powder was mixed, the UCS of the SPCTB specimens was reduced, which increased rapidly after 7 days. Additionally, the more the powder added, the faster the increase in the USC value.
- (4) With the increase in the content of stone powder, the peak strength and the elastic modulus of the specimen gradually decreased. In addition, the peak strength appeared under the condition of larger strain. The strength and the elastic modulus of the specimens after the curing time of 3 d were low, and the plastic deformation of the specimens was large. The elastic modulus of Group A3 after the curing time of 28 d was lower than that of Group A1 after 7 d. The increase in the content of stone powder reduced the elastic modulus of the backfill. The residual strengths of the six groups of backfill specimens in the postfailure were large and decreased slowly and gradually to stable values, which ensured that the backfill had sufficient strength to keep the backfill and stopes stable.

4. Results and Discussion

4.1. Various States of Bound Water. With the hydration of backfilling slurry, a part of the water in the slurry did not participate in the hydration reaction, which was either sequestered or evaporated into the air. The rest remained in the backfill. Water in the hydration backfilling slurry was divided into free water, capillary water, adsorbed water (physical adsorption through hydrogen bonding), interlayer water, and chemically bound water. The loss of water gradually increased as the fluidity of the water gradually deteriorated.

After the NMR sampling, the T2 distribution of the slurry, which was obtained by T2 inversion software, is shown in Figures 9(a) and 10(a). In these figures, the horizontal axis is the relaxation time T2, while the vertical axis is the signal intensity. The peaks from left to right are defined as Peak 1, Peak 2, and Peak 3. Previous relevant studies have shown that different bound states have different T2

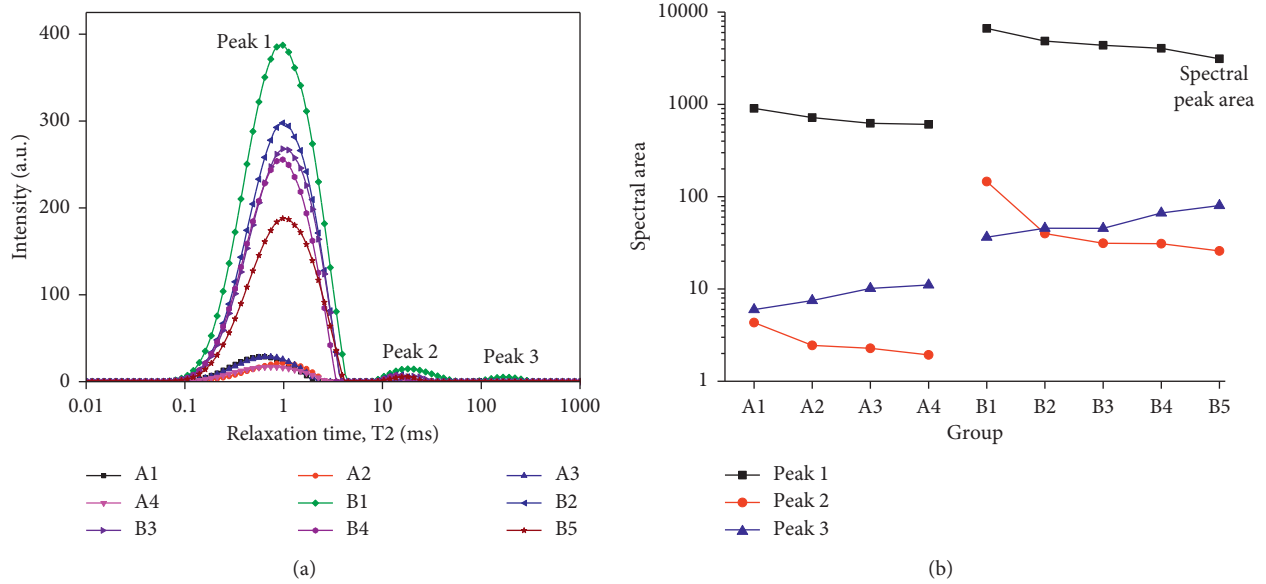


FIGURE 9: (a) NMR T2 spectrum distribution and (b) areas of Peak 1, Peak 2, and Peak 3 after the curing time of 3 d.

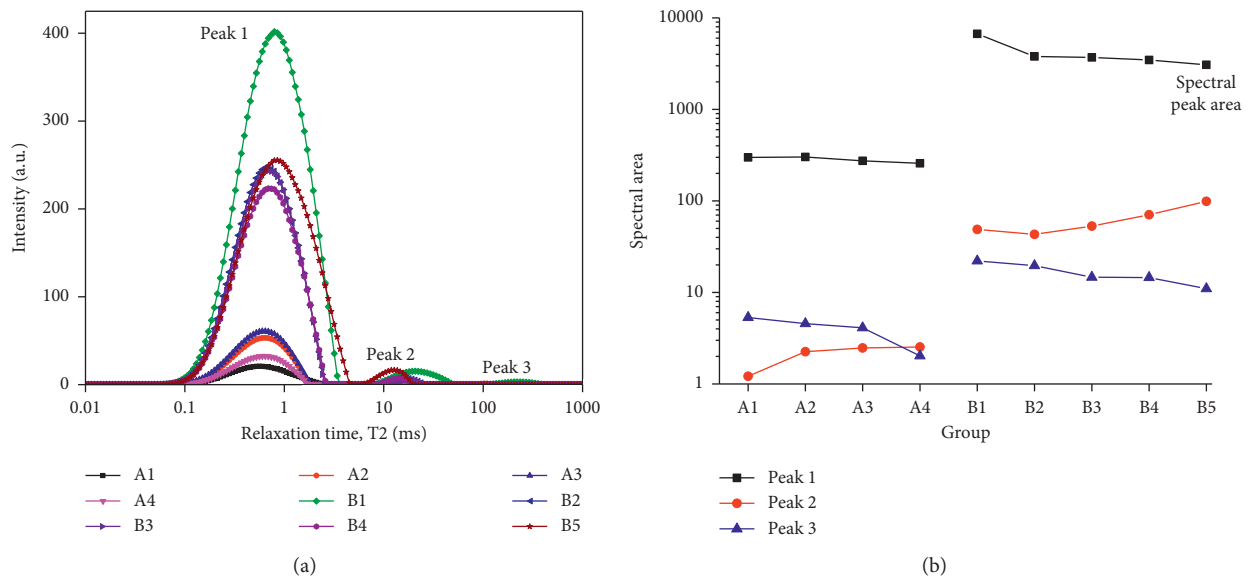


FIGURE 10: (a) NMR T2 spectrum distribution and (b) areas of Peak 1, Peak 2, and Peak 3 after the curing time of 7 d.

distributions of water. Each peak represents a particular bound state of water. The tighter the water bound is, the worse mobility the water has and the shorter the relaxation time T2 is [23–25]. Since the time of relaxation of chemisorbed water in the slurry and interlaminar water is short and the Carr–Purcell–Meiboom–Gill (CPMG) experiment cannot acquire the NMR signal, Peak 1 could be considered as the relaxation signal generated by the adsorbed water. Peak 2 was generated by the capillary water, and Peak 3 was generated by the free water. The relaxation time represented the various states of bound water, whereas the signal intensity represented the content of water and the spectral area represented the content of water of the same type.

(1) The relaxation times of Peak 1 of Groups A and B were nearly the same, followed by those of Peak 2 and Peak 3. In the T2 spectrum, the amplitudes, the signal peak intensities, and the peak areas of Peak 1 and Peak 2 in Group B were larger than those in Group A, which indicated that there were more adsorbed water and capillary water in Group B. With the increase in the curing time, the relaxation time did not change significantly, and the peak amplitude decreased, indicating that the contents of various types of water in the backfill specimen decreased with the increase in curing time. In Groups A and B, the proportion of Peak 1 was more than 97%,

indicating that the majority of adsorbed water was contained in the backfill specimen.

- (2) After the curing time of 3 d, the contents of adsorbed water and capillary water in the backfill specimen gradually decreased with the increase in the content of stone powder, while the content of free water increased. Under the same proportioning parameters, the content of bound water in Group B exceeded that in Group A, which indicated that different tailings had some influence on the change in water content in the backfill specimen.
- (3) Since some free water adsorbed on the stone powder particles (SPPs) after 3 d, which caused the decrease in capillary water and the content of adsorbed water in the system, there was no medium for hydration reaction and the rate of hydration reaction was reduced. The adsorbed water and the free water in the backfill specimen decreased with the increase in the content of stone powder, whereas the content of capillary water increased as well. However, with the hydration reaction going on, the free water adsorbed on SPP gradually entered the pores and became the medium of hydration reaction. This was also the reason why the strength of SPCTB increased significantly in the later stage of the addition of stone powder.

The three peak relaxation time ranges and the corresponding water categories are provided in Table 4. Each group NMR T2 spectrum distribution and the peak areas after the curing times of 3 d and 7 d are shown in Figures 9 and 10.

4.2. Analysis of the Pore Structure. The microstructure of the cross section of the specimen with different proportions after 28 d was obtained using SEM with the magnification of 5000 times. Figures 11(a) and 11(b) show the two micromorphologies of Groups A4 and B4. The results show that the gelled structure was fairly compact, though there were some pores around the particles. As can be seen, the structural stability was good when the particles were densely packed. The cementing mesh structure was compact, and the pores were small. The gray areas in SEM images were small, based on which the variation in plane porosity in different proportions can be observed [26, 27].

The images were binarized to ensure the preciseness of the pore results. The process is also known as the threshold segmentation. In view of the differences between the grayscale distribution and the values of the pixels of the particles, the cementing structure, and the pores, the pores in the image could be calculated using the binarized image. Assuming that the size of the SEM image was $M \times N$, $f(x)$ represented the gray area of the pixel located in the line $(x - 1)$ and column $(y - 1)$ of the image. The principle of binarization of the SEM image is given as follows:

$$f(x, y) = \begin{cases} 0, & f(x, y) < T, \\ 1, & f(x, y) > T, \end{cases} \quad (1)$$

where T represents the threshold grayscale. The SEM image can be binarized and converted to a black-and-white image,

TABLE 4: Relaxation time range of Peak 1, Peak 2, and Peak 3 and the corresponding bound state water.

Peak	Peak 1	Peak 2	Peak 3
Relaxation time range, T2 (ms)	0.3~3	7~60	78~310
Bound-state water	Adsorbed water	Capillary water	Free water

which is represented by a matrix of black-and-white pixels, in which 0 is the white pixel and 1 is the black pixel, and represents the pores and particles, respectively. With the help of Image-Pro Plus software, and for the threshold of 35, the SEM image of every group was processed (Figures 11(c) and 11(d)). The number and the area of pores contained within each group were calculated, and the plane porosity was determined. Each image consisted of four sets of data in four different positions to avoid any accidental error. The plane porosities of Groups A and B were linearly fitted and are shown in Figure 12.

- (1) Fitting curves of Groups A and B are represented by the equations: $Y = 0.1594X + 2.033$ and $Y = 0.8894X + 8.178$, respectively. It can be seen that the plane porosities of Groups A and B gradually increased with the increase in the content of stone powder, which led to the decrease in the intensity of the SPCTB specimen.
- (2) For the same ratio, the plane porosity of Group B was larger than that of the Group A. Because of this, not only the stone powder but also the nature of tailings will have an effect on the change in pores. The plane porosity of Group B increased faster, indicating that the addition of stone powder exhibited a greater influence on the plane porosity of SPCTB made up of tailings B.

4.3. Analysis of the Hydration Products. The results for the component analysis (done using XRD) are shown in Figure 13. The figure shows the hydration products of backfill specimens after different curing times. Based upon the results, the following conclusions can be drawn:

- (1) There was no hydration product in the backfill in the absence of cement, indicating that the stone powder was in an inert state, and therefore, the hydration reaction did not occur. Gypsum existed throughout the hydration process, while in CTB and SPCTB, gypsum almost disappeared after the curing time of 28 d, indicating that the gypsum in tailings and the cement were involved in the hydration reaction.
- (2) Some C-S-H gel dispersions and hydroxide diffraction peaks appeared in the SPCTB and CTB after the curing time of 3 d, though they were not very obvious. With the increase in the hydration time, some dispersive peaks with low intensity and discrete diffraction angles appeared after the curing time of 28 days. These were ascribed to C-S-H dispersion. At the same time, there was an increase in the diffraction

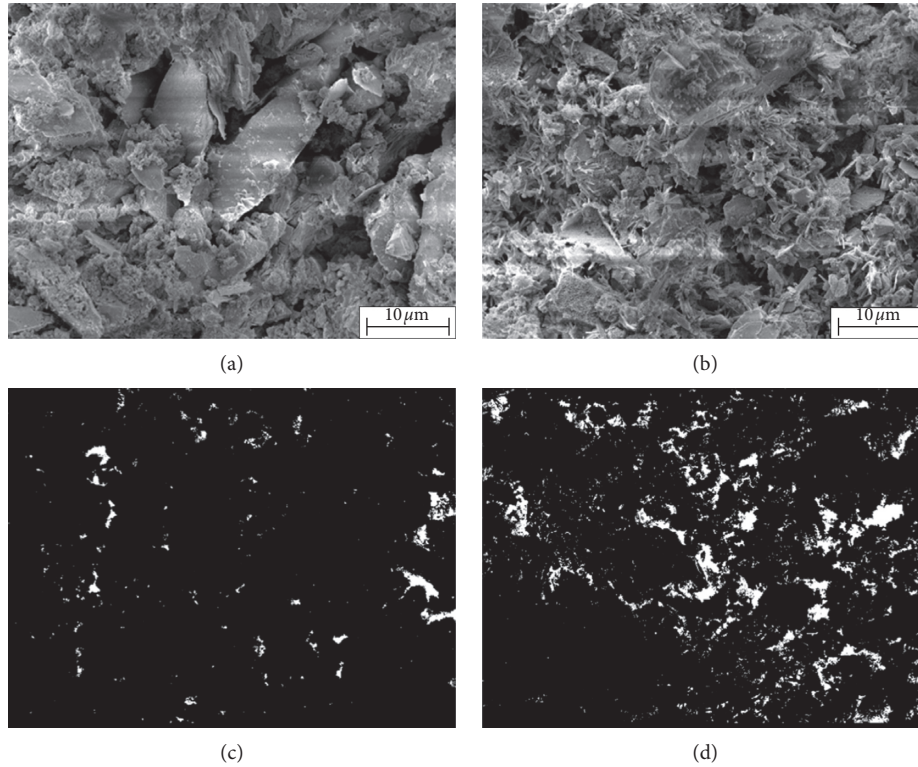


FIGURE 11: Microtopography and its binarized image; (a) magnified SEM image of Group A4; (b) magnified SEM image of Group B4; (c) Group A4 after binarization; (d) Group B4 after binarization.

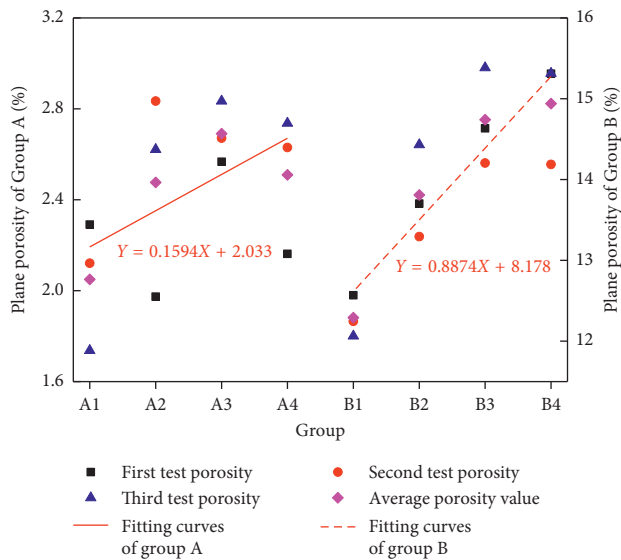


FIGURE 12: Plane porosity of each group and the fitting curves of the plane porosity of Groups A and B after the curing time of 28 d.

peak of the hydroxide, which indicated that the hydration reaction continued with the increase in curing time. AFt and some AFm in hydration products after the curing time of 3 d gradually decreased after 7 d and 28 d, which indicated that the hydration products at the early stage were mainly AFt, while at the later stage, they were the C-S-H gel.

(3) Comparing Figure 13(a) with Figure 13(b), it can be seen that the intensities of AFt and AFm diffraction peaks in SPCTB were weaker at 3 d, while AFt was the main reason for the early strength of backfill. Therefore, the early strength of SPCTB would be lower. At 28 d, Ca(OH)₂ diffraction peaks were weaker and C-S-H gel dispersion peaks were basically the same, indicating that the stone powder consumed Ca(OH)₂ to generate C-S-H gel after the hydration reaction, which was more stable than AFt. This ensured the poststrength and volume stability of SPCTB.

4.4. Analysis of the Micromorphology. Figure 14 shows the microstructural and micromorphology features of different cementitious materials at different curing times. Based upon the results, the following conclusions are drawn.

(1) For the curing time of 7 d, a large amount of hydration products, including a large amount of acicular AFt crystals, some amorphous C-S-H gel, some stone powder, and tailings particles were formed in the CTB and SPCTB. Acicular AFt crystals grew on the surface and in the pores of the particles, which developed into a three-dimensional (3D) network structure that was covered with SPP and tailings particles, having some early strength. AFt of the SPCTB acicular crystal grew sparser, though the microstructure was more compact than the CTB. This was due to the reason that the

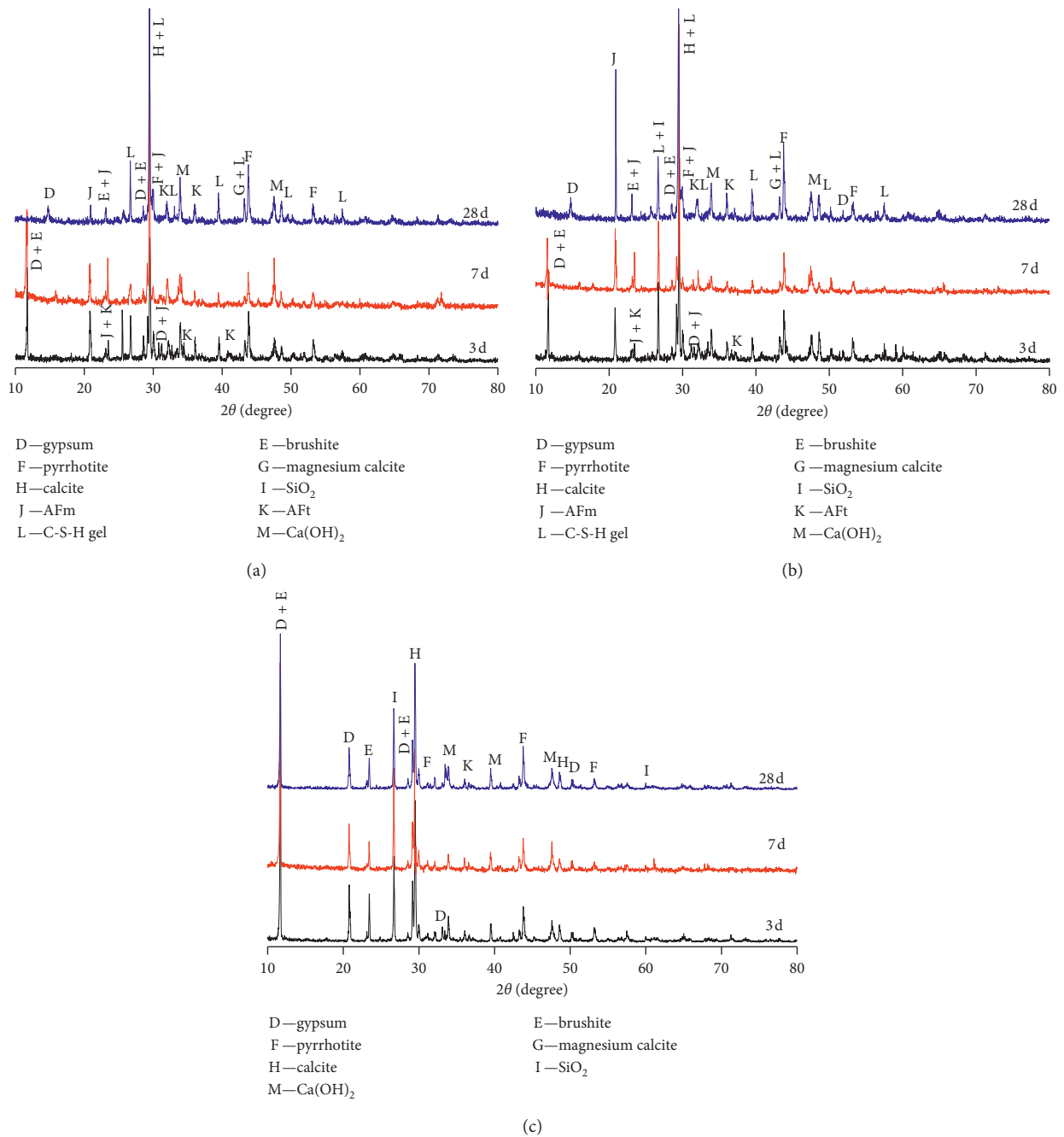


FIGURE 13: XRD patterns of the hydration products; (a) cement tailings backfill (CTB); (b) stone powder cement tailings backfill; (c) stone powder tailings backfill (SPTB). AFt represents ettringite; AFm represents monosulfate hydrate.

shape of SPP can fill the pores formed by the rod-shaped tailings particles.

- (2) For the curing time of 28 d, the AFt crystals of acicular structure almost disappeared. The amorphous C-S-H gel grew on the surface of tailing particles and closely combined with it. Compared with the results for the curing time of 7 d, the microstructure was more compact. The strength of backfill and the other aspects were improved for amorphous and rod-like C-S-H gel structure, which grew in the original pores and was tightly combined with the tailings particles. The SPP

became obscure, while the smooth surface became uneven, indicating that the stone powder reacted with the hydration products to generate secondary products. The growth of a rod-like structure in the pores and the overall absence of obvious pores indicated that the microstructure was basically similar to that of the CTB.

4.5. Reaction Mechanism of SPC in Backfill. According to the different times and the characteristics of hydration between the SPCTB and CTB, the hydration process of backfilling material system can be divided into following four stages:

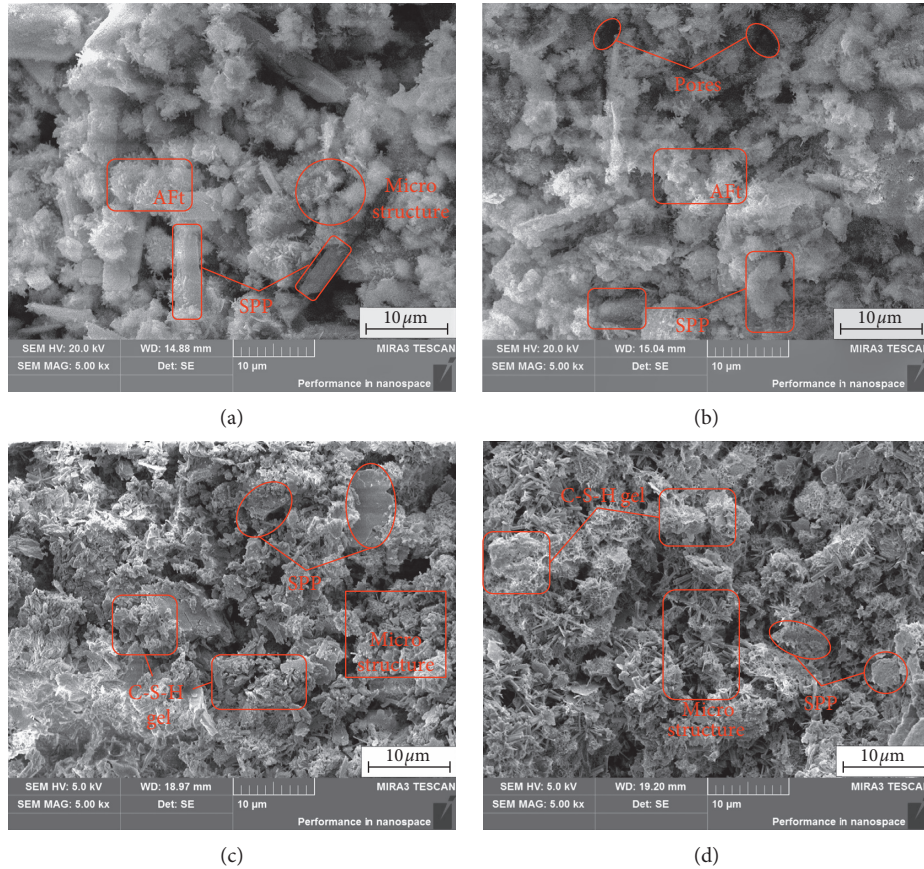


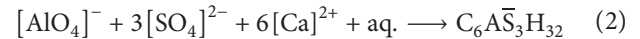
FIGURE 14: SEM image of the hydration product in the backfill; (a) CTB at 7 d; (b) SPCTB at 7 d; (c) CTB at 28 d; (d) SPCTB at 28 d.

dissolution period, condensation period, infiltration period, and hardening period. Figure 15 shows the model of hydration process of SPCTB.

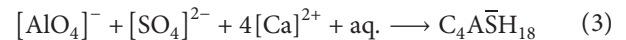
- (1) *Dissolution Period.* One mechanism [28] of hydration of Portland cement shows that the through-solution hydration involves the dissolution of anhydrous compounds into their ionic constituents, which results in the formation of hydrates in the solution. This phenomenon happens due to their low solubility and eventual precipitation of the hydrates from the supersaturated solution. From SEM images of 3D hydrating cement pastes (Figure 15), it appears that the through-solution mechanism is dominant in the early stages of cement hydration. The hydration reactions are most violent during the dissolution period. C_3A and C_4AF in the cement particles dissolved first and produced large amounts of $[AlO_4]^-$, $[SO_4]^{2-}$, $[Ca]^{2+}$, and $[OH]^-$ ions. However, both SPP and tailings dissolved in water containing these ions. Water acted as a reaction medium in the violent hydration reaction of these ions.
- (2) *Condensation Period.* Depending on the concentration of aluminate and sulfate ions in the solution, the precipitating crystalline product is either calcium aluminate trisulfate hydrate or calcium aluminate monosulfate hydrate. In solutions saturated with

calcium and hydroxyl ions, the former crystallizes as short prismatic needles and is also referred to as high sulfate or by its mineralogical name, ettringite (AFt crystals). The monosulfate is also called low sulfate and crystallizes (AFm crystals) as thin hexagonal plates. The relevant chemical reactions may be expressed using the reaction equations [28].

Ettringite:



Monosulfate:



The hydration reaction produced a large number of acicular AFt crystals and hexagonal plate-shaped AFm crystals. AFt is the main cause of the early strength of the specimens and represents the generation of AF. It is also the beginning of coagulation period and reaches the final coagulation state until the complete formation of AFt crystals. At the same time, the hydration reaction will also generate a part of amorphous C-S-H gel, which is attached to the surface of tailings particles and SPP.

- (3) *Infiltration Period.* At later ages of hydration reaction, when the ionic mobility in the solution becomes restricted, the hydration of residual

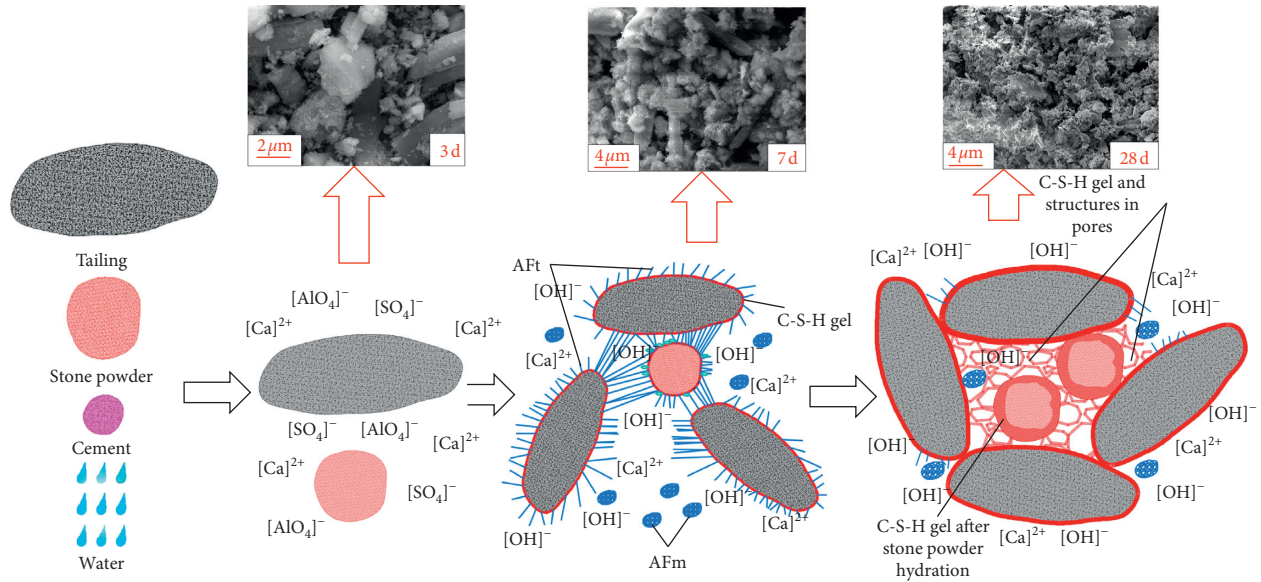


FIGURE 15: Model for the SPCTB hydration process.

cement particle may occur through solid-state reactions. Meanwhile, stone powder acts as nucleation sites for hydration products [29]. It is not surprising that the inclusion of stone powder increases the rate of hydration. At the same time, according to Section 4.3 of hydration products, the proportion of SiO_2 decreased in 7 d and 28 d, which means that SiO_2 reacted with hydration products. In this period, C_3S and C_2S in cement dissolve in water in large quantities and start the hydration reaction. A large amount of C-S-H gel, $[Ca]^{2+}$, and $[OH]^-$ are formed to produce the strong alkaline environment. AFt crystals and AFm crystals formed in the coagulation period under the strong alkaline environment rapidly dissolve and are converted into more stable C-S-H gel. The unstable structure of the surface of stone powder will be destroyed by the strong alkaline environment, and the strong alkali and active SiO_2 of stone powder react to generate C-S-H gel covering the surface of the stone powder. When the osmotic pressure and other factors are not sufficient to drive the continued inward layer reaction, the hydration reaction on the surface of the stone powder would stop. Figure 16 shows the relative amount of hydration products during hydration age.

- (4) *Hardening Period.* According to the micromorphology analysis of 28 d, the products of C-S-H gel in the pores and on the surface of the stone powder are gradually formed, whereas the C-S-H gel of every part gradually contacts with other parts to form a stable 3D network-like gel structure, which tends to be stable. In this case, the reaction medium is the little amounts of capillary water and free water. Afterwards, the hydration reaction slows down, and the hydration reaction time continues to increase even for several years.

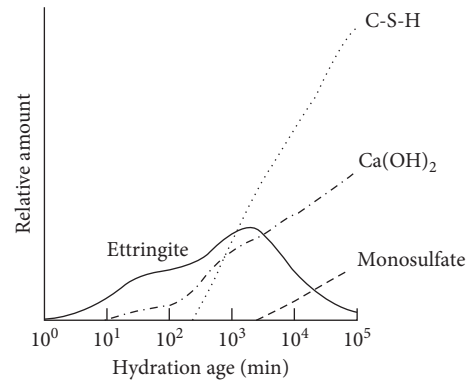


FIGURE 16: Relative amount of different hydration products during hydration age.

During the condensation period, the amount of the cement SPP system is relatively small, and many parts are needed to be cemented. The existing infiltration period slows down the rate of hydration reaction, resulting in low early strength of the SPC system. In the later stage of the infiltration period and the hardening period, the stone powder begins to participate in the hydration reaction, and the strength of the SPC system increases rapidly. At present, the strength has been analyzed only for the curing time of 28 d, while the increasing trend of strength even after 28 d has not been studied. This part of the experiment needs to be studied in a future work to further discuss the reaction mechanism of the SPC in backfill.

5. Conclusions

In this paper, the backfill specimens consisting of stone powder, cement, and tailings were analyzed to study whether the strength of SPCTB meets the requirements of mine backfilling or not. The reaction mechanism of SPC in

backfilling slurry hardening process has also been analyzed. The analysis was conducted using techniques, including uniaxial compressive tests (UCTs), nuclear magnetic resonance (NMR), scanning electron microscopy (SEM), and X-ray diffraction (XRD). The main conclusions are as follows:

- (1) With the increase in the stone powder content, the strength of each age gradually decreases, whereas different types of tailings also affect the strength of backfill specimens. The strength of Group A with the content of stone powder less than 15% meets the requirements of mine backfilling strength, and therefore, it is more practical for potential applications in mines. The incorporation of stone powder will reduce the early strength of the backfill specimens, while it promotes the strength growth during the hydration reaction in the middle and later stages.
- (2) The incorporation of the stone powder will affect the proportion of all kinds of bound states of water in the backfill specimens. With the increase in the stone powder content, the adsorbed water decreases gradually, while the capillary water increases at 3 d, which reduces the rate of hydration reaction. However, it decreases for 7 d period, which results from the free water adsorbed on SPP that gradually enters the pores and becomes the medium of hydration reaction. This was also the reason why the strength of SPCTB increased significantly in the later stage of the addition of stone powder.
- (3) The incorporation of stone powder will increase the plane porosity of backfill specimens for 28 d curing period, which will lead to the decrease of strength. Different types of tailings will affect the plane porosity. The backfill specimens consisting of tailings B have larger plane porosity.
- (4) When only the stone powder is used as the cementitious material, the hydration reaction would not occur, while the hydration reaction occurred in Groups 2, 3, and 4. The results showed that SiO₂ contained in stone powder reacted with hydration products at later stages of hydration reaction. The hydration products of SPCTB were mainly AFt at the early stages and amorphous C-S-H gel in the final stage. The stone powder particles disappeared in the final stage, indicating that the stone powder reacted with the cement hydration product in the middle and later stages. Additionally, it participates in the hydration reaction, which further promoted the increase in strength of the backfill specimens. Meanwhile, the C-S-H gel and the stone powder hydration products are closely combined, forming a close three-dimensional mesh structure.
- (5) The hydration process of the backfilling material system can be divided into following four stages: dissolution period, condensation period, infiltration period, and hardening period. At the third and fourth stages of hydration reaction, the stone powder acts as nucleation sites for the hydration products. At

the same time, the unstable structure of the surface of stone powder will be destroyed by the strong alkaline environment, and the strong alkali and active SiO₂ of stone powder react to generate C-S-H gel covering the surface of the stone powder. When the osmotic pressure and other factors are not sufficient to drive the continued inward layer reaction, the hydration reaction on the surface of the stone powder would stop.

Data Availability

The data used to support the findings of this study are available from the corresponding author upon request.

Conflicts of Interest

The authors declare that there are no conflicts of interest regarding the publication of this paper.

Acknowledgments

This research was supported by the National Key Research and Development Program of China (2017YFC0602901), National Key Technology Support Program (2015BAB12B01), and National Natural Science Fund (41672298) funded by Ministry of Science and Technology of the People's Republic of China and the Postgraduate Research and Innovation Foundation (2018zzts769) funded by Central South University.

References

- [1] S. J. Choi, S. S. Jun, J. E. Oh, and P. J. M. Monteiro, "Properties of alkali-activated systems with stone powder sludge," *Journal of Material Cycles and Waste Management*, vol. 12, no. 4, pp. 275–282, 2010.
- [2] G. Marchetti, V. F. Rahhal, and E. F. Irassar, "Influence of packing density and water film thickness on early-age properties of cement pastes with limestone filler and metakaolin," *Materials and Structures*, vol. 50, no. 2, p. 111, 2017.
- [3] M. J. Al-Kheetan, M. M. Rahman, and D. A. Chamberlain, "A novel approach of introducing crystalline protection material and curing agent in fresh concrete for enhancing hydrophobicity," *Construction and Building Materials*, vol. 160, pp. 644–652, 2018.
- [4] M. J. Al-Kheetan, M. M. Rahman, and D. A. Chamberlain, "Development of hydrophobic concrete by adding dual-crystalline admixture at mixing stage," *Structural Concrete*, vol. 19, no. 5, pp. 1504–1511, 2018.
- [5] A. A. Ramezani-pour, S. S. Mirvalad, E. Aramun, and M. Peidayesh, "Effect of four Iranian natural pozzolans on concrete durability against chloride penetration and sulfate attack," in *Proceedings of Second International Conference on Sustainable Construction Materials and Technologies*, Ancona, Italy, June 2010.
- [6] A. Kumar and D. M. Roy, "A study of silica fume modified cements of varied fineness," *Journal of the American Ceramic Society*, vol. 67, no. 1, pp. 61–64, 1984.
- [7] A. A. Ramezani-pour, A. Pilvar, M. Mandikhani, and F. Moodi, "Practical evaluation of relationship between

- concrete resistivity, water penetration, rapid chloride penetration and compressive strength,” *Construction and Building Materials*, vol. 25, no. 5, pp. 2472–2479, 2011.
- [8] S. Tsivilis, E. Chaniotakis, E. Badogiannis, G. Pahoulas, and A. Ilias, “A study on the parameters affecting the properties of Portland limestone cements,” *Cement and Concrete Composites*, vol. 21, no. 2, pp. 107–116, 1999.
- [9] I. Soroka and N. Stern, “Effect of calcareous fillers on sulfate resistance of Portland cement,” *American Ceramic Society Bulletin*, vol. 55, no. 6, pp. 594–595, 1976.
- [10] I. Mohammadi and W. South, “The influence of the higher limestone content of General Purpose cement according to high-strength concrete test results and construction field data,” *Materials & Structures*, vol. 49, no. 11, pp. 4621–4636, 2016.
- [11] H. El-Didamony, T. Salem, N. Gabr, and T. Mohamed, “Limestone as a retarder and filler in limestone blended cement,” *Ceramics-Silikáty*, vol. 39, no. 1, pp. 15–19, 1995.
- [12] J. Albeck and B. Sutej, “Characteristics of concrete made of portland limestone,” *Beton- und Stahlbetonbau*, vol. 41, no. 5, pp. 240–244, 1991.
- [13] H. El-Didamony, A. M. Sharara, E. Ebied, and A. El-Aleem, “Hydration characteristics of β -C₂S in the presence of some pozzolanic materials,” *Cement and Concrete Research*, vol. 26, no. 8, pp. 1179–1187, 1996.
- [14] C. Kemal, S. Hocine, E. H. Y. Yang, and V. C. Li, “Use of high volumes of fly ash to improve ECC mechanical properties and material greenness,” *ACI Materials Journal*, vol. 104, no. 6, pp. 620–628, 2007.
- [15] A. E. M. Abd Elmoaty, “Mechanical properties and corrosion resistance of concrete modified with granite dust,” *Construction and Building Materials*, vol. 47, pp. 743–752, 2013.
- [16] D. M. Kannan, S. H. Aboubakr, A. S. El-Dieb, and M. M. Reda-Taha, “High performance concrete incorporating ceramic waste powder as large partial replacement of Portland cement,” *Construction and Building Materials*, vol. 14, pp. 435–441, 2017.
- [17] S. S. Berriel, A. Favier, E. R. Domínguez et al., “Assessing the environmental and economic potential of limestone calcined clay cement in Cuba,” *Journal of Cleaner Production*, vol. 124, pp. 361–369, 2016.
- [18] O. Akhlaghi, T. Aytas, B. Tatli et al., “Modified poly(carboxylate ether)-based superplasticizer for enhanced flowability of calcined clay-limestone-gypsum blended Portland cement,” *Cement and Concrete Research*, vol. 101, pp. 114–122, 2017.
- [19] W. G. Shen, Y. Liu, L. H. Cao et al., “Mixing design and microstructure of ultra high strength concrete with manufactured sand,” *Construction and Building Materials*, vol. 143, pp. 312–321, 2017.
- [20] K. P. Zhou, R. G. Gao, and F. Gao, “Particle flow characteristics and transportation optimization of superfine unclassified backfilling,” *Minerals*, vol. 7, no. 1, p. 6, 2017.
- [21] C. H. Hou, Z. Q. Yang, Q. Gao, and D. X. Chen, “Experimental research on a new filling material compound of whole tailings and rod milling sand in Jinchuan mine,” *Journal of Shandong University of Science and Technology*, vol. 34, no. 3, pp. 78–84, 2015.
- [22] Y. J. Xu, K. P. Zhou, J. L. Li, and Y. M. Zhang, “Study of rock NMR experiment and damage mechanism analysis under freeze-thaw condition,” *Rock and Soil Mechanics*, vol. 33, no. 10, pp. 3001–3005, 2012.
- [23] J. Y. Jehng, *Microstructure of Wet Cement Pastes: a Nuclear Magnetic Resonance Study*, Ph.D. thesis, Northwestern University, Evanston, IL, USA, 1995.
- [24] M. G. Prammer, E. D. Drack, J. C. Bouton et al., “Measurements of clay-bound water and total porosity by magnetic resonance logging,” *Log Analyst*, vol. 37, no. 6, 1996.
- [25] J. L. Shang, J. H. Hu, K. P. Zhou, X. W. Luo, and M. Aliyu, “Porosity increment and strength degradation of low-porosity sedimentary rocks under different loading conditions,” *International Journal of Rock Mechanics and Mining Sciences*, vol. 75, pp. 216–223, 2015.
- [26] Q. R. Xu, W. Y. Deng, B. Xu et al., “Quantitative analysis of soft clay three-dimensional porosity based on SEM image information,” *Chinese Journal of Rock Mechanics and Engineering*, vol. 37, no. 7, pp. 1497–1502, 2015.
- [27] R. G. Gao, K. P. Zhou, and J. L. Li, “Research of the mechanisms of backfill formation and damage,” *Materiali in Tehnologije*, vol. 52, no. 2, pp. 163–169, 2018.
- [28] P. J. M. Monteiro and P. K. Mehta, *Concrete: Microstructure, Properties and Materials*, Prentice-Hall, London, UK, 2006.
- [29] A. A. Ramezani-pour, *Cement Replacement Materials: Properties, Durability, Sustainability*, Springer-Verlag, Berlin, Heidelberg, Germany, 2014.

Research Article

Comparison of Asphalt Mixtures Designed Using the Marshall and Improved GTM Methods

Jianbing Lv ¹, Xu Zhancheng,¹ Yin Yingmei,¹ Zhang Jiantong,¹ Sun Xiaolong,¹ and Wu Chuanhai²

¹Guangdong University of Technology, Guangzhou 510006, Guangdong, China

²Guangdong Hualu Traffic Technology Co. Ltd, Guangzhou 510006, Guangdong, China

Correspondence should be addressed to Jianbing Lv; ljbzh@126.com

Received 9 June 2018; Accepted 16 September 2018; Published 1 November 2018

Guest Editor: Ghazi G. Al-Khateeb

Copyright © 2018 Jianbing Lv et al. This is an open access article distributed under the Creative Commons Attribution License, which permits unrestricted use, distribution, and reproduction in any medium, provided the original work is properly cited.

The Marshall method is today considered the standard method of asphalt mixture design for practical engineering applications. By using this method, engineering designers reap the benefits of its easy implementation and inexpensive equipment requirements. However, the Marshall method also has shortcomings and limitations, such as the difficulty in simulating the actual working conditions of a road under heavy load. Therefore, it is desirable to develop alternative methods for designing asphalt mixtures that can simulate the actual conditions under which the road will be used and so enable technically superior road construction. The emergence of the gyratory testing machine (GTM) method represents a new direction in asphalt mixture design that could plan more effectively for heavy loads in a hot and humid environment. In this paper, the two design methods are compared on the basis of the oil-stone ratio, high-temperature stability, water stability, and rutting resistance of the mixes they recommend. We put forward an improved GTM method suitable for the high temperatures and heavy traffic in Guangdong Province. This work provides a foundation for the large-scale popularization and application of the GTM method.

1. Introduction

The premature destruction of asphalt pavement in high-grade Chinese highways mainly occurs through the formation of grooves, oil pan, and water damage. Studies have shown that these early failure phenomena are attributable to a high asphalt content, the low density of the mixture, the degree of compaction, high porosity, or poor gradation [1–4]. At present, the most commonly used asphalt mixture design methods are the Marshall method, the Wim method, the superpave volume method, and the gyratory testing machine (GTM) method. The formation process with the GTM method simulates the actual conditions experienced by the road, enabling the design of an asphalt mixture with good antirutting performance. Due to this major advantage, GTM is gaining increasing attention in national road engineering circles [5–10].

At present, asphalt mixtures designed using the Marshall method cannot control the density of the final specimen

formed, which means that the porosity cannot be adequately controlled. In theory, GTM design takes the final density of the pavement mixture as a design constraint. This significantly remedies some of the flaws inherent in the Marshall design method. The early GTM design method was mainly aimed at preventing the deformation of the rut and did not pay special attention to the durability, aging resistance, and fatigue resistance of the pavement structure. And the GTM method has not proposed a special method for the selection of aggregate gradation; hence, only the traditional grading specifications and determining methods were used (used in the Marshall design method). In addition, it is still controversial for how to use GSI and GSF indicators to determine the best asphalt ratio of asphalt mixtures. Therefore, the early GTM design method is necessary to be improved.

The density of a GTM-designed asphalt mixture at equilibrium is determined by instrumental parameters such as the machine angle, vertical pressure, and test temperature. However, it can be challenging to determine

the optimal oil-stone ratio for the GTM method due to a lack of consensus as to the appropriate gyratory stability index (GSI), with some scholars advocating for using a GSI of 1, and others, a GSI of 1.03. Additionally, the performance of mixtures designed using the GTM method is not demonstrably superior, indicating that the method still needs improvement.

2. A Comparative Analysis of the Improved GTM and Marshall Methods

2.1. Selection of Raw Materials

2.1.1. Selection of Asphalt and Minerals. The asphalt used in this study is Grade A No. 70 asphalt produced by the China National Petroleum Company (CNPC). Its technical indicators are in accordance with the requirements of current Chinese regulations [11] (Table 1). The coarse aggregate is granite gravel produced by Qingyuan (stone specifications: 11–22 mm, 11–16 mm, 6–11 mm, and 3–6 mm), and fine aggregates are granite produced by Qingyuan. The filler is ground limestone produced by Conghua, and the anti-stripping agent is a cement produced in Pingtang Town. Its technical indicators are in accordance with the requirements of current Chinese regulations [11] (Table 2). To minimize variability in the test data, the aggregates were washed and sieved and then backmatched.

2.1.2. Selection of Mineral Aggregate Gradations. GTM rotary compaction and Marshall compaction tests were carried out on four kinds of AC-16-type asphalt mixtures commonly used in Guangdong Province. The high-temperature stability and water stability of the mixes produced using the two methods were compared and analyzed. The gradations of the mineral aggregate tested are listed in Table 3.

2.2. Determination of the Best Oil-Stone Ratio Using the Marshall Method. Marshall asphalt mixture tests were carried out according to the current standard practice in China, being compacted 75 times on both sides at a compaction temperature of 140°C–150°C. The best oil-stone ratios for each gradation were determined by plotting the data and are shown in Table 4. Both light and heavy traffic were considered in determining the optimum oil-stone ratio, for which design porosities of 4.0% and 5.0%, respectively, were adopted.

Table 4 indicates the following:

- (1) The characteristics of gradations 1 and 2 are very similar to each other and are consistent with past experience; gradations 3 and 4 also show very similar characteristics to each other but differ significantly from 1 and 2. It is necessary to use a higher proportion of asphalt to achieve the same porosity for gradations 3 and 4.
- (2) The VMA (voids in mineral aggregate, calculated by theoretical maximum relative) with the best oil-stone ratio for gradations 1 and 2 does not meet the

requirements of the specification [11]. To meet the requirements, the porosity would need to be reduced to 3.5%, significantly increasing the amount of asphalt required.

- (3) New technical specifications for asphalt pavement construction have recently been published [11]. Because the absorbency of asphalt is taken into account in the calculation of mineral aggregate porosity, the calculated VMA is ~1–2% lower than that with the previous method. This has rendered it the most difficult requirement to meet in gradation design. For the materials used in this case, the composition of gradations 1 and 2 should be adjusted according to the actual materials that would be used. Adjusting the size of the gradation is the simplest way to make the indicators of the Marshall test meet the requirements.
- (4) When designing for heavy traffic, the best oil-stone ratio of AC-16 asphalt was reduced by 0.3–0.5%. However, only the porosity and not the saturation and mineral aggregate gap met the requirements [12].

2.3. Improved Optimal Design of the Oil-Stone Ratio Using the GTM Method. In the GTM test, each asphalt mixture was molded according to ASTM D3387. The rotation parameters were set to a vertical pressure of 0.7 MPa and a machine angle of 0.8° (oil pressure gauge); the specimen model was controlled as a limit equilibrium. The sample diameter was set at 101.6 mm and the mold temperature at 60°C, and the initial temperature of compaction was 140–150°C. The test results are shown in Figures 1–6.

Figures 1–6 indicate that the gyratory shear factor (GSF) of the asphalt mixtures tested is greater than 1.3 and the rotation stability coefficient, GSI, is less than 1.05. It is not, however, possible to meet the requirements of the design [11] (Table 5) using either the initial GTM design method (when the gyratory stability index, GSI, is close to 1.0, the corresponding amount of asphalt is the maximum amount of asphalt in the mixture, and when the GSF of the mixture is greater than 1.0, the mixture density reaches the maximum value) or the results of relevant research (GSI = 1.05, oil-stone ratio for GSF >1.3) as the best asphalt mix dosage standards.

It is therefore necessary to find an alternative method for determining the optimum amount of asphalt for the GTM mixture. We have devised an improved GTM asphalt mixture design methodology for selecting the best oil-stone ratio, as follows:

- (1) As in Figures 1–6, data are plotted using the oil-stone ratio or weight of asphalt as the abscissa and the volume index and mechanical indicators of the GTM specimens on the vertical axis. A smooth curve is plotted to fit the results.
- (2) Firstly, the asphalt dosage range OAC_{\min} – OAC_{\max} (OAC = optimum asphalt content) that would meet the technical standards for GTM design of an asphalt

TABLE 1: No. 70 asphalt test results.

Test	Method	Specified value	Measured value
Penetration (0.1 mm)	25°C, 100 g, 5 s	60–80	61
	15°C, 100 g, 5 s	—	20
	30°C, 100 g, 5 s	—	113
Penetration index (PI)	—	−1.5 to +1.0	−1.42
Ductility (cm)	5 cm/min, 15°C	≥100	>100
	5 cm/min, 10°C	≥15	>100
Softening point (°C)	Ring and ball method	≤46	47.0
Dynamic viscosity (Pa·s)	60°C	≤180	191.9
Kinematic viscosity (Pa·s)	135°C	—	0.365

TABLE 2: Aggregate physical and mechanical indicators.

Material name	Test project					
	Apparent relative density (g/cm ³)	Gross volume relative density (g/cm ³)	Needle particle content (%)	Crushing value (%)	<0.075 particle content (%)	Water absorption (%)
11–22 mm gravel	2.740	2.699	5.5	—	0.3	0.56
11–16 mm gravel	2.744	2.701	4.8	11.7	0.2	0.63
6–11 mm gravel	2.752	2.692	—	—	0.4	0.82
3–6 mm gravel (≥2.36 mm)	2.726	2.652	—	—	—	1.02
3–6 mm gravel (<2.36 mm)	2.705	2.644	—	—	2.1	0.96
0–3 mm gravel (≥2.36 mm)	2.725	2.639	—	—	—	1.21
0–3 mm gravel (<2.36 mm)	2.714	2.639	—	—	4.8	1.06
Filler	2.784	—	—	—	—	—
Cement	3.099	—	—	—	—	—

TABLE 3: Selected AC-16 asphalt mixture design gradations.

Gradation number	Sieve hole (mm) pass rate (%)											
	26.5	19	16	13.2	9.5	4.75	2.36	1.18	0.6	0.3	0.15	0.075
1	100	100	95.0	80.0	60.0	40.0	29.5	22.0	17.5	13.0	9.5	6.5
2	100	100	97.5	80.0	60.0	35.0	26.5	22.0	17.5	13.0	9.5	6.5
3	100	100	97.5	82.5	68.0	52.5	41.0	29.5	22.0	16.0	11.0	6.0
4	100	100	97.3	78.5	56.9	30.0	23.0	19.3	15.6	11.9	9.0	6.5

TABLE 4: Summary of the oil-stone ratios for asphalt mixtures selected using the Marshall method.

Gradation number	Selected oil-stone ratio (%)	Theoretical maximum relative density (g/cm ³)	Measured density (g/cm ³)	Porosity (%)	Mineral material clearance rate (%)	Saturation (%)	Marshall stability (kN)	Flow value (0.1 mm)	
									1
	Overload	4.17	2.512	2.387	5.0	13.2	62.3	13.20	33.5
2	Light load	4.56	2.504	2.405	4.0	13.0	69.6	11.70	33.0
	Overload	4.15	2.518	2.391	5.0	13.1	61.5	12.50	28.0
3	Light load	4.84	2.488	2.388	4.0	13.5	70.2	13.30	23.9
	Overload	4.50	2.499	2.374	5.0	13.7	63.5	14.80	24.4
4	Light load	4.98	2.488	2.388	4.0	14.0	71.3	9.60	34.9
	Overload	4.60	2.501	2.375	5.0	14.2	64.5	9.70	34.9

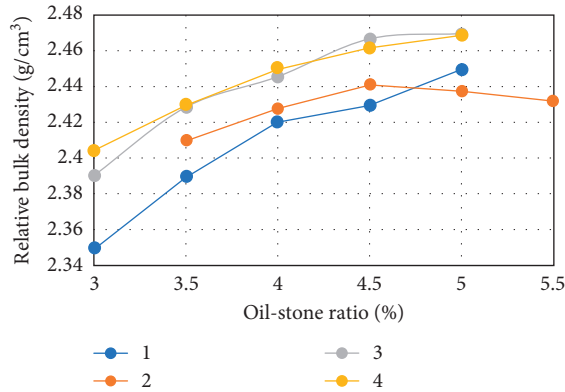


FIGURE 1: Relation between AC-16 relative bulk density and oil-stone ratio.

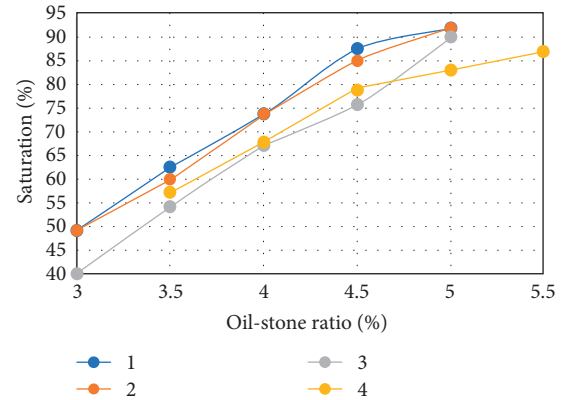


FIGURE 4: Relation between AC-16 saturation and oil-stone ratio.

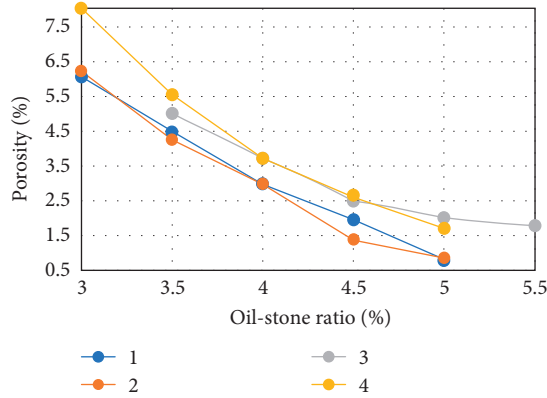


FIGURE 2: Relation between AC-16 porosity and oil-stone ratio.

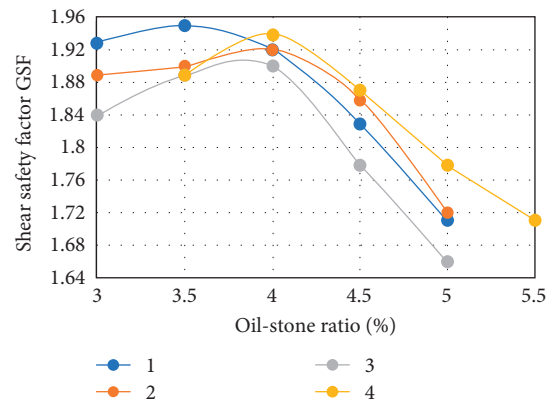


FIGURE 5: Relation between AC-16 shear safety factor and oil-stone ratio.

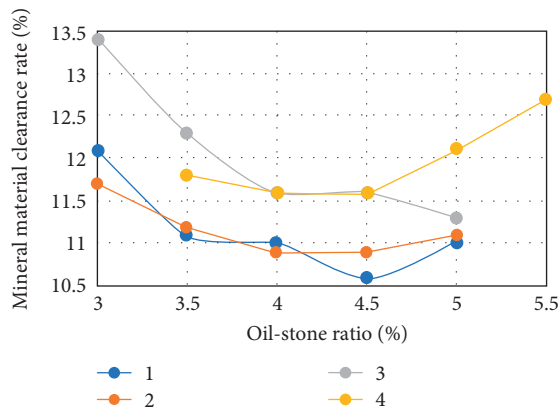


FIGURE 3: Relation between AC-16 mineral material clearance rate and oil-stone ratio.

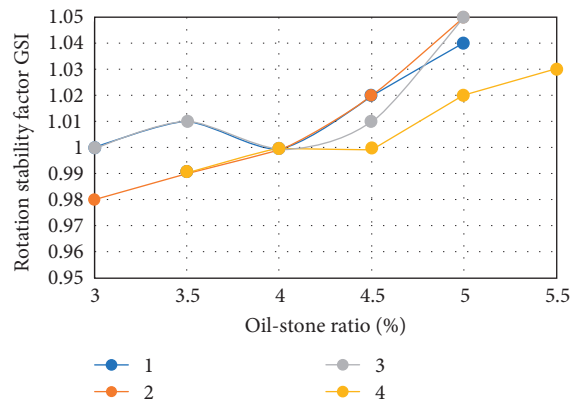


FIGURE 6: Relation between AC-16 rotation stability factor and oil-stone.

mixture (Table 5) is determined. The selected range of bitumen usage must cover the full range of porosity. Furthermore, it should cover as much of the range in the asphalt saturation requirements as possible and produce a peaked GSF curve. If the full range of design porosity is not covered, the test must be repeated.

(3) The maximum density, a_1 , the maximum shear safety factor GSF, a_2 , the target void fraction (or median), a_3 , and the asphalt dosage, a_4 , in the asphalt saturation range are taken from the curves. If the range of asphalt used in the test fails to cover the required range of asphalt saturation, the average value of a_1 , a_2 , and a_3 is taken as OAC_1 . If the GSF or the density

TABLE 5: Technical standards for an asphalt mixture designed by the GTM method (0.7 Mpa).

Pilot projects	Technical indicators
Dimensions of the specimen (mm)	101.6 × 100
Standard density	GTM final density about rotational compaction
Porosity (%)	2.0~4.0
Saturation VFA (%)	60~80
Rotation stability GSI	≥1.05
Shear stability GSF	≥1.30
<i>The minimum VMA requirement corresponding to the nominal particle size (mm)</i>	
Nominal particle size (mm)	26.5 19.0 16.0 13.2
Mineral material clearance rate VMA (%)	10.0 10.0 10.5 11.0

does not reach a peak value, we take the goal porosity corresponding to bitumen quantity a_3 as OAC_1 . OAC_1 must be in the range OAC_{min} – OAC_{max} , or else the design should be remixed.

- (4) The median value of OAC_{min} – OAC_{max} with indicators in line with technical standards (excluding VMA) is used for OAC_2 .
- (5) The median of OAC_1 and OAC_2 is used as the best asphalt OAC .
- (6) On the basis of the optimum amount of asphalt, we determine the voidage and check whether the VMA meets the technical requirements.

Applying this improved GTM design methodology to the experimental results shown in Figures 1–6, we determined the best oil-stone ratio for each gradation (Table 6).

2.4. Contrastive Analysis of the Two Design Methods

- (1) For an asphalt mixture with the same proportions, the GTM specimen density was 1.52–3.36% higher than that from the Marshall method (Table 7). The percentage density increase varies with gradation and also differs for different oil-stone ratios at the same gradation level. The density decreases with an increase in the asphalt content.
- (2) Changes in the density, porosity, and mineral void ratio of GTM specimens with a change in the oil-stone ratio are similar to those observed with the Marshall method. When the oil-stone ratio is identical, the porosity and mineral aggregate clearance rate in asphalt concrete designed by GTM are much lower than in that designed with the Marshall method. This is advantageous for the stability and durability of the road.
- (3) With a change in the oil-stone ratio, the change in GTM GSF is similar to that of Marshall, and there is a peak or abrupt change point. The GSF can be used as an indicator of shear strength. It can also be used to evaluate the sensitivity of gradation shear strength to variation in the mass ratio. When the GSF for

asphalt changes slowly, it can be considered that the shear strength is less sensitive to the amount of asphalt. Asphalt has better high-temperature performance when the GSF for asphalt changes slowly.

- (4) The asphalt content that would be selected on the basis of the Marshall method is higher than the maximum quantity determined with the GTM method at 0.7 MPa pressure. This may lead to rutting and the emergence of oil pan. Even when using the heavy traffic standard in the Marshall method, this problem is not fundamentally resolved. Additionally, the increased porosity would lead to poor water stability, and the degree of compaction would need to be increased to 99%.

3. Performance Test of an Antirutting Asphalt Mixture Designed with the GTM Method

3.1. High-Temperature Stability. To evaluate the high-temperature stability of the asphalt concrete, a rutting test was performed, applying JTJ052-2000 regulations [13]. Specimens measuring 300 mm × 300 mm × 50 mm and with 100% compaction were used. The density of the Marshall and GTM specimens were used as the standard density. The test results are shown in Table 8.

Table 7 indicates the following:

- (1) The dynamic stability of different gradations does not increase monotonously with an increase in coarse aggregate content [2, 14]; indeed, extremely high gradation may have a negative impact on high-temperature stability. When using the heavy traffic variation of the Marshall method, the dynamic stability of the rutting test improves [15–17].
- (2) A mixture designed using GTM shows better dynamic stability than the one designed using Marshall and in some cases meets the requirements of a modified asphalt mixture. In addition, GTM-designed mixtures show lower relative deformation than Marshall-designed mixtures.
- (3) Asphalt mixtures of the same grade may have different high-temperature properties under the two methods. Of the four selected AC-16 mixes, gradation 4's high-temperature performance was the worst under the Marshall method but the best with GTM.

3.2. Water Stability. For evaluating the water stability of asphalt mixtures, the Lottman freeze-thaw splitting method currently shows the best correlation with the behavior of actual road surfaces [11, 18]. Therefore, GTM and Marshall mixtures were tested for water stability using this method. The results of this analysis indicate the following:

- (1) The splitting strength indicates that a mixture designed using the GTM method is significantly more resilient than the one designed using the Marshall method: the splitting strength of AC16 was

TABLE 6: Summary table of the optimal oil-stone ratio for selected asphalt mixtures according to the GTM method.

Gradation number	Selected oil-stone ratio (%)	Theoretical maximum relative density (g/cm^3)	Measured density (g/cm^3)	Porosity (%)	Mineral material clearance rate (%)	Saturation (%)	Shear safety factor GSF	Rotation stability factor GSI
1	4.1	2.520	2.454	2.6	10.8	75.7	1.91	1.00
2	4.0	2.518	2.445	2.9	11.0	73.6	1.93	1.00
3	4.2	2.507	2.426	3.2	11.6	72.1	1.85	1.00
4	4.3	2.511	2.436	2.9	11.6	74.2	1.89	1.00

TABLE 7: Difference in bulk density for the two methods of asphalt mixture design.

Percentage increase of GTM forming density relative to Marshall compaction in different asphalt ratios (%)					
Gradation number	Oil-stone ratio				
	3.5	4.0	4.5	5.0	Average
1	3.36	2.64	2.62	1.52	2.54
2	2.75	2.60	2.46	2.15	2.49
3	2.84	3.33	2.40	2.59	2.79
4	2.60	2.88	2.87	2.05	2.60
Average	2.89	2.86	2.59	2.08	2.60

TABLE 8: Results of a rutting test on the selected asphalt mixtures.

Gradation number	Design method		Test temperature ($^{\circ}\text{C}$)	Test pressure (MPa)	Dynamic stability (mm/time)	Deformation rate (%)
1	Marshall method	Light load	60	0.7	1512	8.0
		Overload	60	0.7	2080	8.4
	GTM method	0.7 MPa	60	0.7	3315	5.2
		Light load	60	0.7	1632	9.6
2	Marshall method	Overload	60	0.7	2172	9.1
		0.7 MPa	60	0.7	3480	5.7
	GTM method	Light load	60	0.7	1690	8.1
		Overload	60	0.7	2356	8.4
3	Marshall method	0.7 MPa	60	0.7	3320	5.0
		Light load	60	0.7	828	10.8
4	Marshall method	Overload	60	0.7	1940	9.6
		0.7 MPa	60	0.7	3753	5.6

24.6% higher before freezing and 31.1% higher after freezing.

- (2) The freeze-thaw splitting residual strength ratio also indicates that a mixture designed using GTM is an improvement on the one designed using the Marshall method: it is, on average, 5.1% higher for AC16-type mixtures.

In summary, because of the differences in oil-stone ratio and void ratio between the mixtures designed by the two methods, they have significantly different degrees of water stability. It is generally believed that the water stability of the asphalt mixture is better when the oil-stone ratio is higher or the asphalt film is thicker.

4. Conclusions

- (1) For asphalt mixtures with the same proportions, the density of a GTM specimen is 1.52–3.57% higher

than that of a Marshall specimen. The amount of density increase varies with gradation. For a given gradation, the density decreases with an increase in the oil-stone ratio. Therefore, simply reducing the oil-stone ratio to adapt to heavy traffic conditions in the Marshall method has limited usefulness, as one cannot rely on a consistent relationship between the two variables to replicate the GTM method.

- (2) When using the different methods, asphalt mixtures with the same gradation may have completely different high-temperature performance. Especially for coarsely graded mixtures, special measures must be taken to prevent the selection of asphalt with poor high-temperature performance, such as an appropriate increase in porosity or the use of GTM design.
- (3) The GTM method simulates conditions in the field, and its design performance indices (final density, GSF, GSI, etc.) are directly linked to the mechanical

parameters of the road. However, it abandons the use of the asphalt mixture volume index, which was the result of much practical experience. Its design performance indices are the result of theoretical reasoning, and there is still some debate as to the optimal values. Because of these issues, a valuable approach is to combine GTM mechanical design with traditional volume design and so benefit from the advantages of both. The anti-rutting performance of an asphalt mixture designed in this manner is improved over that of the one designed using the Marshall method, as is the water stability due to a reduction in the void fraction.

Data Availability

The data used to support the findings of this study are available from the corresponding author upon request.

Conflicts of Interest

The authors declare that they have no conflicts of interest.

Acknowledgments

This publication was supported by the National Natural Science Foundation of China Project (51508109 and 51608085). The authors would also like to thank all those who contributed to the experimental part of this study. And thanks are due to Guangdong Hualu Traffic Technology Co. Ltd. for providing some experimental equipment and also for the guidance of engineers Li Shanqiang and Fang Yang in the experimental side.

References

- [1] A. I. Zhangfa, *Structural Analysis and Performance Evaluation of Heavy-Duty Asphalt Pavement*, Southwest Jiaotong University, Chengdu, China, 2002.
- [2] Z. Li and D. Wu, "Design and research on the warm-mix rubber-modified asphalt mixture based on the GTM method," *Advanced Materials Research*, vol. 598, pp. 543–551, 2012.
- [3] W. Zhou, *Asphalt Pavement Engineering Handbook*, China Communications Press, Beijing, China, 2003.
- [4] D. Han, L. Wei, and J. Zhang, "Experimental study on performance of asphalt mixture designed by different method," *Procedia Engineering*, vol. 138, pp. 407–414, 2016.
- [5] X. Feng and Z. Gao, "Comparative study on GTM method and marshall mixes design method for large stone asphalt mixes," in *Proceedings of GeoHunan International Conference 2009*, vol. 193, pp. 106–111, Changsha, Hunan, China, August 2009.
- [6] P. Chakraborty, A. Das, and P. Ghosh, "Determining reliability of an asphalt mix design: case of marshall method," *Journal of Transportation Engineering-ASCE*, vol. 136, no. 1, pp. 31–37, 2010.
- [7] R. Namli and N. Kuloglu, "Experimental comparison of superpave and marshall methods," *Teknik Dergi*, vol. 18, no. 2, pp. 4103–4118, 2007.
- [8] S. D. Hwang and B. Kim, "Method mix design marshall mix design and comparative evaluation with current marshall mix design method," *Journal of the Korean Society of Road Engineers*, vol. 6, no. 4, pp. 13–24, 2004.
- [9] L. J. Ma, J. Y. Zhang, and Z. Li, "The road-test of high performance asphalt mixture with superpave," *Applied Mechanics and Materials*, vol. 361-363, pp. 1576–1579, 2013.
- [10] T. Fan, "Influence of mix proportion of asphalt mixture on marshall index," in *Proceedings of International Conference on Electric Technology and Civil Engineering (ICETCE)*, pp. 5123–5127, Lushan, China, April 2011.
- [11] Highway Research Institute of the Ministry of Communications, *JTG F40-2004 Technical Specifications for Asphalt Pavement Construction*, China Communications Press, Beijing, China, 2009.
- [12] Y. Doh and K. Kim, "Volumetric property difference in mix design results by superpave and marshall method," *Journal of the Korean Society of Road Engineers*, vol. 6, no. 4, pp. 65–73, 2004.
- [13] Ministry of Communications of the People's Republic of China, *JTG F40-2004 Technical Code for Construction of Highway Asphalt Pavement*, China Communications Press, Beijing, China, 2001.
- [14] C. Wu and B. Tan, "Study on verification of evaluation indexes of shear resistance of asphalt mixtures based on GTM method," *Advances of Transportation: Infrastructure and Materials*, vol. 1, pp. 171–179, 2016.
- [15] S. Saride, D. Avirneni, and S. C. P. Javvadi, "Utilization of reclaimed asphalt pavements in indian low-volume roads," *Journal of Materials in Civil Engineering*, vol. 28, no. 2, article 04015107, 2016.
- [16] T. Xu and X. Huang, "Investigation into causes of in-place rutting in asphalt pavement," *Construction and Building Materials*, vol. 28, no. 1, pp. 525–530, 2012.
- [17] P. Ayar, F. Moreno-Navarro, and M. C. Rubio-Gámez, "The healing capability of asphalt pavements: a state of the art review," *Journal of Cleaner Production*, vol. 113, pp. 28–40, 2016.
- [18] J. Mills-Beale, Z. You, E. Fini et al., "Aging influence on rheology properties of petroleum-based asphalt modified with bio-binder," *Journal of Materials in Civil Engineering*, vol. 26, no. 2, pp. 358–366, 2014.

Research Article

Influence of Macrotexture and Microtexture on the Skid Resistance of Aggregates

Bowen Guan ¹, Jiayu Wu,¹ Chao Xie,¹ Jianhong Fang,² Haile Zheng,³ and Huaxin Chen ¹

¹School of Material Science and Engineering, Chang'an University, Xi'an, Shaanxi 710064, China

²Qinghai Research Institute of Transportation, Xining, Qinghai 810008, China

³The 2ND Engineering CO, LTD of China Railway 17 Bureau Group Corporation, Xi'an, Shaanxi 710064, China

Correspondence should be addressed to Huaxin Chen; chenhx_paper@163.com

Received 15 May 2018; Revised 3 September 2018; Accepted 6 September 2018; Published 18 October 2018

Guest Editor: Ghazi G. Al-Khateeb

Copyright © 2018 Bowen Guan et al. This is an open access article distributed under the Creative Commons Attribution License, which permits unrestricted use, distribution, and reproduction in any medium, provided the original work is properly cited.

This article intends to study the influence of macrotexture and microtexture on the skid resistance of four types of aggregates. For this purpose, fractal dimension (D), root mean square height (R_q), and Polished Stone Value (PSV) were tested. The Pearson correlation coefficients between PSV and D or R_q in the interval of different polishing cycles were calculated and analyzed with correlation analysis. The relationships between PSV and R_q were also established. The results showed that the PSV development was approximately divided into 3 stages including accelerated attenuation stage, decelerated attenuation stage, and stabilization stage. There is a critical point of the entire polishing cycles. When the number of the polishing cycles exceeds this critical point, microtexture replaces macrotexture to play a major role in the skid resistance of aggregates. In the accelerated attenuation stage, macrotexture plays a major role in the skid resistance of aggregates. In the decelerated attenuation stage and stabilization stage, microtexture gradually plays a major role in the skid resistance of aggregates. Because of roughest microtexture in the stabilization stage, bauxite can provide the highest levels of skid resistance for high friction surface treatment over the long-term period.

1. Introduction

High friction surface treatment (HFST) is the application of very high quality aggregate with an epoxy binder, which is designed to improve friction of the pavement in the location with high crashes, such as horizontal curves and intersections. As an approach widely used in the pavement construction and maintenance, HFST has been demonstrated to provide significant increases in friction [1–3].

Due to surface texture characteristics directly affecting the skid resistance of the pavement, lots of researchers focus on the influence of surface texture on the skid resistance of HFST. Heitzman et al. [4] evaluated the HFST test slabs with eight aggregates including bauxite, granite, flint, basalt, silica sand, steel slag, emery, and taconite under accelerated laboratory polishing and testing procedures. They found that all eight surfaces maintained predominately greater than 1.0 mm mean profile depth (MPD), and however, there is no correlation between HFST surface friction and particle shape

and angularity. Li et al. [5] reported that friction surfacing such as HFST with larger surface MPD does not necessarily produce greater surface friction. Chen et al. [6] put forward that the surface of the coarse aggregate tended to have a smooth microstructure due to the reducing actual effective contact area of the road surface greatly. Even if with the same macrostructure depth of the road surface, the skid resistance ability of the road surface would be also decreased. Most of the studies have found that not only macrotexture varies with aggregate geometric properties (shape and size) but also microtexture has significant influence on the skid resistance of HFST. However, their effects have not been quantified.

Because aggregate in the pavement materials accounts for more than 90%, surface texture of aggregate is important for friction of HFST. The appearance of aggregates is mainly divided into two levels: macrotexture and microtexture. The first level is characterized by a shape that reflects the change in the size of a particle, that is, the macroscopic overall variation of the aggregate particles and the state. The second

level is characterized by texture used to describe the surface of a body in an irregular range. The impact of texture is often so small which cannot affect the shape or edges and corners, reflecting the aggregate particles microscopic-scale changes within the scope of the situation. In order to understand the relationship between surface texture and skid resistance of aggregates, the effect of macrotexture and microtexture was quantified, and their contributions to the skid resistance of aggregates were studied in this paper.

2. Materials and Methods

2.1. Raw Materials. Four types of aggregates (bauxite, granite, limestone, and basalt) were used in this research. The bauxite, used for antiwear purposes in pavement engineering, was calcined to 1600°C, which is commonly used in HFST [7]. The alternative aggregates granite and basalt were also selected. Limestone was chosen as a control group, which is commonly used in wear course. The bauxite samples were obtained from Yangquan city, China. The other aggregates samples were obtained from Xi'an city, China. Aiming at measurement of surface morphology and antipolishing, these four types of aggregates were determined with different test methods on grains with a size of 9.5/13.2 mm.

2.2. Experimental Method

2.2.1. PSV Test. As the key factor in estimating the quality of aggregates used for HFST, Polished Stone Value (PSV) was used to evaluate the friction resistance of aggregate. The PSV test was carried out according to the Chinese standard JTGE42-2005 [8]. Samples of coarse aggregate were mixed up in resin to form the specimens which were coupled onto the circumference of a wheel in an accelerated polishing machine. Fourteen specimens were clamped around the periphery of the wheel and subjected to two phases of polishing by wheels with rubber tyres. To eliminate the effect of the aggregate manufacturing process on the microtexture of aggregate, the preparatory phase was of abrasion by corn emery for 40000 cycles. The polishing action was carried out with a velocity of 320 ± 5 r/min and with a load of 725 ± 10 N. Then, 40000, 80000, 120000, 160000, 200000, 240000, and 280000 cycles of polishing with emery flour were followed. The degree of polish of the specimens was then measured by means of the British Pendulum device. Results were expressed as Polished Stone Value (PSV), the mean of the fourteen test specimens of each aggregate.

2.2.2. Macrotexture Measurement. Fractal dimension is an index for characterizing fractal patterns or sets by quantifying their complexity as a ratio of the change in detail to the change in scale. Many researchers have found that fractal dimension is the suitable parameter for characterizing a pavement surface, and it is an effective measure to describe shape and angularity of the surface [9, 10]. With increasing complexity or surface roughness, the fractal dimension increases [11]. For the purpose of obtaining the

macrotexture characteristics of aggregate, the images of the specimens in different polishing cycles were collected by the Sony DSC-RX100M2 digital camera. The resolution of the images was 200 μ m. A red-green-blue (RGB) image was converted to grayscale first. The images can be considered as a 3D space, in which the two coordinates (X, Y) represent the 2D position and the third coordinate I represents the image grey level intensity. Then, image data were converted to a numeric array, and box-counting dimension (D) was calculated by MATLAB software.

2.2.3. Microtexture Measurement. 3D color laser microscope system was mainly used for 3D surface analysis and characterization. The laser is used to scan the surface in the XYZ directions and collect data throughout the entirety of a specified range. The result is a high-resolution, large depth-of-field, color image with nanometer-level height resolution for accurate profile and roughness measurements [12, 13]. As shown in Figure 1, the 3D color laser microscope system which was produced by Keyence Inc was used to measure and calculate the root-mean square height of four aggregates in this work. To reduce the acquisition error of the microscopic test data, five surfaces of aggregates on a polished specimen were observed. According to the BS EN ISO 4287:2000 standard, the surface texture parameter (the root-mean square height R_q) was obtained by the VK-Analyzer [14]. VK-Analyzer is the software module which complies with ISO 25178 and allows users to complete measurements of several surface parameters.

3. Results and Discussions

3.1. Variation of PSV during the Long-Term Polishing Process. Figure 2 showed that the four types of aggregates exhibited approximately the same PSV development trend.

From Figure 2, it can be seen that the value of PSV decreases with the increase of polishing cycles. The attenuation rate of PSV increased first and then decreased. After the polishing cycles reached a certain value, the value of PSV stayed roughly the same. In order to distinguish the inflection point of increase and decrease of attenuation rate of PSV, the second-order differential results of the PSV curves are obtained by using Origin software dealing with the PSV curves. Differential results of the PSV curves can show the change rate of attenuation rate of PSV, which is described in Figure 3.

From Figure 3, it can be seen that the change rate of attenuation rate of PSV increases first and then decreases with the increase of the polishing cycles. The peak point was the inflection point of increase and decrease of attenuation rate of PSV. When attenuation rate of PSV was first close to 0, the point was the inflection point of decrease and steady of attenuation rate of PSV. The PSV development was approximately divided into 3 stages including the accelerated attenuation stage, decelerated attenuation stage, and stabilization stage.

In the PSV test, different types of aggregates exhibit different skid resistance during the long-term polishing

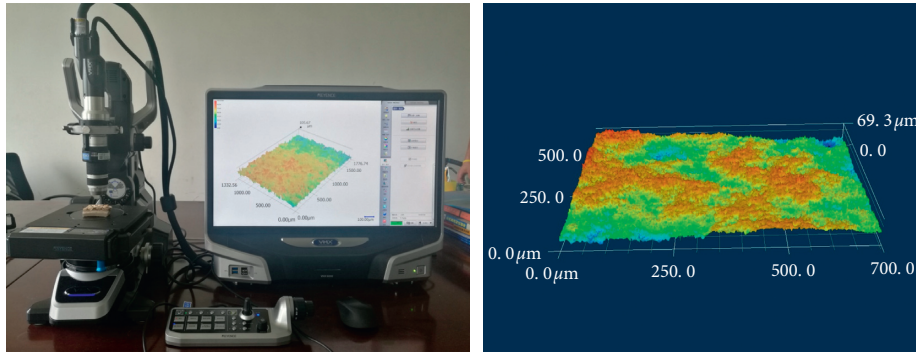


FIGURE 1: Illustration of 3D laser microscopy measurement.

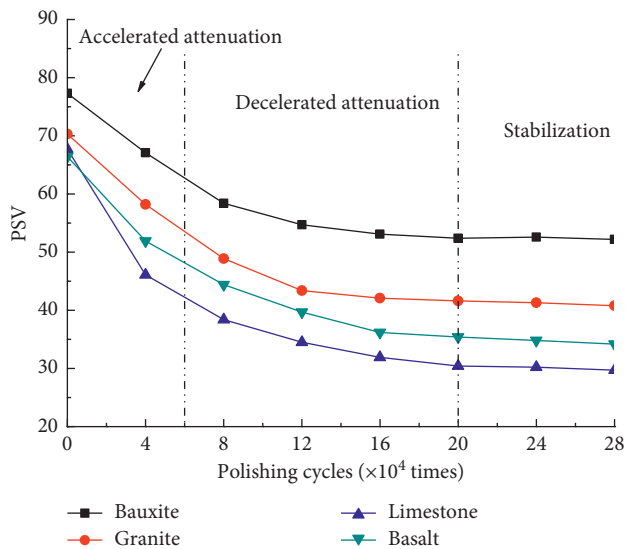


FIGURE 2: Variation of PSV during the long-term polishing process.

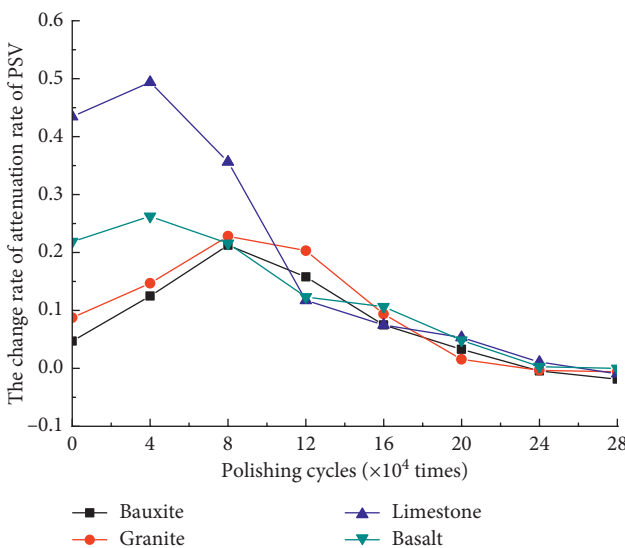


FIGURE 3: Second-order differential PSV curves.

process. The value of PSV of bauxite was decreased by 32%, and the final value of PSV was around 52. Skid resistance of bauxite was maintained at a relatively high level. Granite and

basalt ranked second and third, respectively. Limestone has the lowest value of PSV in the stabilization stage. Therefore, bauxite was more suitable for the wearing course, especially high friction surface treatment.

3.2. Variation of D and R_q during the Long-Term Polishing Process. Figure 4 presents variation of D during the long-term polishing process. D is calculated by image analysis. The images are obtained by a digital camera, and the resolution of the images is $200 \mu\text{m}$. This test method meets the accuracy requirements for testing macrotexture.

As seen from Figure 4, the value of D decreases with the increase of polishing cycles. When the polishing cycles reach 240,000 times, the values of D of different aggregates are similar. Figure 5 shows the change of macrotexture after the long-term polishing process.

From Figure 5, it can be seen that the angularity of the aggregate surface is polished, and the macrotexture of aggregates become smooth and were difficult to distinguish. Therefore, the value of D in the stabilization stage is similar; that is, the macrotexture of different aggregates is similar.

Figure 6 presents variation of R_q during the long-term polishing process. R_q is obtained by the 3D color laser microscope system. The 3D color laser microscope system is a laser scanning microscope to perform noncontact 3D observations and measurements of surface features at 10 nanometer resolutions. This equipment meets the accuracy requirements for testing microtexture.

From Figure 6, it can be seen that the R_q curve is similar to the PSV curve. The value of R_q decreases with the increase of polishing cycles. Figures 7–10 display the change of micromorphology of surface of different aggregates before and after the polishing process.

From Figures 7–10, it can be found that the mineral on the aggregate surface was first destroyed rapidly, and it was peeled off from the surface of aggregate or become powder filled in pores. The surface microtexture is destroyed by the external friction obviously, and the surfaces of aggregates become smooth. After the polishing cycles reach a certain time, the value of R_q stayed roughly the same. The R_q development was approximately divided into 2 stages including the attenuation stage of microtexture and the stabilization stage of microtexture. Figure 11 is a schematic

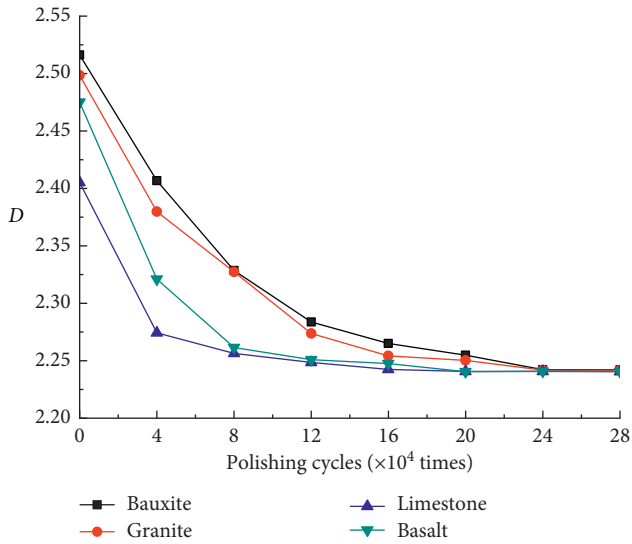


FIGURE 4: Variation of D during the long-term polishing process.

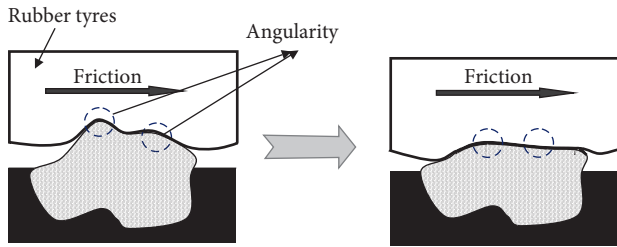


FIGURE 5: The change of macrotexture after the long-term polishing process.

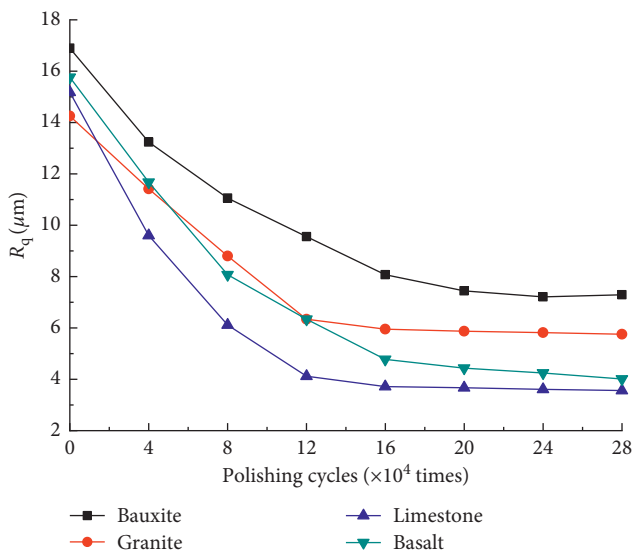


FIGURE 6: Variation of R_q during the long-term polishing process.

diagram of microtexture change during the long-term polishing process.

According to the value of R_q of different aggregates after the long-term polishing process, bauxite can provide the

roughest surface against external forces. Granite and basalt ranked second and third, respectively. Limestone has the smoothest surface and has the lowest value of R_q . Due to different mineral compositions, the final microtexture of different aggregates is different. The main mineral composition of limestone is calcite and dolomite. The Mohs hardness of the two minerals are similar (3~4) [15]. The mineral particles are soft and easy to be polished. Therefore, the microtexture of limestone is smoother than the other aggregates. The main crystal phase of bauxite is composed of corundum and mullite. The Mohs hardness of corundum and mullite are 9 and 6.5, respectively [15]. The mineral particles are hard and difficult to be polished. This is the reason why the microtexture of the bauxite surface is roughest and has good ability to resist the damage of external friction.

3.3. *The Correlation between PSV and D or R_q .* According to the above analysis, the macrotexture and the microtexture of aggregates affect the value of PSV of aggregates together. However, the degree of influence is different. In order to analyze the difference in the degree of influence, the correlation coefficient between PSV and D or R_q in the interval of different polishing cycles were calculated with Pearson correlation analysis. The results are shown in Figures 12 and 13.

From Figures 12 and 13, it can be seen that the Pearson correlation coefficient between D and PSV is higher than the Pearson correlation coefficient between R_q and PSV in the early stage of the polishing process, and the macrotexture has a greater influence on PSV. With the increase of the polishing cycles, the Pearson correlation coefficient between D and PSV decreases, and the degree of influence of macrotexture on skid resistance of aggregates becomes smaller. While the Pearson correlation coefficient between R_q and PSV increases, the degree of influence of microtexture becomes larger. The microtexture has the larger degree of influence on PSV in the late stage of the polishing process. It can be inferred that there is a critical point of the polishing cycles, and when the number of the polishing cycles exceed this point, microtexture will replace macrotexture to play a major role in the skid resistance of aggregates.

In order to find out the critical point, 4×10^4 , 8×10^4 , 12×10^4 , 16×10^4 , and 20×10^4 polishing cycles are assumed to be demarcation points, respectively. The Pearson correlation coefficients of PSV and D in the front interval ($0 \sim 4 \times 10^4$, $0 \sim 8 \times 10^4$, $0 \sim 12 \times 10^4$, $0 \sim 16 \times 10^4$, and $0 \sim 20 \times 10^4$ times) and the Pearson correlation coefficients of PSV and R_q in the after interval ($4 \times 10^4 \sim 28 \times 10^4$, $8 \times 10^4 \sim 28 \times 10^4$, $12 \times 10^4 \sim 28 \times 10^4$, $16 \times 10^4 \sim 28 \times 10^4$ and $20 \times 10^4 \sim 28 \times 10^4$ times) are calculated, which are shown in Figure 14.

From Figure 14, it can be found that when 4×10^4 times is selected as the demarcation point, the Pearson correlation coefficients of PSV and D in the front interval ($0 \sim 4 \times 10^4$ times) is higher than the Pearson correlation coefficients of PSV and R_q in the after interval ($4 \times 10^4 \sim 28 \times 10^4$ times). Macrotexture plays a major role in the skid resistance of aggregates. When 8×10^4 times is selected as the

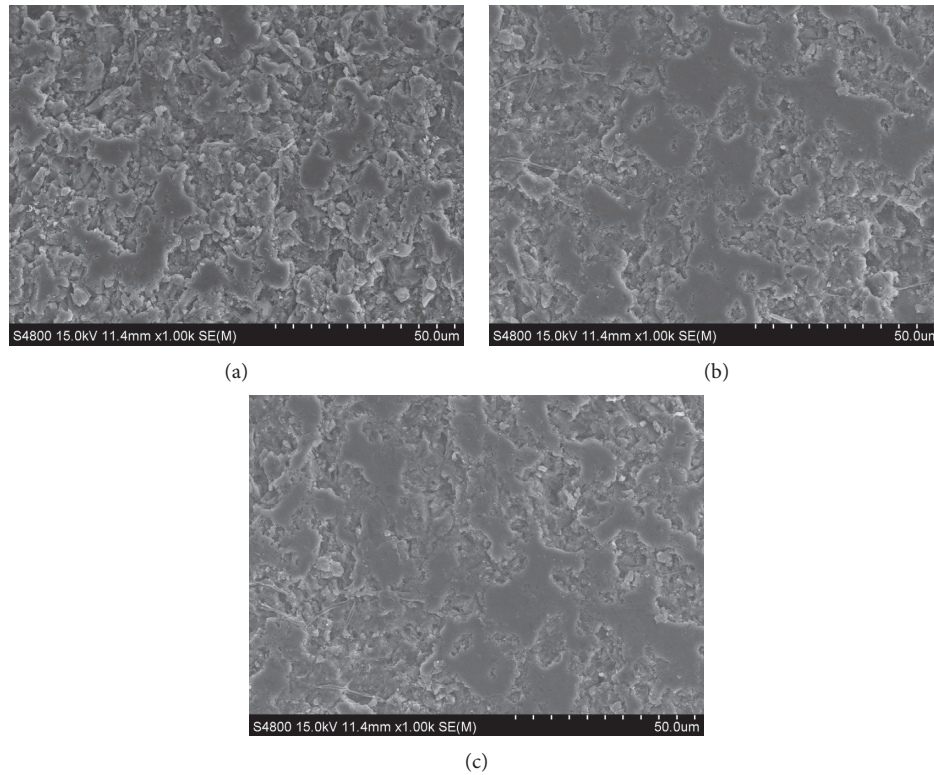


FIGURE 7: Micromorphology of the bauxite surface: (a) before the polishing process; (b) after 20×10^4 polishing cycles; (c) after 28×10^4 polishing cycles.

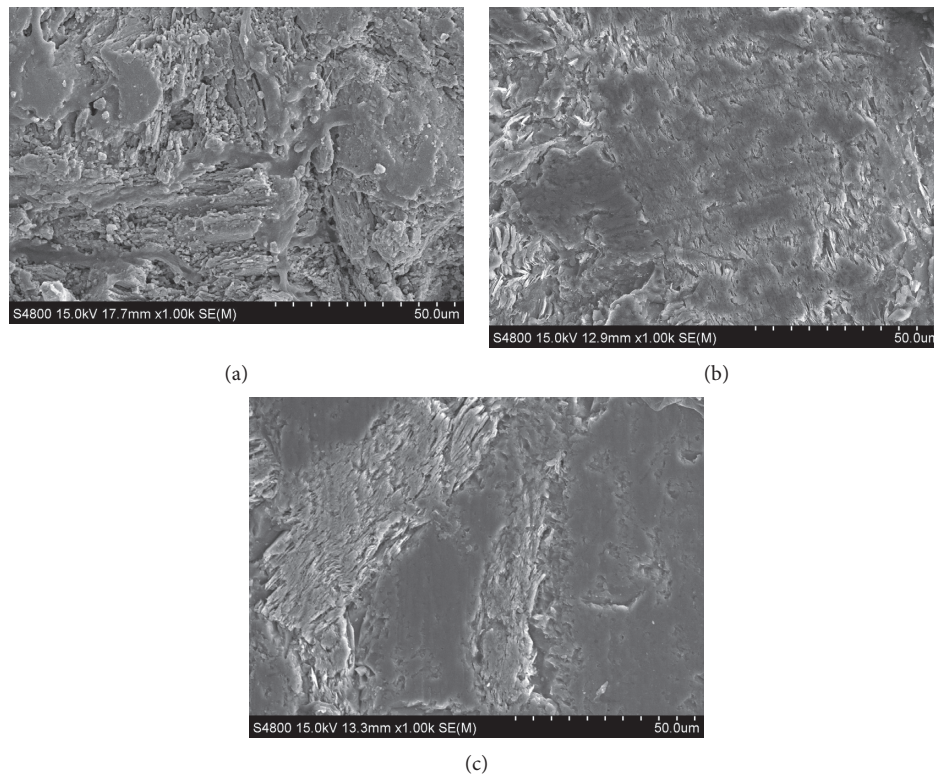


FIGURE 8: Micromorphology of the granite surface: (a) before the polishing process; (b) after 20×10^4 polishing cycles; (c) after 28×10^4 polishing cycles.

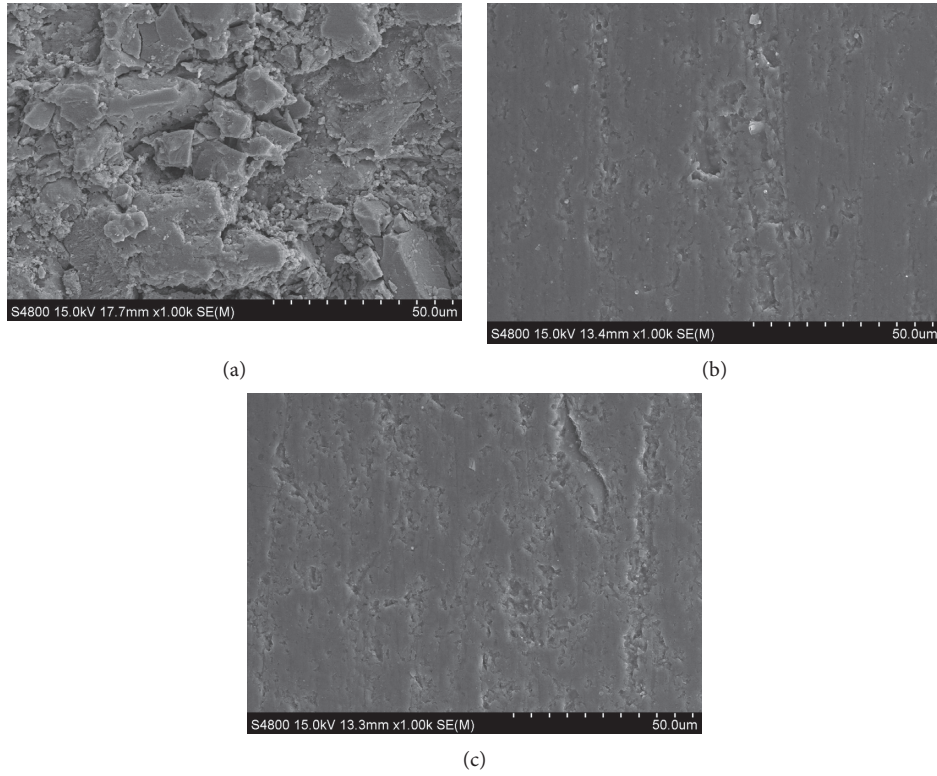


FIGURE 9: Micromorphology of the limestone surface: (a) before the polishing process; (b) after 20×10^4 polishing cycles; (c) after 28×10^4 polishing cycles.

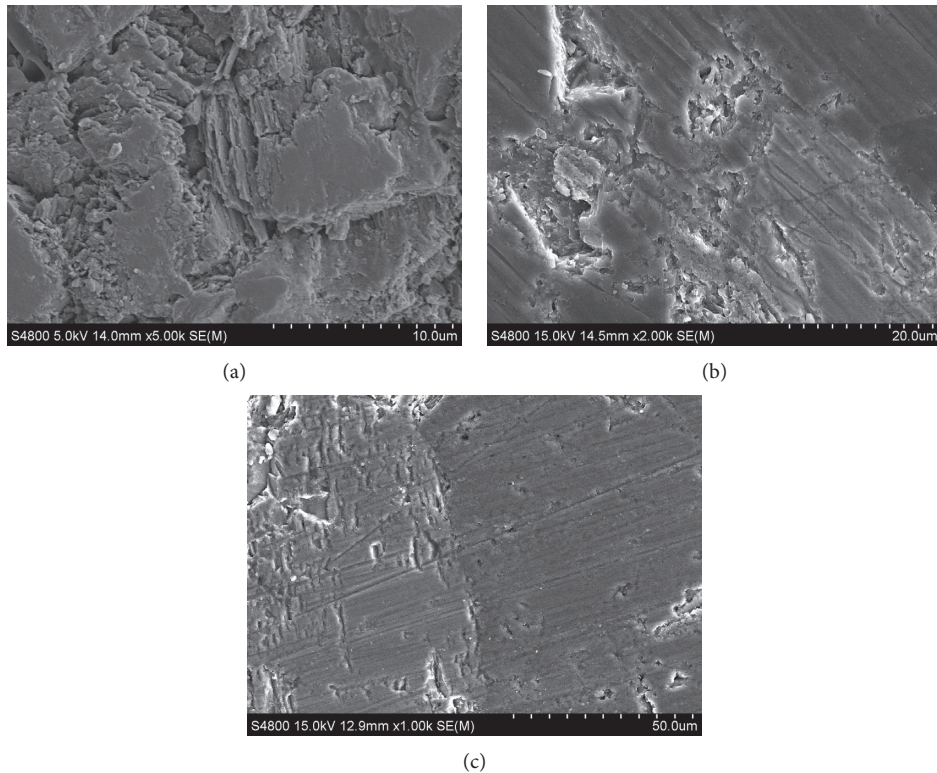


FIGURE 10: Micromorphology of the basalt surface: (a) before the polishing process; (b) after 20×10^4 polishing cycles; (c) after 28×10^4 polishing cycles.

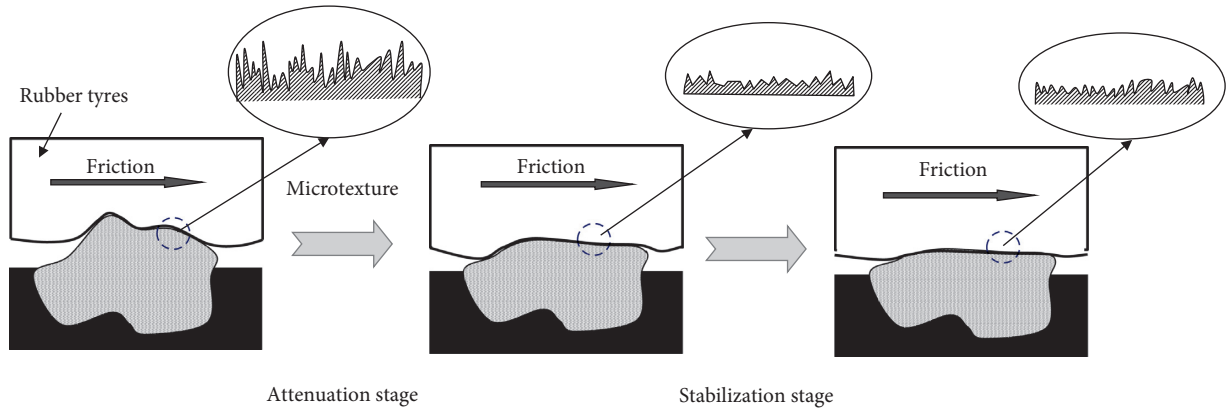


FIGURE 11: Schematic diagram of microtexture change during the long-term polishing process.

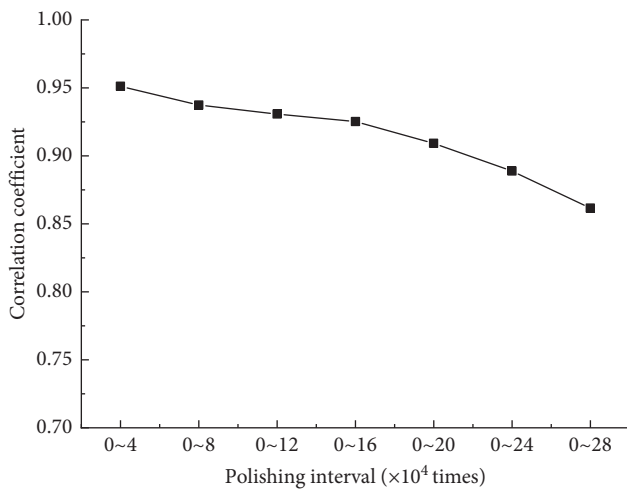


FIGURE 12: Pearson correlation coefficient between PSV and D at different polishing intervals.

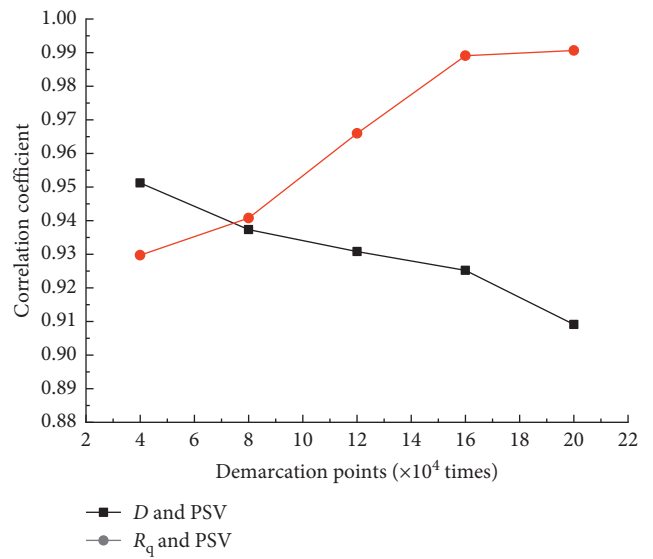


FIGURE 14: The Pearson correlation coefficient between PSV and D or R_q at different demarcation points.

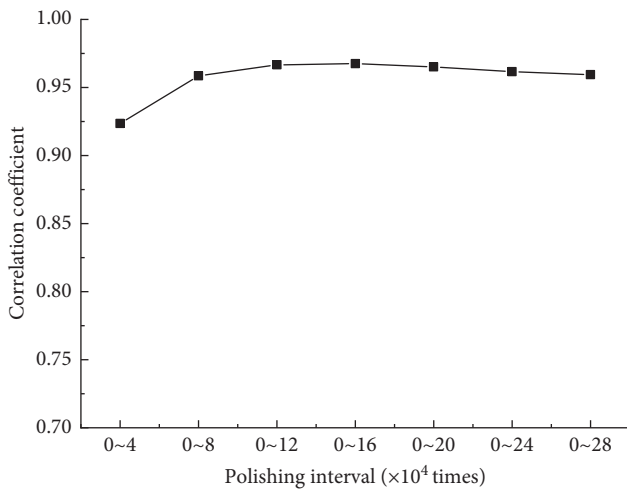


FIGURE 13: Pearson correlation coefficient between PSV and R_q at different polishing intervals.

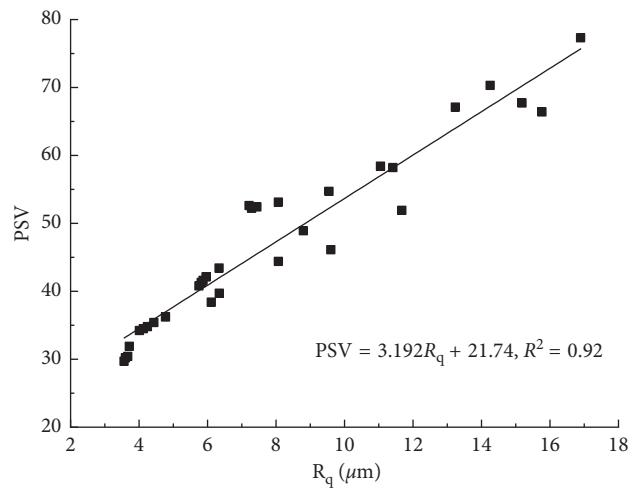


FIGURE 15: Correlation between PSV and R_q .

demarcation point, the Pearson correlation coefficients of PSV and R_q in the after interval ($0 \sim 8 \times 10^4$ times) is higher than the Pearson correlation coefficients of PSV and D in the front interval ($8 \times 10^4 \sim 28 \times 10^4$ times). The microtexture had replaced macrotexture to play a major role in the skid resistance of aggregates. Therefore, the critical point is between 4×10^4 times and 8×10^4 times.

This point may have a relationship with the inflection point of increase and decrease of attenuation rate of PSV, which is shown in Figure 3. In the accelerated attenuation stage, macrotexture plays a major role in the skid resistance of aggregates. When the aggregate is subjected to friction, the angularity of the aggregates is destroyed, and the value of PSV decreases in acceleration. In the decelerated attenuation stage, microtexture gradually plays a major role in the skid resistance of aggregates. The microtexture is destroyed by the external friction slowly, and the value of PSV decreases in the deceleration stage. In the stabilization stage, under the effect of friction, the mineral crystal gradually emerges, and the microtexture maintains a stable state.

In summary, macrotexture has significant influence on the early skid resistance performance of aggregates, and microtexture has significant influence on the long-term skid resistance performance. Due to the fact that polishing of the aggregate in the pavement is the long-term process, microtexture is more important for long-term skid resistance of aggregates. R_q is a suitable indicator to evaluate the long-term skid resistance of aggregates. The correlations between PSV and R_q were studied by a mathematical fitting, which is illustrated in Figure 15. From Figure 15, it can be seen that the correlation coefficient of the linear-fitted equation is 0.92, which shows the good linear correlation between PSV and R_q .

4. Conclusions

- (1) The PSV development is approximately divided into 3 stages including the accelerated attenuation stage, decelerated attenuation stage, and stabilization stage.
- (2) There is a critical point in the entire polishing cycles. When the number of the polishing cycles exceeds this critical point, microtexture replaces macrotexture to play a major role in the skid resistance of aggregates.
- (3) R_q in the stabilization stage is a suitable indicator to evaluate the long-term skid resistance of aggregates.
- (4) Due to the highest value of R_q in the stabilization stage, bauxite had higher skid resistance during the long-term polishing process, and it was suitable for the wearing course, especially high friction surface treatment.

Data Availability

The authors would like to declare that all the data in the manuscript were obtained by experiment, and the data are true and effective in the manuscript.

Conflicts of Interest

The authors declare that they have no conflicts of interest.

Acknowledgments

The authors wish to thank the National Key R&D Program of China (2017YFB0309903), the Qinghai Provincial Natural Science Foundation (2017-ZJ-764), Traffic Construction Project of Science and Technology of Shaanxi Province (16-16K), National Natural Science Foundation of China (51608046), and Special Fund for Scientific Research of Central Colleges, Chang'an University (310831172201, 300102318401, and 300102318501).

References

- [1] K. W. Anderson, M. Russell, J. S. Uhlmeier et al., *Kwik Bond Polymers® High Friction Surface Treatment*, Washington State Department of Transportation, Olympia, WA, USA, 2015.
- [2] Q. J. Li, G. W. Yang, K. C. Wang, Y. Zhan, D. Merritt, and C. Wang, "Effectiveness and performance of high friction surface treatments at a national scale," *Canadian Journal of Civil Engineering*, vol. 43, no. 9, pp. 812–821, 2016.
- [3] V. Reddy, T. Datta, P. Savolainen et al., "A study of the effectiveness of tyre grip high friction surface treatment," *Accident Reconstruction Journal*, vol. 19, no. 5, pp. 53–57, 2009.
- [4] M. Heitzman, P. Turner, and M. Greer, "High friction surface treatment alternative aggregates study," NCAT Report 15-04, Auburn University, Auburn, AL, Australia, 2015.
- [5] S. Li, R. Xiong, D. Yu, G. Zhao, P. Cong, and Y. Jiang, "Friction surface treatment selection: aggregate properties, surface characteristics, alternative treatments and safety effects," Tech. Rep. FHWA/IN/JTRP-2017/09, Purdue University, West Lafayette, IN, USA, 2017.
- [6] X. Chen, S. Dai, Y. Guo, J. Yang, and X. Huang, "Polishing of asphalt pavements: from macro-to micro-scale," *Journal of Testing and Evaluation*, vol. 44, no. 2, pp. 885–894, 2015.
- [7] S. J. Dews and R. J. Bishop, "Factors affecting the skid-resistance of calcined bauxite," *Journal of Chemical Technology and Biotechnology*, vol. 22, no. 10, pp. 1117–1124, 2010.
- [8] JTG E42-2005, *Test Methods of Aggregate for Highway Engineering*, Research Institute of Highway of the Ministry of Communications, Ministry of Communications of the PRC, Beijing, China, 2005.
- [9] K. D. Lawrence and B. Ramamoorthy, "Surface texture evaluation of cylinder liners using machine vision," in *Proceedings of the 11th WSEAS International Conference on Electronics, Hardware, Wireless and Optical Communications, and Proceedings of the 11th WSEAS International Conference on Signal Processing, Robotics and Automation, and Proceedings of the 4th WSEAS International Conference on Nanotechnology*, World Scientific and Engineering Academy and Society (WSEAS), pp. 143–148, Cambridge, UK, February 2012.
- [10] R. A. Boby, M. Hanmandlu, A. Sharma et al., "Extraction of fractal dimension for iris texture," in *Proceedings of Iapri International Conference on Biometrics*, pp. 330–335, New Delhi, India, September 2012.
- [11] R. Kumar, P. Kulashakar, B. Dhanasekar, and B. Ramamoorthy, "Application of digital image magnification for surface roughness evaluation using machine vision," *International Journal of Machine Tools and Manufacture*, vol. 45, no. 2, pp. 228–234, 2005.

- [12] Z. Qian and L. Meng, "Study on micro-texture and skid resistance of aggregate during polishing," *Frontiers of Structural and Civil Engineering*, vol. 11, no. 3, pp. 346–352, 2017.
- [13] B. K. Abban, A. T. Papanicolaou, C. P. Giannopoulos et al., "Quantifying the changes of soil surface micro roughness due to rainfall impact on a smooth surface," *Nonlinear Processes in Geophysics*, vol. 24, no. 3, pp. 569–579, 2017.
- [14] International Organization for Standardization, *Geometrical Product Specifications (GPS)-surface Texture: Profile Method-terms, Definitions and Surface Texture Parameters*, ISO, Geneva, Switzerland, 1997.
- [15] G. V. Samsonov, *Mechanical Properties of the Elements, Handbook of the Physicochemical Properties of the Elements*, Springer, New York, NY, USA, 1968.

Research Article

High- and Low-Temperature Properties and Thermal Stability of Silica Fume/SBS Composite-Modified Asphalt Mortar

Cao Kai,¹ Xu Wenyuan ,¹ Chen Dan,² and Feng Huimin¹

¹College of Civil Engineering, Northeast Forestry University, Harbin 150040, China

²Beijing Municipal Engineering Design and Research Institute Co., Ltd., Beijing 100082, China

Correspondence should be addressed to Xu Wenyuan; xuwenyuan@nefu.edu.cn

Received 2 April 2018; Accepted 20 June 2018; Published 12 July 2018

Academic Editor: Ghazi G. Al-Khateeb

Copyright © 2018 Cao Kai et al. This is an open access article distributed under the Creative Commons Attribution License, which permits unrestricted use, distribution, and reproduction in any medium, provided the original work is properly cited.

Recently, China has started paying more attention to environmental protection, and the efficient utilization of exhaust gases produced by smelting has emerged as a key problem concern. The silica fume collected from the exhaust gases produced by smelting ferrosilicon or industrial silicon was often used as a cement concrete admixture. Using silica fume as an asphalt modifier can make exhaust gases profitable. In this study, silica fume/SBS composite-modified asphalt mortar was prepared to improve the performance of asphalt. The effects of the silica fume content, temperature, and ratio of filler asphalt on the composite-modified asphalt mortar were studied through the cone penetration, softening point, viscosity, dynamic shear rheological (DSR) test, and bending beam rheometer (BBR) test. The thermal stability of composite-modified asphalt was analyzed through the thermal analysis test. The results showed that with the increase of silica fume content and ratio of filler asphalt, the high-temperature performance of asphalt mortar was improved; the content of silica fume had a great influence on the low-temperature performance of asphalt mortar, the optimum silica fume content was 7%; increasing the ratio of filler asphalt reduced the low-temperature cracking resistance of asphalt mortar; the incorporation of silica fume enhanced the initial decomposition temperature, thermal residual rate, temperature in which the weight loss rate reaches the maximum, and the endothermic peak of maximum temperature and improved the properties of asphalt.

1. Introduction

Asphalt pavement constitutes more than 90% of the expressway in China for its good smoothness, low noise, convenience, and ease of maintenance [1, 2]. Therefore, the study of the high-quality modified asphalt and its mixtures has become an important research area in the field of road traffic, for reducing the early disease and prolonging the service life of asphalt pavement. SBS-modified asphalt is widely used in highway construction because of its excellent comprehensive performance. However, rutting, translation, bleeding, shoving, bulging and cracking, aging, and other diseases arising from the use of the pavement are also difficult problems that have been plaguing road practitioners for long [3–5]. Therefore, it is imperative to study the composite-modified asphalt mixture to meet the requirements of high flow, heavy load, stability, durability, and high strength.

It has been found that silica fume has many properties, such as abundant reserves, low cost, large specific surface area, low thermal conductivity, strong thermal stability, and strong adsorption capacity. It has great advantages in improving asphalt's high- and low-temperature performance, fatigue performance, and water stability [6–11]. Wei et al. studied the diatomite and SBS composite-modified asphalt by using regression analysis and a modified grey model. They found that diatomite could reduce the air void and improve the indirect tensile strength and indirect tensile stiffness modulus of crumb rubber-modified stone mastic asphalt (SMA) [12]. Luo et al. analyzed a modified mechanism of diatomite-modified asphalt by using the infrared (IR) spectrum and scanning electron microscope (SEM). They also inferred a model diagram of the modification process with four components of asphalt [13]. Tan et al. carried out the low-temperature bending test, low-temperature compression test, and contraction coefficient test of matrix

asphalt mixture and diatomite-modified asphalt mixture. Their test results indicated that the addition of silica fume could improve the low-temperature performance and increase the contraction coefficient of the mixture [14].

In this paper, the preparation of silica fume/SBS composite-modified asphalt was investigated. The high-temperature performance and low-temperature performance of silica fume/SBS composite-modified asphalt mortar were evaluated by the cone penetration, softening point, viscosity, DSR, and BBR. The mechanism of modification and the microscopic characteristics of composite-modified asphalt were analyzed through a thermal analysis test.

2. Test Preparation

2.1. Materials. The matrix asphalt used in this experiment was AH-90 (Panjin) asphalt, and the modifiers were made of SBS (4601, LCY Rubber Co., Ltd., Huizhou, Guangdong Province of China) and silica fume (Anmei International Trade Industrial Development Co., Ltd., Anshan, Liaoning Province of China). The technical indicators of the raw materials are shown in Table 1.

2.2. Preparation of Composite-Modified Asphalt. In this study, a high-speed shear stirred emulsifier (FLU-KOAF25) for modified asphalt was used to prepare modified asphalt. Firstly, the matrix asphalt was heated to a molten state. Then, SBS (mass fraction 4%) and dry silica fume were added into the matrix asphalt. Shearing was initiated at a speed of 5000 r/min at 170°C to 190°C. The shearing duration was performed for one hour. Finally, the finished silica fume/SBS composite-modified asphalt was made by stirring for 30 min. Composite-modified asphalt mortars were obtained by adding fillers into the modified asphalt.

The effects of silica fume content on composite-modified asphalt were studied by fixing the ratio of filler asphalt at 1.0 and varying the amount of silica fume (mass fraction 1%, 4%, 7%, 10%, and 13%). Similarly, the effects of the ratio of filler asphalt on composite-modified asphalt were studied by fixing the content of silica fume at 7% and varying the ratio of filler asphalt (0.6, 0.8, 1.0, 1.2, and 1.4).

2.3. Experimental Methods

2.3.1. Cone Penetration Test. Silica fume/SBS composite-modified asphalt mortar is a heterogeneous material, and the discreteness of data would be very large if the conventional penetration test is used to evaluate its denseness [15–17]. In this paper, the cone penetration test was used to evaluate the consistency of the asphalt mortars. The angle of the cone was 30°, and the cone was made of stainless steel. The inner diameter of the dish was 70 mm, and the inner depth was 45 mm. The total weight of the cone, the connecting rod, and the balancing weight were 195 g. The test temperature was 25°C (ASTM D5/D5M-2013).

TABLE 1: Indicators of raw materials.

Materials	Property	Value
Matrix asphalt	Penetration (25°C, 0.1 mm)	83
	Ductility (15°C, cm)	>100
	Softening point (°C)	46
	Penetration index	-1.4
	Dynamic viscosity (60°C, Pa·s)	175
	Density (g/cm ³)	1.004
SBS	Block ratio	30/70
	Tensile strength (MPa)	21.6
	Elongation at break (%)	850
	Relative molecular mass	28×10^4
Silica fume	Appearance	Grey
	SiO ₂ content (%)	>92
	pH	6~8
	Particle size distribution (μm)	0.1~0.3
	Granularity (mesh)	300~500
	Loose density (g/cm ³)	0.1~0.2
	Tight heap density (g/cm ³)	0.3~0.4
	Specific surface area (m ² /g)	>25
	Burning loss (%)	<5
	Impurity content (%)	<8
Water content (%)	<5	

2.3.2. Softening Point Test. The softening point test is another test that can be used to measure the denseness of the asphalt mortar. The ring and ball method was used to determine the softening point (ASTM D36/D36M-2014).

2.3.3. Brookfield Viscosity Test. Brookfield viscosity is an important index of rheological properties of asphalt. The high-temperature performance of asphalt is evaluated by measuring the torque of the shaft rotating at certain speed in the asphalt. In this study, the test was conducted at a temperature of 177°C (ASTM D4420).

2.3.4. Dynamic Shear Rheological (DSR) Test. The flow characteristics of the polymer materials are evaluated by rotational shearing at a certain speed. In this paper, a stress control mode was adopted. The stress level was 0.1 kPa, and angular frequency was 10 rad/s. The diameters of the samples were 25 mm (the thickness is 1 mm) and 8 mm (the thickness is 2 mm) (AASHTO T315-09).

2.3.5. Bending Beam Rheometer (BBR) Test. The flexural creep stiffness (S) and creep rate (m) were obtained by studying the stiffness modulus of a bituminous beam under creep load in the BBR test. The low-temperature cracking resistance of asphalt mortars is evaluated from S and m . The size of the bituminous beam: the length was 102.00 mm, the width was 12.70 mm, and the height was 6.35 mm (AASHTO T313-09).

2.3.6. Thermal Analysis Test. These experiments were conducted in the analysis and testing center of Northeast Forestry University. The data were acquired using the synchronous thermogravimetric analyzer (STA409PC,



FIGURE 1: Silica fume.

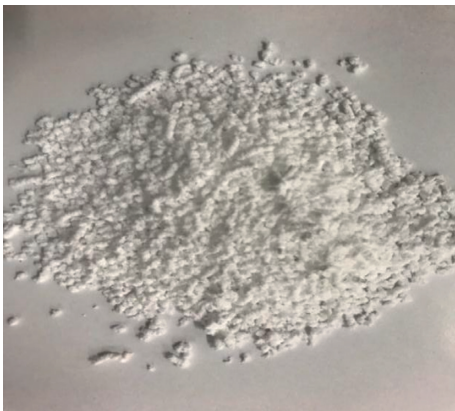


FIGURE 2: SBS.

NETZSCH Instrument Company, Germany). The atmosphere was nitrogen gas atmosphere, the rate of ventilation was 120 ml/min, the heating rate was 20°C/min, and the range of temperature was 35~600°C Figures 1 and 2.

3. Results and Discussion

3.1. Cone Penetration. As could be seen from Figure 3, the cone penetration of the asphalt mortar decreased with the increase in the content of silica fume. The results showed that the shear strength of the asphalt mortar was enhanced by the addition of silica fume. The saturated and aromatic components in the asphalt were sucked into the pores of silica fume, which increased the content of asphaltene and pectin relatively. Thus, asphalt became thicker, the shear strength increased, and the cone penetration decreased [18, 19]. Figure 4 shows that the cone penetration of asphalt mortar decreased with the increase in filler content. It could be seen that increasing the ratio of filler asphalt greatly improves the high-temperature performance of asphalt mortar.

3.2. Brookfield Viscosity at 177°C and Softening Point. According to the data in Figure 5, the viscosity at 177°C and the softening point of silica fume/SBS composite-modified

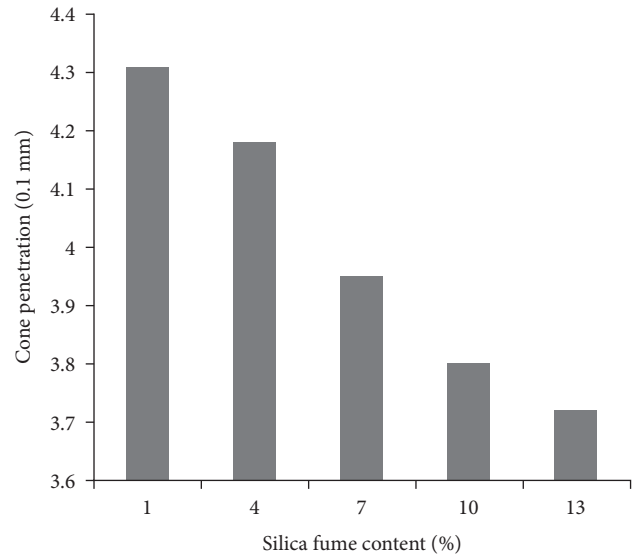


FIGURE 3: Influence of the content of silica fume on the cone penetration.

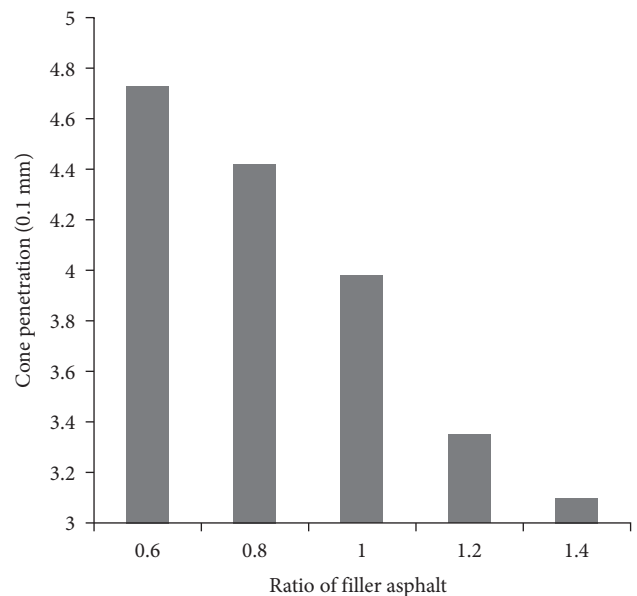


FIGURE 4: Influence of the ratio of filler asphalt on the cone penetration.

asphalt mortar increased obviously with increasing the content of silica fume. These data suggested that the small particle size and large specific surface area of silica fume cause the particles to come in closer contact with the asphalt. The strong adsorbability of silica fume was beneficial in strengthening the intermolecular force and increasing the thickness of the structural asphalt [18]. Thus, the coherence between the asphalt and the aggregate was enhanced, and the high-temperature stability of the asphalt mortar was improved.

As is shown in Figure 6, the softening point and the Brookfield viscosity of the asphalt mortar were improved greatly because of the increase in the ratio of filler asphalt. It was similar to the researches conducted by Wu et al. [20] and

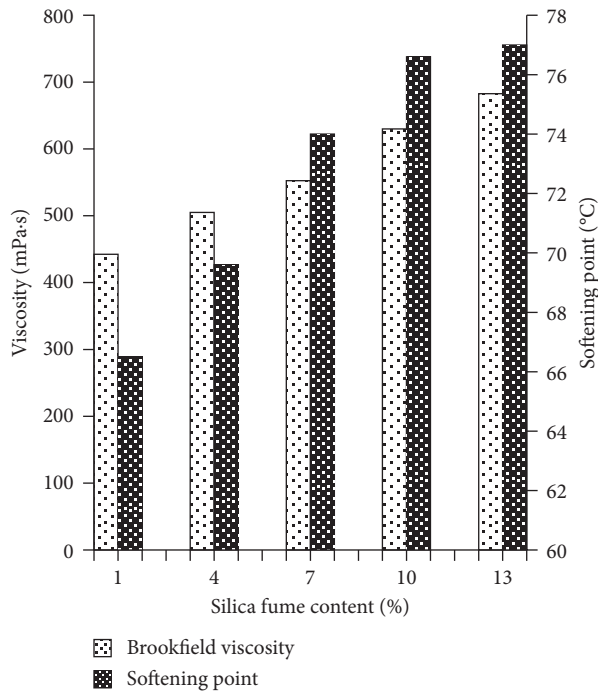


FIGURE 5: Influence of the content of silica.

Zhang et al. [21]. They assumed that the increase of the content of filler would enhance the adsorption between asphalt and filler. Therefore, the ratio of structural asphalt was increased, and the viscosity and strength of asphalt were enhanced.

3.3. DSR. According to the data from Table 2, as the content of silica fume increased, the complex shear modulus (G^*) increased gradually, whereas the phase angle (δ) decreased gradually. It could be concluded that the addition of silica fume enhanced the ability of asphalt mortar to resist stress, increased the relative proportion of the elastic components in the asphalt, and reduced the permanent deformation. The rutting factor ($G^*/\sin \delta$) increased with the increase in the content of silica fume. With increase in the content of silica fume, the ability of the asphalt mortar to resist the high-temperature rutting increased.

When the content of silica fume was the same, through comparing G^* and δ of 58°C, 64°C, 70°C, 76°C, and 82°C, it was found that with the increase in the test temperature, the complex shear modulus (G^*) of asphalt mortar decreased and δ increased. The results showed that the asphalt mortar was a typical temperature-sensitive material. The change in temperature could change the ability of asphalt mortar to resist stress rapidly. As the temperature increased, some of the elastic components of the asphalt mortar changed into viscous components, resulting in the decrease of $G^*/\sin \delta$, which indicated the decline of high-temperature performance of the asphalt mortar.

The relationship between the rutting factor and the ratio of filler asphalt is illustrated in Figure 7. It could be observed that the rutting factor ($G^*/\sin \delta$) increased gradually with the increase in the ratio of the filler asphalt. It is indicated that

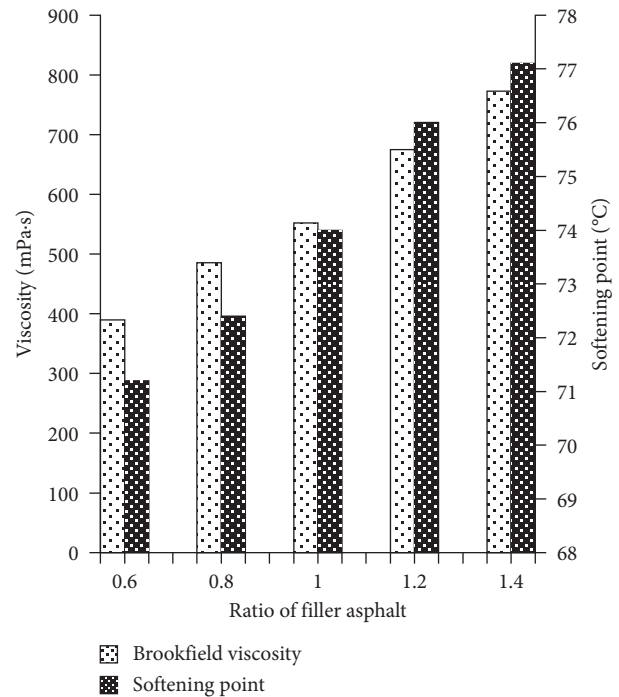


FIGURE 6: Influence of the ratio of filler asphalt on softening point and Brookfield viscosity.

the increase of the content of filler is helpful to improve the high-temperature performance of the asphalt mortar. Adding filler into asphalt mortar would increase the volume of mortar significantly because of the specific surface area of the filler. Therefore, the proportion of structural asphalt would increase and the cohesive force of asphalt mortar would be improved. Thus, the high-temperature stability of the asphalt mortar would be improved.

In order to obtain rheological properties of asphalt in wider frequency range, the frequency sweep test was carried out. As is shown in Figures 8 and 9, with the increase of frequency, the complex modulus of three kinds of asphalt increased. However, the phase angle had a downtrend as a whole. The complex modulus of silica fume/SBS composite-modified asphalt at low frequency (high temperature) was larger than SBS-modified asphalt, and the complex modulus was smaller than SBS-modified asphalt at high frequency (low temperature). On the contrary, it was proved that the addition of silica fume further improved the high- and low-temperature performance of asphalt.

3.4. BBR. The creep rate (m) reflects the stress relaxation performance of the asphalt mortar and the sensitivity of the stiffness with time, and the creep stiffness (S) reflects the flexibility of the mortar. The higher the value of m was, the better the anticracking performance of the asphalt mortar at low temperature would be. Moreover, the smaller the S was, the better the flexibility of the asphalt mortar at low temperature would be. As could be seen from Figure 10, with the increase in silica fume content, the bending creep stiffness of asphalt mortar at -12°C, -18°C, and -24°C

TABLE 2: Results of DSR.

Test parameters	Temperature (°C)	Silica fume content (%)				
		1	4	7	10	13
G^* (kPa)	58	19.8	20.091	20.125	20.156	20.847
	64	9.716	9.847	10.123	10.234	10.319
	70	4.966	5.086	5.222	5.229	5.286
	76	2.693	2.724	2.771	2.771	2.805
	82	1.531	1.538	1.544	1.556	1.58
Δ (°)	58	76.14	76.12	75.52	75.07	74.33
	64	79.3	78.81	77.6	77.17	76.66
	70	81.44	81.33	79.85	78.89	78.39
	76	84.46	83.88	83.2	81.19	79.66
	82	84.94	84.71	83.97	82.56	80.45
$(G^*/\sin \delta)$ (kPa)	58	20.394	20.695	20.785	20.860	21.652
	64	9.888	10.038	10.474	10.496	10.605
	70	5.022	5.145	5.305	5.329	5.396
	76	2.706	2.740	2.791	2.804	2.872
	82	1.537	1.545	1.553	1.569	1.602

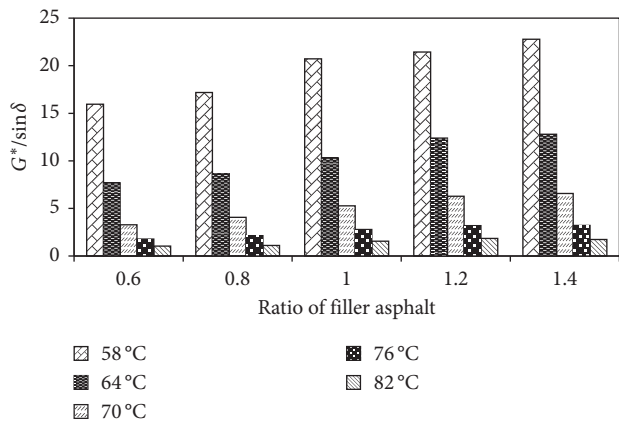


FIGURE 7: Influence of the ratio of filler asphalt on the rutting factor.

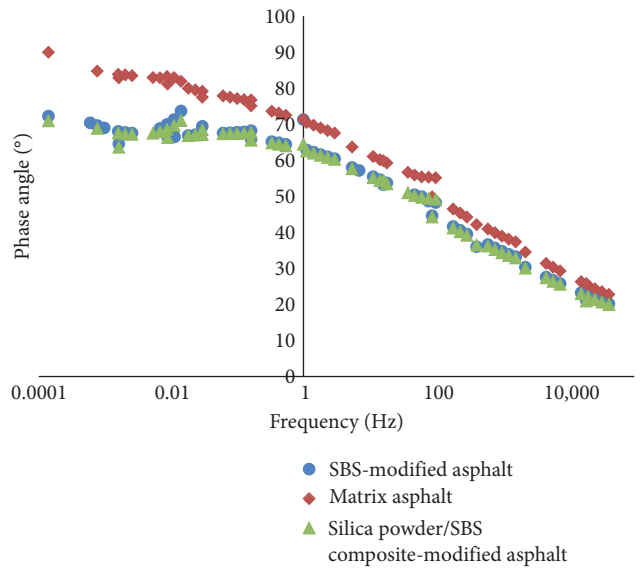


FIGURE 9: Phase angle master curve.

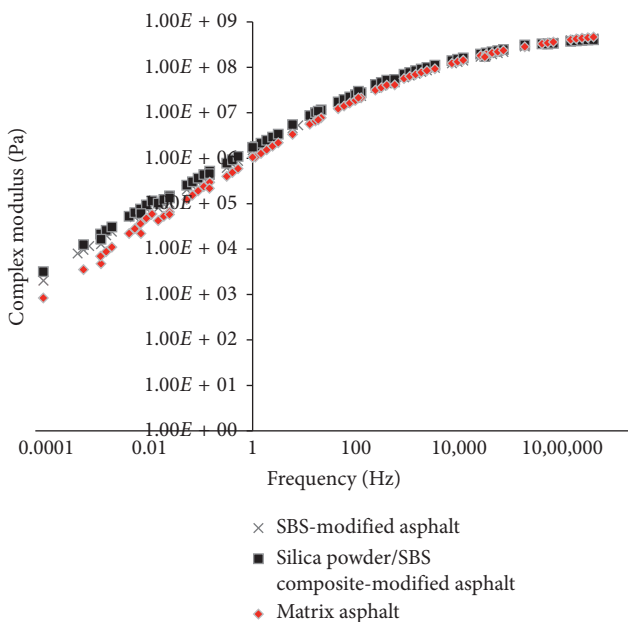


FIGURE 8: Complex modulus master curve.

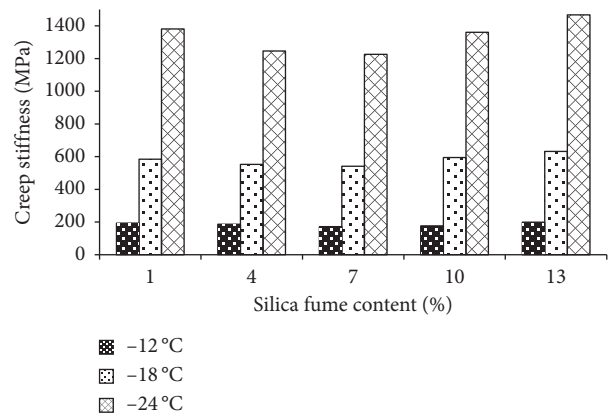


FIGURE 10: Influence of the content of silica fume on the creep stiffness.

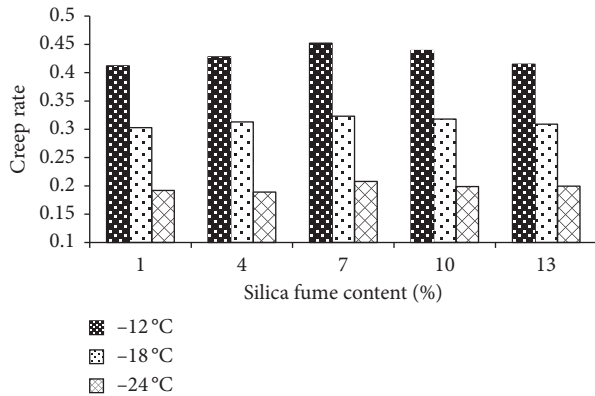


FIGURE 11: Influence of the content of silica fume on the creep rate.

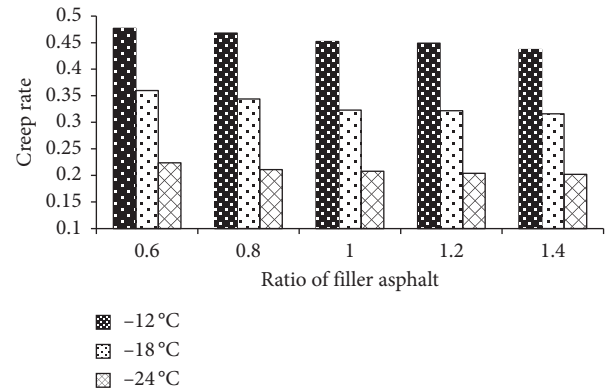


FIGURE 13: Influence of the ratio of filler asphalt on the creep rate.

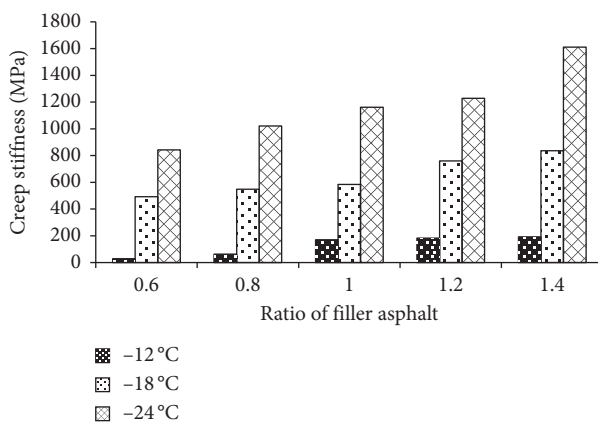


FIGURE 12: Influence of the ratio of filler asphalt on the creep stiffness.

decreased initially and then increased, indicating that a small amount of silica fume was helpful to improve the low-temperature anticracking performance, however, more than 7% would damage its low-temperature performance. It could be seen from Figure 11 that the creep rate of asphalt mortar increased initially and then decreased with the increase in the silica fume content, indicating that the stress relaxation ability was the best for approximately 7% silica fume content. Therefore, the recommended percentage of silica fume is not more than 7%.

Figures 12 and 13 show that the bending creep stiffness of the asphalt mortar increased and the creep rate decreased with the increase in the ratio of silica fume. It was indicated that the addition of filler would reduce the fluidity of structural asphalt and reduce the flexibility of the mortar. Therefore, the increase in the ratio of filler asphalt was not beneficial to the improvement of the anticracking performance of the asphalt mortar at low temperature.

4. Thermal Analysis Test

The thermogravimetric test will generate a thermogravimetric analysis (TGA) curve, which takes the temperature or time as the transverse coordinate and the mass change as the longitudinal coordinate. The pyrolysis properties of the

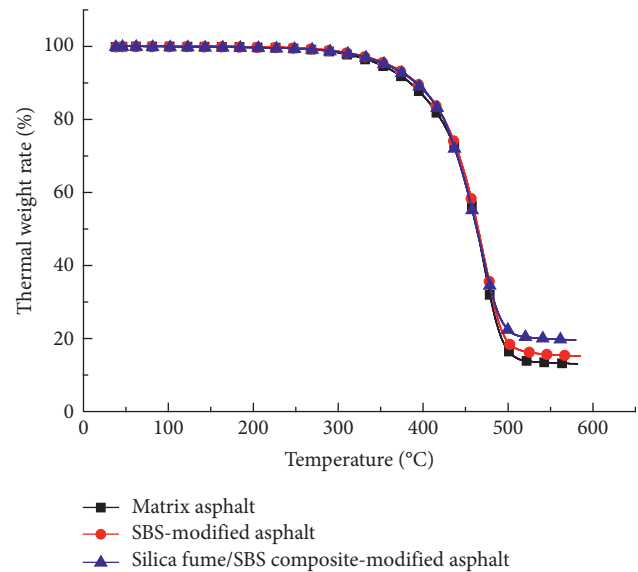


FIGURE 14: TGA curve.

asphalt, such as the initial decomposition temperature, maximum decomposition rate, and the mass residual rate, can be obtained from the TGA curve. The differential thermogravimetry (DTG) curve is the first derivative of the TGA curve to temperature (or time), and it reflects the relationship between the change rate of the quality of asphalt (dm/dt) and temperature (or time): $dm/dt = f(T)$ or $f(t)$. The rate of weight loss can be analyzed using the DTG curve. The differential scanning calorimetry (DSC) test shows that the peak, peak width, and peak area of the DSC curve are closely related to the microstructure characteristics of the sample. The macroperformance of composite-modified asphalt is mainly affected by the aggregation state of asphalt and modifier, while the aggregation state of asphalt and modifier in the range of endothermic peak temperature is also reflected in the location and area of endothermic peak [22]. The thermal analysis curves of matrix asphalt, SBS-modified asphalt, and silica fume/SBS composite-modified asphalt are shown in Figures 14–16.

The analysis of the TGA curve showed that the thermal weight loss rate of the matrix asphalt was 100% when the

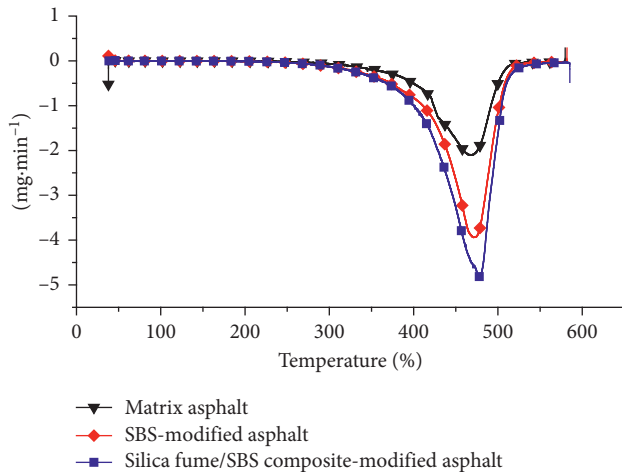


FIGURE 15: DTG curve.

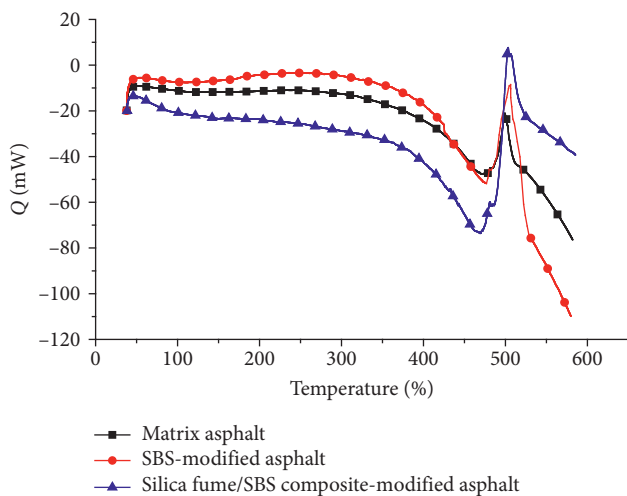


FIGURE 16: DSC curve.

temperature was within the range of (35°C, 220°C). When the temperature increased to 220°C, the thermal weight loss rate of matrix asphalt began to decrease, which indicated that the matrix asphalt began to decompose at 220°C. When the temperature was above 350°C, the TGA curve decreased rapidly and the mass residual rate of the sample decreased rapidly until it was almost lost. At the end of the test, the mass residual rate was approximately 12%. In the same way, the SBS-modified asphalt was decomposed at 235°C, and the final mass residual rate of the sample was approximately 16%. The silica fume/SBS composite-modified asphalt was decomposed at about 255°C, and the final mass residual rate of the sample was approximately 20%.

By analyzing the DTG curve, it was found that the matrix asphalt had a peak at 468°C, indicating that the decomposition rate of the asphalt was the fastest at 468°C. When the weight loss rate of SBS-modified asphalt reached the maximum value, the temperature was 474°C, and the temperature of the weight loss rate of the silica fume/SBS composite-modified asphalt reached the maximum value at 477°C.

As we could see from the DSC curve, the slope of the curve was larger when the temperature of the matrix asphalt was 35°C and 50°C. Then, the curve began to slow down when the temperature exceeded 50°C. It was shown that with the increase of temperature, the heat absorption of asphalt was larger before the softening point was reached, and the absorption heat was reduced after reaching the softening point. When the temperature reached 350°C, the DSC curve dropped rapidly and the heat absorption increased obviously. The curve reached the peak of an endothermic peak at 468°C and the area of the absorption peak was 2681 mJ. When the temperature reached 475°C, the curve of SBS-modified asphalt reached the peak of heat absorption and the area of the absorption peak was 3189 mJ. When the temperature reached 473°C, the curve of silica fume/SBS composite-modified asphalt reached the peak of heat absorption and the area of the absorption peak was 6014 mJ. Compared with the matrix asphalt and SBS-modified asphalt, the trend of the DSC curve of silica fume/SBS composite-modified asphalt is relatively gentle in the early stage. The whole endothermic peak is relatively backward. The temperature of the heat absorption peak is larger, and the acreage of the endothermic peak is larger. On the contrary, it indicated that the addition of silica fume improved the high-temperature performance of asphalt.

To sum up, the high-temperature performance of composite-modified asphalt is better than that of SBS-modified asphalt. Therefore, the addition of silica fume and SBS has a positive effect on the high-temperature performance of asphalt. Because the thermal conductivity of silica fume is very low. Adding this material to the asphalt will definitely reduce the thermal conductivity of composite-modified asphalt, improve its thermal resistance, and make it stable at high temperatures. Moreover, being a porous filler, silica fume has a lot of excellent characteristics such as small particle size of microvoids, large dead volume, strong adsorption capacity, low packing density, high filling amount, and large specific surface area. Silica fume is homogeneously dispersed in asphalt after physical mixing, and a homogeneous suspension system is formed. Then, the effective flow volume of the system would be reduced. At the same time, the large specific surface area and absorbability give it large surface energy; therefore, it can selectively adsorb light components in asphalt. The bonding strength of the adsorption layer of the boundary is enhanced, which greatly reduces the flow characteristics of modified asphalt and increases the rheological resistance. Therefore, the composite-modified asphalt shows better high-temperature performance.

5. Conclusions

In this paper, a series of tests were performed on matrix asphalt, SBS-modified asphalt, and silica fume/SBS composite-modified asphalt to study their properties. From the cone penetration test and DSR, it was observed that the cone penetration and the phase angle (δ) decreased with increase in silica fume content. However, the softening

point, Brookfield viscosity, complex shear modulus (G^*), and the rutting factor ($G^*/\sin \delta$) increased, indicating that the addition of silica fume could significantly improve the high-temperature performance of the asphalt mortar. The creep stiffness (S) decreased initially and then increased, whereas the creep rate (m) increased initially and then decreased. Therefore, the recommended percentage of silica fume was fixed at 7%. An increase in the ratio of filler asphalt increased the high-temperature performance of the asphalt mortar greatly; however, the anticracking performance of the asphalt mortar deteriorated at low temperature. The addition of silica fume and SBS could improve the initial decomposition temperature, residual rate of thermogravimetry, the temperature in which the weight loss rate reached the maximum, and the area of the absorption peak. Therefore, the high-temperature stability was enhanced.

Data Availability

All tests were carried out in the standard laboratory according to the methods listed in the paper. The data were reliable.

Conflicts of Interest

The authors declare that there are no conflicts of interest regarding the publication of this paper.

Acknowledgments

This work was supported by Transportation Science and Technology Project of Heilongjiang Province (2015hljtt017).

References

- [1] Z. S. Liu, "China transportation development strategies review," *China Transportation Review*, vol. 39, no. 8, pp. 1–6, 2017.
- [2] C. T. Yang, "13th five-year period development situation and basic thought of transportation," *China Water Transport*, vol. 1, pp. 10–14, 2016.
- [3] X. M. Huang, *Bitumen and Bitumen Mixture*, Southeast University Press, Nanjing, China, 2002.
- [4] L. B. Gao, Z. R. Wang, and C. N. Deng, "Analysis on the producing mechanism and the influence factors of rutting in expressway pavement," *Journal of Shenyang Jianzhu University*, vol. 24, no. 1, pp. 67–71, 2008.
- [5] X. Z. Cui, D. Huang, L. Liu et al., "A review of mechanics of asphalt pavement disease," *Journal of Shandong University*, vol. 46, no. 5, pp. 68–83, 2016.
- [6] D. P. Zhu, J. Z. Zhang, J. B. Chen et al., "Experiment on road performance of diatomite modified asphalt mixture in permafrost regions," *China Journal of Highway and Transport*, vol. 26, no. 4, pp. 23–28, 2013.
- [7] A. Baldi-Sevilla, M. L. Montero, J. P. Aguiar et al., "Influence of nano silica and diatomite on the physicochemical and mechanical properties of the binder at unaged and oxidized conditions," *Construction and Building Materials*, vol. 127, pp. 176–182, 2016.
- [8] P. L. Cong, S. F. Chen, and H. X. Chen, "Effects of diatomite on the properties of asphalt binder," *Construction and Building Materials*, vol. 30, pp. 495–499, 2012.
- [9] Y. Song, J. Che, and Y. Zhang, "The interacting rule of diatomite and asphalt groups," *Petroleum Science and Technology*, vol. 29, no. 3, pp. 254–259, 2011.
- [10] W. F. Chen, P. W. Gao, X. Y. Li, J. X. Le, and S. C. Jin, "Effect of the new type diatomite modifier on the pavement performance of asphalt mixture," *Journal Materials Science and Engineering*, vol. 25, no. 4, pp. 578–581, 2007.
- [11] A. P. Wang, D. C. Li, H. Tan, and H. L. Yu, "Application of diatomite in modified asphalt," *World Geology*, vol. 25, no. 4, pp. 456–459, 2007.
- [12] H. B. Wei, Z. Q. Li, and Y. B. Jiao, "Effects of diatomite and SBS on freeze-thaw resistance of crumb rubber modified asphalt mixture," *Advances in Materials Science and Engineering*, vol. 2017, Article ID 802035, 14 pages, 2017.
- [13] S. J. Luo, N. C. Chen, B. Tan et al., "Mechanism and performance of diatomite modified asphalt," *Acta Material Compositae Sinica*, vol. 34, pp. 2047–2052, 2017.
- [14] Y. Q. Tan, L. Y. Shan, and J. Fang, "Anti-cracking mechanism of diatomite asphalt and diatomite asphalt mixture at low-temperature," *Journal of Southeast University*, vol. 25, no. 1, pp. 74–78, 2009.
- [15] E. R. Brown, J. E. Haddock, and C. Crawford, "Investigation of stone matrix asphalt mortars," *Transportation Research Record*, vol. 1530, pp. 95–102, 1996.
- [16] L. Liu, J. Li, P. W. Hao, and Q. B. Mei, "Evaluation method for property of modified asphalt mortar with diatomite," *Journal of Chang'an University*, vol. 25, no. 3, pp. 23–27, 2005.
- [17] T. Q. Wang, R. F. Yang, A. G. Li et al., "Experimental research on applying the shear strength of cone penetration to performance evaluation of rubber asphalt," *Journal of Hefei University*, vol. 39, no. 3, pp. 380–384, 2016.
- [18] J. P. Xu and Y. N. Bao, "Diatomite-modified-asphalt's mechanism based on microcosmic-test," *Journal of Chang'an University*, vol. 25, no. 6, pp. 14–17, 2005.
- [19] Z. Q. Zhang, X. Y. Zhang, G. Y. Hu et al., "Microcosmic mechanism analysis of the diatomite-modified asphalt," *Journal of Beijing University of Technology*, vol. 33, no. 9, pp. 943–947, 2007.
- [20] M. M. Wu, R. Li, Y. Z. Zhang et al., "Study of high and low-temperature performance of fiber-asphalt mortar," *Journal of China University of Petroleum*, vol. 39, no. 1, pp. 169–175, 2015.
- [21] Z. Q. Zhang, W. P. Zhang, and L. Ping, "Ratio of filler bitumen of asphalt mixture," *Journal of Chang'an University*, vol. 24, no. 5, pp. 7–10, 2014.
- [22] F. Zhang, J. Y. Yu, and J. Han, "Effects of thermal oxidative aging on dynamic viscosity, TG/DTG, DTA and FTIR of SBS- and SBS/sulfur-modified asphalts," *Construction and Building Materials*, vol. 25, no. 1, pp. 129–137, 2011.

Research Article

An Assessment of Reuse of Light Ash from Bayer Process Fluidized Bed Boilers in Geopolymer Synthesis at Ambient Temperature

Woshington S. Brito ¹, André L. Mileo Ferraioli Silva ¹, Rozineide A. A. Boca Santa,²
Kristoff Svensson,³ José Antônio da Silva Souza,³ Herbert Pöllmann,³
and Humberto Gracher Riella²

¹Pará Federal University, 66075-110 Belém, PA, Brazil

²Chemical Engineering Department, Santa Catarina Federal University, 88040-900 Florianópolis, SC, Brazil

³Department of Geosciences and Geography, Martin Luther University of Halle-Wittenberg, Halle 06108, Germany

Correspondence should be addressed to Woshington S. Brito; wsbrito3@gmail.com

Received 31 March 2018; Accepted 20 May 2018; Published 13 June 2018

Academic Editor: Munir Nazzal

Copyright © 2018 Woshington S. Brito et al. This is an open access article distributed under the Creative Commons Attribution License, which permits unrestricted use, distribution, and reproduction in any medium, provided the original work is properly cited.

Sustainable civil construction in the future, besides having low energy consumption and greenhouse gas emissions, must also adopt the principle of reusing wastes generated in the production chain that impact the environment. The aluminum production chain includes refining using the Bayer process. One of the main wastes produced by the Bayer process that has an impact on the environment is fly ash. Geopolymers are cementitious materials with a three-dimensional structure formed by the chemical activation of aluminosilicates. According to studies, some are proving to be appropriate sources of Al and Si in the geopolymerization reaction. The research reported here sought to assess the possibility of reusing fly ash characteristic of the operational temperature and pressure conditions of Bayer process boilers in geopolymer synthesis. Geopolymerization reaction was conducted at an ambient temperature of 30°C, and the activator used was sodium hydroxide (NaOH) 15 molar and sodium silicate (Na₂SiO₃) alkaline 10 molar. Fly ash and metakaolin were used as sources of Al and Si. XRD, XRF, and SEM Techniques were used for characterizing the raw materials and geopolymers. As a study parameter, the mole ratios utilized followed data from the literature described by Davidovits (year), so that the best results of the geopolymer samples were obtained in the 2.5 to 3.23 range. Resistance to mechanical compression reached 25 MPa in 24 hours of curing and 44 MPa after 28 days of curing at ambient temperature.

1. Introduction

The chain for producing aluminum from bauxite to primary aluminum includes refining using the Bayer process. One of the main waste products of the Bayer process is the fly ash collected from the cyclone overflow of the fluidized bed boilers at operational conditions of 900°C of temperature and 120 kPa of pressure. The pressure and temperature conditions influence the specification and morphology of the ash waste generated [1].

In the Bayer process, the circulating-type fluidized bed boilers operate at specific conditions of 900°C and 120 kPa as a means of guaranteeing maintenance of the bed and generate

a specific fly ash characteristic of that process. Fly ashes are classified into two types. These are C type class with a higher amount of calcium oxide and F type class with a lower amount of calcium oxide [2].

When the sum of the levels of silica, alumina, and iron oxide is greater than 70%, the fly ash is classified as class F [3].

Geopolymers are synthesized at a different temperature by the alkaline activation of aluminosilicates derived from natural minerals, calcined clay or industrial by-products 2008. This activation is generally done with metakaolin silicates of sodium or potassium. Geopolymers are inorganic ligands with good resistance to high temperatures and degradation by acid, as well as good mechanical properties. They

are thus an attractive alternative to Portland-type cement, and their use makes it possible to recycle large quantities of industrial wastes. The mechanical properties of geopolymeric materials depend upon the alkaline cation (Na^+), the $\text{SiO}_2/\text{Al}_2\text{O}_3$ molar relation as used by Davidovits and the conditions under which the reaction occurs [4, 5].

The term “geopolymer” describes the chemical properties of aluminosilicate-based inorganic polymers. Geopolymers present properties of cement and therefore have great potential for use in the civil construction industry [6].

The water trapped in a network of geopolymers generates porosity, which results in a reduction of mechanical properties. Their three-dimensional structure is made up of SiO_2 and MAO_4 tetrahedrons, where M is a monovalent cation, typically Na^+ . This network is comparable to some zeolites but differs in its amorphous character. The polymeric character of those materials increases with the $\text{SiO}_2/\text{Al}_2\text{O}_3$ relation, as the aluminum atoms cross the SiO_2 tetrahedron chains [7].

Changing the $\text{SiO}_2/\text{Al}_2\text{O}_3$ relation in geopolymers thus enables the synthesis of materials with different structures. The geopolymerization mechanism is particularly difficult due to the kinetics of the reaction. However, the majority of authors agree that the mechanism involves dissolution, followed by gel polycondensation [8, 9].

Studies show that the mechanical forces of geopolymers increase with elevation of the temperature of kaolin calcination in order to generate metakaolin; however, the ideal temperature for calcination of kaolin is around 700°C for 2 hours [10, 11].

The development of ash-based geopolymer derived from burning coal shows promise as a means of reusing that waste. The worldwide demand for coal will continue to grow up to 2030, achieving a duplication in relation to current demand. With the increasing consumption of coal for generating energy, there will be an increased production of ashes as a byproduct of burning coal [12].

The cements produced by alkaline activation of aluminosilicates were studied in a search for materials with bonding properties more resistant than those of current Portland cements, as well as materials that can be produced with low cost raw materials, little expenditure of energy, and especially with low levels of toxic gas emissions into the atmosphere [13].

Those studies point to excellent possibilities for being implanted around the world and such materials can be produced on a large scale, suppressing the demand for cement in a market that is growing every year. In that context, this study was performed with the objective of assessing the microstructural properties and resistance to compression of geopolymeric materials produced using the light ash characteristic of the Bayer process.

2. Materials and Methods

Fly ash waste was collected from the cyclone overflow of the fluidized bed circulating-type boilers of the Bayer process at conditions of 900°C of temperature and 120 kPa of pressure. That waste was utilized as a source of Si and Al in

TABLE 1: Compositions formulated using fly ashes and metakaolin for obtaining geopolymers.

Geopolymers	Fly ash (mass %)	Metakaolin (mass %)	$\text{SiO}_2/\text{Al}_2\text{O}_3$
1	100	0	4.4
2	94.24	5.76	4.11
3	90.39	9.61	3.94
4	84.62	15.38	3.72
5	75	25	3.4
6	69.2	30.8	3.23
7	61.54	38.46	3.041
8	53.85	46.15	2.87
9	42.31	57.69	2.65
10	34.62	65.38	2.52

TABLE 2: Molar concentration and proportions of the activating solution.

Activator	NaOH	Na_2SiO_3
Molar concentration	15	10
Proportion ($\text{NaOH}:\text{Na}_2\text{SiO}_3$)	1 : 3 in mass of solution	

geopolymer synthesis. Besides the fly ash, another source of Si and Al was metakaolin produced by the calcination of kaolin at a temperature of 800°C for two hours.

To analyze the crystalline structure of ash, kaolin, and metakaolin, X-ray diffractometry (XRD–Bruker LyuxEye) was utilized. For chemical analyses, X-ray fluorescence was employed using equipment from AxiosMinerals (PANalytical), with a ceramic X-ray tube and rhodium anode. For the morphology study, we made use of the scanning electron microscopy (SEM) technique using Zeiss MEO 1430 equipment. Ash and metakaolin were submitted to granulometric analysis of their particles, in a Fritsch Analysette 22 Micro tec plus laser granulometer.

The mole ratios utilized by Davidovits ($\text{SiO}_2/\text{Al}_2\text{O}_3$) are an important parameter for orienting the best compositions for geopolymer synthesis [14]. Ten compositions of geopolymers were formulated using fly ash and metakaolin as a base, with different mole ratios among $\text{SiO}_2/\text{Al}_2\text{O}_3$. Table 1 presents the geopolymers studied with their respective $\text{SiO}_2/\text{Al}_2\text{O}_3$ ratios.

The alkaline activator used for synthesizing the geopolymer was composed of a solution of sodium hydroxide (NaOH) micro pearl (neon, 97% purity). A solution of alkaline sodium silicate (Na_2SiO_3) (Manchester Química do Brasil S.A., $\text{SiO}_2/\text{Na}_2\text{O} = 3.2$) was also used. Table 2 shows the composition of the activator.

The compositions were prepared in a mechanical mixer and placed in cylindrical molds with 100 mm height and diameter of 50 mm. After molding, the molds were submitted to curing at an ambient temperature of 30°C . Geopolymers at 24 hours and 7 and 28 days of curing were submitted to compression resistance testing in an Emic SSII300 press. Geopolymers before and after synthesis were submitted to XRD analysis in order to assess their degree of polymerization. SEM tests were performed after the geopolymer synthesis.

TABLE 3: Chemical composition in % of ash and of metakaolin.

Material	SiO ₂	Al ₂ O ₃	CaO	Fe ₂ O ₃	Na ₂ O	MgO	TiO ₂	P ₂ O ₅	Loi
Ash	42.531	16.399	19.005	7.081	0.941	0.264	0.897	0	12.882
Metakaolin	53.36	43.58	0	0.6	0.33	0	1.51	0.13	0.49

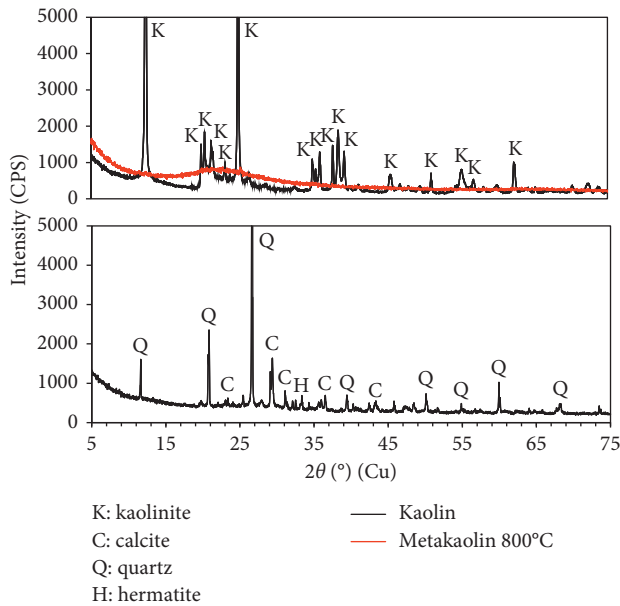


FIGURE 1: XRD of kaolin, of metakaolin, and of fly ash.

3. Results

Table 3 presents the results of the XRF analyses of the materials used in geopolymer synthesis. One may observe (Table 3) the 42.531% level of SiO₂ and 16.399% level of Al₂O₃ in the fly ash used, which indicates that ash is a rich source of Al and Si. Metakaolin (Table 3) is composed of 43.58% Al₂O₃ and 63.36% SiO₂ which characterizes it as a predominant source of aluminum in proportion [15–18].

The use of fly ash waste from burning charcoal as a source of Si and Al favors the geopolymerization reaction and guarantees good durability for the geopolymer [19–23].

According to the result from XRF, the fly ash generated in the Bayer process under the operational temperature and pressure conditions may be classified as C class type fly ash, due to the sum of the levels of silica, alumina, and iron oxide being lower than 70%.

Figure 1 presents the result of the XRD test of fly ash, of kaolin, and of metakaolin calcined at 800°C for 2 hours.

As shown in Figure 1, the calcination of kaolin at 800°C for two hours was satisfactory because it generated a change in the crystalline phase, transforming into an amorphous phase, which characterizes metakaolin.

The change occurring in the material after thermal treatment frees Al and Si for the geopolymerization reaction. Kaolin calcined at a range from 600°C to 800°C for a time interval from 2 to 4 hours, shows itself to be adequate for obtaining metakaolin applied to the development of geopolymer [24–26].

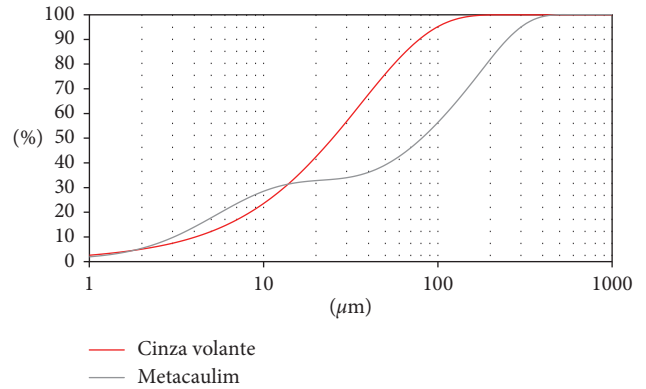


FIGURE 2: Distribution of the size particles for fly ash and metakaolin.

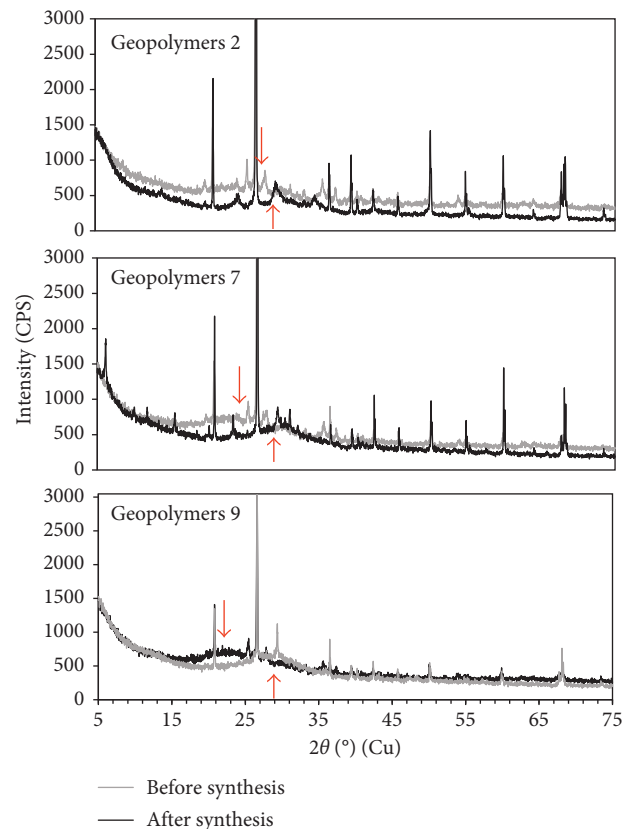


FIGURE 3: XRD of geopolymers 2, 7, and 9 before and after synthesis.

The fly ash generated in aluminum refineries presents quartz and calcite in its composition as shown in the diffractogram for ash in Figure 1.

The distribution of the particle size for the raw materials used in synthesizing the geopolymer resulted in an average

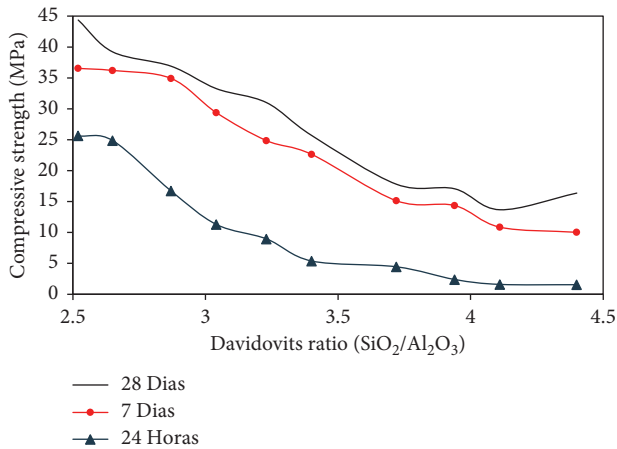


FIGURE 4: Compressive Strength (MPa) of the geopolymers.

diameter (d_{50}) of $24\ \mu\text{m}$ for the fly ash and $88\ \mu\text{m}$ for the metakaolin. Figure 2 presents the results of the laser granulometric analysis for fly ash and metakaolin.

Nath et al. [27] worked on a synthesized geopolymer with fly ash at a granulometry of $4.7\ \mu\text{m}$ and studied the geopolymerization reaction using metakaolin with an average diameter of $18\ \mu\text{m}$.

Figure 3 presents the result of the XRD analysis for geopolymers 2, 7, and 9 with the arrow showing the halo before and after synthesis. According to Salih et al. [5] the geopolymer with the best formed and defined halo indicates larger amorphous zones and thus greater regions of reaction occurrence. In his studies, Salih et al. [5] showed that the greater displacement of the halo after synthesis indicates geopolymers with a greater degree of geopolymerization and thus greater mechanical resistance.

According to the data presented in Figure 3, geopolymer 2 presented a low halo formation, indicating a lower degree of geopolymerization in relation to geopolymer 7. Geopolymer 9 presented a good definition and displacement of the halo before and after the synthesis. That agrees with Figure 4 that presents the results of mechanical compressive strength in MPa, indicating that geopolymer 9 has greater mechanical compressive strength to geopolymers 7 and 2.

Geopolymers with a ratio in the 2.5 to 3.23 range, as indicated by Davidovits, presented mechanical resistance to geopolymers with a greater ratio. Geopolymer 9 with a ratio of 2.65 presented a high compressive strength, reaching values of 25 MPa, 36.22 MPa, and 44 MPa in 24 hours, 7 days, and 28 days of cure, respectively, at ambient temperature. From the results of Figure 4, the geopolymers from samples 8, 9, and 10 in 24 hours achieved the resistance of conventional Portland-type concrete at 28 days of curing, but compressive strength continues to increase in the tested range and is thus higher [28].

Figure 5 presents the result of scanning electron microscopy (SEM) with 500x expansion of geopolymer 9 in (a) and of geopolymer 4 in (b).

In Figure 5, one may observe that geopolymer 9 presented a denser and more homogenous morphology when compared to geopolymer 4. The more uniform morphology

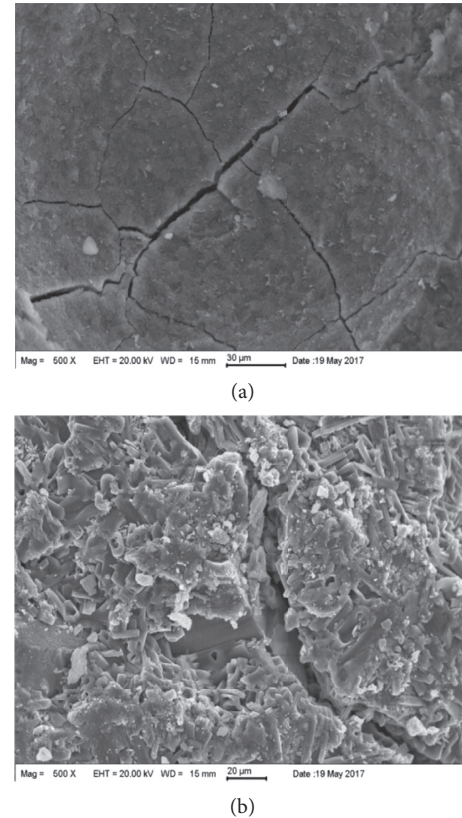


FIGURE 5: Scanning electron microscopy (SEM): (a) Geopolymer 9 increase 500x; (b) Geopolymer 4 increase 500x.

of geopolymer 9 is in accord with the results obtained in the compression resistance tests and also indicated a greater degree of geopolymerization after the reaction. Salehi et al. [29] found in his studies that the denser and more uniform morphological aspects provide greater mechanical performance to the geopolymers and thus greater advance in the geopolymerization reaction.

4. Conclusion

This research made it possible to develop a geopolymer from metakaolin and industrial waste from the Bayer process that contained amorphous aluminosilicates in their composition. The waste utilized was fly ash generated in the operational conditions of the Bayer process. As seen in the procedures, the synthesis of the geopolymer according to the 2.5 to 3.3 mole ratios utilized by the researcher Davidovits was favorable to the process, and geopolymers with greater mechanical compressive strength were obtained. Geopolymers synthesized at ambient temperature with an activator having a composition of 15 molar of sodium hydroxide and 10 molar of alkaline sodium silicate appear to be a viable alternative for supplying demands for cement, achieving resistance superior to that of conventional concretes derived from Portland-type cement. Furthermore, the geopolymers were produced with low emissions of CO_2 , when compared with conventional cements, which is environmentally favorable. With the characterization of the synthesized

geopolymers, it was concluded that the waste from the Bayer process presents a characteristic favorable to the synthesis of geopolymeric materials, classified by the study as class C ash. Our research concludes that synthesized geopolymers have great potential for production of geopolymeric materials.

Conflicts of Interest

The authors declare that they have no conflicts of interest.

Acknowledgments

The authors would like to thank CNPq, CAPES, UFPA, PRODERNA, UFSC, Martin Luther University Halle-Wittenberg, and the Hydro Alunorte company.

References

- [1] M. Ahmaruzzaman, "A review on the utilization of fly ash," *Progress in Energy and Combustion Science*, vol. 36, pp. 327–363, 2010.
- [2] A. Narayanan and P. Shanmugasundaram, "An experimental investigation on flyash-based geopolymer mortar under different curing regime for thermal analysis," *Energy and Buildings*, vol. 138, pp. 539–545, 2017.
- [3] J. B. M. Dassekpo, X. Zha, and J. Zhan, "Synthesis reaction and compressive strength behavior of loess-fly ash based geopolymers for the development of sustainable green materials," *Construction and Building Materials*, vol. 141, pp. 491–500, 2017.
- [4] P. Duxson, J. L. Provis, G. C. Lukey, S. W. Mallicoat, W. M. Kriven, and J. S. J. Deventer, "Understanding the relationship between geopolymer composition, microstructure and mechanical properties," *Colloids and Surfaces A: Physicochemical and Engineering Aspects*, vol. 269, pp. 47–58, 2005.
- [5] M. A. Salih, A. A. A. Abang, and N. Farzadnia, "Characterization of mechanical and microstructural properties of palm oil fuel ash geopolymer cement paste," *Construction and Building Materials*, vol. 65, pp. 592–603, 2014.
- [6] J. Davidovits, *Geopolymer: Chemistry and Applications*, Institut Géopolymère, Saint-Quentin, France, 3rd edition, 2011.
- [7] J. Davidovits, *Geopolymer: Chemistry and Applications*, Institut Geopolymere, St-Quentin, France, 2nd edition, 2008.
- [8] P. Duxson, J. A. Fernandez, J. L. Provis, G. C. Lukey, A. Palomo, and J. S. J. Van Deventer, "Geopolymer technology: the current state of the art," *Journal of Materials Science*, vol. 42, no. 9, pp. 2917–2933, 2007.
- [9] P. Duxson, J. A. Fernandez, J. L. Provis, G. C. Lukey, A. Palomo, and J. S. J. Van Deventer, "The role of inorganic polymer technology in the development of 'green concrete'," *Journal of Materials Science*, vol. 42, pp. 2917–2933, 2007.
- [10] M. R. Wang, D. C. Jia, P. G. He, Y. Zhou, and M. Lett, "Influence of calcination temperature of kaolin on the structure and properties of final geopolymer," *Materials Letters*, vol. 64, no. 22, pp. 2551–2554, 2010.
- [11] R. Cioffi, L. Maffucci, and L. Santoro, "Optimization of geopolymer synthesis by calcination and polycondensation of a kaolinitic residue," *Resources, Conservation and Recycling*, vol. 40, pp. 27–38, 2003.
- [12] J. P. Castro-Gomes, A. P. Silva, R. P. Cano, J. Durán Suarez, and A. Albuquerque, "Potential for reuse of tungsten mining waste-rock in technical-artistic value added products," *Journal of Cleaner Production*, vol. 25, pp. 34–41, 2012.
- [13] J. D. Gavronski, *Mineral Coal and Renewable Energies in Brazil*, Federal University of Rio Grande do Sul, Porto Alegre, Brazil, 2007.
- [14] R. A. A. B. Santa, A. M. Bernardin, H. G. Riella et al., "Geopolymer synthesized from bottom coal ash and calcined paper sludge," *Journal of Cleaner Production*, vol. 57, pp. 302–307, 2013.
- [15] H. K. Tchakoute, C. H. Rüscher, J. N. Y. Djobo, B. B. D. Kenne, and D. Njopwouo, "Influence of gibbsite and quartz in kaolin on the properties of metakaolin-based geopolymer cements," *Applied Clay Science*, vol. 107, pp. 188–194, 2015.
- [16] H. Y. Zhang, V. Kodur, S. L. Qi, L. Cao, and B. Wu, "Development of metakaolin-fly ash based geopolymers for fire resistance applications," *Construction and Building Materials*, vol. 55, pp. 38–45, 2014.
- [17] P. Duan, C. J. Yan, W. J. Luo, and W. Zhou, "A novel surface waterproof geopolymer derived from metakaolin by hydrophobic modification," *Materials Letters*, vol. 164, pp. 172–175, 2016.
- [18] M. Ardanuy, J. Claramunt, and R. D. T. Filho, "Cellulosic fiber reinforced cement-based composites: a review of recent research," *Construction and Building Materials*, vol. 79, pp. 115–128, 2015.
- [19] M. Marcin, M. Sisol, and I. Brezani, "Effect of slag addition on mechanical properties of fly ash based geopolymers," *Procedia Engineering*, vol. 151, pp. 191–197, 2016.
- [20] M. Soutos, A. P. Boyle, R. Vinai, A. Hadjierakleous, and S. J. Barnett, "Factors influencing the compressive strength of fly ash based geopolymers," *Construction and Building Materials*, vol. 110, pp. 355–368, 2016.
- [21] X. Ma, Z. H. Zhang, and A. G. Wang, "The transition of fly ash-based geopolymer gels into ordered structures and the effect on the compressive strength," *Construction and Building Materials*, vol. 104, pp. 25–33, 2016.
- [22] C. D. Atis, E. B. Gorur, T. Karahan, C. Bilim, S. Likentapar, and E. Luga, "Very high strength (120 MPa) class F fly ash geopolymer mortar activated at different NaOH amount, heat curing temperature and heat curing duration," *Construction and Building Materials*, vol. 96, pp. 673–678, 2015.
- [23] F. N. Okoye, J. Durgaprasad, and N. B. Singh, "Effect of silica fume on the mechanical properties of fly ash based-geopolymer concrete," *Ceramics International*, vol. 42, no. 2, pp. 3000–3006, 2016.
- [24] B. B. K. Diffoa, A. Elimbi, C. J. D. Manga, and H. T. Kouamo, "Effect of the rate of calcination of kaolin on the properties of metakaolin-based geopolymers," *Journal of Asian Ceramic Societies*, vol. 3, no. 1, pp. 130–138, 2015.
- [25] J. Davidovits, *Geopolymers Based on Natural and Synthetic Metakaolin—A Critical Review*, Elsevier, New York, NY, USA, 2015.
- [26] V. Medri, S. Fabbri, J. Dedecek, Z. Sobalik, Z. Tvaruzkova, and A. Vaccari, "Role of the morphology and the dehydroxylation of metakaolins on geopolymerization," *Applied Clay Science*, vol. 50, no. 4, pp. 538–545, 2010.
- [27] S. K. Nath, S. Maitra, S. Mukherjee, and K. Sanjay, "Microstructural and morphological evolution of fly ash based geopolymers," *Construction and Building Materials*, vol. 111, pp. 758–765, 2016.
- [28] A. M. Rajabi and F. O. Moaf, "Simple empirical formula to estimate the main geomechanical parameters of preplaced aggregate concrete and conventional concrete," *Construction and Building Materials*, vol. 146, pp. 485–492, 2017.

- [29] S. Salehi, M. J. Khattak, A. H. Bwala, and F. S. Karbalaei, "Characterization, morphology and shear bond strength analysis of geopolymers: implications for oil and gas well cementing applications," *Journal of Natural Gas Science and Engineering*, vol. 38, pp. 323–332, 2017.